Characterising Dust Emission Events From Long-term Surface Observations in Northern Africa

Sophie Margaret Cowie

Submitted in accordance with the requirements for the degree of
Doctor of Philosophy

The University of Leeds
School of Earth and Environment
November 2014

Declaration of Authorship

The candidate confirms that the work submitted is her own, except where work which has formed part of jointly authored publications has been included. The contribution of the candidate and the other authors to this work has been explicitly indicated below. The candidate confirms that appropriate credit has been given within the thesis where reference has been made to the work of others. The publication: Cowie, S.M., Knippertz, P. & Marsham, J.H. (2013). Are vegetation-related roughness changes the cause of the recent decrease in dust emission from the Sahel? *Geophysical Research Letters*, **40**, 1868–1872 was jointly authored with Peter Knippertz (Karlsruhe Institute of Technology) and John Marsham (University of Leeds) and forms the majority of Chapter 3. The candidate produced the initial plots, analysis and first draft. Discussion then took place between the co-authors and the candidate on what the main points to focus on were and they both gave advice on further plots and analysis to do. The co-authors helped refine the structure of the paper and with the wording of important results and conclusions to ensure maximum clarity. The publication: Cowie, S.M., Knippertz, P. & Marsham, J.H. (2014). A climatology of dust emission events from northern Africa using long-term surface observations. *Atmospheric Chemistry and Physics Discussions*, **14**, 7425–7468 was also jointly authored with Peter Knippertz and John Marsham and forms the majority of Chapter 5. The contribution from the co-authors was the same as in Chapter 3. This chapter has been revised by the candidate based on reviewers comments which are available online at the ACPD website. A further draft is currently being considered by the editor for inclusion in the Atmospheric Chemistry and Physics journal.

Acknowledgements

My biggest thanks go to my supervisors Peter Knippertz and John Marsham. Peter, for giving me this opportunity and for always being available to give advice, feedback and (a lot of) encouragement. John, thank you for being extremely patient and supportive, particularly in the past year, and for being equally encouraging and not losing faith in my work, even when I almost had. Without fail you both knew exactly how to pick me up and get me going again when I had lost motivation and confidence. I feel extremely lucky to have had the opportunity to work with you both and look forward to continuing this in the future.

I could not have got through difficult times without the help and support of many others. My fellow office colleagues in 11.121 - although the inhabitants have changed over the 4 years, there has always been lively chats, structural disasters and lunchtime problem solving and sharing. Thanks to Matt Woodhouse, Lars Weigand and Kerstin Schepanski for teaching me all the scripting and computing I know. Thank you Richard Rigby for all the great IT support. To Ann, Kathryn and Erin for all the lovely lunches in the sun and to Jim Watson for the great conversations. Thank you Aaron O'Leary for introducing me to Headphone Commute, I can't concentrate or sleep without ambient music now.

My friends in Coffee and Cakes Cycling Club have provided all of the background entertainment, support and distractions - you all mean the world to me and I can't thank you enough. Thanks for the early morning winter rides, chasing the Tour de France in the French Pyrénées, climbing, camping, stew nights and late nights. Thank you to my good friend Nathan Gopichandran, for always looking out for me, rescuing me from bike mishaps, feeding me steak and inspiring me to live life to the full.

I am grateful to my lovely and supportive family in Perth. Thank you for always being there to take the pressure off, when I couldn't manage it myself.

Thank you to the BADC for providing the MIDAS Land and Marine Surface Station Data which most of this thesis is based on. Thanks to the European Research Council for providing my funding for this work (Grant: 257543).

Abstract

Dust plays multiple important roles in the Earth system with emissions from northern Africa contributing on the order of 60% to the global total. Current model estimates of annual dust production from this crucial region vary by a factor of up to 5. This low agreement between models is to a great extent due to differences in the representation of near-surface winds. One barrier to better understanding of wind processes is the sparse observation network in northern Africa combined with regionally varying, but not necessarily documented, reporting procedures that lead to uncertainties and biases.

Previous studies have utilised long-term station observations of visibility over this region to investigate dust climatology, but this work is the first to focus specifically on emission, based on quality-controlled reports from station observers and measurements of 10 m wind-speed. The interannual, seasonal and diurnal cycles of dust emission frequency (FDE), as well as trends, are investigated using existing and new analysis methods, such as the estimation of emission thresholds.

Spatially, it is shown that threshold wind-speeds for dust emission are highest in northern Algeria and lowest in Sudan and around the latitude band 16°N - 21°N. FDE peaks in spring at most stations, while in the Sahel seasonal cycles vary between stations depending on their proximity to the Saharan Heat Low, and as a result of seasonal exposure to both the summer monsoon and winter Harmattan. Seasonally, FDE is largely controlled by changes in strong winds, rather than changes in emission thresholds.

The relative contribution of different wind-speeds to dust uplift are investigated using the observed winds and calculated thresholds. Case studies and field campaign data are analysed to determine the plausibility of SYNOP high-wind reports. In northern regions, 50% of uplift is associated with high winds which occur only 0.3% - 0.5% of the time. This contrasts with an occurrence range of 0.7% - 2.5% for southern regions. Winds of 12 - 15 ms^{-1} contribute the most to northern total DUP, while in the south the range is lower at 7-11 ms^{-1}. A percentage occurrence of 0.3% equates to only 5.5 events per year.

Previous studies have documented changes in the dust output from northern Africa on interannual to decadal time scales, though the reasons for this variability are still debated. This study shows that the likely contributors to an observed decreasing trend in FDE are

changes in circulation patterns, changes to the Bowen ratio and, most significantly, the effect of a change in roughness on wind-speed as a result of a greening of the Sahel.

This work forms a base for further investigations into mechanisms for dust emission in northern Africa and their relative importance, as well as providing reference material for model and reanalysis evaluation.

Contents

List of Figures

List of Tables

Symbols

U	Wind-speed
V	Mean wind-speed
U^*	Friction velocity
U_t^*	Threshold friction velocity
τ	Wind shear stress
ρ_a	Air density
z_0	Roughness length
z	Height
g	Gravity
ρ_p	Particle density
A	Dimensionless threshold parameter
D_p	Particle diamater
F_h	Horizontal flux parameter
F_v	Vertical flux parameter
α	Sandblasting mass efficiency
C	Constant of proportionality
V_s	Terminal velocity
U	Dynamic viscosity of air
C_c	Correction slip factor
λ	Mean free path of gas molecules in air
R_a	Aerodynamic resistance
R_s	Quasi-Laminar (surface) resistance
V_d	Dry deposition

Abbreviations

AEJ	**A**frican **E**asterly **J**et
AEW	**A**frican **E**asterly **W**ave
AERONET	**A**erosol **R**obotic **NET**work
AI	**A**erosol **I**ndex
AMMA	**A**frican **M**onsoon **M**ultidisciplinary **A**nalysis
AOD	**A**erosol **O**ptical **D**epth
AOT	**A**erosol **O**ptical **T**hickness
AVHRR	**A**dvanced **V**ery **H**igh **R**esolution **R**adiometer
BDF	**B**lowing **D**ust **F**requency
BODEx	**BOD**élé Field **Ex**periment
CALIOP	**C**loud-**A**erosol **LI**dar with **O**rthogonal **P**olarization
CCN	**C**loud **C**ondensation **N**uclei
DD	**D**ust **D**evils
DODO	**D**ust **O**utflow and **D**eposition to the **O**cean
DP	**D**ust **P**lume
DSF	**D**ust **S**torm **F**requency
DUP	**D**ust **U**plift **P**otential
ECMWF	**E**uropean **C**entre for **M**edium-range **F**orecasts
FDE	**F**requency of **D**ust **E**mission
GERBILS	**G**eostationary **E**arth **R**adiation **B**udget **I**ntercomparison of **L**ongwave and **S**hortwave Radiation
GIMMS	**G**lobal **I**nventory **M**odeling and **M**apping **S**tudies
IPCC	**I**ntergovernmental **P**anel on **C**limate **C**hange
IR	**I**nfra **R**ed
ITCZ	**I**nter-**T**ropical **C**onvergence **Z**one

ITD	**I**nter-**T**ropical **D**iscontinuity
ITF	**I**nter-**T**ropical **F**ront
LLJ	**L**ow **L**evel **J**et
MCS	**M**esoscale **C**onvective **S**ystem
MISR	**M**ulti-angle **I**maging **S**pectro**R**adiometer
MODIS	**MOD**erate Resoltion **I**maging **S**pectroradiometer
MSG	**M**eteosat **S**econd **G**eneration
NAO	**N**orth **A**tlantic **O**scillation
NCEP	**N**ational **C**enters for **E**nvironmental **P**rediction
NCAR	**N**ational **C**enter for **A**tmospheric **R**esearch
NDVI	**N**ormalized **D**ifference **V**egetation **I**ndex
OMI	**O**zone **M**onitoring **I**nstrument
PBL	**P**lanetary **B**oundary **L**ayer
PIBAL	**PI**lot **BAL**loon Reports
PDF	**P**robability **D**ensity **F**unction
RF	**R**adiative **F**orcing
POLDER	**POL**arization and **D**irectionality of the **E**arth's **R**eflectances
SAMUM	**SA**haran **M**ineral D**U**st Experi**M**ent
SCBL	**S**aharan **C**onvective **B**oundary **L**ayer
SEVIRI	**S**pinning **E**nhanced **V**isible and **I**nfrared **I**mager
SRL	**S**aharan **R**esidual **L**ayer
SWF	**S**trong **W**ind **F**requency
TOMS	**T**otal **O**zone **M**apping **S**pectrometer
WAM	**W**est **A**frican **M**onsoon
UV	**U**ltra **V**iolet

Chapter 1

Introduction

1.1 Motivation

Mineral dust in the atmosphere has a number of impacts not only on climate, but also on daily human life. To predict future impacts we need to better quantify how much mineral dust is in the atmosphere, its geographical distribution, and improve understanding of how it got there. Northern Africa has been identified as the most important source in the global dust cycle (Prospero, 2002; Washington *et al.*, 2003), yet the size and variability of the contribution, and the source locations, are widely debated and a rapidly expanding area of research. Current model estimates of northern Africa (herein N Africa) dust emissions range from 400 to 2200 Tg yr^{-1}; a factor of 5.5 (Huneeus *et al.*, 2011). Advances in satellite remote sensing and modelling in the past 20 years have greatly increased understanding of the N African dust cycle, though there is still significant debate regarding the relative contributions of the different meteorological mechanisms towards the overall dust loading. Motivated by this debate, this thesis aims to improve understanding of the key meteorological processes which generate high wind events and dust emissions in arid and semi-arid regions of N Africa. This chapter will provide a background on: the effect of airborne mineral dust in the atmosphere in section 1.2, a discussion on the dust cycle in N Africa in section 1.3, and the different ways in which N Africa meteorology and mineral dust are observed in section 1.4.

1.2 Mineral Dust in the Climate System

1.2.1 Dust Emission

The lifting of dust particles into the atmosphere is dependent firstly on the wind providing sufficient momentum and secondly on characteristics of the surface over which the wind blows. Surface characteristics dictate the minimum wind velocity required to transfer momentum from the wind to particle movement.

There are two main processes which entrain dust to the atmosphere; aerodynamic entrainment and saltation. Initially proposed by Bagnold (1941), particle movement can be described as suspended, saltating or creeping and these descriptions do no necessarily involve the particles becoming airborne (in the case of creep).

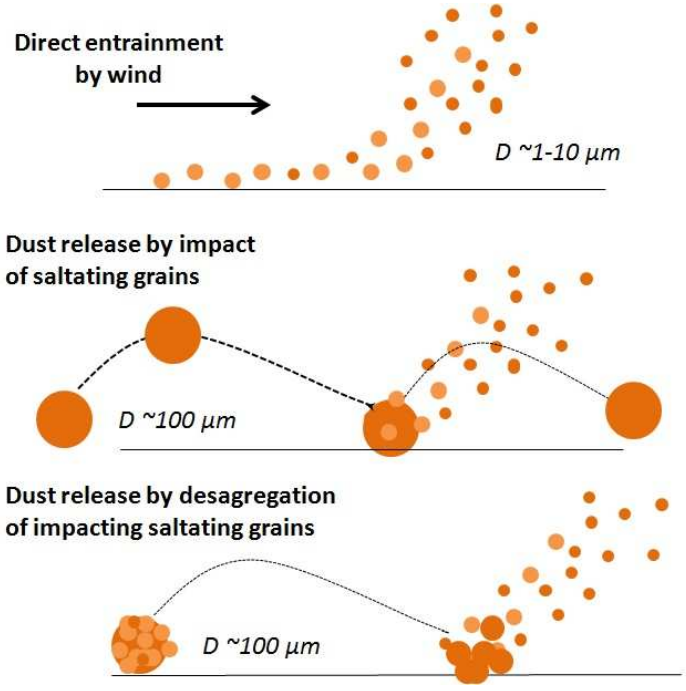

FIGURE 1.1: Mechanisms for dust emission, from Marticorena (2014) and adapted from Shao (2009). a) dust emission by aerodynamic lift, b) by saltation bombardment and c) by disaggregation.

Aerodynamic entrainment occurs when small particles (generally < 60 μm) are mobilised directly by the wind (Fig. 1.1, top panel). In reality this rarely occurs, as wind-tunnel studies such as Shao *et al.* (1993) suggest that this would require high wind-speed due to the high interparticle cohesion forces between small particles. The overall flux to the atmosphere by aerodynamic forces alone is small compared to other mechanisms (Loosmore

& Hunt, 2000). Particles of this size are indeed common in desert soils and have been observed to be transported globally (Goudie & Middleton, 2001) which implies dust is mostly entrained via another mechanism: saltation.

Saltation is the main process by which dust is entrained to the atmosphere. The saltating movement of particles is shown in the middle and bottom panels of Fig. 1.1 for soil grains of diameters anywhere from 60 - 2000 μm (Marticorena & Bergametti, 1995), but in particular those of 70-100 μm (Marticorena, 2014). These particles are lifted (typically tens of centimeters, but can be up to one meter (Marticorena & Bergametti, 1995)) from the surface before following a ballistic trajectory and finally falling back to the surface some distance downwind. The drag is not sufficient to exceed their weight and so they fall back down to earth, rather than becoming suspended. Impact with other particles on return to the surface is strong enough to overcome interparticle binding forces. As a result, momentum is transferred to other similar sized particles which go on to also rise and fall in a similar way or to smaller particles which may then become suspended in the atmosphere. The ejection of smaller particles, which can then become suspended via saltation is generally know as sandblasting. Saltation also removes some momentum from the air, providing a resistance to the wind (Marticorena & Bergametti, 1995). Particles clumped together may break up during this process, also known as disaggregation (bottom panel, Fig. 1.1) and these will not necessarily go on to eject other particles in the same way as particle release by impact alone (middle panel, Fig. 1.1). If not considering soil type, both types of saltation (by impact alone, or by disaggregation) are important. However, for hard soils, Shao (2001) found disaggregation to be more important, and impact alone for soft soils.

Particles with diameters > 2000 μm, or as little as > 500 μm suggested by Sterk *et al.* (1996), are generally too heavy to be lifted (Marticorena & Bergametti, 1995). However, momentum from the wind is enough to mobilise them so they roll or "creep" horizontally along the surface from a distance of centimetres up to several meters (Sterk *et al.*, 1996).

The entrainment processes shown in Fig. 1.1 require momentum from the wind. In aeolian erosion studies this momentum transfer is described by the parameters; wind friction velocity (U^*) and thresold wind friction velocity (U_t^*). The wind friction velocity can be described as a function of the wind shear stress, τ and air density ρ_a:

$$U^* = \sqrt{\frac{\tau}{\rho_a}} \tag{1.1}$$

and also as the standard deviation of velocity fluctuations (Shao, 2009):

$$U^* = \sqrt{\overline{u'w'}} \propto \sigma \tag{1.2}$$

where u' and w' are the deviations from the u and w vectors of the wind velocity field. In neutral conditions where there is no vertical gradient in potential temperature, the wind friction velocity can be described as:

$$U^* = U_0 kln\left(\frac{z}{z_0}\right)^{-1} \tag{1.3}$$

where k is the von Karman constant (0.4), z_0 is the aerodynamic roughness length and z is height, where $z > z_0$. However, to allow the transfer of energy the threshold wind friction velocity U_t^* must first be exceeded. The U_t^* term can calculated by:

$$U_t^* = A\sqrt{\frac{\rho_p g D_p}{\rho_a}} \tag{1.4}$$

Where g is gravitational acceleration, ρ_p is particle density, D_p is particle diameter, ρ_a ia air density and A is a dimensionless threshold parameter which depends on the friction Reynolds number (Marticorena & Bergametti, 1995).

As U_t^* is a function of particle size, it is therefore desirable to know what the size distribution of particles are in source regions. The relationship between U_t^* and D_p is given in Fig. 1.2, based on Marticorena & Bergametti (1995) and Iversen & White (1982). Three of the main points to note from Fig. 1.2 are as follows: 1) a high U_t^*(>100 cm s$-$1) for small particles, 2) optimum U_t^* values are achieved by the most easily erodible particles with diameters of 60 - 100μm and 3) U_t^* increases for particles >100μm and decreases for diameters smaller than 60μm.

Under ideal conditions, with no influence from roughness elements, the size distribution of soil particles is a key factor to the emission threshold. In reality, arid and semi-arid regions

have an abundance of particles in the optimum size range (Chatenet *et al.*, 1996), so the erosion threshold is more likely to be controlled by soil moisture and surface roughness.

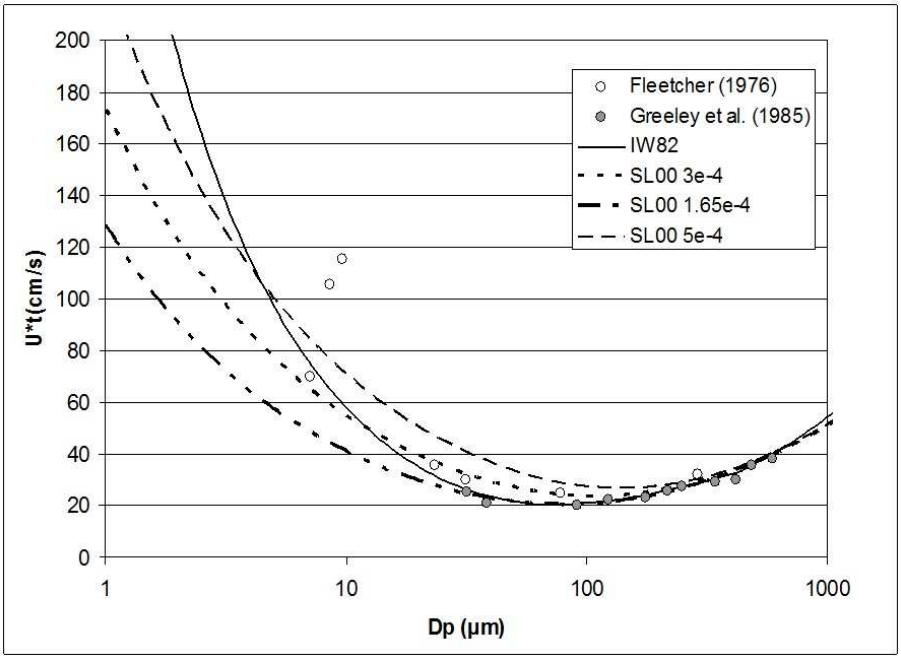

FIGURE 1.2: Threshold wind friction velocity (U_t^*) as a function of particle diameter based on Iversen & White (1982) (IW82) and Shao & Lu (2000) for different values of interparticle forces, (SLOO). White dots are experimental data from Fletcher (1976a,b) and grey dots from Greeley & Iversen (1985). Figure taken from Marticorena (2014) and Shao (2009).

It is well documented in the literature that, in a general sense, U_t^* increases as soil moisture increases (Chepil, 1956). The relationship between soil moisture and erosion depends on a number of factors such as the soil texture and vegetation growth (Fecan *et al.*, 1999). Fecan *et al.* (1999) introduce a minimum soil moisture parameter, w', required to induce a threshold increase. Experimental data revealed that this w' term increased as clay content increased in soils. Field measurements of erosion thresholds in wet and dry conditions from the Taklamakan desert are in agreement with the parameterisation of Fecan *et al.* (1999). Another approach by Cornelis *et al.* (2004) presents an expression for threshold shear velocity which considers soil moisture content alongside particle size and density.

For hot, dry and sandy deserts such as the Sahara, soil moisture may be less important. In these environments wind erosion has been observed to take place as little as 10 - 30 mins following a rainstorm (Gillette *et al.*, 2001), due to a thin eroding layer which can dry quickly under the low humidity and high temperatures. In general, soil moisture is critical

to U_t^* in temperate climates with higher clay content, while in the drier, arid deserts, such as the Sahara, soil moisture is less of a factor.

The roughness of a surface can also influence U_t^* values (Menut *et al.*, 2013). Aerodynamic roughness length (or roughness length, z_0) is defined in the AMS meteorological glossary as a theoretical height above the displacement plane at which the mean wind become zero when extrapolating the logarithmic wind-speed profile downward through the surface layer. In dust modelling, z_0, is used to calculate the wind friction velocity (Eq. 1.3) which estimates the wind-speed at the surface. Two different drag partition schemes, one by Raupach *et al.* (1993) and another by Marticorena & Bergametti (1995), are widely used in the modelling of erosion thresholds over rough surfaces. These schemes aim to take into account non-erodible roughness elements and their influence on the surface wind shear stress alongside the surface wind shear stress un-hindered by non-erodible objects. Non-erodible (rough) features can create an apparent increase in emission threshold in two ways. Firstly, the area covered by the non-erodible element decreases the total area available for potential erosion and secondly, they absorb part of the wind momentum that could otherwise initiate erosion at the surface. In equation. 1.2, U_t^* is based on the assumption that the shear stress component, τ, is acting on a smooth (erodible) surface. Using a partition scheme, with z_0 derived from satellite, Laurent *et al.* (2005) produced wind velocity thresholds over East Asian Deserts which were in remarkable agreement with those calculated from wind velocities associated with surface observations of dust storms (Kurosaki & Mikami, 2007).

When the thin surface layer of soil is compacted, through natural processes such as intense rainfall, or anthropogenic causes such as trampling by livestock or vehicles, crusts may be formed. Crusts can inhibit emission by covering up erodible soil, or modifying soil sediment supply. If, however the crusts are broken up, or prevented from forming, dust emission may be enhanced (Gillette *et al.*, 1982). Crust formation and destruction could be important for the temporal and spatial variability of dust fluxes in semi-arid areas (Marticorena, 2014).

Taking the theory previously discussed on processes and the parameterization of U^* and U_t^* the next step is to calculate the erosion fluxes. By estimating vertical fluxes it is possible to model how much dust can actually be entrained to the atmosphere, where it then enters the transport and deposition stages of the dust cycle. As previously mentioned, direct

entrainment of particles via the wind is negligible due to the high U_t^* as a result of the stronger cohesive forces between smaller particles (Zender *et al.*, 2003). Hence, to calculate the vertical flux (often called dust flux) to the atmosphere, the horizontal (saltation) flux must first be considered. If assumed that all wind momentum is transferred to the soil, it was initially suggested by Bagnold (1941) that the horizontal flux is proportional to U^* to the power of 3. This relationship has been confirmed by wind tunnel experiments (Gillette, 1979; Shao *et al.*, 1993).

In their parameterisation of horizontal flux, Marticorena & Bergametti (1995) first assume that:

$$G \approx ML \tag{1.5}$$

where G = horizontal flux, M = mass of material falling per unit area time and L is the characteristic pathlength of saltating particles. White (1979) experimentally observed the relation between mass of particles in motion and erosion threshold to be:

$$M \approx \rho_a \left(U^* - U_t^*\right) \tag{1.6}$$

where ρ_a is the air density in kg m^{-3} and mean pathlength, L, to be:

$$L \propto \frac{\left(U^* + U_t^*\right)^2}{g} \tag{1.7}$$

which led Marticorena & Bergametti (1995) to the following horizontal flux parameterisation, assuming particles are of suitable and uniform size for saltation:

$$F_h = C \left(\frac{\rho_a}{g}\right) U^{*3} \left(1 + \frac{U_t^*}{U^*}\right) \left(1 - \frac{(U_t^*)^2}{(U^*)^2}\right) \tag{1.8}$$

where C is the constant of proportionality (2.61), determined from the wind tunnel experiments of White (1979).

The typical particle size boundary for either saltation or suspension of the particles is $\sim$ 50μm. Small particles (<50μm) suitable for suspension must therefore require saltation,

as previously described, to get them into the atmosphere. As sandblasting is the main process feeding the vertical (dust) flux, its efficiency can be determined from the horizontal (saltating) flux (Eq. 1.8). The ratio of vertical to horizontal does not vary with U^*, so dust flux is a constant fraction of the horizontal flux. However, sandblasting efficiency depends on soil type which is not taken into account in the horizontal flux. In Zender *et al.* (2003) a sandblasting mass efficiency term, α, is used to create a vertical flux F_v parameter:

$$F_v = \alpha F_h \tag{1.9}$$

where α is very sensitive to the parent soil texture. Zender *et al.* (2003) had to use a uniform value in the global model as soil characterisation was not reliable enough globally at that time.

Despite a good understanding of which processes and factors influence emission fluxes, without better understanding of the real-world spatial and temoporal variations of these factors, such as particle size distribution, soil moisture or vegetation cover (for roughness parameterization), the accuracy of thresholds and hence modelled emissions, will be limited.

1.2.2 Dust Transport

Airborne dust particles can be carried large distances around the world. Depending on the atmospheric conditions and any changes undergone by the particles in transit, deposition can take place at some distance remote from the original source. Deposition processes are discussed in section 1.2.3. There is inevitably some overlap between emission-transport and transport-deposition factors. For example, a strong wind caused by the downward transport of momentum from a low-level jet (LLJ) breakdown (section 1.3.2.1) will not only create strong enough surface winds to mobilise surface soils, but the turbulence itself can deepen the day-time boundary layer, hence mixing the airborne dust to heights suitable for transport. The focus of this section will be how meteorological mechanisms control the transportation of a dust particle to regions far from its source. Understanding the spatial and temporal evolution of dust composition and concentrations in the atmosphere

is important, as airborne dust can impact the radiative budget of the atmosphere (section 1.2.4) and be of concern to human health due to the effects of small particles on the human body (section 1.2.6).

The size distribution of emitted dust is extremely important. Particles with a diameter $<$ 60 μm are small enough to remain suspended in the air long enough to become entrained into larger scale meteorological patterns which export them from the source region. Particles larger than 60 μm in diameter will typically be deposited by dry deposition processes, close to source (section 1.2.3). The type of particle movement will also affect how far the particles are transported. For example, particles may "creep" anywhere from a few centimeters to several metres during a storm, while the same storm could move saltating particles up to a hundred metres and suspended dust thousands of kilometers (Sterk *et al.*, 1996). By parameterising dust transport as a function of partical size and distance travelled Shao (2009) came to the conclusion that particles with a diameter $<$20 μm are able to travel the furthest, though larger particles have been found in samples (Gillette, 1981).

The vertical layering of concentration and characteristics of dust suspended has implications for how much is transported off the continent and very much depends on the day/night evolution of the boundary layer. Surface heating in the daytime creates turbulent eddies at the surface. These grow in size through the course of the day, as sensible heating of the surface increases (Fig. 1.3; I). This layer can reach up to 6 km in height over the Sahara (Cuesta *et al.*, 2008) and may be referred to as the Saharan Convective Boundary Layer (SCBL). At night, radiative cooling of the surface stabilises the lower boundary layer. An inversion forms below this new surface shallow boundary layer top, which is significantly lower than the day-time boundary layer top. The air left behind between the inversion and previous days convective layer top is called the Saharan Residual Layer (SRL), and significant amounts of suspended dust may become trapped there. Directly above the night-time shallow-layer inversion, a low-level wind-speed maximum known as a low-level jet (LLJ) may occur. LLJs are capable of transporting dusty air from the residual layer a long distance from the source. As heating begins the next day the turbulence again forces the boundary layer to grow. As daytime turbulence mixes into the stratified layers formed at night, including the LLJ. As it mixes up to the LLJ altitude, energy from that height is brought to the surface, not only creating emission, but

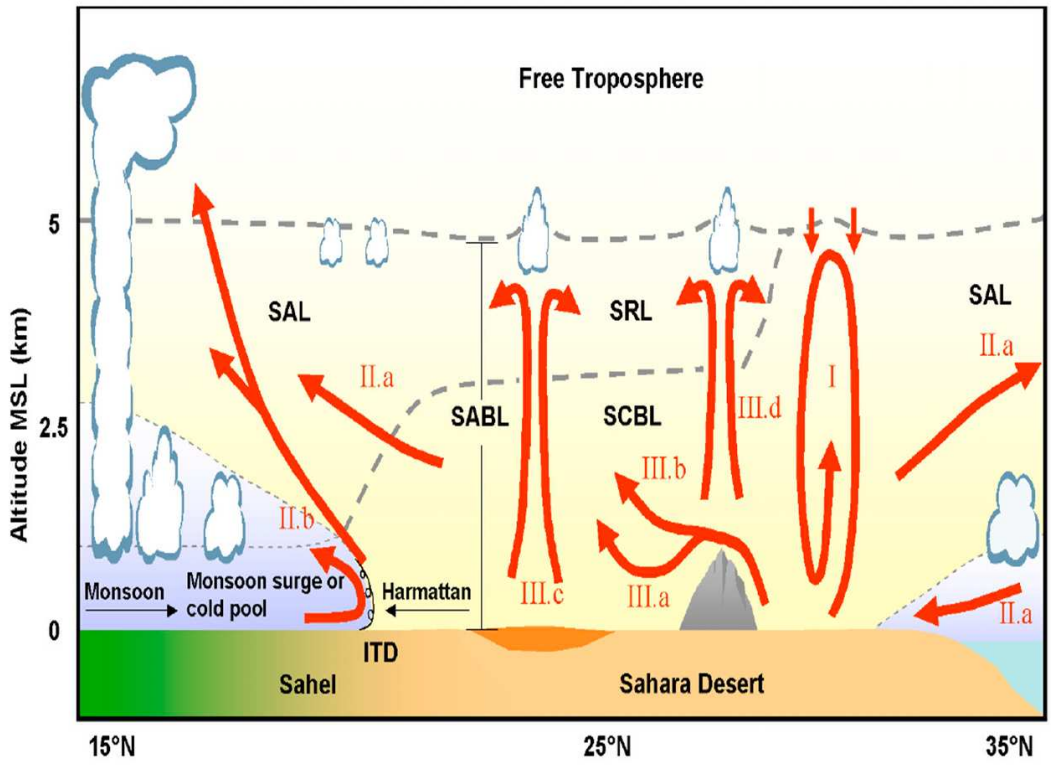

FIGURE 1.3: Schematic of the mechanisms (red arrows) which control the SABL structure and dust vertical redistribution (labels refer to Section numbers in Cuesta *et al.* (2009), but are explain in the text here): I: Diurnal vertical mixing, IIa, b: Dynamical lifting (upgliding, gravity currents and cold air outbreaks) and IIIa, b, c: Topographic effects (mountains and albedo anomalies). Shading (yellow or light blue) indicates air masses origin (i.e. from the SABL, Gulf of Guinea or mid-latitudes) and temperature. This representation does not correspond to any day nor suggest that the SABL is more likely to be well-mixed in the north than the south. Commonly, the SABL state is mostly horizontally homogeneous. From Cuesta *et al.* (2009).

also enhancing the growth of the SCBL and distrbuting emitted dust vertically through the atmospheric column.

In addition to the role of vertical mixing through insolation, any combination of a number of dynamical lifting features, such as cold air intrusions or density currents, may be acting on a source area at one time. Topography is important to the vertical distribution of dust layers and can create effects such as; Hydraulic jumps downstream of orography, flow separation in the lee of mountains, surface albedo and orographic "hot spots" (Birch *et al.*, 2012; Cuesta *et al.*, 2008; Huang *et al.*, 2010).

Cold air intrusions in the form of a cold front may approach from the fringes of N Africa to the interior, driven by mid-latitude troughs (Knippertz & Fink, 2006). The warm and dusty SCBL is forced to rise up and over such an intrusion. The monsoon flow itself can

act as a cold air intrusion, which undercuts the Saharan Air Layer (SAL)(Fig. 1.3; II). The SAL is the term given to the deep mixed layer which forms over the Sahara in summer and is composed of warm and dust laden air which can reach up to 15 - 20000 ft in the warmest month of July (Carlson & Prospero, 1972). Once decoupled from the surface, this elevated SAL can be transported long-range, in a fairly direct westerly direction across the Atlantic (Fig. 1.4; bottom panels). The leading edge of the monsoon flow can also be considered a density current, by the lifting of dust at its turbulent front edge, then elevating it isentropically to the SAL (Bou Karam *et al.*, 2008). On the mesoscale, cold pools formed from thunderstorms (section 1.3.2.2) are not only a major uplift mechanism in the Sahel and southern Sahara (Marsham *et al.*, 2008b, 2011, 2013) but can act as a cold air intrusion and force uplift of the already dust present in the warm air it encounters as it propagates. Also known as "haboobs" (section 1.3.2.2), these events can transport dust large distances across the N Africa continent, or off the coast.

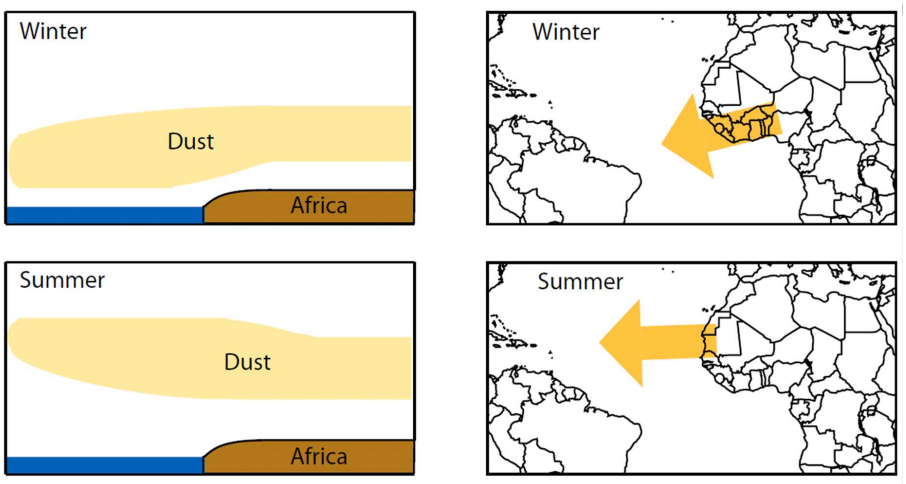

FIGURE 1.4: Schematic diagram of vertical and horizontal dust export from North Africa towards the tropical East Atlantic for Northern Hemisphere winter (top panels) and summer (bottom panels). From Schepanski *et al.* (2009a)

A hydraulic jump occurs when horiztonal wind-speed slows and vertical increases downstream in the lee of a topographic feature (Drobinski *et al.*, 2001). This can occur in the case of the strong north-easterly Harmattan wind in N Africa interacting in this way with the Hoggar Mountains, as captured by CALIOP lidar analysis in Cuesta *et al.* (2009). In this case the vertical mixing created by the hydraulic jump appeared to enhanced the vertical transport of a dust plume initiated the day before.

Another impact of orography, this time in stable conditions, is the separation of the boundary layer into two vertically distinct flows, often including a lower-level reversed flow. In the case of the Hoggar Mountains, this can result in the advection of clean air below a dust plume. In the example given in Cuesta *et al.* (2009), the low-level easterly flow shown is deflected north from an easterly flow, by the elevated terrain.

In the daytime, areas of low albedo can create stronger surface heating, an increased sensible heat flux and therefore a deeper boundary layer (Marsham *et al.*, 2008a) (Fig. 1.3; IIIc). Under these conditions, with a large enough sensible heat flux and low enough background winds, circulations are possible (Segal & Arritt, 1992). It is not known what effect low albedo could have on the SRL, but the suggestion by Cuesta *et al.* (2008) that a hot spot in one part of the SRL would require subsidence and suppression of the boundary layer elsewhere is upheld with evidence from large eddy model simulations in Huang *et al.* (2010).

Evidence from Flamant *et al.* (2007) suggests that elevated heating over mountainous regions creates ascending air directly above, with subsequent subsidence elsewhere (Fig. 1.3; IIId). For example, the height of the Hoggar Mountains of southern Algeria are greater than the height of the morning SCBL, and so the SRL drops below the mountain tops (Cuesta *et al.*, 2009). This means that plumes of hot air can form directly above the Hoggar and into the SRL which in theory will suppress growth of the SCBL elsewhere. In fact, model simulations by Birch *et al.* (2012) suggest that it is the changes to horizontal winds by mountains (in this study, the Hoggar Mountains), which can suppress SCBL growth and that subsidence effects are small.

The development of an SRL and SCBL through the diurnal cycle of surface heating and cooling is a strong control on the vertical distribution of mineral dust. Identifying when and where these two layers occur is a current area of research being investigated through observation campaigns and modelling (Cuesta *et al.*, 2009), though current BL schemes in global models are not able to simulate the complex nature of a layered Saharan BL.

Long-range transport from N Africa dust sources usually follows one of four typical paths for N African emissions. The majority of suspended dust ($\sim 60\%$) is transported southward towards the Sahel and Gulf of Guinea (Shao *et al.*, 2011). However, out of 60% of Saharan emission which tracks south, only $< 5\%$ will make it as far south as 5°N at the surface, as

this is the southern extent of the retreat of the front edge of the monsoon (Afeti & Resch, 2000). The majority of dust at this latitude and southwards will either be subjected to wet deposition processes as it meets the Inter-tropical Convergence Zone (ITCZ) on its southward migration, or pushed up and over the monsoon as it acts as a cold air intrustion.

In winter, when the monsoon circulation has retreated south towards the Gulf of Guinea, transport across the Atlantic is more likely to follow a southwesterly track (Fig. 1.4; top panels), indicated by an annual peak in mean mineral dust concentration in March at Cayenne in French Guiana, South America (Goudie & Middleton, 2001; Prospero, 2002). Most of the transport in this season occurs at lower altitudes (Fig. 1.4; top panels) because the dust-bearing air masses are not forced to rise up and over the cooler monsoon surface air which has retreated further south in this season, before travelling across the Atlantic. Surface winds over the Sahara are also much stronger in this season.

In summer, a more westerly flow is present over Algeria, while south of this, mean wind vectors will be either southwesterly within the monsoon flow, which advances as far north as 20°N (Moulin *et al.*, 1997) or light and variable where the north-easterly trade winds and south-westerly monsoon winds converge. In this season, dust travelling across the Atlantic generally takes a more direct westerly path to Central and North America (Fig. 1.4: bottom panels), and at higher elevations. Shao *et al.* (2011) predict that 25% of emissions follow this path. Dust concentrations at Barbados and Miami are shown to peak in summer (Goudie & Middleton, 2001). An unknown amount of suspended dust may also be precipitated out through below-cloud scavenging (section 1.2.3) as the dust layer meets the monsoon summer rains. Summer dust transport events across the Atlantic typically occur in pulses, related to Africa Easterly Waves (AEW). These wave-like structures are caused by disturbances in the African Easterly Jet (AEJ). The AEJ is a strong mid-tropospheric wind-speed maximum of around 12.5 ms^{-1} which is present due to the strong temperature gradient between the Sahara and the equatorial areas (Thorncroft & Blackburn, 1999). AEWs have a periodicity of 3-5 days and can influence; the variability of dust transport, dust emissions (around the AEW surface vortex) and indirectly support convection and subsequent dust-emitting cold-pools (Knippertz & Todd, 2010, 2012).

The North Atlantic Oscillation (NAO) has been suggested as a key influence on the interannual variability of dust transport across the Atlantic (Chiapello & Moulin, 2002; Chiapello

et al., 2005; Ginoux *et al.*, 2004). The NAO Index is calculated from the normalised (Hurrell, 1995) or standardised (Jones *et al.*, 1997) difference in atmospheric pressure at two stations located in Iceland and Portugal. The NAO directly controls winter dust export through changes to strength and location of the Azores anticyclone (Chiapello & Moulin, 2002; Chiapello *et al.*, 1995). A positive phase in the NAO is associated with stronger trade winds (Chiapello *et al.*, 2005). Riemer *et al.* (2006) found Atlantic dust load correlated the highest with the position of the Azores high and that when it is shifted to low latitudes, wind anomalies have lower magnitudes and an eastward component. When situated at higher latitudes, westerlies are stronger and can potentially increase transport through emitting more dust, or more efficient transport in the strengthened westerlies. When the Azores high is stronger this can also drive "surges" within the north-easterly Harmattan flow, another mechansim to increase uplift (Knippertz & Fink, 2006). Although a link between a stronger and shifted Azores high and increased dust presence in the Atlantic has been established, the relative contribution of transport pattern changes and increased emissions to this relationship is not clear from the literature. It is likely to be a combination of the two which varies from year to year.

Roughly 10% of N African dust is transported northwards to Europe (Shao *et al.*, 2011), brought there by Saharan (also known as Sharav or Khamsin) Cyclones which most frequently occur in spring (Alpert *et al.*, 1990; Hannachi *et al.*, 2011); the season of maximum temperature gradient between the Mediterranean basin and African continent (see section 1.3.2.1). The main sources of dust which is transported northwards are; Eastern Algeria, Tunisia, Libya and Egypt. Saharan dust has been found as far north as the UK (Wheeler, 1986) and northern Scandinavia (Franzen *et al.*, 1994), but mostly only makes it to the southern parts of Europe.

Dayan *et al.* (1991) distinguished central Mediterranean events from eastern Mediterranean events in terms of their vertical layer structure and duration. Events which intrude into central Europe typically have a duration of two days or more, originate from deeper pressure centres, have deeper vertical structures and orginate from the Sahara Desert. Events which affect eastern Europe typically originate from the Arabian Peninsula, have shallower vertical structure, higher pressure centers and are of shorter duration. Transport of dust to Europe shifts from the western Mediterranean in August to the eastern Mediterranean

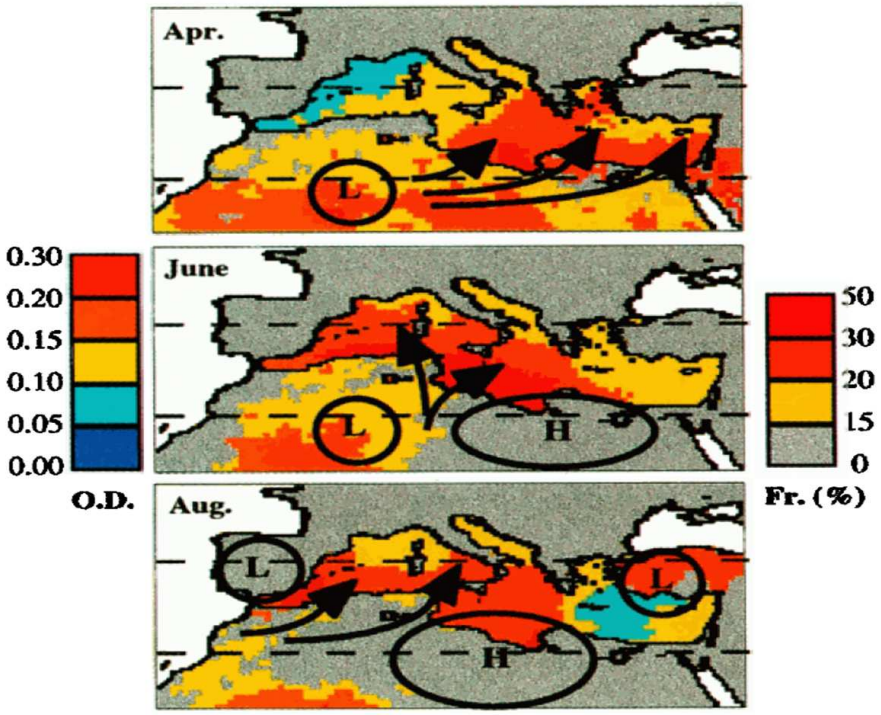

FIGURE 1.5: The main meteorological synoptic situations which generate dust transport during spring and summer. Locations of the major lows (L) and highs (H) are shown. The cyclogenesis is adapted from Alpert *et al.* (1990). It shows the Sharav cyclones in April; the coupling between Saharan low and Libyan high in June; and the effect of the Balearic cyclogenesis in August. The frequency (Fr.) of dust mobilization over North Africa during these months has been estimated from IDDI and computed from Meteosat infrared images between 1984 and 1994, using the method of Legrand *et al.* (1994). Monthly dust optical depths (O.D.) over the sea surface use data from Meteosat images between 1984 and 1994.The lower and upper horizontal dashed lines correspond to latitudes of 30° and 40°N, respectively. From Moulin *et al.* (1998)

in March/April (Fig. 1.5). Different types of Synoptic set up, as shown in Fig. 1.5 drive this variation in cyclone path (Moulin *et al.*, 1998).

Dust transport to the Middle East is thought to be relatively minor ($< 5\%$), usually occurring in spring in conjunction with the easterly movement of low-pressure systems and fed with mineral dust from the Hoggar and Tibesti area sources (Shao *et al.*, 2011).

1.2.3 Dust Deposition

When assessing the dust deposition part of the global dust cycle there are a number of different processes which fall under two main categories: wet and dry deposition. The relative importance of wet and dry deposition changes as a function of distance from a source. Close to the emission source region, dry deposition is most important, but further out,

once dust particles have been transported some way around the earth, wet deposition processes are more efficient at returning the particles to the surface. Dry deposition processes are most important in terms of the overall flux present at any one time in the atmosphere. Because most of the large particles are deposited out, it is important to know the size distribution of surface soils in order to predict both the transport and deposition. Smaller particles (generally, < 60 μm) which are not deposited fairly quickly close to sources due to dry deposition can feed into the major wind regimes of the upper atmosphere, and achieve long-range transport (section 1.2.2). For these particles, wet deposition processes dominate. After emission, dry deposition is most likely to occur first. The largest particles are filtered out, hence leaving only a certain amount of particles with smaller D_p available to wet deposition processes. Wet deposition process will typically occur after a period of time in which the particles are transported elsewhere,most likely to a region in which rainfall is more frequent. Dry deposition velocity, V_d, is a function of particle size. For particles of $D_p < 0.1$ μm, Brownian diffusion is important. Brownian diffusion describes the instantaneous imbalance at any one time on a larger particle caused by the smaller surrounding particles. Where $D_p > 5$ μm, V_d is high and mainly due to gravitational settling. For the intermediate sizes of 0.1 - 5 μm V_d is at a minimum and the inefficient turbulent processes of interception and impaction dominate (Bergametti & Foret, 2014). In addition to particle size, distance from the surface is also a key consideration. There are two layers to be considered; the immediate few cms above the surface, where Brownian diffusion and gravitational settling are important, and above this in the constant flux layer where turbulent processes and gravitational settling become important (Slinn & Slinn, 1980). To represent gravitational settling in theoretical terms, stokes equation can be modified to give V_s (also called the terminal velocity)

$$V_s = \frac{D_p^2 \rho_p g C_c}{18 \mu_{air}} \tag{1.10}$$

Where D_p is the particle diameter, ρ_p is the particle density (2.6 g m^3 for dust particles), C_c is the slip correction factor (Eq. 1.11), μ_{air} is the dynamic viscosity of air and g is the gravitational acceleration (9.81 ms^{-1}) (Bergametti & Foret, 2014; Zhang *et al.*, 2001). The correction slip factor is applied to small particles (Zhang *et al.*, 2001), and can affect those with a diameter ~ 1 μm (Seinfeld & Pandis, 2012).

$$C = 1 + \frac{2\lambda}{D_p}\left[1.257 + 0.4^{\left(\frac{-0.55D_p}{\lambda}\right)}\right] \tag{1.11}$$

where λ is the mean free path of gas molecules in air (6.6 10^{-6} cm).

Turbulent deposition occurs in series (considering the two layers mentioned previously) and so gravitational settling (Eq. 1.10) is added to the diffusion processes which are split up according to layer. When split up, the layers are considered separately as a set of pseudo resistances: aerodynamic resistance (R_a) and quasi-laminar (or surface) resistance (R_s). Both have units of s m^{-1}. In the upper flux layer, R_a takes into account the atmospheric stability and surface roughness (Bergametti & Foret, 2014). Closer to the surface, depends on the particle microphysical characteristics, Brownian diffusion, inertial impaction (when a large particle with higher inertia is unable to follow the flow when it changes direction) and interception (when a particle passes an obstacle at a distance shorter than its physical dimension and collides with the obstacle). The total dry deposition of a system, V_d can therefore be represented by the inverse of the total equivalent resistance plus the gravitational settling velocity, defined in Eq. 1.10:

$$V_d = V_s + (R_a + R_s + R_a R_s V_s)^{-1} \tag{1.12}$$

Wet deposition is the scavenging of particles by various forms of water (Bergametti & Foret, 2014). As dry deposition is inefficient for smaller particles, wet deposition dominates for transported dust (as larger particles do not make it into long-range transport). The importance of wet deposition increases as a function of distance from source, and increasing precipitation amounts (Tegen & Fung, 1994; Zhao *et al.*, 2003). It is the main mechanism for total deposition to the oceans, and in the north Pacific wet exceeds dry deposition by a factor of 10 (Zhao *et al.*, 2003). Removal by wet deposition can take place in two main ways; in-cloud (typically involving submicron particles) or beneath-cloud (larger, coarse-mode particles with diameter > 0.1 μm are scavenged). In-cloud dust particles can become embedded in raindrops by acting as condensation nuclei (Twohy *et al.*, 2009) or ice nuclei (Atkinson *et al.*, 2013). In-cloud scavenging is not currently included in models as these processes are too poorly understood. In transport, particles may undergo

transformation which can make them less or more efficient nuclei. Beneath-cloud scavenging (collision scavenging) is better understood and generally considered to dominate over in-cloud processes. It describes the mechanism whereby larger particles are impacted by falling raindrops. The proportion of aerosol particles removed this way can be represented by the collision efficiency, which itself takes into account diffusion, inertial impaction and interception. These effects are parameterized separately by Garcia Nieto *et al.* (1994) to estimate the overall below-cloud aerosol scavenging. In Zender *et al.* (2003), in-cloud and below-cloud processes were also both treated separately for convective and stratiform precip, as vertical cloud structure can be important.

Dry deposition is hard to measure, as the method of sampling must be able to reproduce the characteristics of a natural surface (Fowler *et al.*, 2009). Geometric properties of the surface can influence the characteristics of the fluid close to it (Goossens, 2005). The thermal stability of the near-surface fluid and absoption rate (ratio of retained to resuspended particles on the surface itself) should also be taken into account when measuring dry deposition (Goossens, 2005). These factors can all have an impact on the R_s (surface resistance) term when calculating the total dry deposition flux (Eq. 1.12).

A summary of existing dust deposition measurements over N Africa and southern Spain are shown in Fig. 1.6. Close to sources regions, the deposition rates are clearly maximised, with values over 110 g m^{-2} yr^{-1} at the stations of Cinzana, Banizoubou and Libya. The decrease in deposition rates as a function from the Saharan/Sahelian sources is identifiable as rates drop in southern Europe and in the south Sahel in Ghana. This could be partly due to high dry deposition rates close to the sources which leave a decreased amount of dust available for transport, and also partly due to meteorological regimes which are less favourable for transport to particular areas, e.g. Spain than Turkey. The AeroCom initiative, which evaluates and compares different global models with each other and observations (Textor *et al.*, 2006) found estimated model values of deposition close to the Sahara (50 - 100 g m^{-2} yr^{-1}) to be in line with the observations shown in Fig. 1.6. Greater research effort is needed to improve model estimates of dust deposition. Improved theoretical and numerical representation of both wet and dry processes is needed, but in order to have this it is crucial to have more observations, year round, in order to evaluate and understand these processes.

FIGURE 1.6: Annual dust deposition fluxes measured over North Africa and in the Mediterranean basin. The data from Banizoumbou, Cinzana and M'Bour are unpublished data provided by LISA (B. Chatenet, B. Marticorena, J.L. Rajot) from measurements performed in the framework of the Sahelian Dust Transect; (2) O'Hara *et al.* (2006); (3) Breuning-Madsen & Awadzi (2005); (4) Avila (1996), Bergametti *et al.* (1989), Kubilay *et al.* (2000), Mattsson & Nihlen (1996). Figure taken from Bergametti & Foret (2014).

1.2.4 Direct and Indirect Radiative Effects

Radiative forcing (RF) is a parameter used to quantify the change in energy fluxes whereby a positive (negative) RF can lead to surface warming (cooling). In the 2013 Intergovernmental Panel on Climate Change (IPCC) report RF is estimated from a mixture of observed and numerically modelled processes. Aerosol particles change the radiation balance through the processes of scattering/reflecting and absorption of incoming short wave and outgoing long-wave radiation, at both the surface and top of troposphere (Sokolik *et al.*, 2001). Cooling takes place when absorbing and scattering reduces the amount of energy which reaches the surface (Kaufman *et al.*, 2002; Spyrou *et al.*, 2013) while atmospheric warming takes place when aerosols absorb and re-emit outgoing long-wave radiation (Dufresne *et al.*, 2002). Current estimates of the RF due to all aerosol species is -0.9 (-1.9 to 0.1) W m^{-2} (Stocker *et al.*, 2013), with all of the positive forcing coming from black carbon absorption of solar radiation, and the negative contributions from organic

carbon, nitrate, sulphate and mineral dust. RF from individual aerosol species is thought to be even more uncertain and the contribution from mineral dust is calculated to be -0.1 ($\pm$0.2) W m^{-2} (Stocker *et al.*, 2013).

Mineral dust has the ability to change the properties of clouds through several processes, which are grouped into indirect and semi-direct effects. Mineral dust acting as cloud condensation nuclei (CCN) creates more, smaller, droplets within a cloud and increases the amount of incoming short wave radiation which is reflected or scattered back out to space (Solomos *et al.*, 2011). This is known as the cloud-albedo effect and is treated purely as a radiative forcing (Denman & Brasseur, 2007). Smaller droplets will also mean less efficient precipitation and could extend the cloud lifetime. The semi direct effect is when aerosols absorb solar radiation, thereby changing the static stability of the atmosphere which in turn can influence the likelihood of convection. There are two possible effects of aerosols on mixed phase clouds. First, glaciation may take place when aerosols provide extra ice nuclei to the cloud and increases the likelihood of precipitation from the cloud. Second, an increase in smaller droplets can delay freezing, which in super-cooled clouds can allow them to reach higher altitudes and colder temperatures. This is known as the thermodynamic effect and it is not even known if this could have a positive or negative effect on RF, let alone the magnitude. All effects of mineral dust in clouds are complex and involve feedbacks to the climate system, which are extremely difficult to quantify and make up the largest source of uncertainty in climate sensitivity estimates (Denman & Brasseur, 2007).

1.2.5 Dust and the Carbon Cycle

Iron (Fe) and Phosphorus (P) are two elements which are particularly important to nutrient-limited ocean and land ecosystems and both are found in aeolian mineral dust. Primary production in the ocean is performed by microscopic organisms called phytoplankton. The method whereby the iron in mineral dust can influence the carbon cycle is commonly know as the "biological pump" and is depicted in Fig. 1.7, taken from Shao *et al.* (2011). Phytoplankton remove CO_2 from the atmosphere and transport it to the deep ocean where it may remain for thousands, if not millions, of years (Shao *et al.*, 2011). The efficiency of the biological pump relies on nitrogen fixation (conversion of N_2 to ammonia), which is turn is speculated to depend on both Fe and P (Mills *et al.*, 2004).

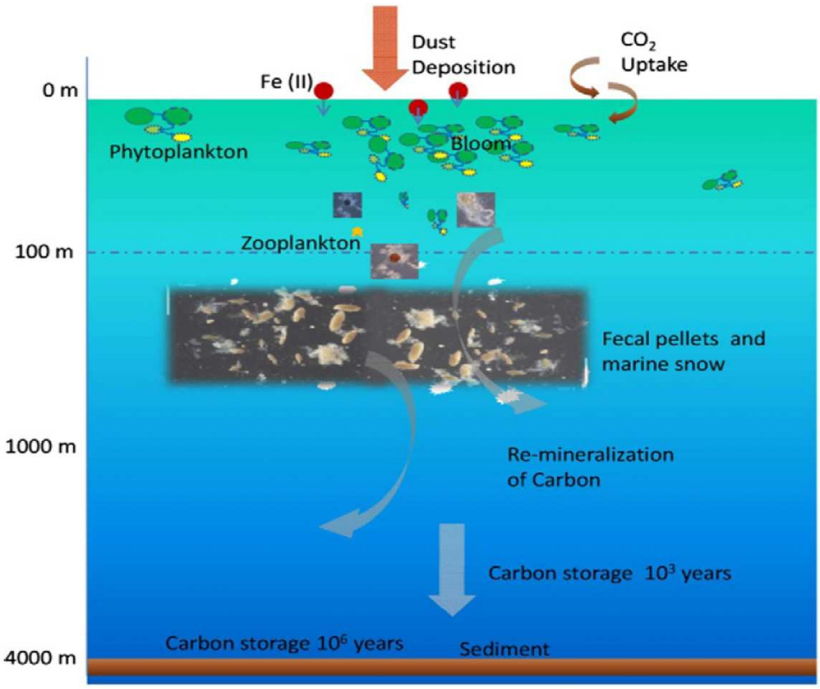

FIGURE 1.7: Removal of iron in mineral dust, known as the "biological pump", from Shao *et al.* (2011)

The sensitivity of the oceans to dust deposits is highly variable, as is the chemical content of dust reaching these regions, which makes it difficult to quantify the impact of mineral dust deposition on ocean carbon cycles (Jickells *et al.*, 2005). Correlations have been made however between increased dust flux and glacial periods of low CO_2 (Maher *et al.*, 2010). Most research has been focussed on the role of iron as a micronutrient to the ocean due to the fact that it is only required in small quantities compared to phosphorus and is also supplied to the surface ocean through upwelling processes. However, the quantity of Fe, which itself may vary by a factor of 2 in aerosols (Mahowald *et al.*, 2005), is not the limiting factor; Fe must be in its soluble form, Fe^{2+} , in order to be bioavailable (useful for phytoplankton growth). Only 0.5% of iron in soils is soluble (Hand *et al.*, 2004), but this increases to a widely uncertain range of 0.01% to 80% in aerosols (Mahowald *et al.*, 2005).

The processes which allow the transition to take place are not well understood (Mahowald *et al.*, 2005), but it has been shown that factors such as the time spent exposed to solar radiation, or interacting with clouds, can enhance the amount of bioavailable iron (Hand *et al.*, 2004). There is also evidence that phosphorus is important (Mahowald *et al.*, 2008),

though the relative contribution compared to iron is not well understood (Mills *et al.*, 2004).

1.2.6 Health Impact of Desert Dust

Links between natural environment and human health are of increasing interest to researchers, especially as 25 - 33% of the global disease burden can be attributed to environmental factors (Smith *et al.*, 1999). The contribution of desert dust to this burden is largely unknown, and while the number of studies is slowly increasing, they tend to focus on Asia and America and not the region of greatest dust presence: N Africa (De Longueville *et al.*, 2010; Karanasiou *et al.*, 2012). The importance of this region for desert dust and health effects is twofold: not only are PM (particulate matter) levels far above "standard" levels for the rest of the world, but the N African population are particularly vulnerable due to the age demographic, poor healthcare and nutrition and the increased exposure to diseases such as malaria, pneumonia and diarrhea which increase the population susceptibility to desert dust-related health problems (De Longueville *et al.*, 2010). However, quantatively linking increases in natural mineral dust to specific health effects, or even general mortality and morbidity statistics is not trivial, and particularly difficult in developing countries where there is a lack of reliable health and air quality data (De Longueville *et al.*, 2010).

Different sized suspended particles create different problems for the human body. Often in air quality monitoring particulate matter (PM) levels PM_{10} and $PM_{2.5}$ are used to express the abundance of different sized particles. Derbyshire (2007) found that PM_{10} made up 40% and $PM_{2.5}$, 20%, of natural Saharan dust deposited on Gran Canaria in March 2004.

Research on exactly how desert dust can affect health is limited and those few studies which do present evidence often disagree due to several differing factors; methods for determining $PM_{2.5}$ and PM_{10}, time periods, areas, methods for defining "dust days" and source areas of desert dust (different sources will have differing composition and therefore different effects). These factors are also why so few studies exist - it is a complex issue to investigate. However, a wide body of evidence does exist which suggests an increase in the amount of suspended particles is detrimental to the overall health of a populated area. The size of a particle size determines where it will come to rest, and the effect it will have on the body

Very coarse particles > 10 μm will generally be ejected by coughing, but may become lodged in the upper respiratory tract. The main health risk from this size of particles are in the chemical composition, i.e. if they contain toxic trace elements or biologically active compounds (Derbyshire, 2007)

PM_{10} was the first PM "standard" to be defined by the US Environmental Protection Agency. PM_{10} describes "inhaleable coarse particles" which have potential to cause health problems and include a range of diameters from 2.5 μm to 10 μm (http://www.epa.gov/air/particlepollution/). Particles of this size may remain suspended in the air for a period of weeks, and create a wide range of respiratory problems (Goudie, 2014), including silicosis (also known as Desert Lung Syndrome; Derbyshire (2007).

Fine particles of diameter < 2.5 μm ($PM_{2.5}$) can penetrate the body further to create problems for the cardiovascular system and other organs (Goudie, 2014).

The impact of mineral dust particles on health may be exacerbated by the presence of pathogens (particles which can cause disease) such as bacteria, fungi and viruses but current research is only beginning to understand the role of these microorganisms within desert dust and health implications (Griffin, 2007).

In their review of European studies linking Sahara dust events to mortality and morbidity through PM standards, Karanasiou *et al.* (2012) found no statistical evidence of a link between fine particles, $PM_{2.5}$, and mortality or morbidity. For the slightly larger particle range PM_{10}, although not in complete agreement, three of the four studies found mortality was increased on Saharan dust days. The overall conclusions of the review were that Saharan dust outbreaks may negatively affect health but further studies were needed.

The connection between chemical composition of desert dust and health remains widely unexplored due to the lack of data and complex nature of the problem. The strongest evidence of a link is provided by Sultan *et al.* (2005) who quantatively link the meningococcal meningitis (MCM) outbreaks in the Sahelo-Sudanian West African band to climate variability. In the dry and windy winter climate, the mucous membranes of the oral cavity may be damaged and create favourable conditions for the bacteria responsible for MCM to thrive.

1.3 Northern Africa Dust Cycle

This section aims to describe the overall climate of N Africa, and a background to the current understanding of the particular meteorological processes and conditions which uplift dust in this region.

1.3.1 Climate of Northern Africa

Northern Africa consists of an area of hyper-arid, arid and semi-arid land larger than the area of the continental United States (Warner, 2004). The largest desert in the world, the Sahara, is situated here. The semi-arid Sahel is generally regarded as the transition zone linking the arid Sahara to the humid, tropical Savannas and experiences a steep north-south gradient in mean annual rainfall (Herrmann *et al.*, 2005; LeHouerou, 1980). The estimated locations of the Sahara, Libya and Nubian deserts, as well as the Sahel and Savanna regions are shown in Fig. 1.8

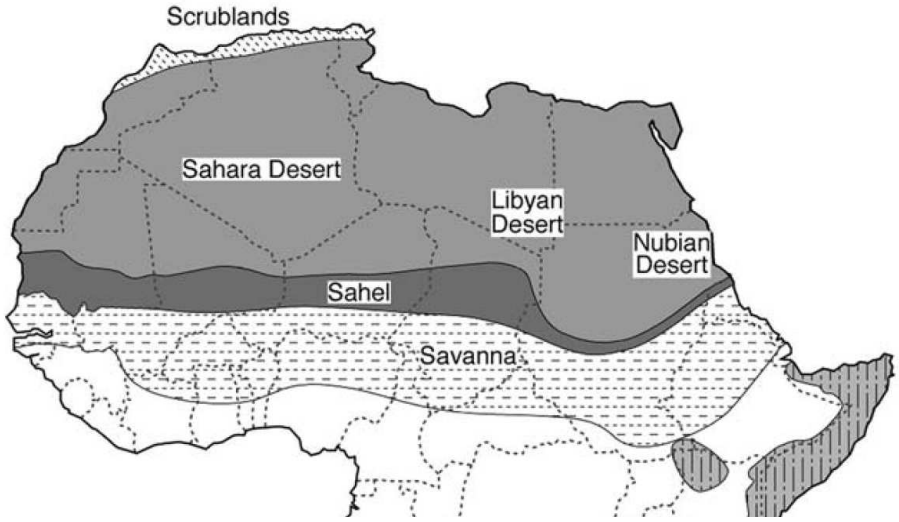

FIGURE 1.8: The deserts of N Africa, from Warner (2004)

Aridity

There are many different ways to define the degree of aridity, which is often more useful than defining a strict separation between desert and non desert. A range of 19 climate indices which can be used to describe aridity are presented in Dzerdzeevskii (1958). Different methods include taking into account the ratio of precipitation (P) to potential evapotranspiration (PET; based on observed solar radiation, wind-speed and humidity). Another

measure, the Budyko index, is concerned with the depth of water that could be evaporated by the observed total annual net radiation, divided by the depth of the observed annual precipitation. This method does not take into account temperature, wind-speed or humidity as the P:PET ratio does, but it can identify less arid coastal areas. Many of these indices are limited by the fact they use annual-averaged data (Warner, 2004), though there are others which can account for seasonal effects, such as the classification scheme by Meigs (1953). The Bukydo index for N Africa, shown in Fig. 1.9, highlights eastern Libya, southern Egypt and northern Sudan as the most arid.

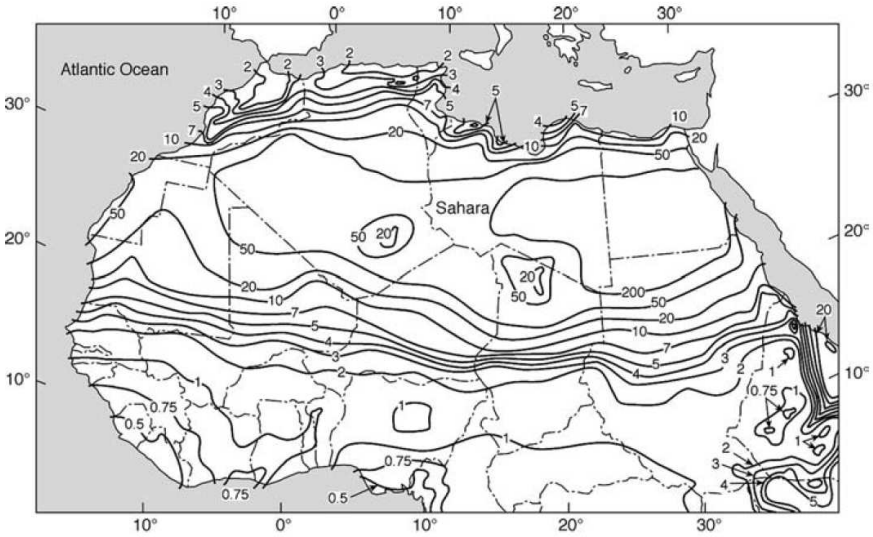

FIGURE 1.9: Aridity distribution for N Africa, based on the Budyko ratio. This is the depth of water that could be evaporated by the observed total annual net radiation, divided by the depth of the observed annual rainfall. From Warner (2004).

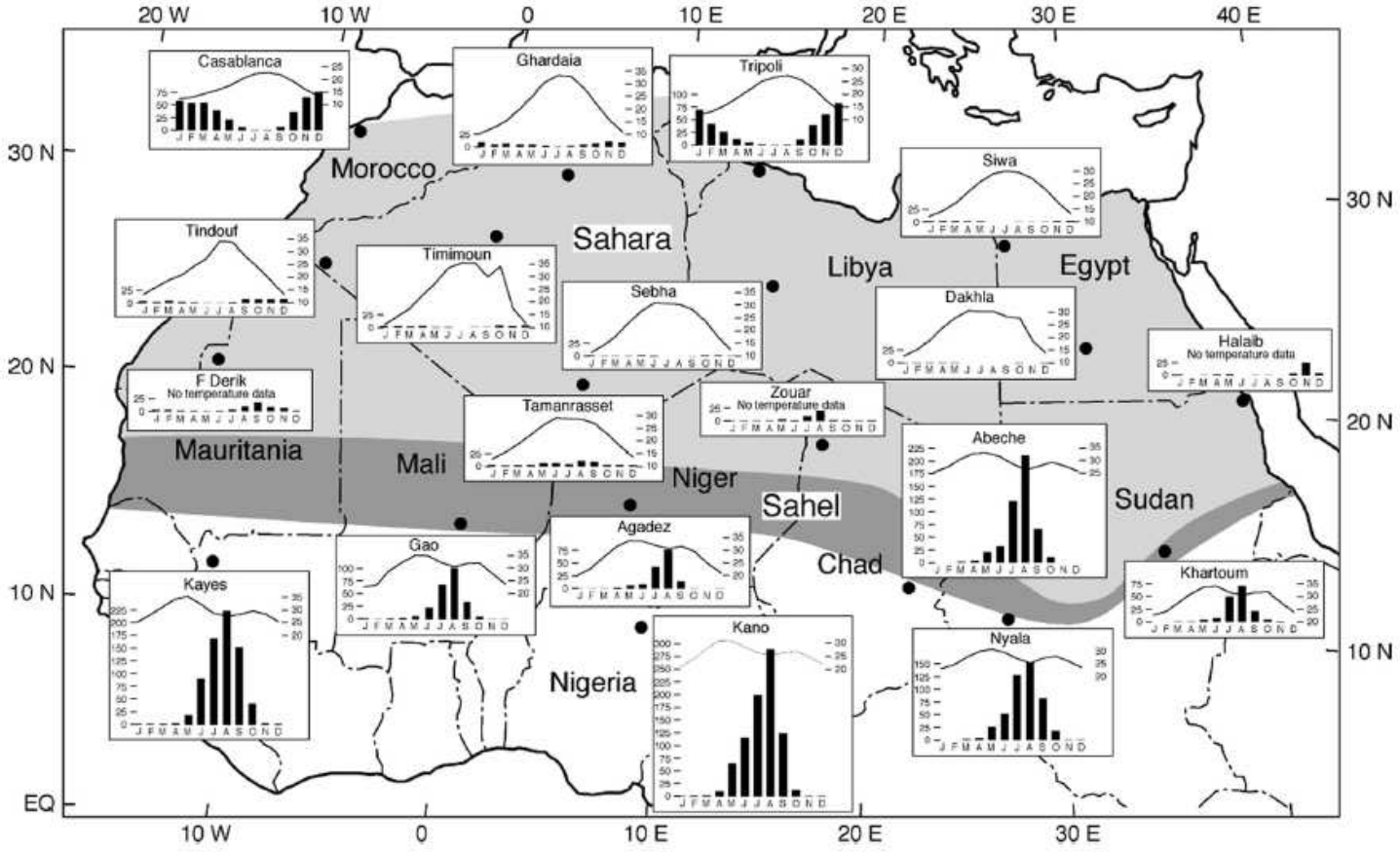

FIGURE 1.10: Monthly distributions of rainfall (mm) and temperature (°C) for selected locations (dots) in the Sahara and Sahel. Shading shows the approximate limits of the Sahara (light) and the Sahel (dark). From Warner (2004).

Rainfall Patterns

Rainfall may be scarce over much of N Africa, but there is a clear seasonal pattern to that which does occur. Seasonal patterns differ for three general areas; northern Sahara close to the Mediterranean coast, central Sahara and south Sahara/Sahel (Fig. 1.10). The northern regions, including Morocco, Algeria, Tunisia, Libya and Egypt experience a Mediterranean climate with wet winters and hot, dry summers. Atlantic cyclones and Mediterranean depressions are the main source of the winter rainfall here. In the central Sahara, very little rainfall occurs at all, though when it does it may be heavy and can cause the localised flooding of wadis (dry and eroded watercourses) which could actually be important in providing new wind-erodible sediment. In the southern Sahara and Sahel, seasonal rainfall is controlled by the advance and retreat of the summer monsoon, and the deep convection associated with it. The exact timing and amounts of precipitation at a particular station is likely to vary largely from year to year due to the sporadic and extreme nature of the convective events.

Large-scale Pressure Systems

The seasonality of large-scale pressure features are the main driving factor of surface wind, and hence dust emission, seasonal patterns. Large-scale pressure changes are mostly driven by changes in the amount of solar radiation received at the surface. The Azores anticyclone is a relatively stationary region of high pressure situated over the Atlantic, one of the two "Centers of Action" (COA), the other being the Icelandic Low (Rossby, 1939). In winter the Azores high extends into the northern Saharan continent where it becomes the Saharan high and a region of large-scale subsidence (Fig. 1.11, top panel). Also at this time, the equatorial trough, a low pressure region where maximum solar insolation occurs, is situated at its most southerly position over the Gulf of Guinea and the ITCZ is close to 5°N.

The ITCZ is commonly associated with the band of maximum deep convection of precipitation and is more easily defined over the oceans. It has been suggested that over the N Africa continent the term ITCZ should be used to describe an area just north of the band of maximum rainfall as maximum surface convergence (as the name "convergence zone" suggests) does not necessarily coincide with maximum rainfall (Mohr & Thorncroft, 2006; Nicholson, 2009). The difference in pressure between these two pressure systems creates a strong northeasterly trade wind over much of the N African continent (Fig. 1.11, top

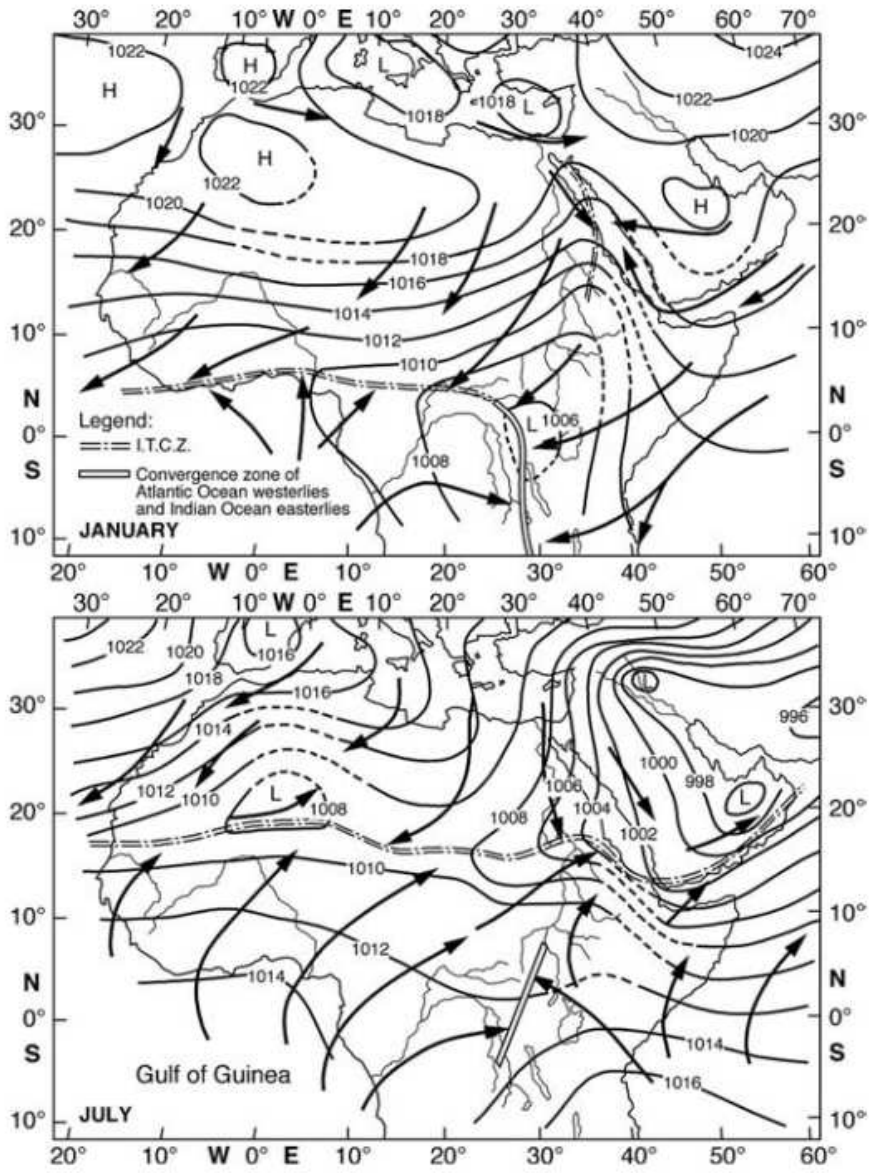

FIGURE 1.11: Large-scale weather patterns over N Africa in January (top panel) and July (bottom panel). The solid lines are sea-level pressure in mb (plotted with 2 mb interval) and arrows are streamlines of surface winds. See the key on the top panel for ITCZ and convergence zone markings. From Warner (2004) and based on Griffiths (1972)

panel), commonly know as the Harmattan. Along the northern Sahara and Mediterranean coastline surface westerlies are largely driven by low pressure in the Mediterranean, but frequent eastward moving depressions in this area give the coastal winds high variability. In the summer season, the Azores high retreats to a more northerly position in the Atlantic and is replaced by the Libya high and over the central Sahara the Saharan Heat Low (SHL) develops (Fig. 1.11, bottom panel). Stronger sensible heating over an area of desert can create a region of low surface pressure which is about 3 - 10 mb lower than that of

the surrounding area (Warner, 2004). As is the case for the SHL, heat lows are generally a summer phenomena due to greater solar input. In the Saharan summer, despite surface low pressure, high pressure is still present at upper levels and this, combined with the extremely dry desert air, acts to inhibit precipitation.

In summer the ITCZ moves to it most northerly position of 15 - 20°N, drawing moist southwesterlies up onto the continent (Fig. 1.11, botttom panel). This is the known as the West African Monsoon (WAM), though for the purposes of this thesis will be referred to as the summer monsoon. From the center of the SHL, in the direction towards the monsoon trough, the height of the boundary layer increases along with the height of convection. A strong gradient in moisture occurs where dry northeasterly desert air meets the moist southwesterlies coming from the Gulf of Guinea. This is known as the intertropical discontinuity (ITD) (Bou Karam *et al.*, 2008), or sometimes the Inter-Tropical Front (ITF) (Cairo *et al.*, 2010; Parker *et al.*, 2005b).

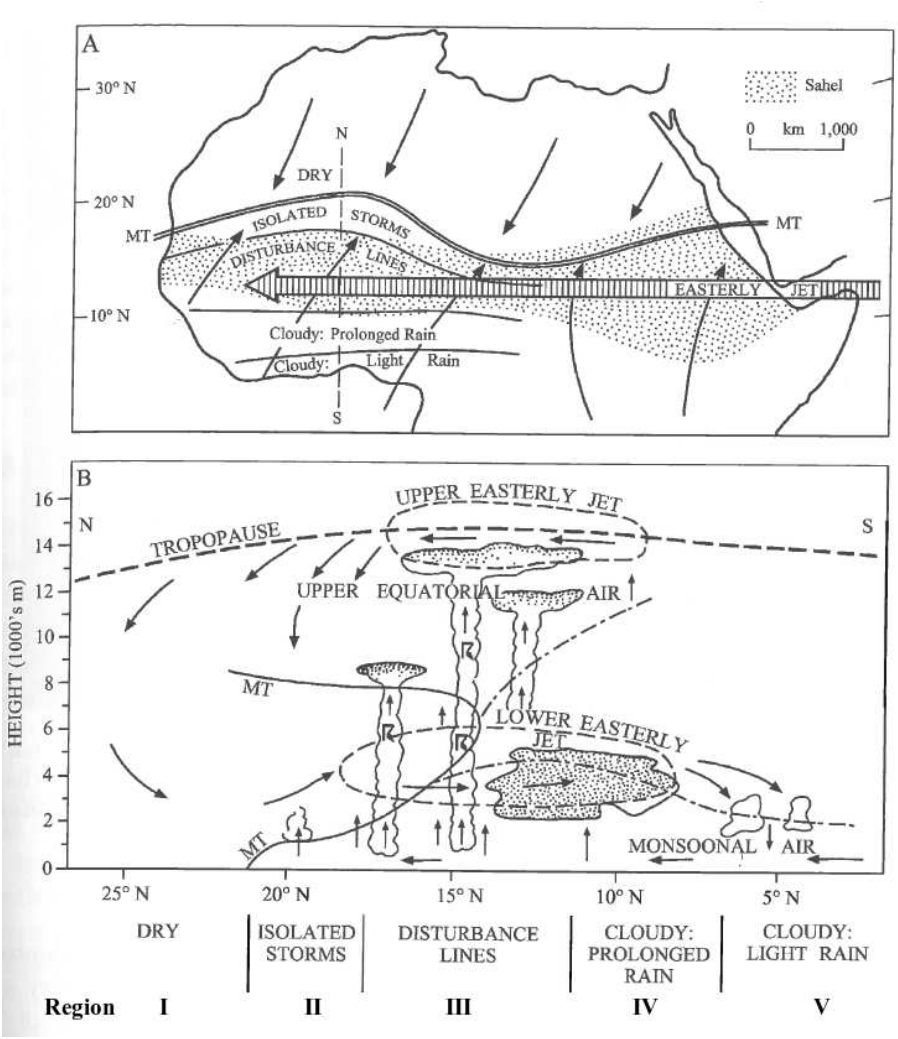

FIGURE 1.12: The structure of the atmosphere circulation over N Africa in August. A: Location of the monsoon trough and the low-level easterly jet over the Sahara. To the north of the monsoon trough at about 20°N blows the north-easterly Harmattan. B: Vertical structure of the atmosphere along the dashed line in A. Redrawn in Shao (2009) from Barry & Chorley (2009).

The West African Monsoon (Summer Monsoon)

North of the summer monsoon (∼20°N), the Harmattan controls surface winds and conditions are generally dry and stable (Fig. 1.12B: region I). At night-time, LLJs may form (see section 1.3.2.1). At the northern extent of the monsoon trough, ∼20°N, lies the ITD, where the Harmattan and monsoon converge. Surface level moisture gradients are high here. Generally only shallow convection can form, though occasionally larger events may break through the trade wind inversion (where the Harmattan overrides the surface monsoon flow). Precipitation from convective events in region II of Fig. 1.12B is evaporated before it can reach the surface. Further south, around 15°N, in region III of Fig. 1.12, the monsoon boundary layer is deeper, allowing for deeper, more intense thunderstorms. Here, convection typically becomes organised into Mesoscale Convective Systems (MCSs) (Mathon & Laurent, 2001; Mathon *et al.*, 2002). The general definition for these systems is a "contiguous precipitation area ∼ 100 km in at least one direction", though they may be organised into a variety of cloud and precipitation structures (Houze, 2004; Houze *et al.*, 1990). A subset of MCSs, named Organised Convective Systems (OSCs), were found to provide the majority of rain to the Sahel, to have lifetimes > 3hrs and to move relatively quickly at 10 ms^{-1} (Mathon *et al.*, 2002). Many of the systems identified by these criteria could be considered squall lines (Houze *et al.*, 1990). These fast-moving OCSs were found to account for 90% of the Sahelian rainfall, but only 12% of the total population of MCSs. Much larger and more rain productive Mesoscale Convective Complexes (MCCs) (Maddox, 1980) with lifetimes > 6 hrs and cold cloud top shield areas of at least 100 000 km^2 were found to account for only 16% of seasonal rainfall over the central Sahel due to their rare occurances (Mathon *et al.*, 2002).

Convection in this region is generally associated with disturbances in the mid-tropospheric African Easterly Jet (AEJ; Fig. 1.12). The AEJ typically forms in summer at 650 hPa in response to the strong temperature gradient between the hot Sahara to the north and the cooler equatorial monsoon air southwards towards the Guinea Coast (Parker *et al.*, 2005b). The resulting wind-speed maximum is ∼ 12.5 ms^{-1} at 15°N (Thorncroft & Blackburn, 1999), though Parker *et al.* (2005b) observed a speed of 21.3 ms in the jet core at 10°N, which they suggested was above the climatological average. Disturbances in the flow of the AEJ, known as African Easterly Waves (AEWs), can create baroclinic or barotropic instabilities, though there is little consensus on how these are initiated. Thorncroft *et al.*

(2008) presents evidence that latent heating over Darfur in western Sudan, close to the AEJ entrance region, is a main trigger for AEWs.

Strong, deep convection in these two northern regions of the monsoon flow, the variability of which is driven by AEWs, can create a downward flow of cold air, also known as a density (or gravity) current in the weakening stage of their life cycle. The high surface wind-speeds associated with these density currents can create large dust storms known as haboobs. For more information on the formation and relevance of haboobs for dust production see section 1.3.2.2. In region IV, Fig. 1.12, over the latitudes ∼7 - 10°N, the main equatorial trough, or ITCZ, is stationed in August. Cloud cover is consistent, heavy rainfall is prolonged and this is where the monsoon atmospheric layer is at its deepest (Fig. 1.12). Southwards of 6°N in region V, the monsoon layer becomes shallower, cloud cover is persistent and precipitation is lighter.

1.3.2 Meteorological Mechanisms for Dust Emission in Northern Africa

1.3.2.1 Synoptic-scale

Dust emission on synoptic scales are driven by the large surface pressure gradients associated with cyclonic and anti-cyclonic pressure systems. In the boreal winter this occurs between the Azores High intruding into Morocco, Algeria and Libya and the tropical pressure trough near the Gulf of Guinea which drives the Harmattan as mentioned in the previous section. The Harmattan is particularly important for dust sources in southern parts of the Sahara and the Sahel in winter (Klose *et al.*, 2010). LLJs are often embedded in the Harmattan, and can transfer momentum to the surface through boundary-layer mixing.

LLJ Inertial Oscillation

In the cloud-free desert areas, strong surface heating occurs during the day and strong radiative surface cooling at night. The rapid loss of heat from the surface stabilises the surface atmospheric layer at night, decoupling the well mixed layer above from the cool and stable bottom layer. The decoupling shields the upper layer from surface frictional effects, and when a background gradient is present an inertial osciallation is able to form around the equilibrium wind (Blackadar, 1957; Van de Wiel *et al.*, 2010). The size of

the background pressure gradient, latitude and surface roughness all affect the size of the oscillation. An example of this for 940 hPa mean winds simulated over the Bodélé Depression during the BoDEx field campaign (field campaign details are given in section 1.4.2) is given in Fig. 1.13. In many cases the full oscillation is not completed, and so by morning highly supergeostrophic winds have formed into a LLJ, sometimes referred to as a Nocturnal LLJ (NLLJ) (Fiedler *et al.*, 2013a). As the sun begins to heat the surface in the morning, sensible heating creates turbulence which grows vertically until it reaches the height of the LLJ, usually in the hours 0900 - 1200 UTC (Fig. 1.14, middle panel). As it does so, LLJ momentum is mixed down to the surface in the form of strong gusts capable of uplifting significant amounts of dust. By the afternoon, the momentum from the LLJ has become more uniformly mixed throughout the boundary layer, which itself has significantly increased in depth.

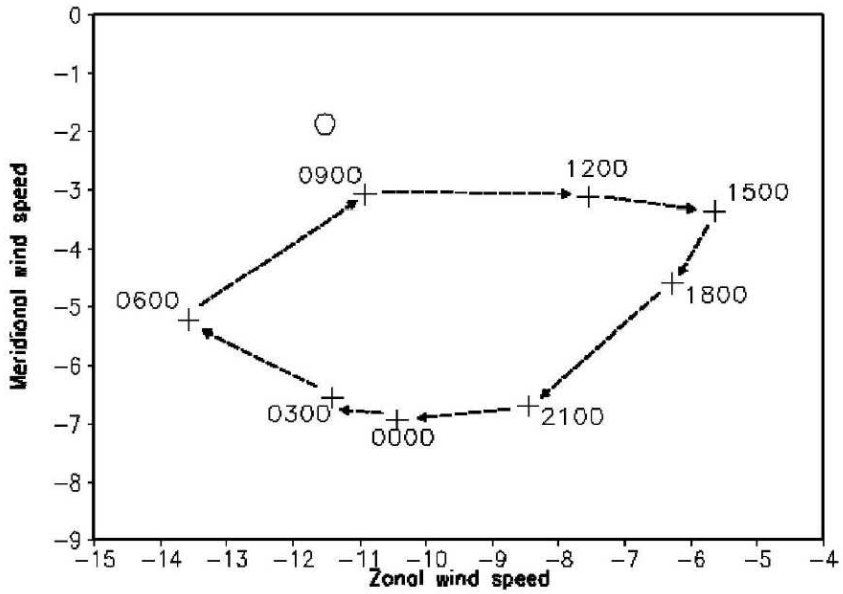

FIGURE 1.13: Mean diurnal cycle of 940 hPa modelled wind, at 27 km resolution, at Chica, Chad, close to the Bodélé Depression. Zonal and meridional components of wind in ms^{-1} are plotted for the period 27 Feb - 13 March 2005.

LLJs occur in the southern Sahara and Sahel during summer, when surface pressure gradients around the SHL encourage their formation. The ridging of either the Libyan (in summer) or Azores (in winter) subtropical highs can also increase the spatial occurance and intensity of LLJs by strengthening the background pressure gradient. This particular mechanism is usually associated with strong anti-cyclogenesis behind a surface cold front intruding into the Sahara (Knippertz & Todd, 2012). Daytime LLJs can occur due to

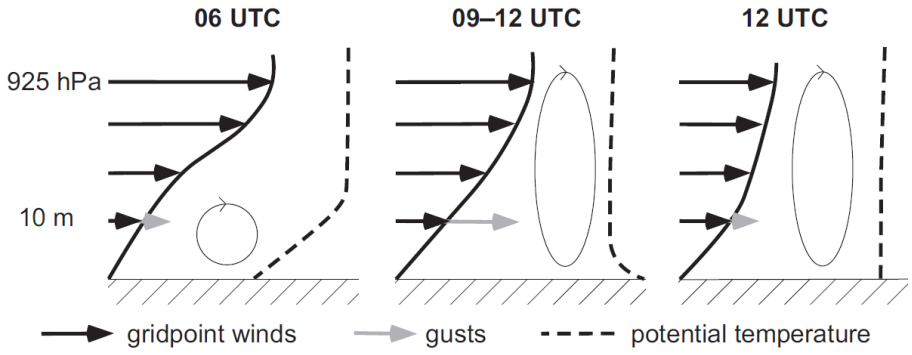

FIGURE 1.14: Schematic of changes in low-level winds, gusts, potential temperature and turbulence over the Saharan Heat Low region during the morning hours. From Knippertz (2008).

baroclinic conditions forced by coastlines and complex terrain (Stensrud, 1996), but these are more likely on meso-scales.

The ITD as a Density Current

Another synoptic-scale mechanism is uplift by the leading edge of the summer monsoon flow (the ITD), which can essentially act as a large density current (Bou Karam *et al.*, 2008). Variability in the position of the ITD has been linked to variability in dust uplift over West Saharan dust sources (Engelstaedter & Washington, 2007a) through associated LLJs (Knippertz, 2008) and haboobs (Marsham *et al.*, 2008b). This variability is partly controlled by AEWs which can alter the position of the ITD, creating northward excursions of southerly monsoon flow and uplift in the southern Sahara (Marsham *et al.*, 2013). The AEW surface vortex itself can also produce winds strong enough for emission (Knippertz & Todd, 2010).

Cyclonic Systems

Initial conditions for cyclone formation in N Africa involve an upper level trough stationed close to the Morocco and Algeria, while a springtime maximum in baroclinicity occuring along the Mediterranean coast supports cyclogensis as the cyclones propagate eastward. On the east side of the upper level trough, a depression may form at the surface in response to positive vorticity advection on the right hand side of the upper trough and intensify due to lee effects of Atlas Mountains which can also create cyclogenesis. As these Saharan cyclones, locally known as Sharav cyclones to the Middle East or Khamisin depressions to Libya and Egypt (Alpert & Ziv, 1989; Knippertz & Todd, 2012), track eastward parallel

to the north African coast they advect hot, dry and dust-laden air from the south on their eastern side, while entraining cooler air masses from the west behind a cold front.

Another type of cyclonic depression capable of dust uplift over N Africa is the Soudano-Saharan Depression (SSD). SSDs have typically been described in the literature as mobile, cyclonic disturbances associated with AEWs which initially migrate northwards from the Sahel, before turning eastwards at about 15°N (Nicholson, 1981; Warner, 2004). Based on a satellite and reanalysis investigate of these systems, Schepanski & Knippertz (2011) question this classical definition, arguing that SSDs can often be related to interactions of AEWs and subtropical upper-level waves. They propose that the term "Saharan Disturbance"is more appropriate for trackable surface depressions in this region.

Using an identification criteria of a minima in 925hPa Geopotential height, and a tracking algorithm from Schepanski & Knippertz (2011), Fiedler *et al.* (2013a) found that depression systems are a significant contibutor to the N Africa emission, with seasonal contributions up to 90% in some areas. These events are much more frequent, but less intense, than the spring cyclones previous mentioned, but could contribute to 55% of the total annual dust emission of N Africa, compared to only 4% of that from cyclones (Fiedler *et al.*, 2013b).

1.3.2.2 Meso-scale

In addition to the leading edge, dust emission has been observed within the moist south-westerly monsoon flow from the Gulf of Guinea. Some evidence suggests that the dominant mechanism is gusty cold-pool outflows from convection (Marsham *et al.*, 2008b), though LLJs are also known to be embedded in the monsoonal flow (Parker *et al.*, 2005a). Warm, dry air is sucked into the back high-levels of a thunderstorm. This air is cooled by the evaporation of precitation droplets and descends quickly to the ground where it spreads outwards (Fig. 1.15). This cool outflow contains strong and gusty winds which can create a dust "wall"as seen in (Fig. 1.16) and is commonly known as a haboob. The speed of the density current flow can be up to 50 ms^{-1}, though 20 ms^{-1} is more likely (Lawson, 1971; Shao, 2009) and they can propagate for several hundred kilometers from their source. Typical changes in conditions as a density current passes through a surface observation station could include: a dew point temperature increase, an air temperature drop, increases in wind-speed and a change in wind direction (Emmel *et al.*, 2010; Knippertz *et al.*, 2007,

2009b). Observing haboobs from satellite imagery is easier during the day due to the temperature contrast between airborne dust and the surface (Brindley *et al.*, 2012).

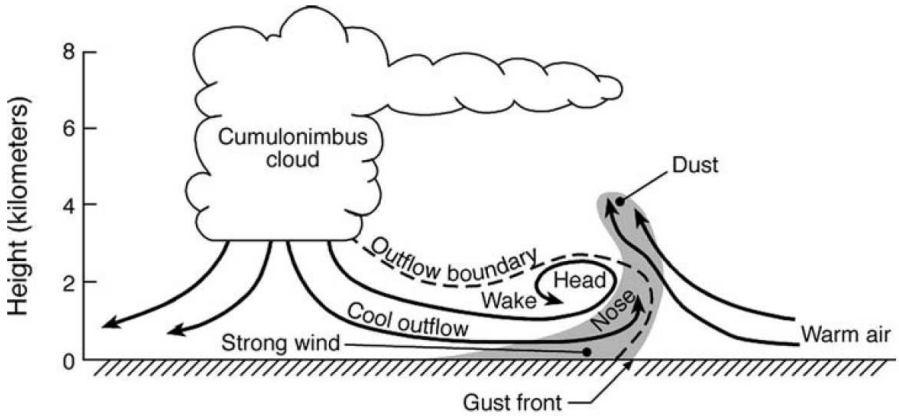

FIGURE 1.15: Cross section schematic of a haboob caused by the cool outflow from a thunderstorm. From Shao (2009)

FIGURE 1.16: A haboob in Mali, August 2004. Copyright AMMA/Guichard/Kergoat.

Dust emission due to haboobs has been documented in the north-west Sahara (Emmel *et al.*, 2010; Knippertz *et al.*, 2007), in the Sahel (Sutton, 1925; Williams *et al.*, 2009) and southern Sahara (Allen *et al.*, 2013; Knippertz & Todd, 2010; Marsham *et al.*, 2013). It is difficult to assess the frequency of haboobs due to satellite sensing limitations in cloudy conditions (Heinold *et al.*, 2013; Kocha *et al.*, 2013) and the sparse network of surface observation stations.

Haboobs are not always acting alone in emitting dust and their contribution to dust flux at the leading edge of the monsoon as it advances may be significant (Bou Karam *et al.*, 2008; Flamant *et al.*, 2007; Marsham *et al.*, 2008b). South of the ITD (mostly inaccessible to satellite studies due to cloud) Marsham *et al.* (2008b) observed increased dust uplift with the first in-situ measurements from this area collected during the GERBILS campaign. High ozone concentrations suggested that the areas of increased dust uplift were most likely due to convective storm cold pool outflows, feeding air to the surface directly from the ozone richer SAL. Using observations from TOMS AI, Engelstaedter & Washington (2007b) showed that dust emissions peaked when the convergence line passed through the source area as it moved north. Within this convergence area Marsham *et al.* (2008b) found pockets of increased dust uplift, which evidence suggested could likely be related to cold pools merging with the convergence zone.

Density currents can also have an impact on the short-term structure of the monsoon leading edge, by creating northward excursions of the ITD into the Sahara (Knippertz, 2008). Haboobs may be enhanced by synoptic mechanisms, such as a Harmattan surge.

1.3.2.3 Micro-scale

Dust devils (herein DDs), also referred to in the literature as "dusty convective vortices"(Ansmann *et al.*, 2009), "whirlwinds" (Buckle, 1996) or locally in Australia as a "willy-willy", and dust plumes (herein DPs), sometimes known as convective plumes, are the two dry convective mechanisms which occur in the lower levels of the Planetary Boundary Layer (PBL). Their contribution to the global dust cycle could be significant, but as current understanding is based on only a few observational and modelling studies (Koch & Renno, 2005; Takemi *et al.*, 2006), exactly how important they are is uncertain. These micro-scale processes occur under similar background conditions; a relatively flat and smooth terrain (Hess & Spillane, 1990), clear skies which facilitating intense surface heating and the setup of a superadiabatic temperature gradient in the lowest 10 m of the ground and wind speeds between 1.5 and 7 ms^{-1} (Ansmann *et al.*, 2009; Oke *et al.*, 2007).

DDs differ from DPs in average height, diameter, lifetime and hence dust flux. DPs are a more stable and long lived, non rotating equivalent to DDs (Fig. 1.17). Kaimal & Businger (1970) provides a good review, based on case studies, of the different dymanics of DDs and

FIGURE 1.17: A dust devil observed in Morocco during the Fennec field campaign in June 2011. Courtesy of Clare Ryder.

DPs. During the SAMUM field campaign (see section 1.4.2) lidar was used to measure DP height for the first time. Up until then, plume height data had been based on subjective eyewitness accounts from pilots, traffic controllers and meteorologists (Hess & Spillane, 1990) and as a result Ansmann *et al.* (2009) came to the conclusion that it is "impossible" to accurately estimate the top of a convective plume by eye. Their lidar analysis found most DPs had heights < 1 km, and that the maximum values ranged from 1.1 to 2.9 km. DDs have yet to be studied in this way, but Ansmann et al., 2009 suggest that DD heights tend to be less than 500 m, and hence were too low for their study. Warner (2004) also

support this height value with suggested typical DD depths of 100 m. Horizontal diameters range from 3 to 5m and ∼100m for DDs and DPs respectively, though 100 m DDs have been reported (Koch & Renno, 2005). Lifetimes range from a few minutes to over an hour for DD, while DPs tend to live for about an hour (Ansmann *et al.*, 2009; Koch & Renno, 2005). In their study of DDs in Australia, Hess & Spillane (1990) consider a wide range of dimensions for DDs (diameters from a few cm to 100 m and lifetimes of a few seconds to over an hour), while Ansmann *et al.* (2009) defines a typical DD (or dusty convective vortex) to have a diameter of less than 20 m and a lifetime of a few minutes. Significantly less recent literature exists on dry convection in Africa compared to haboobs and LLJs due to the challenge of characterising a micro-scale process which occurs over large desert areas with vast unobserved expanses. Large errors are incurred when attempting to extrapolate findings from research over small areas to the wider global role in the emission budget. Koch & Renno (2005) speculate that DDs and DPs could contribute about 35% to the global mineral dust budget, but with an error bar of ±19%. Ansmann *et al.* (2009) point out that these figures are based on theory and assumptions which do not have supporting measurements.

Complex interaction between synoptic conditions, topography and surface characteristics must be considered at different dust source regions before trying to estimate the importance of each mechanism. Some mechanisms may be more dominant in different regions due to these interactions and so a comprehensive study must include detailed studies of difference source regions.

1.4 Observations of Dust Emission in Northern Africa

1.4.1 Remote Sensing

To retrieve information on atmospheric aerosols, of which mineral dust is one component, remotely sensed data must be able to separate the radiative signature of the surface from that of the aerosols. To separate dust, its radiative signature must also be distinguished from that of other aerosol types such as biomass burning (soot) or water vapor. Since the 1980s satellite remote sensing techniques have been developed which can identify both aerosols, and more recently dust alone, using the Ultraviolet (UV), near-UV, visible and

Infra-red (IR) spectra. This section will give a brief overview of the satellites and instruments which can remotely sense dust and have advanced knowledge of global atmospheric dust properties and cycles. Aerosol Optical Thickness (AOT, or AOD - Aerosol Optical Depth) is a measure of the integrated aerosol load through the atmosphere and is used to investigate aerosol load and variability. It is possible to determine this parameter for nearly all the current aerosol retrievals used in dust studies (Figs.1.18 and 1.19). Alongside this the Angstrom exponent is also commonly calculated. This measures the column integrated aerosol size distribution (Tanré, 2010). The aerosol absorbing index (AI) is applied to instruments which use the UV spectrum. This index distinguishes UV-absorbing aerosols (dust and smoke) from non-absorbing aerosols (sulphate aerosols and sea salt particles) (Prospero, 2002). Dust can be detected from both polar orbiting and geostationary satellites. Polar orbiting instruments can collect information in the four different spectra mentioned in Figs. 1.18 and 1.19. As these satellites fly closer to the earth they can provide a higher spatial resolution of the area below the flight track swath. However, images are usually only available at a maximum of twice daily which limits their usefulness to climatological studies.

For detecting source regions, a high temporal resolution is crucial. The geostationary Meteosat Second Generation (MSG) satellite, which contains the Spinning Enhanced Visible and Infrared Imager (SEVIRI) instrument has the advantage of 15-min resolution data (Schmetz *et al.*, 2002). This time resolution allows for the tracing of features such as cloud, water vapour structures, and now dust, through the atmosphere. Although spatial resolution is less than that of polar orbiting instruments, it is adequate to produce qualitative pink-dust imagery (Schepanski, 2009; Schepanski *et al.*, 2007) and more recently quantitative AOD (Banks & Brindley, 2013). A limitation of SEVIRI pink-dust imagery is that dust emission may continue along the corridor of the dust plume transport (Ashpole & Washington, 2013). Through investigating all the limitations of SEVIRI imagery, Brindley *et al.* (2012) found column water vapour to have the largest influence on dust imagery.

Ground-based remote sensors are important not only for validating satellite retrievals, but also to compliment surface in-situ measurements. The Aerosol Robotic Network (AERONET) ground network of nearly 500 automated sun photometers (Holben *et al.*,

1998) provide high-quality retrievals of aerosol optical depth and physical properties (Knippertz & Todd, 2012).

TOMS AI was one of the first indexes used to identify dust sources (Prospero, 2002). However, as TOMS data are restricted to midday, the images can not represent the original source as many dust plumes are activated in the morning hours (Schepanski, 2009; Schepanski *et al.*, 2007). AI values from TOMS and OMI are a function of not only the strength of emission, but also the height of the dust layer.

The key polar orbiting products currently available are;

1. High spatial resolution AOT estimates from the nadir-viewing Moderate Resolution Imaging Spectroradiometer (MODIS) Deep Blue algorithm (Hsu *et al.*, 2004) and the multiangle visible data from Multiangle Imaging SpectroRadiometer (MISR) (Diner *et al.*, 2005).

2. Fine mode optical depth and partitioning of spherical and non-spherical components in coarse mode which allows for the separation of desert dust from other aerosols, over the ocean from POLDER (Tanré *et al.*, 2011).

3. Vertical profiles of aerosol backscatter from CALIOP (Fig. 1.20) (Liu *et al.*, 2008).

The MODIS, CALIOP, POLDER and OMI instruments are all part of the A-train satellite mission; the first time in which a series of satellite instruments have been coordinated specifically to measure aerosols, clouds and precipitation (Tanré, 2010).

Comparison Studies

With instrument limitations well documented in literature, it is also important to assess what the implications of these are for dust source identification and dust load (AOT/AOD/-DOD) calculations. Agreement in AOD and the Angtrom exponent are investigated for the polar orbitting POLDER, MODIS, MISR and CALIOP sensors by Tanré (2010). Overall, accuracy and agreement was found to be better over the ocean than land, but this was expected and the errors and divergence between sensors is well understood. This implies more caution is required when using the land retrievals.

Schepanski *et al.* (2012) assessed the difference in source areas identified by MSG SEVIRI, MODIS Deep Blue and OMI Aerosol Index. The clear discrepancies in source locations

are shown in Fig. 1.21. The conclusion from this study was that the overarching prerequisit for accurate source identification is sub-daily resolution of retrieval. Incorporating AERONET and flight campaign data, Banks & Brindley (2013) compared AOD algorithms from IASI, MISR, MODIS and SEVIRI and found that SEVIRI performs best during thick dust events while IASI and MODIS were better at lower AODs.

Instrument	Spectral characteristics	Record length	Space/time resolution	AOT	Retrieval coverage					Other strengths/limitations. Key references
					Desert	Other land	Sea	Day	Night	
OMI	UV channels (312-380nm)	2004-present	13*24km; daily	Y	Y	Y	Y	Y	N	AOT, single scattering albedo and absorbing aerosol index; Longest near continuous record (with OMI). Sub-pixel cloud contamination, sensitivity to aerosol layer height. [Torres et al. 1998]
TOMS	UV channels (312-380nm)	1979-1993; 1996-2005	50km; daily	Y	Y	Y	Y	Y	N	AOT and single scattering albedo and absorbing aerosol index; Longest near continuous record (with OMI). Sub-pixel cloud contamination, sensitivity to aerosol layer height. Daytime only. [Torres et al. 1998]
MODIS collection 5	Visible channels (412-670nm)	2000-present	10km, Twice daily (daytime)	Y	N	Y	Y	Y	N	AOT and angstrom coefficient, fine mode fraction, effective radius (ocean only), and asymmetry factor (ocean only), high spatial resolution and with extensive time coverage. Cloud free only. [Remer et al., 2005]
MODIS 'Deep-Blue'	Visible channels plus UV blue (412-670nm)	2002-present	10km, Twice daily	Y	Y	Y	Y	Y	N	AOT over oceans and land, near global spatial extent at high spatial resolution and with extensive time coverage. Cloud free only. [Hsu et al., 2004]
MISR	Visible-Near infrared channels with multiple viewing angles	2000-present	17.6km; 9-day global repeat cycle	Y	Y	Y	Y	Y	N	AOT, Ångström exponent, small, medium, large fractions, non-spherical fraction, single scattering albedo over land and ocean with high accuracy. Cloud free only. [Diner et al. 2001]
SEVIRI	Visible, near, mid and thermal infrared channels	2002-present	3km nadir, 15-minute.	Y	Y	Y	Y	Y	Y (false color only)	AOT and dust false color product; High space-time resolution. Day and night for qualitative products. Cloud free only. [Brindley and Ignatov, 2006; Thomas et al., 2007]
AVHRR	Visible and near infrared channels	1981-present	4km, daily	Y	N	N	Y	Y	N	AOT and angstrom coefficient, Long continuous record. Cloud free only. [Husar et al., 1997, Evan et al., 2006]

FIGURE 1.18:

AATSR	Visible and near infrared channels	1995-present	3*4km; 3-day repeat cycle	Y	N	Y	Y	Y	N	AOT and angstrom coefficient. High spatial resolution. Cloud free only. [Thomas et al., 2009]
MERIS	Visible channels	1995 -present	~1km, 3-day repeat cycle	Y	N	Y	Y	Y	N	AOT and angstrom coefficient. High spatial resolution. Cloud free only. [Ramon and Santer, 2001]
POLDER	Spectral, directional and polarized visible radiances.	1997-present	20km; daily	Y	N*	N*	Y	Y	N	AOT, angstrom coefficient, fine mode and non-spherical fractions over ocean (operational) and land (under development). Cloud free only. [Herman et al., 2005, Dubovik et al., 2011]
AIRS	Infrared hyperspectral sounding channels.	2003-present	1-degree. Twice daily (day & night)	Y	N*	N*	Y	Y	Y	AOT at 10µm, aerosol effective radius, mean aerosol layer height. Day and night retrievals. *Land retrievals under development. [de Souza-Mechado et al., 2006); Pierangelo et al., 2006, Peyridieu et al., 2010]
IASI.	Infrared hyperspectral sounding channels;	2007-present	1-degree, Twice daily (day & night)	Y	N*	N*	Y	Y	Y	AOT at 10µm, aerosol effective radius, mean aerosol layer height. Day and night retrievals. Cloud free only. *Land retrievals under development. [Peyridieu et al., in prep]
CALIOP	Polarization lidar, 532, 1064nm.	2006-present	30m vertical, 300m horizontal; 16-day repeat cycle	Y	Y	Y	Y	Y	Y	Vertical profile of aerosol backscatter, aerosol mask over land and ocean, Cloud contamination, poor temporal sampling. [Winker et al, 2009]
ICESat	Laser altimeter. Green channel.	2003-2010 (3 months per year)	91-day repeat cycle	N	Y	Y	Y	Y	Y	Vertical profile of aerosol over land and ocean. Cloud contamination, Very low temporal sampling. [Schutz et al., 2005; Spinhirne et al., 2005]

Figure 1.19:

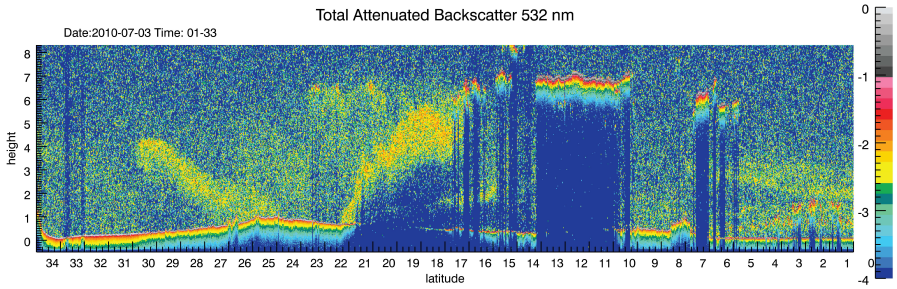

FIGURE 1.20: The 532 nm total attenuated backscatter (km^{-1} sr^{-1}) from the CALIOP instrument. Latitude is marked on the x axis. The sharp inclined leading edge of the haboob is observed from 17°N - 22°N and altocumulus clouds over southern West Africa from 10°N - 14°N. Taken from Knippertz & Todd (2012).

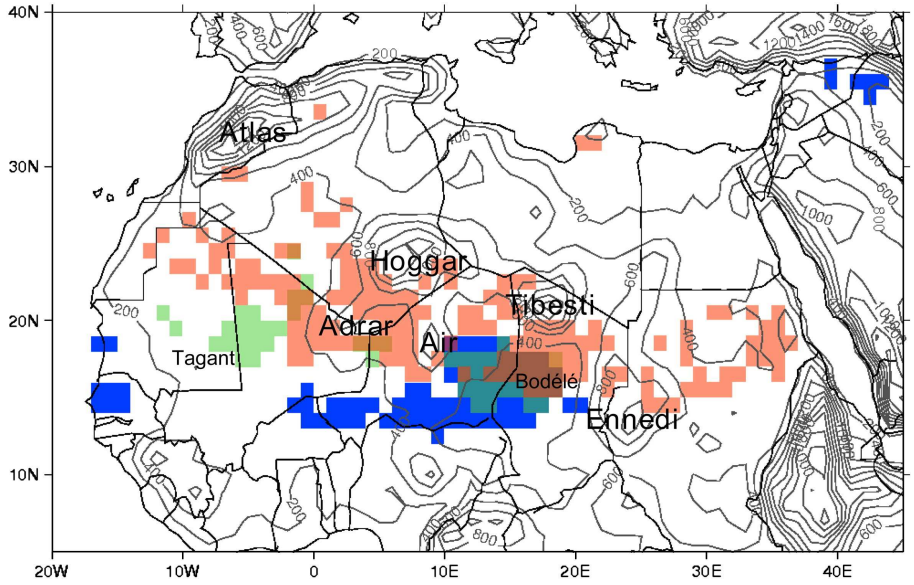

FIGURE 1.21: Summary of main dust source areas inferred from satellite images. Different colours indicate the three satellite dust producst: blue - MODIS DeepBlue AOT frequency > 40%, green - OMI AI frequency > 40%, and red - MSG DSA frequency > 6%. Contour lines represent topography and are given at 200 m-intervals. Taken from Schepanski *et al.* (2012)

With these satellite capabilities we now have a better understanding, globally, of;

1. Long-term global aerosol distribution from TOMs (Prospero, 2002), which was succeeded by OMI in 2004 (Torres *et al.*, 2007).

2. Separation of aerosol types within an atmospheric column, allowing the quantification of dust specifically (referred to as DOD or DAOD in Banks & Brindley (2013); Evan & Mukhopadhyay (2010); Ginoux *et al.* (2012); Kaufman (2005)).

3. Spatial and temporal resolution of atmospheric aerosols, including over deserts such as the Sahara, from work done using MODIS Deep Blue, MISR, OMI, CALIOP, ICESat and SEVIRI (Knippertz & Todd, 2012) and Figs. 1.18 and 1.19

Remotely sensed data are not without limitations. Some of the instrument specific limitations are given in Figs. 1.18 and 1.19. In general, no satellite retrieval is able to detect dust beneath thick cloud and visible wavelengths may not be able to seperate cirrus from thick dust (Knippertz & Todd, 2012; Roskovensky & Liou, 2005). In IR, night-time and daytime signals will be complication by the changing emissivity of the surface and aerosol particles as they warm and cool at different and unknown rates.

Most Recent Developments

Semi-quantitative TOMS AI and IDDI from METEOSAT (Brooks & Legrand, 2000) aerosol products were some of the first to emphasize the importance of the Sahara as a global dust emission source. Since those first studies, satellite products have advanced significantly to allow greater understanding of these sources identified in early climatologies. MODIS Deep Blue (Ginoux *et al.*, 2012) and SEVIRI MSG (Schepanski, 2009) have more recently improved knowledge of dust sources in this area. Ginoux *et al.* (2012) uses Frequency of Occurrence (FoO) statistics of DOD to identify source areas and combines a land-use dataset and 10 m model winds to distinguish between anthropogenic, hydrological and natural sources globally. Schepanski (2009) exploits the high resolution MSG SEVIRI data to trace dust plumes back to their source areas in the Sahara and has produced a detailed Dust Source Activation (DSA) map of the area. Further to this, the high temporal resolution also allows for the diurnal cycle of the source areas to be estimated. More recently, Banks & Brindley (2013) presented a method to quantify dust from SEVIRI in the form of DAOD (Dust Aerosol Optical Depth). This is more tricky to achieve from the

lower spatial resolution of a geostationary satellite instrument, but the seasonal variability of the reliability of the retrieval (validated with AERONET stations) is made clear. Building on the work by Schepanski (2009) a SEVIRI Dust Flag (DSF) was developed by Ashpole & Washington (2012) to allow for quicker and reproducable analysis of pink-dust imagery. The characterisation of dust sources by this dataset in Ashpole & Washington (2013) suggested the importance of the margins of sand-seas as source areas in the Sahara.

1.4.2 Field Campaigns

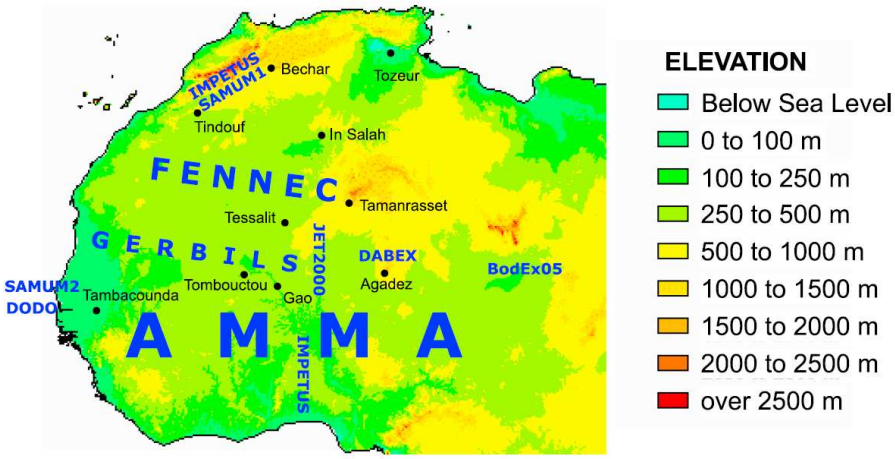

FIGURE 1.22: The general focus areas of recent dust field campaigns (blue text). Surface topography is shaded and radiosonde station locations of interest for Saharan dust emission are marked in black. From Knippertz & Todd (2012).

Field campaigns over the past 14 years, such as the Jet2000, BoDEx (Bodélé Field Experiment), GERBILS (Geostationary Earth Radiation Budget Intercomparison of Longwave and Shortwave Radiation), AMMA (African Monsoon Multidisciplinary Analyses), SAMUM (Saharan Mineral Dust Experiment), IMPETUS (An Integrated Approach to the Effective Management of Scarce Water Resources in West Africa) and Fennec (not an acronym) have provided great insight into dust emission processes. The general focus areas for these campaigns are displayed in Fig. 1.22.

The Jet2000 project, which took place in the last week of August 2000, provided insight into the diurnal cycle of the summer monsoon (Parker *et al.*, 2005a) and in particular the AEJ (Thorncroft *et al.*, 2003).

A dense network of automatic weather stations in southern Morocco was set up by the German research initiative IMPETUS. Although focussed on present and future problems of fresh water availability (Schulz & Judex, 2008), the eleven automatic weather stations situated from the semi-arid High Atlas Mountains down to the arid pre-Saharan landscapes have also been used to create a climatology of convective density currents (Emmel *et al.*, 2010), and to evaluate high resolution simulations of convective cold-pools in the southern foothills of the High Atlas Mountains (Knippertz *et al.*, 2009a). There is now a reasonably long-term (2001 - 2011) high-resolution surface dataset at some IMPETUS stations which is yet to be fully utilised.

AMMA was a long-term programme of research which included long-term (2002 - 2010), special (2006) and enhanced (2-3 years duration linking long-term with special) observing periods with the goal to make sustainable improvements in the monitoring and prediction of WAM variability (Redelsperger *et al.*, 2006). AMMA significantly improved the surface observation network over West Africa and revitalised the West african radiosonde network (Parker *et al.*, 2008). A side group, AMMA-CATCH, focussed on surface properties and processes in West Africa through three intensively instrumented mesoscale sites in Mali, Niger and Benin (Lebel *et al.*, 2009).

Associated with AMMA, the Dust Outflow and Deposition to the Ocean (DODO) project took place in February and August 2006. DODO gave insight into the physical and optical properties, and differing transport altitudes, of wet and dry season dust emission through two airborne campaigns whilst also highlighting the importance of accurately measuring coarse mode particles (McConnell *et al.*, 2008).

Focussed on what is widely regarded as the worlds most active dust source, the Bodélé Depression (Washington *et al.*, 2003), the multidisciplinary field project BoDEx took place in February - March 2005. Ground based measurements including wind-speed, temperature, solar radiation and aerosol properties such as AOT and size distribution gave findings such as an unsually high local threshold wind-speed (10 ms^{-1}) and a $\sim$50% underestimation of surface and LLJ wind-speeds by global atmospheric models (Todd *et al.*, 2007). Using PIBAL data in conjunction with surface observatons from the campaign, the diurnal cycle, height and speed of a LLJ which forms in the region were verified and the role of this LLJ in dust production and transport were discussed (Washington *et al.*, 2006).

Another flight campaign, the Geostationary Earth Radiation Budget Intercomparison of Longwave and Shortwave Radiation (GERBILS), took place in July 2007 (Haywood *et al.*, 2011). Ten flights collected data over the south-west Sahara and coastal stretches of the Atlantic Ocean and improved understanding of the short-wave and long-wave radiative effects of mineral dust (Osborne *et al.*, 2011), how well dust loads are assessed from satellite remote sensing (Christopher *et al.*, 2011) and the accuracy of global and mesoscale forecast models (Johnson *et al.*, 2011). An investigation of GERBILS flight data by Marsham *et al.* (2008a) suggested that land surface anomalies could induce mesoscale circulations and be important for dust loadings to the SRL. In a separate investigation, also with GERBILS data, (Marsham *et al.*, 2008b) conclude that cold pool outflows could be an important mechanism for dust uplift south of the ITD region.

Based in Morocco in May/June 2006 and Cape Verde in winter of 2008, the SAMUM field campaign produced some interesting findings. The size distribution of particles in these two different seasons is characterised by this campaign in Weinzierl *et al.* (2011). Ground-based lidar products were used to profile dust devils and convective plumes in unprecedented detail for the first time (Ansmann *et al.*, 2009), while comparisons to the satellite instrument CALIOP revealed an underestimation of dust optical depth by 25% caused by neglected multiple scattering (Wandinger *et al.*, 2010). All of the key lidar, radiation, dust property and modelling advances from this campaign are summarised in Ansmann *et al.* (2011).

The 2011-2012 Fennec field campaign, involving surface and aircraft observations focussed on the central SHL region of the Sahara, aimed to fill in observational gaps of this key dust-uplift region (Washington *et al.*, 2012). The results from the two observational supersites (based in southern Algeria and northern Mauritania) have already improved understanding of the meteorological processes involved in this region, such as new findings on the interactions of LLJs with the Atlantic inflow (Todd *et al.*, 2013) and the relative contribution of dust uplift from LLJ and haboob mechanisms close to the SHL (Marsham *et al.*, 2013). An analysis of the optical properties of dust measured from aircraft observations found an unexpected abundance of coarse mode particles, including particle diameters $>$ 300μm, which has implications for satellite retrievals over desert surfaces and the radiation budget (Ryder *et al.*, 2013).

1.4.3 Long Term Surface Observations

The real value of SYNOP reports for the study of the dust cycle was first highlighted by Morales (1979). Referencing the WMO manual on codes (WMO, 1974) Morales (1979) discusses the usefulness of the following parameters found in surface SYNOPS; wind-speed, wind-direction, visibility, present weather and past weather. He goes on to give examples of how these data can be used for case studies of dust storms and statistical studies which relate a critical wind-speed with dust emission, as a crude measure for a dust emission threshold. This concept of calculating a critical wind-speed for emission was used by Helgren & Prospero (1987) in the western Sahara and was developed further by Kurosaki & Mikami (2007) for east Asia. These techniques use the present weather (ww) code which describe the current weather conditions at the station at the SYNOP hour. Out of 100 possible weather descriptions, the codes which specifically describe dust emission are 7-9, 30-35 and 98 (Table 1.1). WW code 06 is also useful for dust studies as it specifies that dust is present but not emitted at that location which, in climatological studies, can identify how frequent transported versus emitted dust events occur.

Further to the descriptions in Table 1.1, (WMO, 1996) also states that the "WMO (1975) should be at the observer's disposal as an auxiliary means". In this accompanying document there is a more in depth description of how a dust storm may be distinguised from other, perhaps smaller events:

"*Commentary*: Dust storms or sandstorms generally occur in areas where the ground is covered with loose dust of sand; sometimes, after having travelled over more or less great distances, they may be observed over areas where no dust or sand covers the ground. The forward portion of a dust storm or sandstorm may have the appearance of a wide and high wall which advances more or less rapidly. Walls of dust or sand often accompany a Cumulonimbus which may be hidden by the dust or the sand particles; they may also occur without any clouds along the forward edge of an advancing cold air mass" (WMO, 1975)

It is interesting that these notes above would suggest that dust storms are most likely to be associated with "a wide and high wall which advances" as this is how one might describe a haboob. From this description you could infer that reports of ww=09,30-35,98

are almost exclusively associated with haboobs, assuming that station observers use the guidance descibed above.

There is also a more detailed description for a dust devil as referred to in present weather codes 07 and 08 (Table 1.1) as dust or sand "whirls":

"Definition: An ensemble of particles of dust or sand, sometimes accompanied by small litter, raised from the ground in the form of a whirling column of varying height with a small diameter and an approximately vertical axis. *Commentary*: These lithometeors occur when the air near the ground is very unstable as, for instance, when the soil is strongly heated by insolation."

ww	**weather description**
06	Widespread dust in suspension in the air, not raised by wind at or near the station at the time of observation
07	Dust or sand raised by wind at or near the station at the time of observation, but no well developed dust whirl(s) or sand whirl(s) and no duststorm or sandstorm seen; or, in the case of ships, blowing spray at the station
08	Well developed dust whirl(s) or sand whirl(s) seen at or near the station during the preceding hour or at the time of observation, but no duststorm or sandstorm
09	Duststorm or sandstorm within sight at the time of observation, or at the station during the preceding hour
30	Slight or moderate duststorm or sandstorm - has decreased during the preceding hour
31	Slight or moderate duststorm or sandstorm - no appreciable change during the preceding hour
32	Slight or moderate duststorm or sandstorm - has begun or has increased during the preceding hour
33	Severe duststorm or sandstorm - has decreased during the preceding hour
34	Severe duststorm or sandstorm - no appreciable change during the preceding hour
35	Severe duststorm or sandstorm - has begun or has increased during the preceding hour
98	Thunderstorm combined with duststorm or sandstorm at time of observation

TABLE 1.1: Present weather descriptions of dust phenomena in surface SYNOP code

Visibility values from long-term SYNOPS have previously been used to investigate: the diurnal and seasonal cycles of dust over north Africa (Mbourou *et al.*, 1997), dust storms in the Middle East (Middleton, 1986a), standardized definitions for dust phenomena in conjunction with present weather codes in Australia (McTainsh & Pitblado, 1987), trends in the frequency of dust storms around the world (Goudie & Middleton, 1992), the spatial and temoporal characteristics of dust storms in China (Sun *et al.*, 2001) and more recently reliability of visibility-derived parameters for dust research, as well as the long term trends global aerosols (Mahowald *et al.*, 2007).

When solar radiation encounters a layer of mineral dust in the atmosphere, scattering and absorbtion by the suspended particles (Li *et al.*, 1996) has the net effect of reducing the amount of solar radiation which reaches the surface. In addition to this, diffuse radiation

increases and reduces visibility in the horizontal plane (Mbourou *et al.*, 1997). Thus visibility can be thought of as an indication of the intensity of attenuation of radiation by dust layers (Charlson *et al.*, 1968; Mbourou *et al.*, 1997). In West Africa, vertical and horizontal extinction were found to correlate well (D'Almeida, 1987). Extinction of light by aerosols (surface extinction) is the amount of light which is attenuated from a horizontal view, assuming all of the attenuation is due to aerosols (Mahowald *et al.*, 2007).

In temporal trends, visibility-derived parameters were found to to explain 20% of the variability in AERONET AOD variability. Visibility data was also found to be equally as good (or bad) at representing spatial and temporal variability in surface fluxes. Using a vis <5 km parameter was found to correlate better with AERONET AODs than a vis <1 km parameter (Mahowald *et al.*, 2007).

Despite its extensive use in dust research studies, surface measurements of visibility come with some caveats. Humidity, clouds and precipitation can all influence visibility (Mahowald *et al.*, 2007). It is not always a good indicator of the vertical dust load as it can be clear at the surface with a dusty layer of air present above (Mbourou *et al.*, 1997). Its main limitation in terms of emission studies is that reduced visibility may be the result of aerosols transported in from another region.

Although the temporal and spatial resolution of surface SYNOPs cannot match new satellite products such as METEOSAT SEVIRI (section 1.4.1), its numerous advantages include: reporting beneath cloud, a range of variables measured simultaneously, and (relatively) complete records on long-term timescales generally > 30 years (depending on the region).

It is important to be aware of the bias introduced by the spatial distribution of stations in typically urban, populous areas. The most arid environments are often extremely dry, dusty and inhospitable, hence very few observation stations are based at these locations. On the other hand, the contribution of anthropogenic sources (an increasingly considered aspect of the dust cycle) is perhaps represented better by this network. Ultimately, from surface SYNOPs alone, you cannot distinguish anthropogenic from natural dust emissions.

Present weather codes have been used in the climatological analysis of east Asia (Kurosaki & Mikami, 2005) and the southwest monsoon region (Ackerman & Cox, 1989). Recently, dust emission events from present weather codes 7-9, 30-35 and 98 specifically (Table 1.1),

have been used in conjuction with visibility to study global and regional (including a N Africa region) trends in frequency of dust emission and concentration (which is derived from visibility), but not yet to investigate the seasonal and diurnal cycles of N Africa (Shao *et al.*, 2013).

The focus of dust research has shifted towards the increasing abundance of high spatial and temporal resolution satellite products, from which some climatological studies can be done due to the now reasonable long length of records. However, if the limitations of surface observations over N Africa can be adequately described then characterising emission from station observations, using specific emission codes 7-9, 30-35 and 98 present weather codes, could be extremely useful.

1.5 Summary

This chapter provides a background to the global dust cycle, some of the implications of atmospheric dust for climate and human health, a summary of N African climate and the current literature on meteorological mechanisms which create dust emission there. The final section (1.4) focuses on observation methods which have been used to investigate dust emission in N Africa. This is the area of research which this thesis aims to contribute towards.

The overall aim of the thesis is to fully utilise long-term surface observations over northern Africa to;

1. Produce a comprehensive climatology of the frequency of dust emission, as has been done for other parts of the world, but not yet in N Africa (Chapter 3).

2. Investigate the role of very high wind events towards the total amount of dust uplift (Chapter 4). In doing so, the errors and biases contained in observations from SYNOP stations will be discussed, and the sensitivity of the results to these errors and biases is investigated. Chapter 4 is also motivated by the needs of the modelling community to identify the particular high wind-speeds which contribute the most to dust uplift, as this could provide insight into why models struggle to agree on the annual dust emission load (Huneeus *et al.*, 2011).

3. Understand the possible mechanisms behind a well-documented downward trend in dust emission from northern Africa (Evan & Mukhopadhyay, 2010; Mahowald *et al.*, 2007), also observed in wind-speed and present weather dust emission reports over the Sahel (Chapter 5). Until now, the mechanisms involved in a downward trend in emission have not been clearly described, though the global observed decrease in wind-speed (termed "stilling"; Roderick *et al.* (2007)) has been partly attributed to surface roughness (Vautard *et al.*, 2010), and in China partly attributed to changes in atmospheric circulation (Guo *et al.*, 2011).

These investigations adapt new and old diagnostic tools from literature to suit this particular observational data set and the aims of the thesis. The limitations, biases and uncertainties contained within this problematic dataset are discussed and presented as thoroughly as possible.

Chapter 2

Data and Methods

2.1 Introduction

This chapter gives an overview and background into the datasets used in the following three results chapters. Specific methodologies are presented in each of the results chapters. Of relevance to the whole thesis are the methods used to determine thresholds at each station (section 2.3.2) and the use of the diagnostic parameter, dust uplift potential (section 2.3.1).

2.2 Data

2.2.1 Surface Observations from Long-term SYNOP Reports

Surface observations of wind-speed and present weather in the Met Office Integrated Data Archive System (MIDAS) Land and Marine Surface Stations data set for northern Africa form the basis of this thesis and are accessed from the British Atmospheric Data Centre (BADC). WMO regulations state that observations take place at certain times, in Coordinated Universal Time (UTC). The main SYNOP hours are 0000, 0600, 1200 and 1800 and at stations which report four times a day, these are the main reporting hours. At stations which report more frequently (four to eight times per day), observations may also be made at the inter-SYNOP hours of 0300, 0900, 1500 and 2100. At some stations, only daytime observations are made (see section 3.2 and Appendix A, Fig. 1). In this thesis, stations which report between four to eight times a day are used. The number of reports

at each main and inter-SYNOP hour for the 70 African stations used in this thesis can be found in Appendix A, Fig. 1.

2.2.1.1 Wind-speed

WMO regulations state that wind-speed should be measured at 10 m height, and averaged over a 10 min period in the hour prior to that SYNOP hour (WMO, 1995). Gust measurements would have been extremely useful to this study, but these are not routinely taken in northern Africa. Measurements are stored in the database as knots, though it is not clear if the original measurements from the instrument are in ms^{-1} or knots. Documentation on the type of instruments used could not been found, though through personal communication, photograph evidence and studying the characteristics of the wind-speed data (see sections 4.2 and 4.3) it seems likely that most SYNOP stations use a cup and vane wind-measurement system.

2.2.1.2 Present Weather

Present weather is the weather phenomena present at the time of observation, as determined by the station observer (WMO, 1996). The observer chooses one out of a possible 100 descriptions which best describes the state of the atmosphere that they can see around them (WMO code table 4677). This may include information of the weather phenomena that occurred over the past hour. This thesis focuses on the code numbers 07, 08, 09, 30-35 and 98 which describe dust emission (Table 1.1). A code number of 06 is also used in Chapter 3 to investigate the relative importance of transported events, as this code describes dust presence in the atmosphere which was not emitted locally.

2.2.2 Normalized Difference Vegetation Index (NDVI)

Vegetation changes are assessed using the normalized difference vegetation index (NDVI) data (Tucker *et al.*, 2005) from the Advanced Very High Resolution Radiometer (AVHRR) remote sensing instrument on a seasonal basis in Chapter 3 and through time in Chapter 5. This widely used proxy for vegetation in the Sahel (Huber & Fensholt, 2011) is well suited for studies in semi-arid areas (Olsson *et al.*, 2005). A limitation of this dataset is that NDVI

only detects green vegetation and may overestimate areas with low Leaf Area Indexes (Zhu & Southworth, 2013), such as semi-arid regions. After the main growing season, brown vegetation, which still affects dust emission (Zender & Kwon, 2005), is likely to be left over, but not detected by NDVI. NDVI data, provided on an 8 km by 8 km grid, was obtained from the Global Inventory Modeling and Mapping Studies (GIMMS) database (www.landcover.org) for the time period 1984-2006

2.2.3 Jones North Atlantic Oscillation Index (JNAO)

The Jones NAO (JNAO) index is used in Chapter 5 to correlate with trends in dust emission and wind-speed over the Sahel. The Jones NAO index was used instead of the Hurrell NAO index (Hurrell, 1995) because it represents a center of action closer to Africa. Alternatively, the method from Riemer *et al.* (2006) found that when you separate the two "centers of action", meaning the Azores high and Icelandic low, only the Azores high is found to be important in explaining the variability of dust transport over eastern part of the tropical north Atlantic. Riemer *et al.* (2006) tentatively suggest that emission is increased over Algeria, Mauritania and Morocco when the Azores high is at higher latitudes and that the position of the Azores high is the key factor above the NAO and the Icelandic low position.

2.2.4 MSG SEVIRI Dust

In this thesis, pink-dust imagery is used qualitatively in Chapter 4, on a case-study basis, to investigate suspicious surface observations of wind-speed. It is perhaps unusual to use satellite information to validate surface observations, but due to its high temporal and spatial coverage it can add great detail to the information from 3-hourly surface SYNOPS.

The Spinning and Enhanced Visible and InfraRed Imager (SEVIRI), on board the Meteosat Second Generation (MSG) Geostationary satellite, is located at 3.5°W over the equator with images centered at 0° longitude. With a field of view extending from 70°N - 70°S and 70°E - 70°W it is ideally suited for studying African dust sources (Brindley *et al.*, 2012). The SEVIRI instrument measures radiances at 11 spectral channels with a spatial resolution of 3 km at nadir. These channels cover the visible and IR spectra between 0.6 -

13.4 μm and one high resolution visible (HVR) channel with a resolution of 1km at nadir (Schmetz *et al.*, 2002).

Applying brightness temperature differences (BTDs) from MSG SEVIRI data to red-green-blue (RGB) images is explained in detail in Lensky & Rosenfeld (2008). This technique provides new insight into satellite retrievals and can be used for a wide range of applications including; cloud analysis, fog, snow, fire, convective storms, cyclogensis, jet stream analysis, and atmospheric dust. The original tri-spectral algorithm for detecting dust from InfraRed (IR) wavelengths was proposed by Ackerman (1997).

A composition of the three brightness temperature (BT) channels; seven (8.7 μm), nine (10.8μm) and ten (12 μm), can be applied to red-green-blue (RGB) imagery to produce an image which highlights dust in the atmosphere in the magenta range of colours. The 10.8 μm (blue) channel is used as a reference as it is most indicative of the apparent surface temperatures under clear sky conditions. The BTDs of 12-10.8 μm (red) and 10.8 - 8.7 (green) μm are then compared to this. Clouds, dust plumes and surfaces all have different spectral behaviors in these wavelength bands and appear as different colours. Cold, thick high-level cloud appears in red, mid-level cloud in green, high moisture at low levels in blue and dust in pink (the more intense the emission, the brighter the pink). As this method uses the IR spectrum, dust emission can be detected at night also, but these images are complicated by the changing thermal emissivity of the surface and dust in the atmosphere as the temperature of these features changes at night and are currently treated with caution (Banks & Brindley, 2013).

Since its development and introduction into dust research, SEVIRI dust imagery has been used for a number of purposes. As mentioned in the introduction, subjectively tracing back pink-dust plumes allowed Schepanski *et al.* (2007) to compose a map of source areas in northern Africa, as well as attributing mechanisms based on the time of source activation (Schepanski, 2009). Other authors have also used pink-dust imagery to investigate dust mechanisms and transport (Karam *et al.*, 2010; Knippertz, 2008; Marsham *et al.*, 2008b). Collecting the images in near-real time has been useful for field campaign planning, and even during flight times to advise on routing (Brindley *et al.*, 2012). SEVIRI has also been used to qualitatively assess the Met Office dust forecasts during the GERBILS (Geostationary Earth Radiation Budget Intercomparison of Long-wave and Short-wave Radiation)

campaign using pink-dust images on a case-study basis and through qualitatively comparing with the activation frequency of sources from Schepanski (2009).

The dust signature in SEVIRI is complicated by a number of factors such as; high water vapour (the largest influence), a strong near surface temperature inversion, the height of the dust layer, characteristics of the underlying surface (emissivity), mineralogical composition of dust and the size distribution of particles (Brindley *et al.*, 2012). High resolution pink-dust imagery is provided on a case by case basis from the Imperial College London archive. The original data were acquired from Eumetsat.

2.2.5 Reanalysis

ERA-Interim reanalysis products are used to assess the trends in mean wind over the Sahel for the time period 1984-2010 in Chapter 5. Chapter 4 uses NCEP/NCAR daily mean composites of surface vector winds for a case study of dust emission and high winds in Sudan.

Reanalysis products such as ERA-Interim (Dee *et al.*, 2011) and NCEP/NCAR (Kalnay *et al.*, 1996) reanalysis are excellent tools for examining climate variations. The basic concept involves the reanalysis of observations, which is done by assimilating the most complete set of available, quality controlled, data into a state-of-the-art model and analysis system. By providing an unchanging data assimilation scheme, where only the raw observational input is changing, it is possible to assess climate variations (Kalnay *et al.*, 1996).

Reanalysis can provide a good approximate representation of the climate by filling in the "gaps" between observation stations and therefore provide homogeneous and continuous spatial and temporal coverage. However, reanalysis products must be treated with caution as the reliability is only as good as the local observational network. If there are no observations in an area of interest then the model output will be less constrained by reality.

2.3 Methods

2.3.1 Dust Uplift Potential (*DUP*)

FDE provides occurrence frequency of emission, but not its intensity or quantity. The diagnostic parameter dust uplift potential (*DUP*; Marsham *et al.* (2011)), based on the emission parameterisation of Marticorena & Bergametti (1995) is used to investigate the dust emitting power of the wind:

$$DUP = U^3(1 + U_t/U)(1 - U_t^2/U^2) \tag{2.1}$$

Where U = measured wind speed and U_t = threshold wind speed for dust emission. *DUP* is zero when U<U_t. In their original parameterisation (1.8) Marticorena & Bergametti (1995) use U^*, which has been replaced here by U in 2.1. It was not possible to calculate U^* from the available data (sensible heat and momentum flux data are needed). The implications of this are that second order effects of stability (a stable neutral boundary layer is assumed) and roughness length are neglected (Cakmur *et al.*, 2004; Marsham *et al.*, 2011).

It is worth considering the possible differences in U and U^* for different atmospheric conditions. U and U^* will be most similar when the atmosphere is neutrally stratified (well mixed and temperature doesn't vary too much with height). If the atmosphere is unstable, the friction velocity (if calculated with Eq. 1.2) will be larger and U may underestimate the momentum flux at the surface. Such conditions could occur regularly during the day in the Saharan turbulent boundary layer. In a stable boundary layer, typical of nighttime conditions over northern Africa when radiative cooling allows a stratified profile with cooler air below residual day time boundary layer, it is possible that U^* will be lower than U due to the reduction in turbulence and hence velocity fluctations which would give a higher U^* value via Eq. 1.2. However, Marsham *et al.* (2013) found that U^* was almost proportional to U, using flux data.

This diagnostic takes into consideration the highly nonlinear impact of changes in peak winds on dust emission and has previously been used to isolate the role of meteorology from land surface in model evaluation (Marsham et al., 2011). *DUP* is an indicator of emitted dust mass if the parameterisation is perfect and the surface does not vary in time.

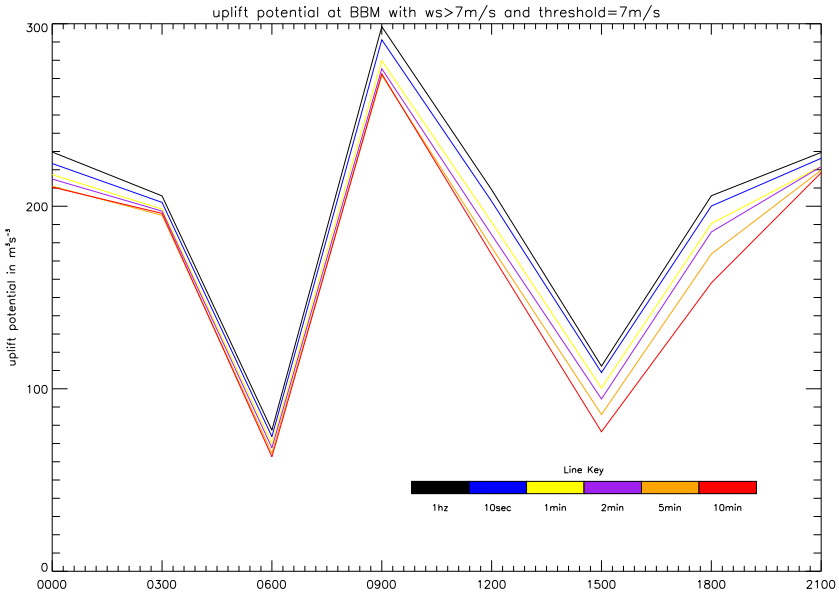

FIGURE 2.1: Diurnal cycle of *DUP* at BBM using a wind-speed threshold of 7 ms^{-1} for the period of June 2011, with time resolutions of 1 hz (black), 10 secs (blue), 1 min (yellow), 2 mins (purple), 5 mins (orange) and 10 mins (red).

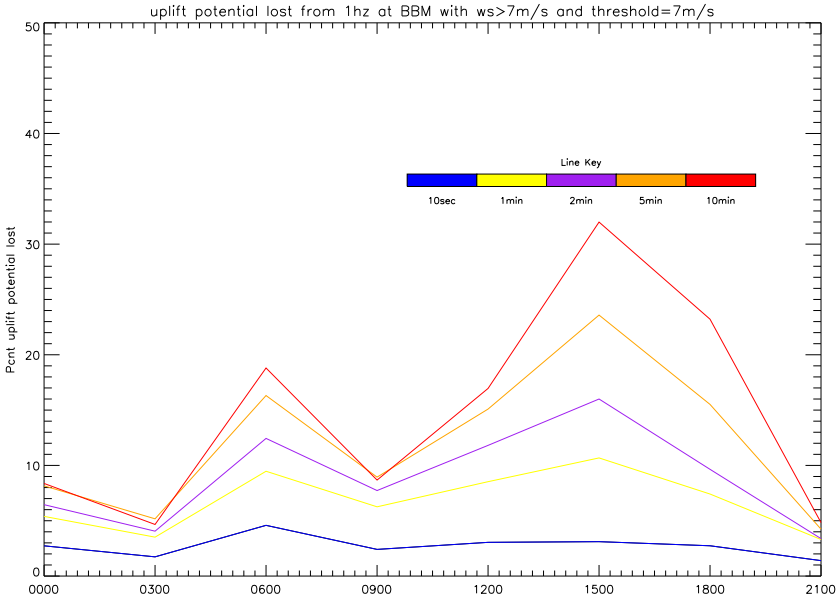

FIGURE 2.2: Diurnal cycle of the % *DUP* lost going from a 1 hz data resolution to 10 secs (blue), 1 min (yellow), 2 mins (purple), 5 mins (orange) and 10 mins (red) at the BBM Fennec supersite (see Fig. 3.1 for location).

To investigate the role of using 10 min means on *DUP*, wind-speed data collected from the IOP of the recent Fennec field campaign at Bordj Badji Mokhtar (BBM; Fig. 3.1 for location) was investigated. The 1 hz resolution Fennec data was averaged over 10 sec,

1 min, 2 min, 5 min and 10 min periods (Fig. 2.1 and 2.1). The diurnal cycle of *DUP* (Fig. 2.1) and the diurnal cycle of % *DUP* lost (Fig. 2.2) show that ∼30% is lost in the afternoon if using a resolution of 10 minutes. This could be due to the more sporadic nature of strong winds in the afternoon when overall *DUP* has significantly dropped from the peak at 0900. These figures also show that the % of *DUP* lost will depend on the time of day and the meteorological conditions at that location. Hobby *et al.* (2013) conducted a similar analysis on *DUP* using Fennec data and came to the conclusion that 10 min mean winds from SYNOP stations may not accurately capture dust uplift using this method.

The evidence here suggests that *DUP* is generally underestimated by amounts which will vary according to location and time of day when averaged over 10 mins. As 10 min mean winds are the best resource we have at northern Africa stations, and any biases will generallly be applied to all stations, it is still worthwhile investigating *DUP* with surface SYNOPs.

2.3.2 Thresholds in Surface Observations

As discussed in section 1.2.1, for any land surface there is a minimum surface stress that must be exerted by the wind to generate dust emission. This closely corresponds to a threshold speed for the low-level wind (Helgren & Prospero, 1987). The threshold wind-speed for a surface is determined by the surface roughness and soil properties (such as particle shapes and sizes, soil composition, moisture content and aerodynamic properties) but can also be influenced by previous disturbance of the soils (Gillette *et al.*, 1980). Although we do not have long term measurements of surface soil conditions, it is possible to statistically evaluate which wind-speeds are most likely to be associated with dust emission.

The main method to determine thresholds from surface observations compares the probability density function (pdf) of winds during dust emission events (bottom black curve in Fig. 2.3) with those of all reports for a given station (top black curve in Fig. 2.3), and is based on work by Morales (1979), Helgren & Prospero (1987) and Kurosaki & Mikami (2007). Based on these pdfs, the wind-speeds at which 25%, 50% and 75% of all observations contain a dust emission report can be computed (herein T25, T50 and T75; see vertical lines in Fig. 2.3). Where a seasonally varying threshold is required for a *DUP*

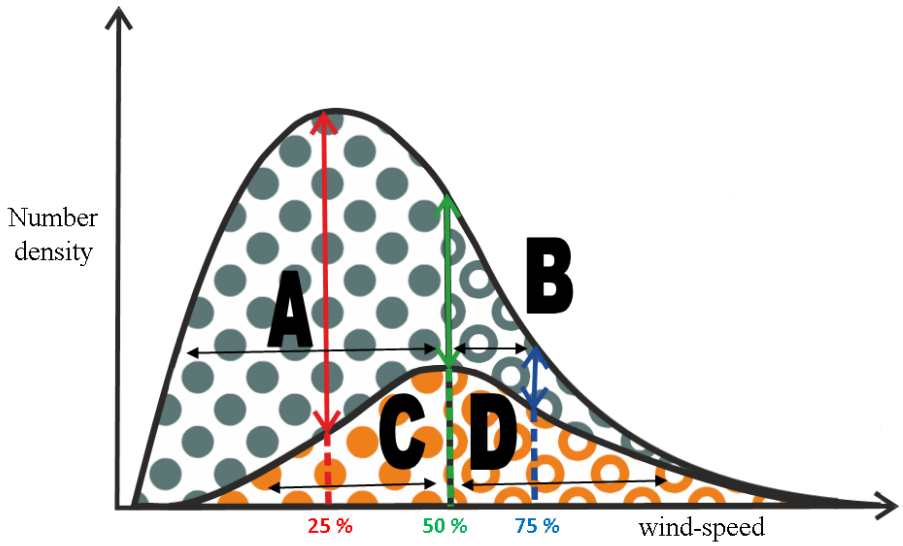

FIGURE 2.3: Schematic to illustrate the estimation of emission thresholds. Orange shading indicates the number density function of wind-speeds associated with dust emission reports and grey shading represents wind-speeds for all observations. The arrows signify the wind-speed at which dust emissions make up 25%, 50% and 75% (red, green and blue respectively) of all reports. Areas A and B are represented by grey dots and circles, C and D with orange dots and circles.

calculation, T50 is used, such as in Chapter 3. T25 and T75 are also useful to describe the range of observed thresholds. A real world example from the station of Faya in Chad is shown in Fig. 2.4. The large majority of observed wind-speeds are in the range of 2 - 6 ms^{-1} (black bars). Dust emission starts around 4 ms^{-1}, but remains a small fraction of all observations up to 7 ms^{-1}. Beyond this value the dust fraction increases quickly and from 10 ms^{-1} onwards practically all observations contain dust emission reports. This is an example of well-defined threshold behaviour with T25 (7.5 ms^{-1}), T50 (8.25 ms^{-1}) and T75 (9.25 ms^{-1}) all being close together.

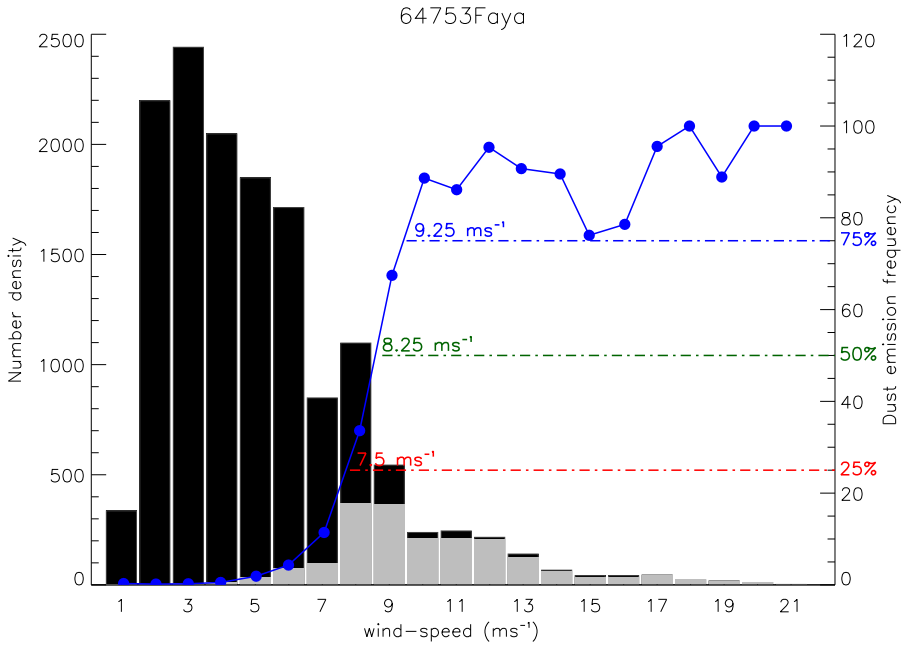

FIGURE 2.4: Example wind climatology for Faya (WMO no. 64753) in Chad (see Fig. 3.1 for location). Number distribution of surface wind-speed for the time period 1984-2012. Black bars and grey bars give the distribution of all winds and those associated with dust emission only, respectively. Dust emission frequency ((grey/black)*100) for each wind-speed bin is given by the blue dots. T25, T50 and T75 threshold values are given in red, green and blue, respectively.

Chapter 3

A Climatology of Dust Emission in Northern Africa Using Surface Observations: 1984 - 2012

3.1 Introduction

This chapter uses long-term observations from standard surface weather stations across North Africa which report at three and six hour intervals to compile climatological statistics, including the diurnal cycle. Despite the sparse area coverage of N Africa, these data have a high value for dust emission studies and have been explored surprisingly little in the literature. Up to now, surface observations of visibility and present weather have been used for statistical analysis in the Sahel and Sahara (Klose *et al.*, 2010; Mahowald *et al.*, 2007; Mbourou *et al.*, 1997), but these have not isolated dust emission events specifically. Climatological studies of dust emission, from surface SYNOP present weather reports, have only been conducted for East Asia (Kurosaki & Mikami, 2005), the southwest summer monsoon region (Ackerman & Cox, 1989; Middleton, 1986b) and Australia (McTainsh & Pitblado, 1987). The seasonal and diurnal cycles of dust are explored in relation to visibility and rainfall in Mbourou *et al.* (1997) while Marticorena *et al.* (2010) discusses dust concentration and strong wind frequency. The time and spatial scales of these two studies are quite different with 53 stations and three four-year periods investigated in Mbourou *et al.* (1997) compared to three stations for a three year period in Marticorena *et al.* (2010).

This chapter intends to build on the information gathered by these studies by including a larger spatial area, a longer data record and new data analysis techniques which aim to clearly separate emission from transport events.

This chapter presents a climatology of dust emission events from SYNOP observations from N Africa, objectively determines wind-speed thresholds for emission and applies new diagnostics and statistics to assess seasonal and diurnal cycles of these events. Section 3.2 explains how dust emission is identified from surface observations, the criteria and quality flags applied to the station data and the diagnostics tools used for analysis. Section 3.3 presents the results of the seasonal and diurnal cycle of dust emission, with discussion on individual stations followed by stations grouped together in section 3.3.2. Changes in emission threshold, both geographically and temporally, will also be discussed in section 3.3.

3.2 Data and Methods

3.2.1 Quality Flags and Station Selection Criteria

Long-term surface observations are recorded as SYNOP reports, which include 3-hourly observations of 10 m 10-min mean wind-speed based on anemometer measurements and present weather subjectively judged by a human station observer using a code defined by the World Meteorological Organisation (WMO). The present weather (ww) codes describing dust emission are 07-09, 30-35 and 98 (section 1.4.3). These descriptions of dust emission weather do not provide information on the physical processes at a particle scale, but simply describe how the dust appears in the atmosphere to the observer. As in Kurosaki & Mikami (2005), these codes are split into "blowing dust" (07 and 08) and "dust storms" (09, 30-35 and 98), which represent dust events on a larger scale and may also be more intense. Information on visibility is purposely omitted, as the relative contribution of advected and locally emitted dust particles to low visibility is unknown. The code 06 ("dust not raised by wind, at or near the station") is extracted to investigate non-emission dust events. For the purpose of this chapter these events are labelled as "transported dust". Groups of reports are transformed into frequency of occurrence parameters. Frequency of Dust Emission (FDE) is the percentage of dust events (all emission codes) reported at a

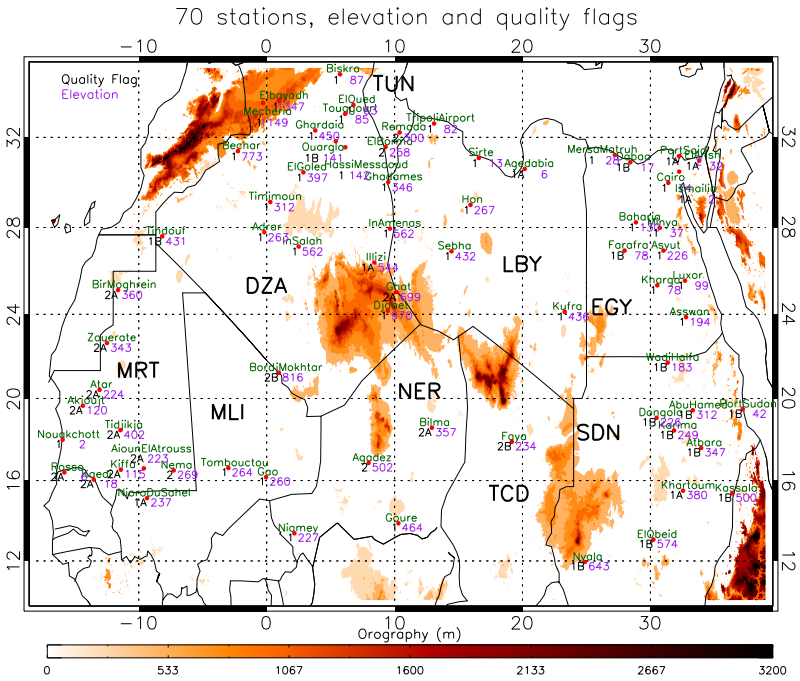

FIGURE 3.1: Geographical overview. Map of observation stations used in the study, with quality flags in black and elevation in purple. Country codes, as defined by ISO (International Organisation for Standardisation): DZA=Algeria, TUN=Tunisia, MRT=Mauritania, MLI=Mali, NER=Niger, LBY=Libya, EGY=Egypt, TCD=Chad and SDN=Sudan. Colour shading gives the orography in m.

given time of day or during a certain month, with respect to the total number of observations. Dust Storm Frequency (DSF), Blowing Dust Frequency (BDF) and Transported Dust Frequency (TDF) are calculated in the same way, but with the particular codes for dust storms and blowing dust as described above.

As dust emission is the primary focus of this chapter, the first criteria for stations to be selected was for 1060 observations of dust emission over the time period 1984 - 2012. 70 stations, displayed in Fig. 3.1, fulfilled this criterion and form the basis of this chapter. The ratio of day to night-time observations, as well as the number of observations per year, was investigated in order to create a quality flag system for the stations. Quality flags consists of a number (1 or 2) proceeded by a letter (A, B or blank). Where the ratio of day to night observations is greater than 2:1 a 2 flag is given, while a 1 is applied to a non biased station. Healthy stations with more than 500 observations per year for each year between 1984 and 2012 do not have a letter flag. Stations which have less (greater) than 5 years with less than 500 observations per year are marked A (B).

The 29 years of SYNOP data included some wind-speed reports above realistic values;

in some cases a typographic error was clear (see section 4.4). Analysis of some of the strongest winds from the study period alongside SEVIRI data (2006 - 2012) found that the strongest (realistic) wind associated with a dust emission report was a 54 kt report accompanied by a noticeable cold pool outflow in the satellite imagery (section 4.4.4). Since reports at wind-speeds greater than this could not be confirmed, those over 55 kts were removed from the analysis.

Station location, elevation and quality flag values are displayed in Fig. 3.1. Not surprisingly, SYNOP stations are rare in the interior of the Sahara and more commonly situated on the fringes, where precipitation is abundant enough to sustain vegetation, crops and livestock. The stations in Sudan are all located along the Nile, as are most Egyptian stations. Southern Mauritania and northern Algeria have a relatively good network. The stations of Bordj Mokhtar (southern Algeria) and Faya (northern Chad) are particularly valuable due to their close location to two well-known dust sources. The former was the location of a supersite during the recent Fennec field campaign (Marsham *et al.*, 2013),

3.2.2 Three and Six-hourly Sampling Regimes

In the Sahel region 6-hourly sampling is more common than 3-hourly sampling. Different sampling regimes tend to be confined to within countries. For example in Mauritania nearly all stations have no night-time observations, while in Mali and Niger sampling tends to be limited to 6-hourly. This is documented in detail in Appendix A, Fig. 1. Analysis of 6-hourly data was applied to stations which have stable 3-hourly sampling. The magnitude of annual FDE varied at a few stations, but overall the seasonal cycle remained similar at all but one station (Appendix A, Fig. 2). It is suspected that this is due to natural inter-station variability in the diurnal distribution of dust emission mechanisms between SYNOP and inter-SYNOP hours. The approach taken here is to highlight the main biases which might affect conclusions that apply to large areas and groups of stations, rather than focusing on the effect of individual station biases on their individual results.

3.2.3 Strong Wind Frequency

In order to test the relationship between the occurrence of dust emission and the occurrence of strong winds, the parameter strong wind frequency (SWF) is defined as the percentage

of all wind observations exceeding T50. If the threshold behaviour is well defined (as in Fig. 2.4), FDE and SWF should behave in a similar way, but this is not generally the case and differences will depend on the exact shapes of the two pdfs. To illustrate this effect, four areas are distinguished in Fig. 2.3. Area A represents winds below T50 without dust emission, B winds above T50 without dust emission, C winds below T50 with dust emission and D winds above T50 with dust emission. All observations can then be represented as N = A+B+C+D. Consequently, Area C+D represents all dust emission events and therefore FDE is the fraction (C+D)/N. SWF is represented by the fraction (B+D)/N. If FDE = SWF then this implies that C = B. Four cases can be distinguished. If both C and B are small, FDE $\approx$ SWF and the threshold must be sharp. If both C and B are large, then still FDE $\approx$ SWF, but a large fraction of strong winds are not accompanied by dust emission events, implying a large difference between T25 and T75. This could be caused by varying threshold behaviour due to changes in soil moisture or vegetation, for example. If B $>$ C, then SWF $>$ FDE and therefore a relatively large fraction of strong winds occur without dust. This implies a rather abrupt start of emissions, and a larger difference between T50 and T75. If B $<$ C, then SWF $<$ FDE and therefore a relatively large fraction of weak winds create dust events, most likely accompanied by a larger difference between T25 and T50. Out of 18387 observations of high winds with no emission from the 70 stations, 434 events (2.3%) experienced a documented rainfall event in the previous 24 hours. This provides evidence that some high wind events do not produce dust due to high soil moisture. However, as the majority of rainfall values are blank in the SYNOP records, and it cannot be ascertained if this is because there was no rainfall or no reading, SYNOP precipitation is not suitable for investigating this any further.

3.2.4 Least Squares Method to Determine Dust Emission Threshold

The SWF concept is used in the second method to determine an emission threshold. Here, SWF is first calculated for a range of wind-speed thresholds. The value that gives the smallest total squared difference between the seasonal mean diurnal cycles of FDE and SWF is then selected. Data are binned seasonally, instead of monthly, in order to give stable pdfs. This method will be referred to as "Least Squares" (LS, hereafter) and is expected to give results on the same order as T50 and be used to test the robustness of the threshold identification approach. A comparison between the threshold values of T25,

T50, T75 and LS gives more insight into the relationship between winds and emission than a single value and highlights the fact that emission occurs over a range of wind-speed values (Helgren & Prospero, 1987).

3.2.5 DUP Mean and Intensity

The seasonally varying T50 for U_t is used at each SYNOP station for *DUP* calculations. The dust-emitting power per strong wind event is given by *DUP* mean (all *DUP* values, including 0 values) / fraction of strong wind events (SWF x 100) and is referred to as "*DUP* Intensity".

3.3 Results and Discussion

3.3.1 Single-station Climatologies

3.3.1.1 Annual Frequencies of Dust Emission and Transported Dust

Fig. 3.2 shows annual mean FDE for all stations for the entire investigation period 1984 - 2012. Despite a lot of variation between stations there are some general patterns in the geographical distribution. All eleven stations with FDE > 10% are located between 15°N and 23°N (large circles, Fig. 3.2). Situated close to an important dust source, the Bodélé Depression, Faya in Chad has a mean FDE of 12%. Spatial variation is high in Egypt, particularly between the two stations of Kharga (10%) and Luxor (1%), which are within 230 km of each other. This could be due to local environmental factors, as Kharga is a desert oasis and Luxor is situated on the Nile. FDE values of 5 to 10% are quite common in the northern Sahel and present at the central Algerian stations of Timimoun, Adrar and In Salah. Values < 5% are frequent north of 24°N in the central and northern Sahara and in the southern Sahel. This pattern indicates that, although dust sources are found across the entire region, dust emission is generally more frequent in the semi-arid transition zone between the Sahel and Sahara. This is in agreement with the identification of a "Sahel dust zone" by Klose *et al.* (2010), though their study included transported events. Comparing Fig. 3.2 with the satellite derived dust activation frequency map in Fig. 3.3 from Schepanski *et al.* (2009b) identifies a similar high frequency

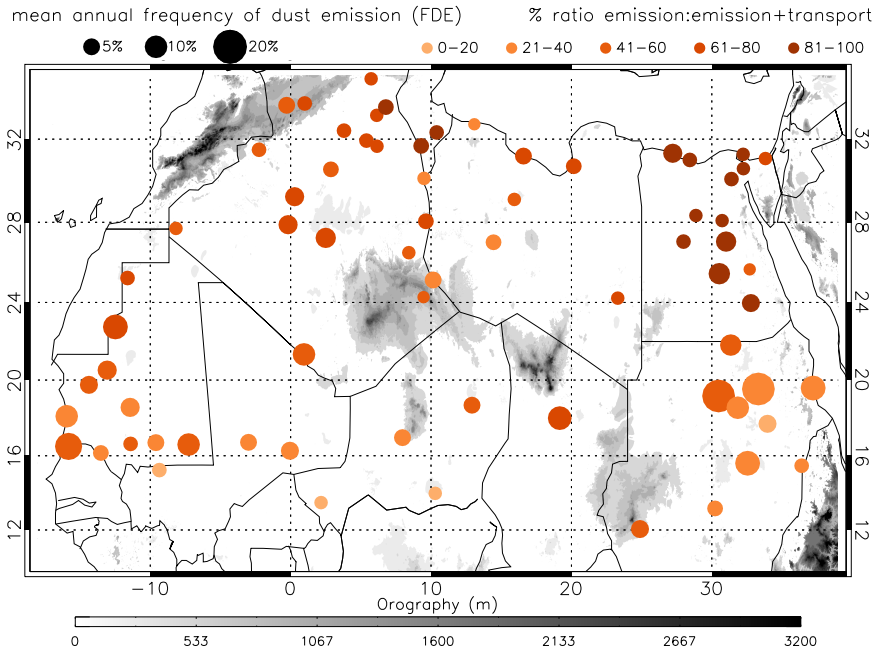

FIGURE 3.2: Annual emission climatology. Spatial distribution of mean annual FDE (dot size) and % ratio of emission to all dust events (including transported events) (dot colour) at 70 stations in N Africa for the time period 1984-2012.

of dust emission in the northern Sahel, but as recently reported in Heinold *et al.* (2013), satellite retrived emission from SEVIRI could miss 60% (90%) due to part (dense) cloud cover in the afternoon and evening hours of 1700 - 2200 LT. The implications of this are that the satellite retrival map may be missing dust emission frequencies from locations further south of this region, where monsoon-related cloud will be particularly frequent in the summer months. Indeed, the south of Mauritania shows frequent emissions in the surface observations, but it is not a strong source in Fig. 3.3. Both methods do pick up on the frequent emissions from Sudan, which are not captured in other satellite retrivals such as TOMS AI (Engelstaedter *et al.*, 2006) due to the particular limitations of once-a-day sampling and the fact it is a measure of aerosol through the atmospheric column and quite different from dust frequency at the source. However, a map of dust storm frequency, compiled using a slightly differently processed surface observation data set (the International Station Meteorological Climate Summary, ISMCS) does also shows a high annual frequency of dust storms around latitudes 16 - 24°N (Fig. 3.4).

To explore the relative contribution of emission to all dust events at a given station, the

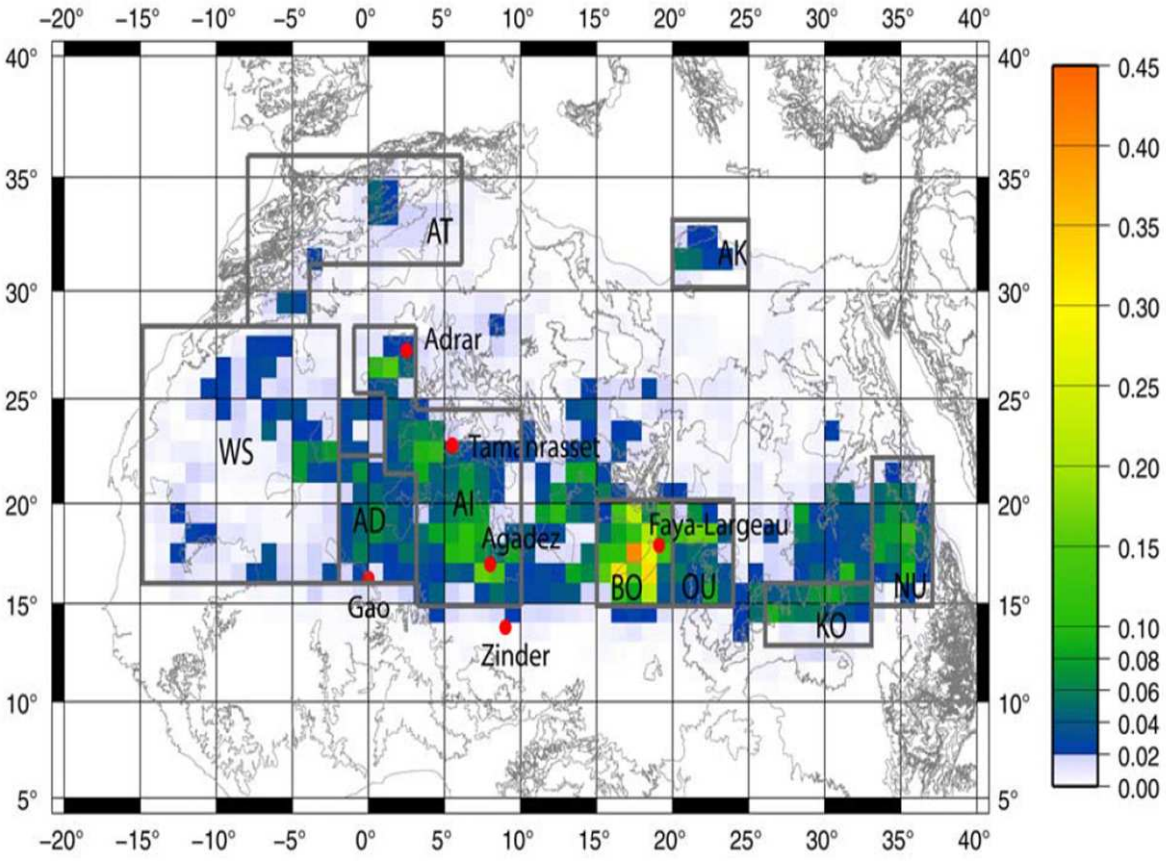

FIGURE 3.3: Fraction of dust source activations (DSA) per day during March 2006 to February 2008 except August 2007 derived from MSG IR dust index. High numbers of DSAs per day are observed in depression areas (Bodélé, sebkas, and chotts) and the foothills of the Saharan mountain areas. Red dots represent the location of synoptic stations considered in this study. The boxes mark the predefined subareas for discussion on the subdaily and monthly variability of observed DSA. Topography indicated by contour lines at 250 m intervals is given by the GTOPO30 digital elevation data set provided by the U.S. Geological Survey. From (Schepanski, 2009).

ratio of emission to emission plus transport (BDF+DSF)/(BDF+DSF+TDF) (for definitions see section 3.2) is displayed in Fig. 3.2 by the shading of circles, where light colours indicate more transport and dark colours more emission. Emission generally dominates the dust records north of ∼22°N. The largest values of > 90% are found at many stations in Egypt. The Algerian and Tunisian stations of El Oued, Remada and El Borma (see Fig. 3.1 for locations) display a local maximum with values >80%. This area has been identified as a major dust source due to the dried lakes associated with Chott Jerid and Chott Melrhir (Prospero, 2002; Schepanski *et al.*, 2012). Generally values > 50% are found in Libya, Tunisia and Algeria, while for the majority of Sahelian stations values

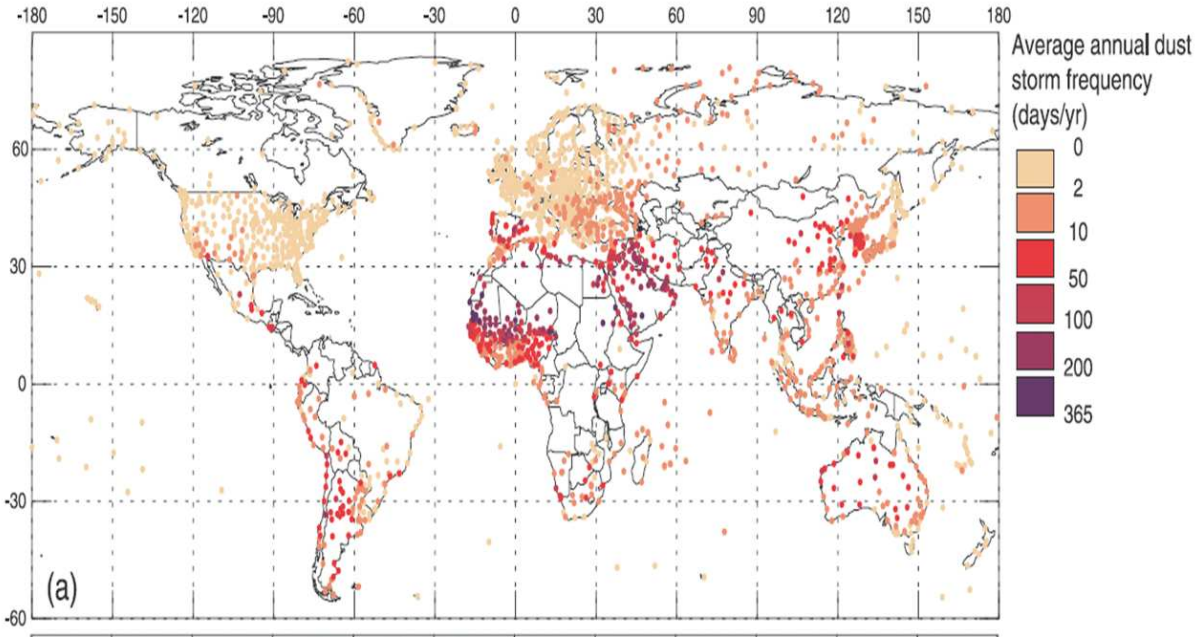

FIGURE 3.4: Map of annual frequency of dust storms, from (Engelstaedter *et al.*, 2003).

are $< 50\%$. Located close to active source regions, the stations of Bordj Mokhtar and Faya have transport ratios of 55% and 68% respectively, which are among the highest of any stations south of 22°N. Transport events generally dominate Sahelian stations south of 20°N. Despite frequent transport reports, these stations also have FDE mean values comparable to those in the north, and sometimes higher, making the Sahel a dust hotspot (Klose *et al.*, 2010). The dustiest subregion in N Africa is Sudan with an FDE of more than 10% at several stations and in addition to this, a high frequency of transport events. It is worth noting that the Sudan stations are all situated in the Nile valley, so may not represent the wider region of northern Sudan. Overall this analysis demonstrates that emission events contribute significantly to all reported dust events in this region.

3.3.1.2 Annual Mean Dust-emission Thresholds

Spatial variations in annual mean dust emission thresholds are displayed in red, green and blue, representing T25, T50 and T75, in Fig. 3.5. Thresholds are generally higher north of 22°N, with T50 between 10 and 15 ms^{-1} at many stations in Algeria, Tunisia, central Libya and Niger. Moderate T50 values of 7 - 10 ms^{-1} are found in Egypt, southern Sudan and in parts of the west Sahelian countries of Mali and Mauritania. The lowest thresholds

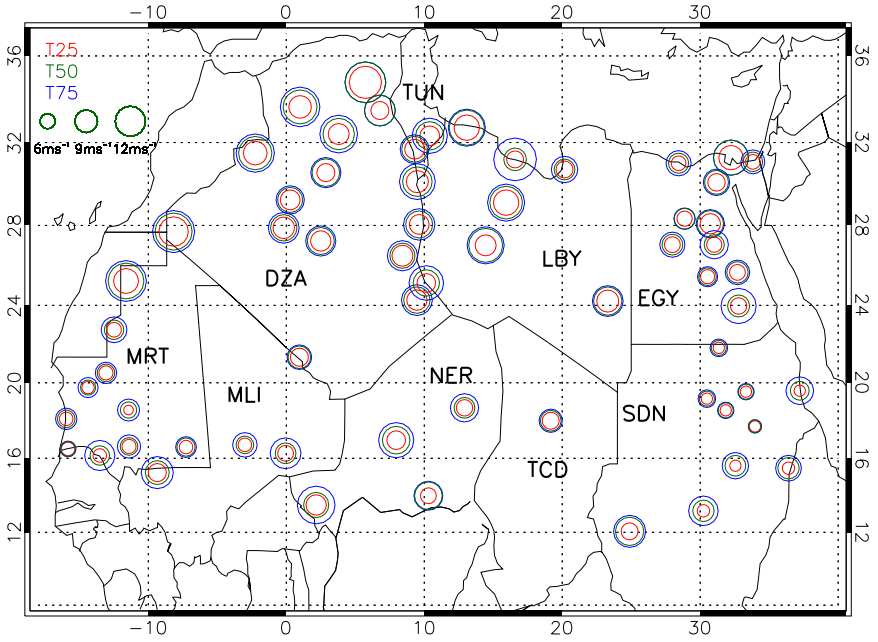

FIGURE 3.5: Geographical distribution of emission thresholds. Shown are annual values of T25, T50 and T75 (for definitions, see section 3.2) in red, green and blue, respectively. Country codes, as defined by ISO (International Organization for Standardization): DZA=Algeria, TUN=Tunisia, MRT=Mauritania, MLI=Mali, NER=Niger, LBY=Libya, EGY=Egypt, TCD=Chad and SDN=Sudan.

are found between 16°N and 20°N in the northern Sahel, in the west over Mauritania and particularly in central/northern Sudan, where T50 values of 5 ms^{-1} and 6 ms^{-1} are present at five adjacent stations. Differences between T25, T50 and T75 tend to be largest in the Sahel, consistent with possible influences from seasonal precipitation and vegetation there. Larger differences are also found for some stations along the Mediterranean coast, where occasional cool season rains may have a similar effect. There is no clear pattern in the relationship between T25, T50 and T75. For many stations, the three values are quite equally spaced. At some stations however, particularly in the Sahel, there is a much larger difference between T75 and T50 than between T25 and T50. This result suggests that these areas are occasionally characterised by soil states that do not allow dust emission, even for rather high winds. This could occur in summer when soils are wetter and more vegetated.

It is interesting to question the extent to which these spatial differences in thresholds affect dust emission or whether meteorological factors dominate. Fig. 3.6 shows a scatter plot of annual mean FDE and T50 for all 70 stations plotted in Fig. 3.5. The anti-correlation

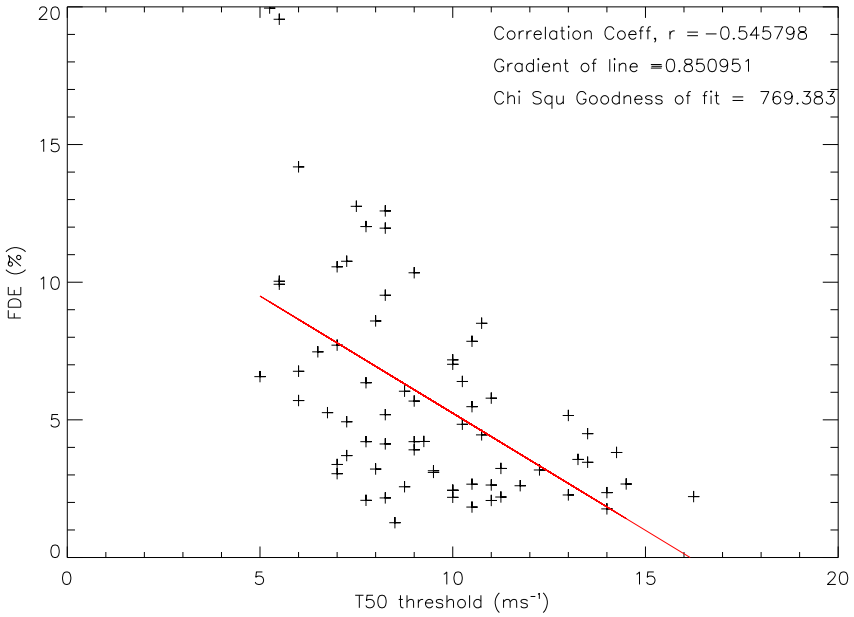

FIGURE 3.6: Scatter of annual mean frequency of dust events (FDE) against annual mean T50 (for definition, see section 3.2) for each of the 70 individual stations for the period 1984-2012. Correlation coefficient, gradient of best-fit line and goodness of fit test are given in the top right corner.

of -0.54 shows that stations with low thresholds tend to have more frequent dust events, but the explained variance is only 30%. The two prominent outliers are Dongola and Abu Hamed in Sudan, which have both very low thresholds and extremely high mean FDEs of almost 20%. These high FDE values could be due to local environmental factors such as an easily erodible local source, or local orographic circulations which allow winds to exceed the threshold regularly.

3.3.1.3 Seasonal Cycles in Frequency of Dust Emission and Vegetation

Fig. 3.7 shows station-mean monthly values of FDE split into the contribution from BDF (green) and DSF (red). Larger versions of the individual station plots can be found in Appendix A, Fig. 4. Not surprisingly BDF dominates at all stations. DSF are quite rare, but relatively more common in the Sahel, particularly between 15°N to 20°N. At many stations across Algeria, Tunisia, Libya, Egypt and Sudan FDE is highest in spring. The remaining stations, mostly situated in the central and western Sahel, have variable seasonal cycles, though most display reduced FDE in autumn. At the southernmost stations FDE

is practically zero in late summer/early autumn when rainfall and vegetation cover are high. FDE peaks in summer at the central Saharan station Bordj Mohktar, which could be related to the SHL and the arrival of convective cold pools from the northern Sahel during the peak of the summer monsoon as discussed in Marsham *et al.* (2013). Faya, the only station in Chad, shows high values of both FDE and DSF during the winter half year (Washington & Todd, 2005), when the Harmattan is strongest, while monsoon related summer dust storms are much rarer here.

Some of the seasonality evident from Fig. 3.7 is consistent with the seasonal cycle of vegetation cover. The most southerly stations, including Nioro Du Sahel, Niamey, Gouré, Nyala and El Obeid, show a marked increase in NDVI (blues lines in Fig. 3.7) in autumn following the summer rainfall maximum (Fensholt *et al.*, 2012). These signals get weaker towards the northern Sahel and are absent in central Mauritania and at Bordj Mohktar. In Egypt, the 3 stations situated on the banks of the Nile (Minya, Asyut and Luxor) contrast with desert oasis stations of Baharia, Farafra and Kharga, which have no seasonal cycle in vegetation. As the Nile river flow in Egypt is controlled by the upstream Aswan Dam, and this region experiences little rainfall, it is possible that the seasonal cycle is driven by agriculture and anthropogenic activities. There are some subtle changes in seasonal vegetation at northern Algerian stations, but overall in Algeria and Libya it is unlikely that vegetation has a major influence on seasonal dust cycles.

3.3.2 Climatologies from Grouped Stations

3.3.2.1 Rationale for Grouping of Stations

As discussed in the introduction, there are numerous dust emitting mechanisms over N Africa, creating distinct seasonal and diurnal cycles in different regions, while individual stations may be also influenced by very local factors as topography or nearby obstacles (trees, buildings etc.). For further discussion of the climatology, six geographical groups of stations are defined: Northern Algeria (N Algeria hereafter), Central Sahara (C Sahara), Western Sahel (W Sahel), Central Sahel (C Sahel), Egypt and Sudan (see ellipses in Fig. 3.7). This was done subjectively by looking for similar characteristics in the seasonal and diurnal dust cycles as well as using literature and wind-direction climatologies to identify similar seasonal wind regimes. The reasoning behind station selection in each

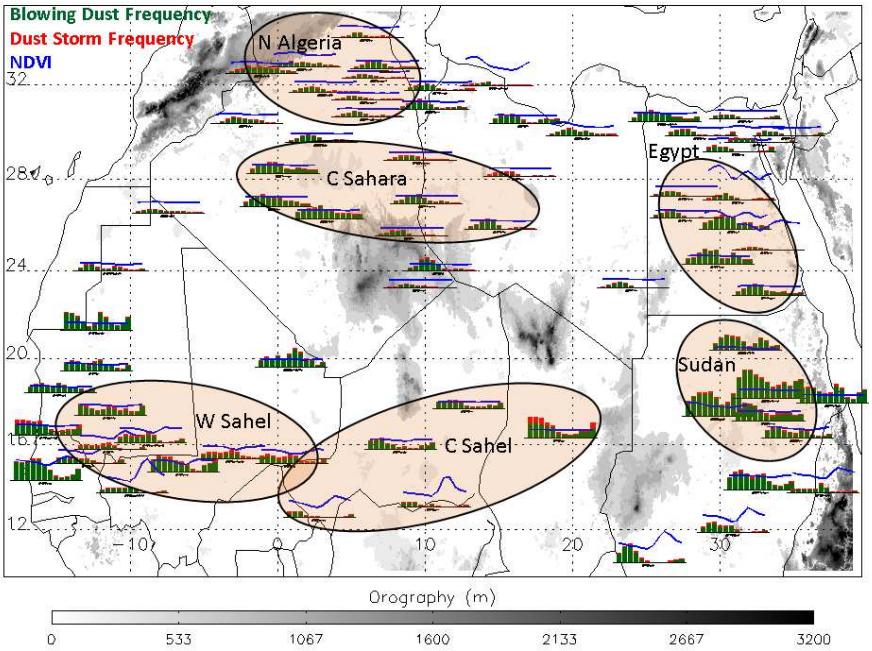

FIGURE 3.7: Mean seasonal cycle. Monthly mean FDE, split into BDF (green bars) and DSF (red bars) (for definitions, see section 3.2), as well as monthly mean NDVI (blue lines) calculated for a 24 km x 24 km box centred on each station. The x-axis runs from January to December. The y-axis scale is 0-40% for FDE and 0-5000 for NDVI. Areas of grouped stations, discussed in section 3.3.2.1, are shown with shaded black ellipses and labels.

group is discussed further below. Grouped values are calculated by taking a mean of a given variable (T25, T50, T75, LS, FDE, DBF, DSF, SWF, *DUP* mean), which has before been calculated separately for each station in the group. *DUP* Intensity is calculated after *DUP* and SWF have been group averaged first. Therefore each station is equally weighted within the group, but this comes with the caveat that stations with gaps and biases in their record are weighted equally to stations with more complete records.

N Algeria experiences a Mediterranean climate with wet winters, associated with Atlantic cyclones and Mediterranean depressions, and hot, dry summers (Warner, 2004). Saharan, or Sharav as they are known in NW Africa, cyclones are a key feature here in spring (Hannachi *et al.*, 2011) and play a role in dust source activation (Fiedler *et al.*, 2013b; Schepanski, 2009). Analysis of the wind direction (not shown) suggests that the background flow, hence large-scale influence, are similar at the stations of Biskra, El Oued, Touggourt, Ghardaia, Elbayadh, Hassi Messaoud, Ouargla and Mecheria which make up

the N Algeria group. Quality flags of 1 apply to all eight stations due to unbiased and unbroken time-series of data (Fig. 3.1). Six of the eight stations are situated in the low-lying area to the southeast of the Atlas Mountains, while Mecheria and Elbayadh are located in the foothills and have elevations of 1149 m and 1347 m, respectively.

The C Sahara group is situated further south, between 27°N - 30°N, and 1°W - 14°E. The stations of Timimoun, Adrar, In Salah, In Amenas, Ghadames and Sebha experience a different meteorological regime to that of N Algerian stations. Rainfall is scarce and winds, which are generally higher, have an easterly or northeasterly direction. Similar to N Algeria, all stations have a quality flag of 1 (Fig. 3.1) and show a peak in FDE in spring (Fig. 3.7). The focus in Egypt is on the seven inland stations of Baharia, Farafra, Kharga, Minya, Asyut, Luxor and Asswan within the region 23°N - 28°N, 27°E - 33°E which are characterised by a similar N - NW wind regime. Only Farafra has quality issues, with a 1B flag indicating a period > 5 years with reduced observations (Fig. 3.1). Despite some seasonal variation in the vegetation cycle at stations on the banks of the Nile (Minya, Asyut and Luxor, see Fig. 3.7), the overall seasonal cycle of dust is similar with a spring peak in FDE, most likely caused by the seasonality of meteorological factors.

Two groups of stations in the Sahel are considered. The W Sahel group is comprised of the inland stations of Kiffa, Aioun El Atrouss, Nioro Du Sahel, Kaedi, Nema, Tombouctou, Gao and Tidjika, and encompasses the region 13°N - 19°N, 13°W - 0°E. The C Sahel stations include Bilma, Niamey, Gouré and Agadez in Niger and Faya in Chad. The main difference between the two groups is that the summer monsoon and its interactions with the SHL drive summer emissions in W Sahel, but have less influence over the C Sahel stations, which are united by the domination of the winter Harmattan winds as a driver of the frequency of dust emission (Fig. 3.7). As is common with nearly all Mauritanian stations, five of the eight stations in the W Sahel group have a daytime bias and four have gaps of < 5 years as indicated with flags of 2 and A respectively (Fig. 3.1). The quality of C Sahel stations is mixed, with healthy stations of Niamey and Gouré achieving quality flags of 1, in contrast to Faya with a 2B flag (Fig. 3.1).

The Sudan group consists of Wadi Halfa, Abu Hamed, Dongola, Karima and Atbara and lies within the coordinates 17°N - 22°N, 30°E - 34°E. This excludes the southern stations, where the influence of the monsoon is felt in summer. Only Atbara receives small amounts of summer rains. From Karima up to Wadi Halfa, the stations remain in a consistently

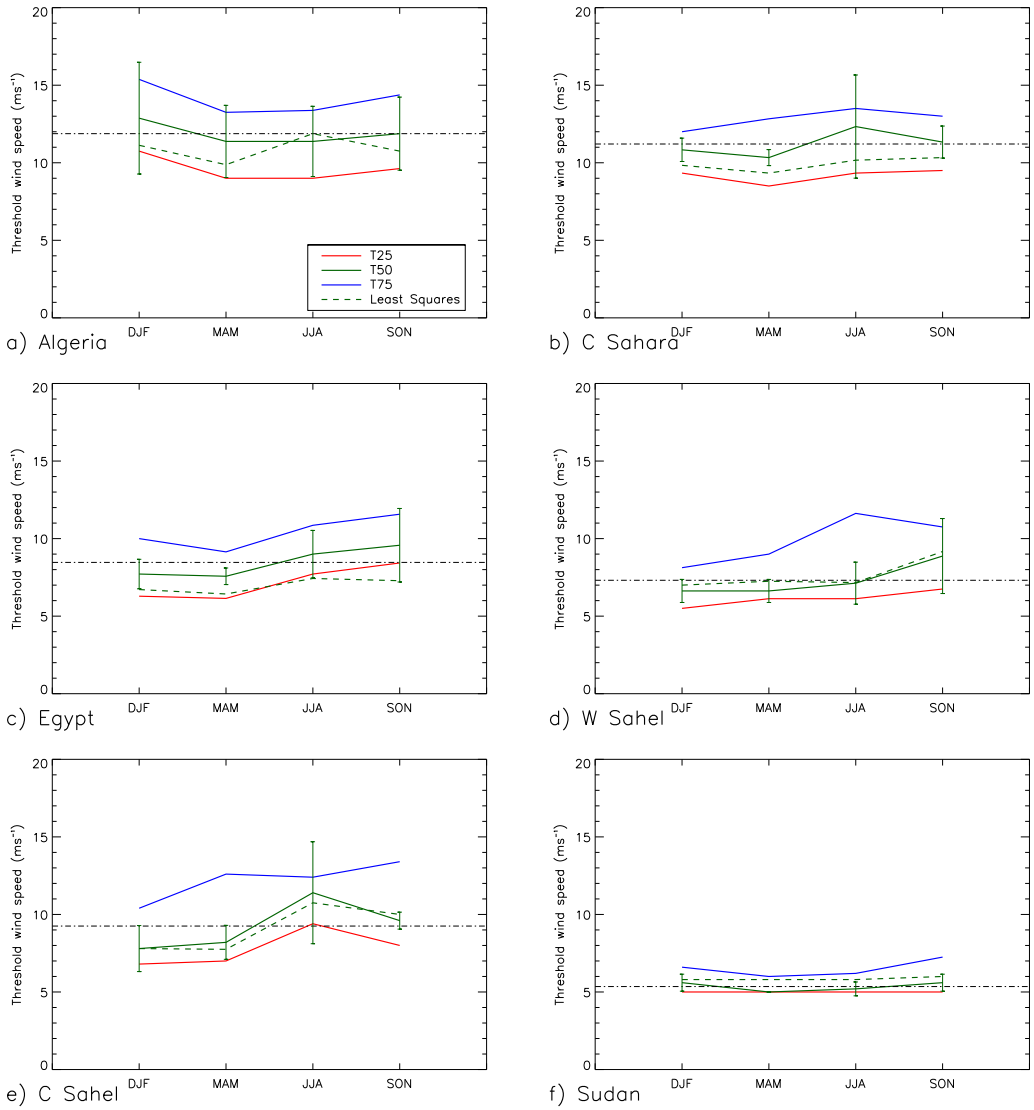

FIGURE 3.8: Seasonal threshold values averaged over six station groups (see section 3.3.2.1 for definition): a) N Algeria, b) C Sahara, c) Egypt, d) W Sahel, e) C Sahel and f) Sudan according to the legend in the top left panel (for definition of thresholds, see section 3.2). The dashed black lines indicate the annual mean T50. Seasons are December, January, February (DJF), March, April, May (MAM), June, July, August (JJA) and September, October, November (SON).

northerly flow and experience almost no rainfall. B quality flags apply to these stations to indicate gaps in the record > 5 years, which coincide with periods of civil unrest (Fig. 3.1).

3.3.2.2 Seasonal Cycle in Dust-emission Thresholds

To summarise and complement the discussion based on Fig. 3.5 in section 3.3.1.2, seasonal values of T25, T50, T75 and LS dust emission thresholds are presented here (Fig. 3.8), which are first calculated for each station and then averaged over the group. The LS values are typically within 1 ms^{-1} from T50, but deviations of up to 2.5 ms^{-1} also occur for some groups in some seasons. Consistent with Fig. 3.5, Fig. 3.8 shows that the highest thresholds are observed at the N Algeria stations with an annual mean of 11.5 ms^{-1} followed by the C Sahara group. The lowest thresholds are observed in Sudan with a mean of 5.7 ms^{-1}. The maximum seasonal threshold of 12.5 ms^{-1} occurs in the wet N Algerian winter, while Sudan thresholds fall to a minimum of 5.5 ms^{-1} in spring.

Seasonal variability is highest in the summer monsoon influenced Sahel, particularly the C Sahel where thresholds are a mean of 2.8 ms^{-1} higher in summer than in winter. In contrast to this Sudan thresholds vary by only 0.5 ms^{-1}. The seasonal transition from low thresholds to high thresholds takes place in summer in W Sahel and in spring in the C Sahel, where two of the southernmost stations are located. In both regions T75 increases before T50 and T25. This could be due to infrequent early-season precipitation events, which moisten soils so that no emission can take place. Just a few of these events could create the increase in D75, while for the majority of the time it is still dry enough to allow for dust emission such that T25 and T50 do not rise similarly.

Standard deviations in thresholds between stations within each group (indicated by error bars in Fig. 3.8) are largest in summer in the C Sahara and C Sahel, in winter in N Algeria and in autumn in the W Sahel and Egypt. Interestingly these increases in spatial variability within a region are usually accompanied by an increase of the threshold itself. This may indicate that the changes in soil moisture and vegetation that cause the threshold to rise are inhomogeneous across the region. However, higher thresholds typically also coincide with fewer dust observations, which reduces confidence in the threshold estimates.

3.3.2.3 Seasonal Cycle in Dust Emission

Fig. 3.9 shows the seasonal evolutions of BDF, DSF and FDE (bars) together with those of SWF, *DUP* and *DUP* Intensity (lines) for the six groups. The latter three are based

on seasonal, rather than monthly, T50 values (season boundaries are indicated by thin vertical lines in Fig. 3.9). This slight inconsistency is undesirable, but necessary to obtain sufficient data to estimate stable thresholds. The influence of using seasonal, instead of annual mean, thresholds is rather insignificant and consistent with the relatively minor changes seen in Fig. 3.8. For example, monthly correlations between FDE and SWF vary on average by only 0.08 from when using either a seasonally varying, or a fixed annual-mean, T50 threshold.

Spring is the dominant season in the N Algeria group as expected from Fig. 3.7, with a maximum FDE of 7% in April. DSF is very low in this region throughout the year with largest values also in April. The annual cycle of SWF follows that of FDE closely with a correlation of 0.99, but with values consistently 1 - 2% lower. As discussed in section 3.2, this implies a relatively large area C (winds below T50 which do produce emission) in Fig. 2.3 and is consistent with the slightly larger difference between T50 and T25 than that between T50 and T75 in Fig. 3.8a. As the region with the highest threshold of all groups, T25 is already well above typical emission thresholds found in the literature (Chomette *et al.*, 1999; Helgren & Prospero, 1987), creating this rather broad range of wind speeds which can and cannot produce dust. The annual cycle of DUP agrees with FDE on the overall peak in spring. The ratio of DUP to SWF ("DUP Intensity") indicates a relatively low mean intensity from February to July and much higher values from September to January. This suggests that less frequent dust events during the cool season are more intense when they occur. Mediterranean cyclones could be the meteorological mechanism creating high intensity events in the cool season. As shown by Fig. 3.8a, winter is also the time when thresholds are slightly increased, requiring a more extreme meteorological event to generate dust.

Several of these features are broadly reproduced in the C Sahara (Fig. 3.9b), but values of both FDE and DUP are significantly higher than in N Algeria (note identical FDE and DUP scales in all panels of Fig. 3.9). Here, FDE peaks at 10% in April with a secondary autumn maximum in both DUP and FDE which is less significant than the spring maximum. DUP Intensity is less seasonally variable than in N Algeria with typical values around 14000 m^3s^{-3}, which is slightly lower than in N Algeria (note variable DUP Intensity scales between panels in Fig. 3.9). Egypt (Fig. 3.9c) also agrees with the former two regions with respect to the spring maximum and secondary maximum in autumn

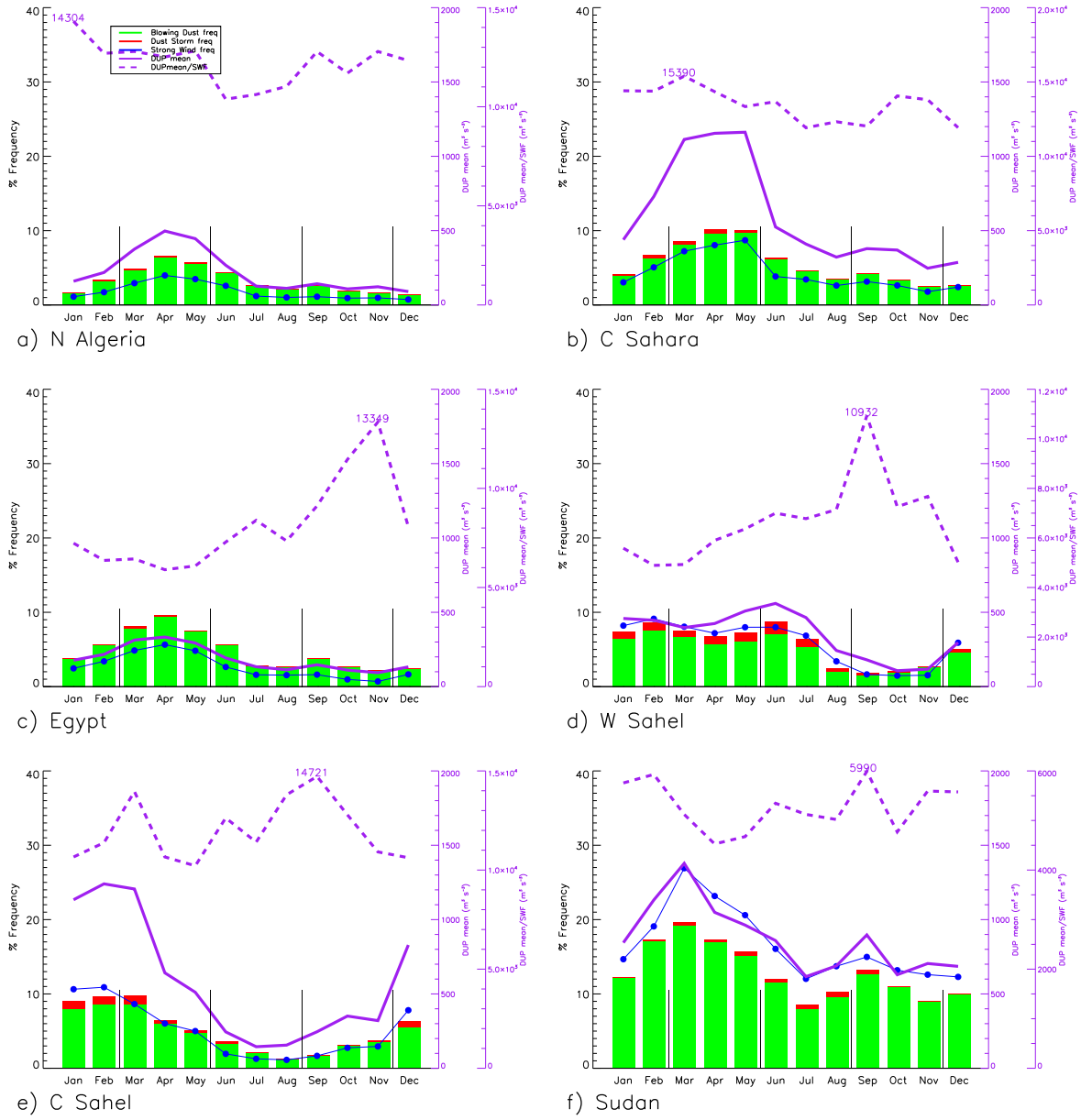

FIGURE 3.9: Mean seasonal cycle for the six station groups (see section 3.3.2.1 for definitions): a) N Algeria, b) C Sahara, c) Egypt, d) W Sahel, e) C Sahel and f) Sudan. Monthly frequency of FDE, split into BDF (green bars) and DSF (red bars), as well as SWF (blue line), DUP mean (solid purple) and DUP Intensity (DUP mean/SWF, dashed purple, maximum values given), all computed using the seasonally varying T50 (for definitions of parameters, see section 3.2). Thin vertical black lines indicate seasonal boundaries where thresholds change. Note the different vertical axes for DUP intensity.

FDE. The annual FDE peak is 10% in April and the annual mean is ∼2% higher than N Algeria. SWF is considerably lower here than FDE but shows a similar annual cycle. Less frequent strong winds could, to some extent, explain the lower *DUP* mean values.

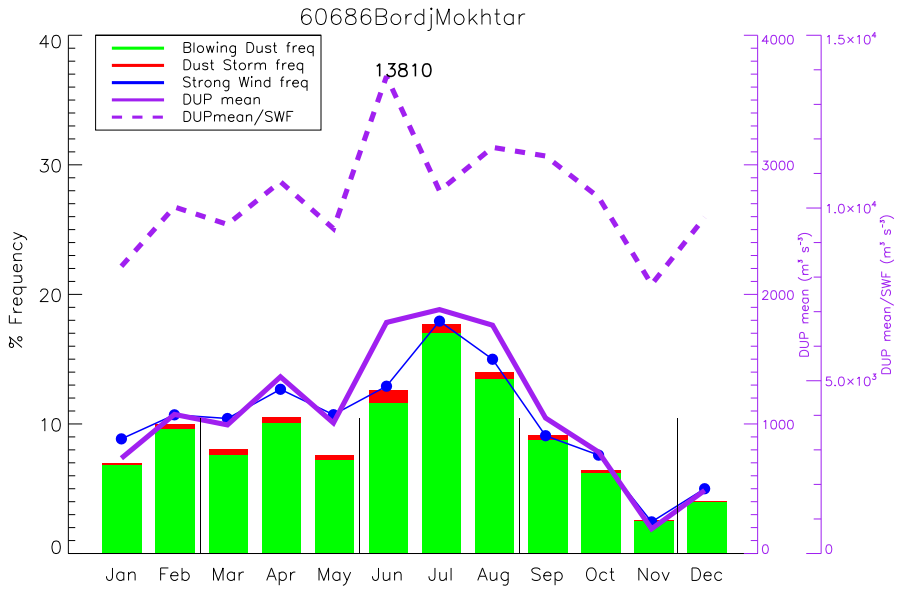

FIGURE 3.10: As Fig. 9 but for Bordj Mokhtar (WMO number 60686).

The clearest difference is the peak in *DUP* Intensity in November, though overall *DUP* Intensity is lower than N Algeria and C Sahara. High *DUP* Intensity in autumn could be due to occasional storms from the Mediterranean affecting north-eastern Africa, during a time when thresholds are slightly increased (Fig. 3.8c).

Behaviour is fundamentally different over the two Sahelian regions (Figs. 3.9d and e). A similar effect on dust concentration was observed by Marticorena *et al.* (2010) for two stations located within the C and W Sahel regions. The C Sahel, which contains more southern stations, displays a longer low-dust season. W Sahel is located closer to the centre of the SHL in summer, which may contribute to dust emissions into June and even July. In both regions the agreement in magnitude between FDE and SWF is better than for the three northern regions, indicating a better balance between low winds with dust and high winds without dust. Annual mean DSF is higher than in the three northern regions, possibly pointing to more productive dust sources. *DUP* mean and SWF correlate well with FDE (0.94 and 0.98, respectively) in W Sahel with absolute values similar to N Algeria. *DUP* Intensity is lowest in winter, despite February being the month of highest FDE. This could be due to the lack of haboobs in this season which have a significant contribution to *DUP* the rest of the year. The annual cycle in FDE is very different

in the C Sahel. Both *DUP* and SWF have correlations of 0.97 with FDE, but here the winter is the only main dust season, driven by strong NE Harmattan winds and frequent LLJ breakdown in this season (Schepanski *et al.*, 2009b; Washington *et al.*, 2006). The southern stations in this region have a clear vegetation increase in autumn (Fig. 3.7) which could also decrease FDE levels and contribute to higher dust emission thresholds (Fig. 3.8e), though this may not necessarily be representative of the more northern and arid stations of Bilma and Faya (Fig. 3.1). Extremely intense, local emissions were found to be important to dust concentrations in Marticorena *et al.* (2010) in the Sahel summer months, associated with the passage of MCSs. However, with their short durations of less than one hour at the observations stations, these may not be properly represented by the 3-hourly SYNOP data used here.

It is interesting to compare the C and W Sahel regions with that at Bordj Mokhtar, immediately to the north of the Sahel (Fig. 3.10). High year round dust emission reaches a maximum of 18% in July, followed by August and June and all 3 months have high DSF. This summer maximum is also identified in TOMS AI measurements (Engelstaedter & Washington, 2007a). This station is too far north to get enough monsoonal precipitation to suppress source strength. However, it is likely that cold pools from Sahelian squall lines could reach Bordj Mokhtar during the summer to cause the observed peak. This leads to high *DUP* values in June, July and August, likely underestimated due to the fact that only daytime cold pools are detected (no data from 2100 - 0300 UTC) which will have weakened by the time they reach the station, if formed the previous night.

Northern Sudan (Fig. 3.9f) stands out as having the highest FDE year round (annual mean of 13%), though *DUP* values are not comparably increased, suggesting frequent lower energy events. DSF is a little higher than in the three northern regions here, particularly during June - September, but not as high as in the W and C Sahel. The most active month is March with an FDE of 20%, while September shows a secondary peak similar to that in the three northern groups (Figs. 3.9a-c). *DUP* Intensity is the lowest of the six regions but peaks during the second maximum in September. SWF is consistently higher than FDE (annual mean of 17%), but with a similar annual cycle resulting in a correlation of 0.95. This may well be a reflection of the very low threshold in this region (Fig. 3.8f), below which dust emission will be very rare.

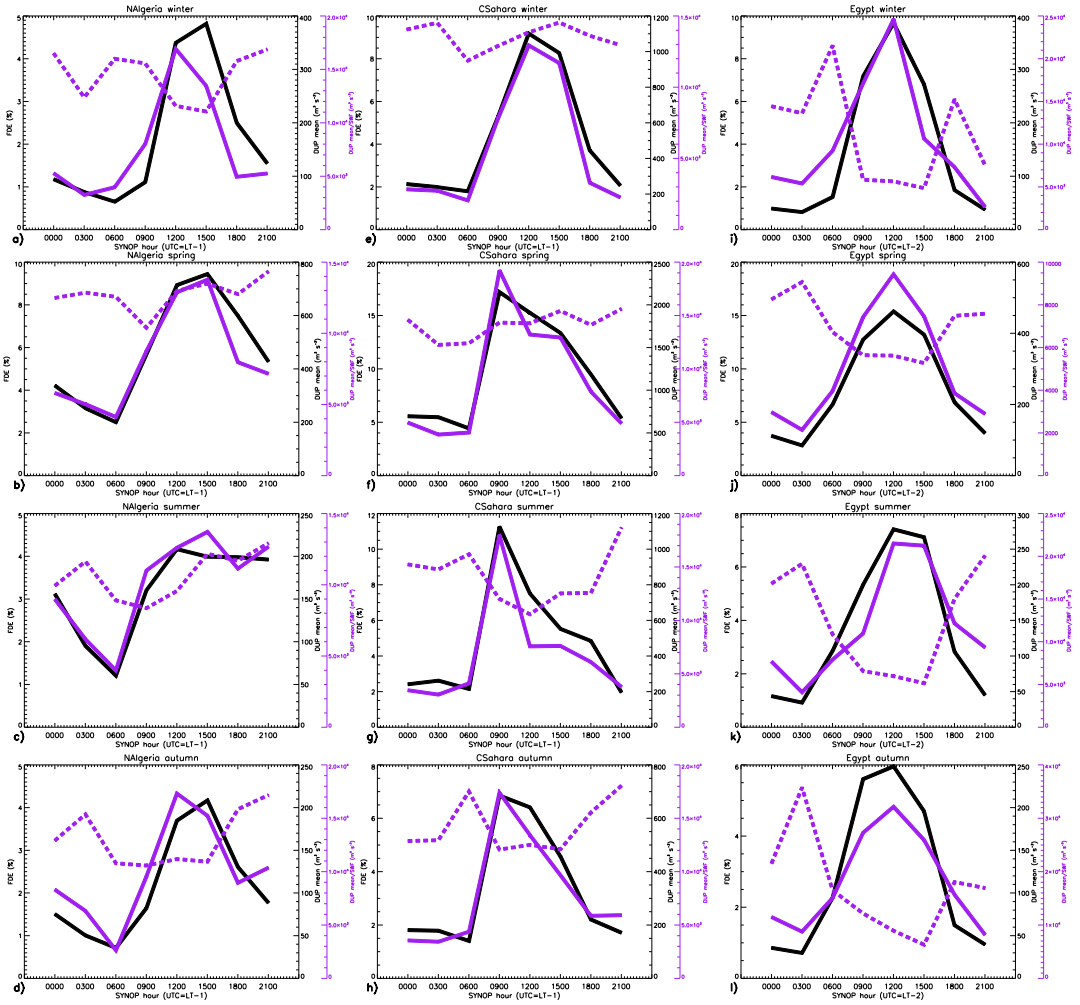

FIGURE 3.11: Diurnal cycles of FDE (solid black), DUP mean (solid purple) and DUP Intensity (dashed purple) for N Algeria (column 1), C Sahara (column 2) and Egypt (column 3) for DJF (row 1), MAM (row 2), JJA (row 3) and SON (row 4) (see section 3.3.2.1 for definition of regions). For definitions of parameters, see section 3.2.

3.3.2.4 Diurnal Cycle and Meteorological Mechanisms

The 3-hourly resolution of SYNOP reports also allows the investigation of seasonal-mean diurnal cycles of FDE, *DUP* and *DUP* Intensity (as defined in Figs. 3.9 and 3.10) for each group (Figs. 3.11 and 3.12). For N Algeria (left column of Fig. 3.11), there are stark contrasts between day and night during all seasons. Maximum FDE is at 1500 UTC (1600 Local Time, (LT)) in all seasons but summer, when values are slightly higher at 1200 UTC and emission extends longer into the night. The minimum is at 0600 UTC year-round. The diurnal cycle of *DUP* largely follows that of FDE with some minor shifts, such as a maximum at 1200 UTC in winter and autumn. Consistent with previous discussions,

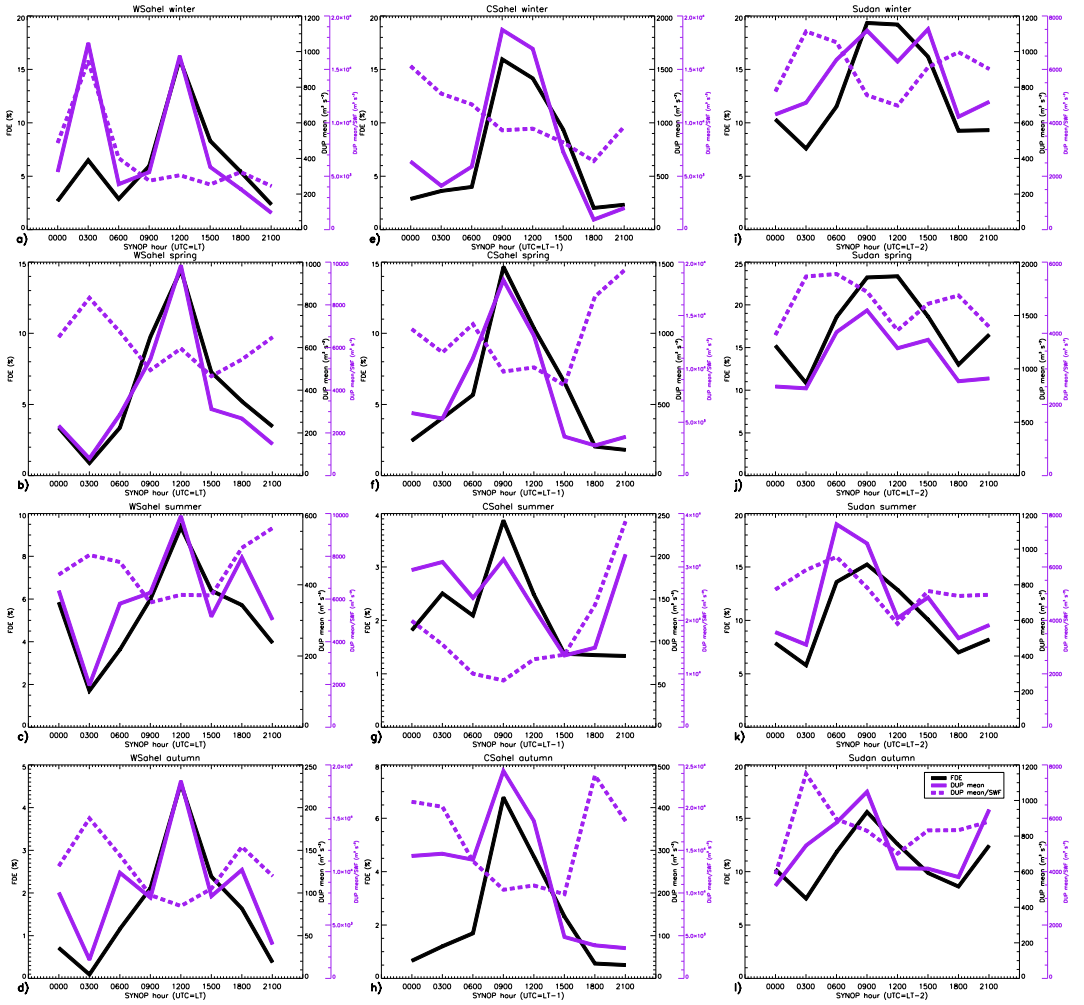

FIGURE 3.12: As Fig. 3.11 but for W Sahel (column 1), C Sahel (column 2) and Sudan (column 3).

FDE and *DUP* reach comparable magnitudes in winter, summer and autumn, but are higher in spring (note the different scales). *DUP* Intensity tends to oppose the FDE and *DUP* diurnal cycles, with peaks at night and smaller values during the day, though this is less pronounced in N Algeria spring (Fig. 3.11b). During winter and autumn, when nights are comparably long and column water vapour tends to be low, radiative cooling can create strong surface inversions that can only be broken by the strongest storms with wind-speed well above the emission threshold, leading to fewer events with larger *DUPs*. This behaviour is still evident in summer and spring, but less pronounced. Overall the diurnal cycle found for this region suggests that NLLJ breakdown in the morning could play a role, leading to rapid increases in FDE and *DUP* between 0600 and 1200 UTC.

The continuation of high values into the afternoon, when the boundary layer typically is deepest, indicates additional momentum sources above that of the NLLJ. These are likely related to thermal wind contributions caused by baroclinic zones due to mountains (Stensrud, 1996), land-sea contrasts (Todd *et al.*, 2013) or the presence of the subtropical jet. The growth of the boundary layer due to heating of the surface will also contribute by accessing these upper level thermal wind contributions around 1200 - 1500 UTC and mixing down more intense turbulence. In summer, the extension of FDE and *DUP* into the evening may be related to convective cold pools as discussed in Knippertz *et al.* (2007) for the Atlas Mountains and in Emmel *et al.* (2010) for Morocco.

The C Sahara regions (middle column in Fig. 3.11) also shows a marked day-night contrast, but with some remarkable deviations from N Algeria. The FDE maximum is at 0900 UTC in all seasons but winter (where it is 1200 UTC), suggesting a relatively more important role of the morning breakdown of NLLJs. This is most likely related to a larger distance from baroclinic zones, which reduces the likelihood of afternoon LLJ breakdown as the boundary layer grows. An additional factor could be that LT is slightly later for the Libyan stations in this region, resulting in some later emissions being included at an earlier SYNOP hour. Consistent with previous figures, FDE and *DUP* are highest in spring, followed by summer and winter, then lowest in autumn. *DUP* Intensity drops during the day in summer and autumn, but actually increases in winter and spring daytime following a dip before sunrise. Diurnal *DUP* Intensity varies less in winter and spring and dips before sunrise in contrast to summer and autumn where *DUP* Intensity is high at night. In summer, when nights are relatively short and stability is weaker, early breakdowns of NLLJ could play a role as well as ageing cold pools from afternoon convection over the Hoggar Mountains.

In Egypt (right column in Fig. 3.11) diurnal cycles in FDE and *DUP* are stable throughout the year with minimum at 0300 UTC (0500 LT) and maximum at 1200 UTC (1400 LT), suggesting some influence of NLLJ breakdown, deep boundary layer mixing during the afternoon and perhaps the general presence of daytime dry convection. *DUP* Intensity is consistent all year, with a peak at 0300 UTC and minimum at 1500 UTC. This is related to the diurnal cycle of stability as discussed before.

The analysis of the diurnal cycles in W and C Sahel is complicated by fewer night-time observations compared with day-time (2 in quality flags, Fig. 3.1). This introduces larger random error in night-time values in these locations. This is unfortunate, as convective

cold pools are expected to affect these regions during the evening and night. Both groups of stations show a clear daytime peak in FDE all year. In the W Sahel (left column of Fig. 3.12) this occurs at 1200 UTC, in the C Sahel (middle column of Fig. 3.12) at 0900 UTC (1000 LT), suggesting a strong influence of the NLLJ in all seasons. The *DUP* Intensity cycle is consistent with the other regions; low during the day and high at night. Any sharp increases in *DUP* and *DUP* Intensity at night, such as 2100 UTC (Fig. 3.12f,g) and 1800 UTC (Fig. 3.12h), are possibly artefacts of the low number of observations at this reporting time which allow a small number of individual events, possibly only reported because they are exceptional, to dominate the statistics.

In Sudan (right column of Fig. 3.12) FDE shows again maxima at 0900 - 1200 UTC (1400 LT) in winter and spring, and only 0900 UTC (1100 LT) in summer and autumn. FDE remains relatively high during the night, too, with values never dropping below 5%. When compared to the diurnal cycle of N Algeria (Fig. 3.11) where emission never exceeds 5% in winter, summer or autumn, this highlights the strong permanent presence of dust emission in Sudan. The high values at night in Sudan could be due to orographic flow in the Nile valley, indicated by consistent dips in emission just before and after sunrise, or occasional haboob storms in summer. *DUP* and *DUP* Intensity show relatively flat diurnal cycles, with lower intensities during the second half of the day which suggests weaker events or an overestimation of emission by the observer due to the already high dust levels in the atmosphere.

3.4 Conclusions

This is the first detailed analysis of dust emission from long-term surface SYNOP observations using the present weather (ww) code, over the Saharan and Sahel region. Data quality is a major issue in this area and an attempt is made to balance quality of the dataset with spatial coverage by including imperfect station records and making their limitations clear. Initial criteria were used to eliminate extremely biased and patchy stations or those that simply did not have enough dust reports to make meaningful statistics from, which left 70 stations to work with. Quality flags assigned to these stations gave indications as to the results that should be approached with caution, such as the diurnal cycle in the Sahel where a daytime bias is present. Frequency of dust emission (FDE) is compiled from

present weather reports of 7-9, 30-35 and 98 divided by the total number of reports. These statistics are further split into dust storm frequency (DSF) which includes only reports of 9, 30-35 and 98 and blowing dust frequency (BDF) with associated reports of 7 or 8. Dust uplift potential (Marsham *et al.*, 2011) is used to investigate the dust emitting power of the wind. Strong wind frequency (SWF) is calculated in the same way as FDE but using 10 m surface winds over a threshold instead of dust emission reports. Reports over 55kts are excluded due to low confidence in their accuracy. *DUP* Intensity is *DUP* mean per SWF and gives an indication of the type of dust events which might be occurring. The regional differences in the seasonal and diurnal cycles of dust emission were presented and discussed by subjectively separating stations into six groups with similar meteorological regimes.

Thresholds were determined objectively in two ways. First, by comparing the pdfs of dust emission and wind-speed observations to give the 25%, 50% and 75% probabilities of dust emission and second, by calculating the least squares difference in the diurnal cycle of the frequency of both dust emission (FDE) and strong winds (SWF). Annual mean grouped thresholds range from 5.7 ms^{-1} in Sudan to 11.5 ms^{-1} in N Algeria. In general, thresholds are higher in the hyper-arid Sahara north of 22°N. Seasonal variations in thresholds are largest in the Sahel and smallest in Sudan. In arid Sudan (this work focuses on the northern stations of Sudan) there is significantly less rainfall than in the Sahel. Hence, there will be less seasonal variation in soil characteristics leading to less variable thresholds in Sudan. There is also evidence of soil moisture varying in time when T75 increases before T25 in the Sahel transition from high to low emission seasons.

Spatially, annual mean observed emission is highest between 16°N and 24°N. Emission events are more frequent than transported events north of 24°N, while south of this, although FDE is high, the frequency of transported events is even higher. This highlights the overall more frequent presence of dust in the atmosphere south of 24°N (Klose *et al.*, 2010). Outside the Sahel, FDE and *DUP* peak in spring, related to strong pressure gradients in this season. The Sahel does have high emission in spring but the seasonal cycle is more complex with the influences of both the Saharan Heat Low and monsoon-related haboobs, which create more summer emission in the W Sahel, but hardly affect the C Sahel. In the C Sahel a particularly strong Harmattan flow, with embedded NLLJs, create strong emissions in winter and early spring. Bordj Mokhtar (southern Algeria), the

only station between the Sahel and the central Sahara, has a strong summer peak in FDE and *DUP*. Despite an absence of night-time data, the presence of haboobs at this location in the Sahara is indicated by the jump in FDE, *DUP* and *DUP* Intensity in June.

Seasonal variation in emission frequency is mostly controlled by strong wind frequency, indicated by high correlations between FDE and SWF in all areas, which changes little when SWF is calculated with a seasonally variable or annually fixed threshold. However, the relationship between FDE and *DUP* is more complex as more frequent events do not necessarily mean more emission. *DUP* is most closely related to FDE in the C Sahara, and so intensity (*DUP* per SWF) is relatively constant. This shows that here the strength of the winds that generate emission does not vary much seasonally. *DUP* and FDE are typically higher during the day, relative to night, when atmospheric stability increases and inhibits strong winds. As a consequence, any emission which does take place is likely to require a stronger wind in order to overcome this stability. High night-time *DUP* Intensity values support this conclusion.

The results here are consistent with currently understanding of vegetation growth in the Sahel and its role in decreasing emissions in late summer and autumn. High levels of summer emissions are found in the SHL region, despite the fact that the only station in this area, Bordj Mohktar, may be missing up to 50% of emission events (Marsham *et al.*, 2013) through absent night-time observations. The NLLJ is observed in the diurnal cycle of Niger and Chad stations which is in line with past work close to the Bodélé Depression by Washington *et al.* (2006, 2009). Evidence here suggests NLLJs, creating frequent morning emission, are the dominant mechanism in the central Sahara and central Sahel, while in other regions it is difficult to separate NLLJ breakdown with other factors, such as boundary layer growth eroding daytime LLJs. These daytime LLJs can be formed in response to complex terrain, mountains or land-sea air temperature contrasts.

This climatology is intended as a stepping stone towards improving our understanding of the overall mechanisms which influence the frequency of dust events and strong winds. Characterising the limitations and advantages of surface SYNOP observations will improve the evaluation of other datasets such as reanalyses, output from dust models and satellite data, which all come with their own caveats. Moving on from the work presented here the aim is to combine these results with additional information from reanalysis data to further explore the relative contribution of different mechanisms to the dust cycle.

Chapter 4

The Importance of Rare, High-Wind Events for Total Dust Uplift

4.1 Introduction

The aim of this chapter is to investigate the importance of rare, but very strong, wind events to the total dust uplift. To investigate the potential "power" of the winds available for emission, the diagnostic parameter dust uplift potential (DUP) can be applied to wind-speed measurements. Because DUP contains a cubic function which can simulate the non-linear nature of dust emission events, it is possible to investigate the relative importance of rare, but very strong, wind events and moderate, but more frequent, wind events. This analysis highlights the importance of accurately predicting events of a particular (high) wind-speed in order to improve long-term dust predictions.

One of the main challenges to such an investigation comes from the data themselves. Surface SYNOPs have very little metadata, which makes it difficult to ascertain and quantify the biases and errors. Hence, the focus of this chapter is split into two parts. The first is to quality control and investigate the plausibility of high wind-speeds observed in surface SYNOPS (sections 4.3, 4.4 and 4.5). This is done by considering the probability density functions (PDFs) of wind speeds above 30 kts and five case studies of high winds, with

observed dust emission, over 40 kts. In addition to the case studies supporting evidence from satellite, METAR and reanalysis data, are investigated to determine how likely the reports are to be true. Maximum wind-speeds from field campaigns, averaged over the same 10-min period as surface SYNOPs are also considered (section 4.5). The second part applies the knowledge gained in the previous sections to test the sensitivity of the results to suspected (but ultimately unknown), erroneous reports (section 4.6). Different subsets are analysed to determine if the uncertainty in the wind-speed measurements affects the conclusions. The optimal subset of data is that which balances the fine line between the quality and quantity needed for statistical analysis. This subset, and the resulting conclusions from its analysis, are discussed in sections 4.6 and 4.7

4.2 Data and Methods

4.2.1 SYNOP wind-speeds

Wind reports which have an accompanying dust emission report are the focus in this chapter, though the sensitivity of results to inclusion of all wind-speeds is also investigated. Dust-only winds are preferable, as a significant percentage of high winds do not create emission. This is assumed to be due to changes in surface characteristics (discussed in Chapter 3), or erroneous reports. The likelihood of erroneous reports are investigated in this chapter. Long-term station observations are from the MIDAS SYNOP database (see section 2.2.1) for stations grouped into the regions of N Algeria, C Sahara, Egypt, W Sahel, C Sahel and Sudan, as defined in section 3.3.2.1, for the time period 1984 - 2012. The upper tail of the surface wind distribution is plotted to look for biases, such as clustering around particular values as reported by DeGaetano (1998) and Cook (2014). These distributions are displayed in Fig. 4.1 for winds over 30 kts. Unusual behaviour, such as the clustering of reports around multiples of 10, in particular 60, and a complete halt of observations at 100 kts, are suspicious. To understand why this clustering occurs, the information available regarding SYNOP station instrumentation is discussed. The key question is: What is a plausible maximum wind-speed value? To answer this, five individual cases of high and dusty winds ($>$ 40 kts) in SYNOP observations are investigated to judge if the high wind could be real, or if there is an alternative explanation for such a reading. The case studies pull together supplementary data as described in the next section to make a subjective

judgement on the validity of the suspicious wind-speed. For the final total *DUP* analysis, the dust uplift potential equation (Eq. 2.1), is applied to SYNOP winds, using a seasonally constant threshold that is varied according to grouped region.

4.2.2 Supplementary datasets

The Spinning Enhanced Visibile and InfraRed Imager (SEVIRI), on board the geostationary Meteosat Second Generation (MSG) satellite dust product is used to check for the presence of haboobs, cyclones and other meteorological phenomena which could create strong winds. Detailed information on the MSG mission and how the SEVIRI dust product is produced are given in Chapter 2.

NCEP/NCAR reanalysis daily mean composites of surface vector winds are calculated for the Sudan case study in section 4.4.3. These are made via an online tool at the web page http://www.esrl.noaa.gov/psd/data/composites/day/ using reanalysis data of daily values averaged over the time period 1948 to present day. For further information on the NCEP/NCAR reanalysis project the reader is referred to Kalnay *et al.* (1996).

The following field campaign data were used to investigate maximum 10-min mean wind-speeds; African Monsoon Multi-disciplinary Analysis (AMMA; Redelsperger *et al.* (2006)), Integrated Approach to the Efficient Management of Scarce Water Source in West Africa (IMPETUS; Speth *et al.* (2010)) and Fennec (Hobby *et al.*, 2013; Marsham *et al.*, 2013). Data availability, resolution and station height are given in Table 4.5 and station locations in Fig. 4.10. Further information and references for these field campaigns are provided in Chapter 1, section 1.4.2.

AMMA and IMPETUS field campaign data were used to investigate maximum 10-min mean wind-speeds. The Atmospheric Radiation Measurement (ARM) mobile facility was based in Niamey during the AMMA campaign to provide high quality, high resolution measurements of the variables related to radiative fluxes such as surface meteorology, AOT, shortwave and longwave radiation. Data availability, resolution and station height are given in Table 4.5 and station locations in Fig. 4.10. Associated with AMMA, the Atmospheric Radiation Measurement (ARM) mobile facility was based in Niamey to provide high quality, high resolution, measurements of the variables related to radiative fluxes such as surface meteorology, AOT and shortwave and longwave radiation.

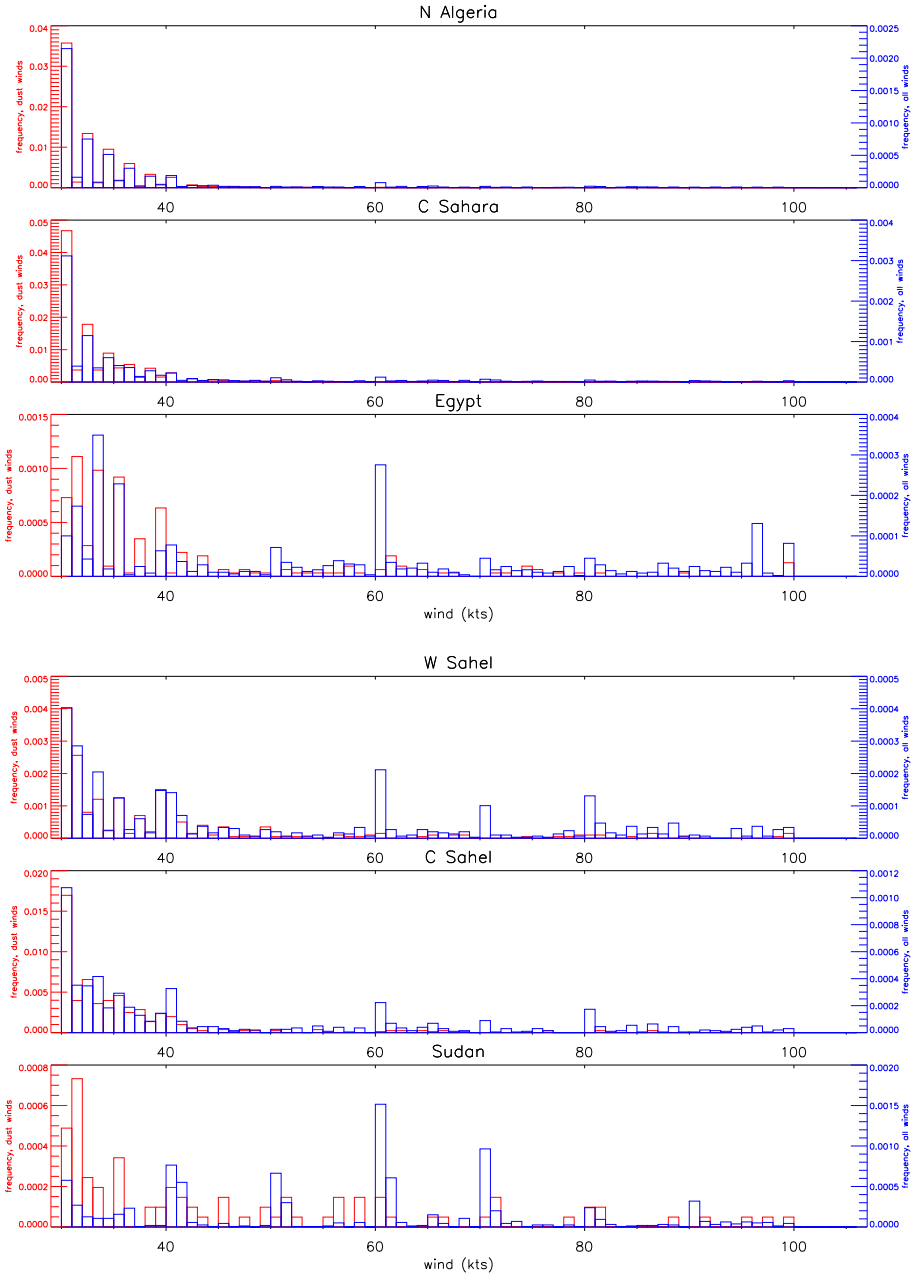

FIGURE 4.1: Probability density functions of wind-speed reports (kts) above 30 at N Algeria, C Sahara and Egypt, W Sahel, C Sahel and Sudan groups of stations. All wind observations are in blue and winds associated with dust emission are in red.

4.3 Characteristics of SYNOP wind-speeds > 30 kts

For an analysis of rare, high wind-speed events it is desirable to first consider what the distribution of this data subset looks like. As the metadata for SYNOP stations is limited, the PDF of the upper tail of the winds can help highlight data biases that might have been stated in metadata, if it were available. The PDF of all wind-speed observations (blue)

and only dust emission wind-speed observations (red) over 30 kts is presented in Fig. 4.1. In the PDF of all observations, all regions show clustering around wind-speeds of multiples of 10 kts, and in particular 60 kts. In the N Algeria and C Sahara groups the fraction of 60 kt reports over 30 kts is at least half that of the other four groups. Sudan itself has over five times the fractional frequency of 60 kt reports than of Egypt. A possible explanation for this could be the wind-speed measurement display and methods used by the observer to determine a 10-min mean. Fig. 4.2 shows a wind-speed display at Parakou, Benin where measurements are made by short-circuiting an electrical circuit in order to read from the analogue scale. This is tricky to do as the display pointer oscillates (personal comm. Andreas Fink, 2014, Karlsruhe Institute of Technology) and observers have to subjectively decide what speed is most representative of the 10-min averaging period. It is conceivable that measurements collected this way could cluster around multiples of 10 (these are marked with numbers in Fig. 4.2) and multiples of 2 (also marked, but only with dashes) due to the psychological effect of having attention drawn to the markings on the scale (Cook, 2014). Of particular concern to this investigation is the scale in Fig. 4.2, which becomes much harder to read as the wind-speed increases. Considering the usually gusty nature of high winds this could make it even more difficult to determine a mean value over 10-mins. These hypotheses could explain the high frequency of 60 kt values (the last annotated value on the scale) and a halt of observations at 100 kts (the maximum value on the scale).

If the above evidence suggests winds above 30 kts have a large random (human) error, it does not mean that they are completely false. Five cases of high winds associated with dust emission reports are investigated in the next section to explore this, using SEVIRI satellite imagery, alternative surface reports such as METARS where available and reanalysis data. The case studies are selected using the following criteria; a wind-speed $>$ 40kts, accompanied by a dust emission report, in the period of SEVIRI dust product availability (2006 - present). From this information the validity of the suspicious reports is discussed.

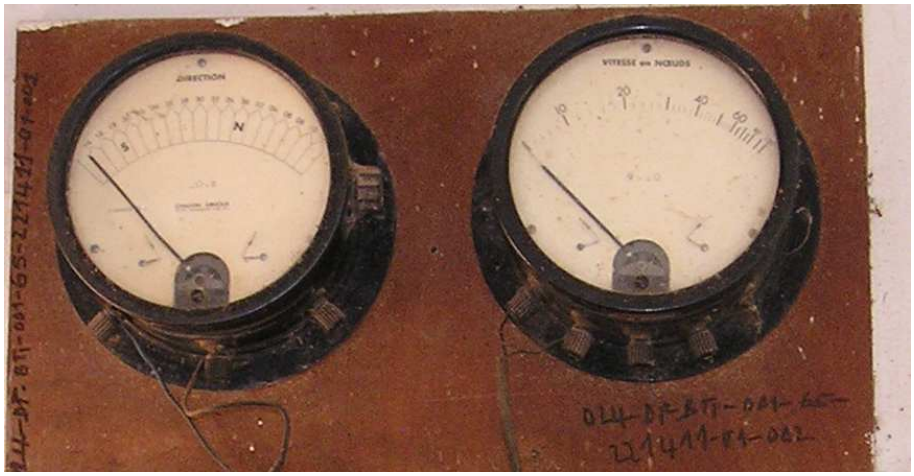

FIGURE 4.2: Display for measuring wind-direction (left) and wind-speed (right, in kts) at Parakou SYNOP station, Benin, courtesy of Andreas Fink.

4.4 Case Studies of Suspicious Reports in SYNOPs

4.4.1 El Borma - 7 March 2010

On 7 March 2010, El Borma (see Fig. 4.3 for location) reported a 79 kt wind, accompanied by a present weather (ww) code 31 (Slight/ moderate dust storm, no change in last hour) at 1500 UTC (Table 4.1). SEVIRI satellite images show large amounts of dust uplift associated with a cyclone system moving east (Fig. 4.3). The raw data values at El Borma in Table 4.1 give clear evidence of a front passing through between 0900 - 1200 UTC when wind direction changes from a southerly (180°) to west-southwesterly (240°) direction, wind speed increases by 10 kts, visibility drops to 200 m and a dust storm is reported in present weather (column 7, Table 4.1). Four other stations also observed this event as it passed over them, the locations of which are marked in Fig. 4.3. To the west of El Borma, the station of Hassi Messaoud reported a similar drop in visibility to 500 m with 40 kt winds recorded at 0000 UTC on the 7th, and an extra METAR report at 2330 of 44 kts on the 6th, followed by 32 kts later that day at 1500 UTC in SYNOPs. South of El Borma, Ghadames reported winds between 26 - 32 kts, visibility of 500 - 700m and ww = 31 between 1200 and 1500 UTC. This system then passed over the Libyan stations of Tripoli and Sirte as it moved east, where dust emission, reduced visibility and winds up to 30 kts were reported. The evidence that 79 kts is false comes from the fact that the four other SYNOP stations show comparable drops in visibility, dust emission code reports and wind-speed values up to 44 kts, but nothing even close to 79 kts. One likely

possibility is a typographic error where the 79 kt report should have read 29 kts, the same as the SYNOP report previous. This is conceivable given the similarities between a 2 and a 7.

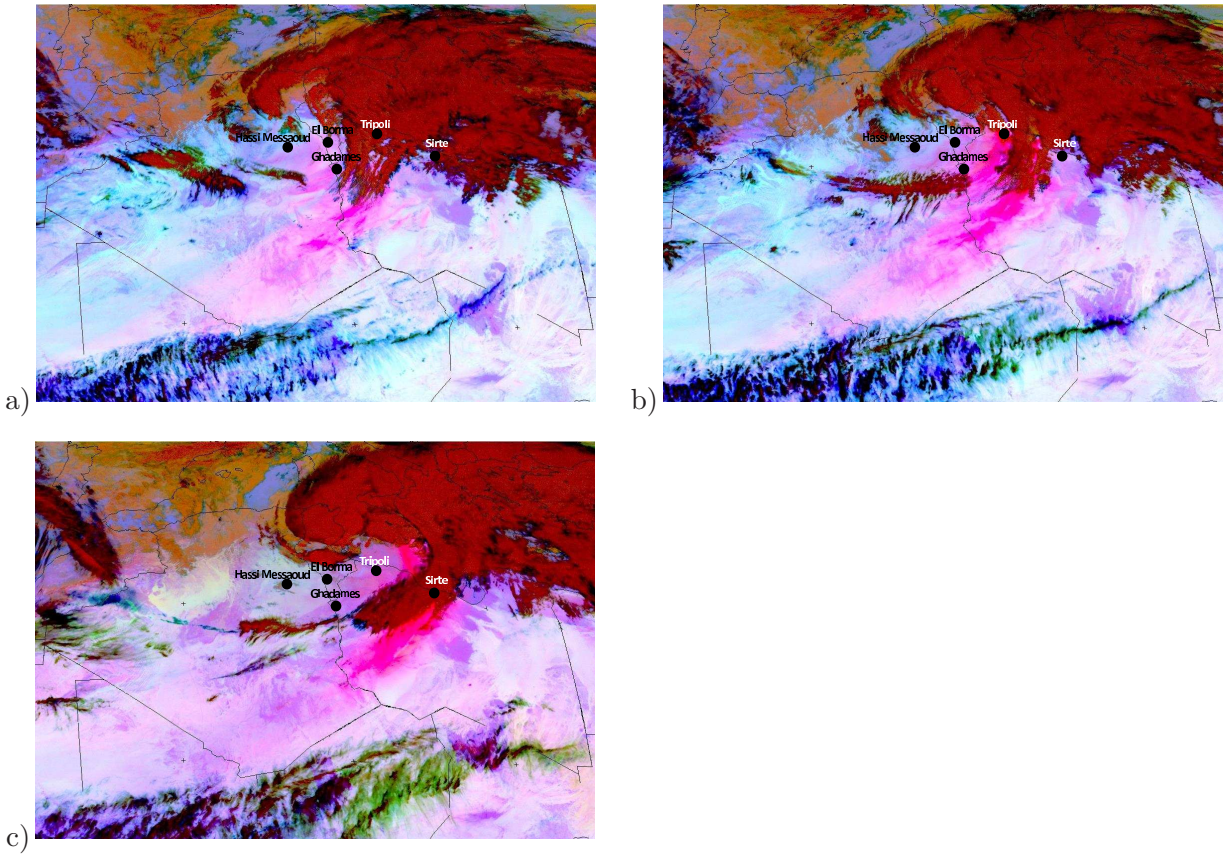

FIGURE 4.3: Position of the dust storm in relation to the SYNOP stations of Hassi Messaoud, El Borma, Ghadames, Tripoli and Sirte at a) 1200, b) 1500 and c) 1900, March 7, 2010.

Year	Month	Day	Time (UTC)	Wind Dir	Wind-Spd (kts)	ww	visibility (dm)
2010	03	07	0600	170	14	–	600
2010	03	07	0900	180	19	7	300
2010	03	07	1200	240	29	32	20
2010	03	07	1500	220	79	31	80
2010	03	07	1800	270	23	7	300

TABLE 4.1: Data values from the MIDAS SYNOP surface station database for the station of El Borma (WMO no. 60780), location in Fig. 4.3. The suspicious wind-speed report is highlighted red.

4.4.2 Nema - 4 September 2008

The station of Nema, Mauritania, reported an 81 kt wind on the 4th September, 2008 at 1500 UTC. A stationary dust feature is present in the 1200 and 1500 UTC SEVIRI images,

though there is no apparent significant atmospheric disturbance (Fig. 4.4). The SYNOP data in Table 4.2 do not give confidence in this report because an 81 kt wind-speed has not reduced the visibility any further, or given rise to a more severe dust storm report, such as ww=30 - 35. A typographic error seems likely, such as the swapped positions of the eight and one, or wind direction and wind-speed in the wrong columns.

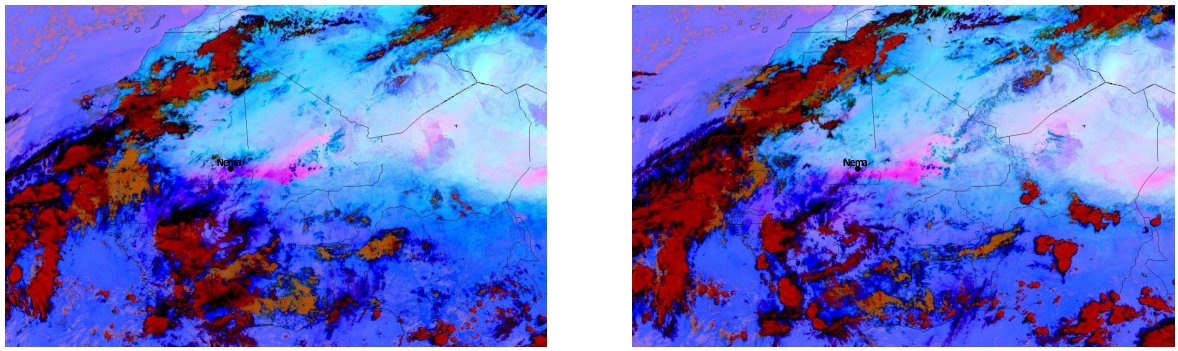

a) b)

FIGURE 4.4: Nema at a) 1200 and b) 1500 on the 4th, October 2008

Year	Month	Day	Time (UTC)	Wind Dir	Wind-Spd (kts)	ww	visibility (dm)
2008	10	04	0600	80	16	7	100
2008	10	04	1200	80	18	7	100
2008	10	04	1500	10	81	7	100
2008	10	04	1800	80	18	7	100
2008	10	05	0600	80	16	7	200

TABLE 4.2: Data values from the MIDAS SYNOP surface station database for the station of Nema (WMO no. 61497), location in Fig. 4.4. The suspicious wind-speed report is highlighted red.

4.4.3 Port Sudan and Khartoum - 25 and 26 June 2007

Port Sudan reported 84 kts on the 25 June, 2007 (Table 4.3). The location of the station in relation to topography is shown in Fig. 3.1. There is elevated terrain to the west and the Red Sea to the east. Just south, close to the Ethiopian border, is a topographic low with elevated terrain directly to the north and south. The SEVIRI imagery in Fig. 4.5 shows dust emission developing in the topographic low to the south of Port Sudan by 0800 UTC, then by 1200 UTC a source to the west, possibly on the other side of the elevated terrain, is also activated. The evolution of surface winds between 25 - 27 June in NCEP reanalysis show a strengthening over the three days (Fig. 4.6). SYNOP reports in Table 4.3 show winds actually drop to 16 kts by 1200 and no dust emission is reported.

It seems unlikely that morning LLJ breakdown could cause an 84 kt wind at 0600 UTC. The reanalysis in Fig. 4.6 suggests that the strongest winds actually occur south of this station. A typographic error seems the most likely as there is no evidence to suggest a possible high-wind mechanism capable of producing a 84 kt wind.

A suspicious report of 61 kts occurs the following day in Khartoum at 1200 UTC. Dust presence north of Khartoum does increase through the course of the day (Fig. 4.7) but there is no clear change in the meteorological situation. Between 0900 and 1200 UTC, the wind-speed jumps from 11 to 61 kts, yet visibility actually improves and only a ww=7 is reported (Table 4.3). A typographic error could again be the explanation where the 6 and 1 digits are mixed around, as the other variables read exactly the same between 1200 and 1500 UTC (Table 4.3).

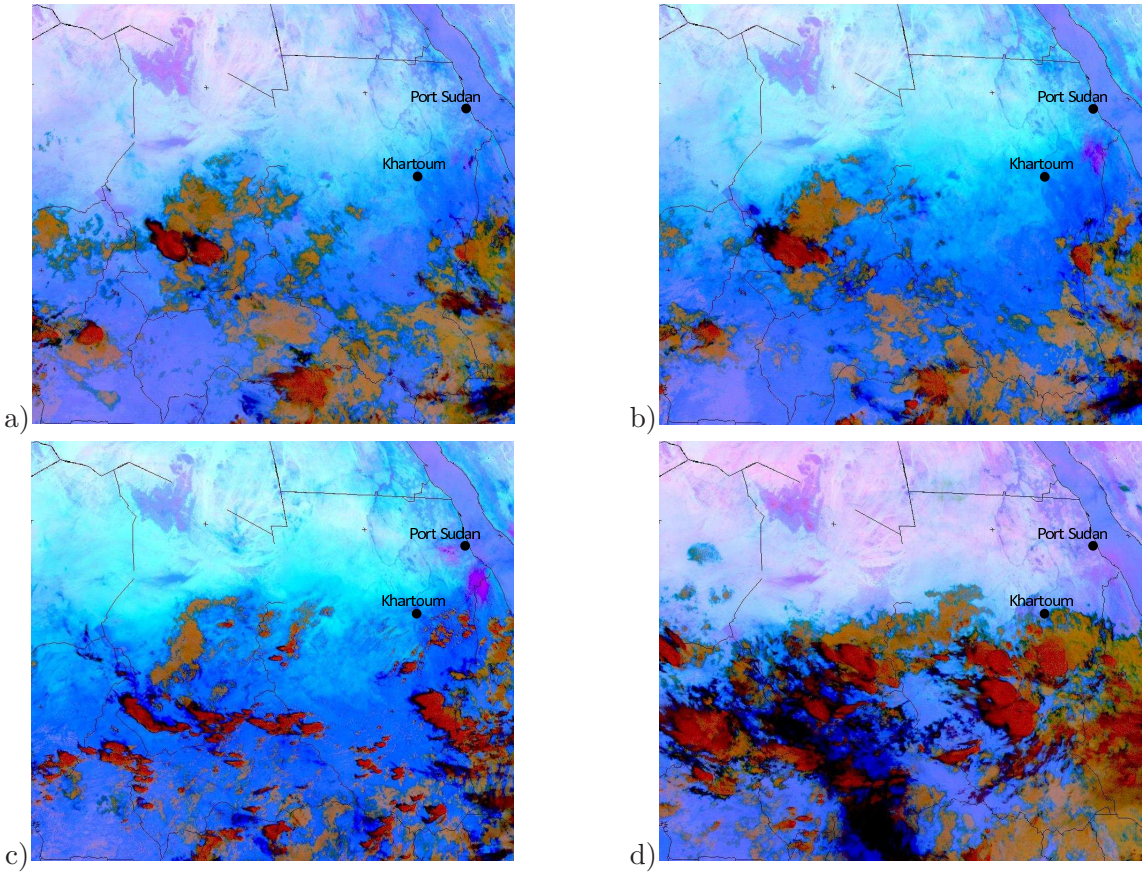

FIGURE 4.5: Port Sudan at a) 0600, b) 0800, c) 1200 and d) 2200, 25 June 2007.

Year	Month	Day	Time (UTC)	Wind Dir	Wind-Spd (kts)	ww	visibility (dm)
Port Sudan							
2007	06	23	0300	250	7	–	2000
2007	06	23	0600	40	4	6	1800
2007	06	25	0600	10	84	7	2000
2007	06	25	1200	270	16	–	2000
Khartoum							
2007	06	26	0600	230	13	–	2000
2007	06	26	0900	230	11	7	1000
2007	06	26	1200	180	61	7	1200
2007	06	26	1500	180	16	7	1200
2007	06	27	0000	170	19	–	2000

TABLE 4.3: Data values from the MIDAS SYNOP surface station database for the stations of Port Sudan (WMO no. 62641) and Khartoum (WMO no. 62721), locations in Fig. 4.5. The suspicious wind-speed reports are highlighted red.

Year	Month	Day	Time (UTC)	Wind Dir	Wind-Spd (kts)	ww	visibility (dm)
2012	08	23	0900	320	16	7	1000
2012	08	23	1500	320	14	–	800
2012	08	23	1800	360	54	33	20
2012	08	24	0900	360	16	–	1000

TABLE 4.4: Data values from the MIDAS SYNOP surface station database for the station of Bir Moghrein (WMO no. 61401), location in Fig. 4.8. The suspicious wind-speed report is highlighted red.

4.4.4 Bir Moghrein - 23 August 2012

The Mauritanian station of Bir Moghrein reported 54 kts on the 23 August, 2012. SEVIRI imagery shows a haboob emerging from an area of cloud which originates close to the station location. Its path eastwards is clearly identified in the later 0030 UTC image (Fig. 4.8b). The SYNOP code in Table 4.4 shows a wind report accompanied by a severe dust storm report. Confidence in the plausibility of this report is higher than the previous 3 examples.

4.4.5 Northern Algeria - 29 April 2011

The intense and widespread dust event on 29 April 2011 is an ideal example of a large-scale event being captured by surface SYNOPs. Satellite imagery in Fig. 4.9 indicates a clear pink-dust front in conjuction with a cyclone-like cloud formation which propagates east between 1500 - 2100 UTC (Fig. 4.9). Surface SYNOP code (not shown) reports a severe dust storm (ww=33-35) at both Touggourt and Ouargla (see Fig. 4.9, for location) and is accompanied by strong winds of 36 - 44 kts between 1800 and 2100 UTC. The good agreement between station SYNOPS and satellite imagery confirms that it is possible to

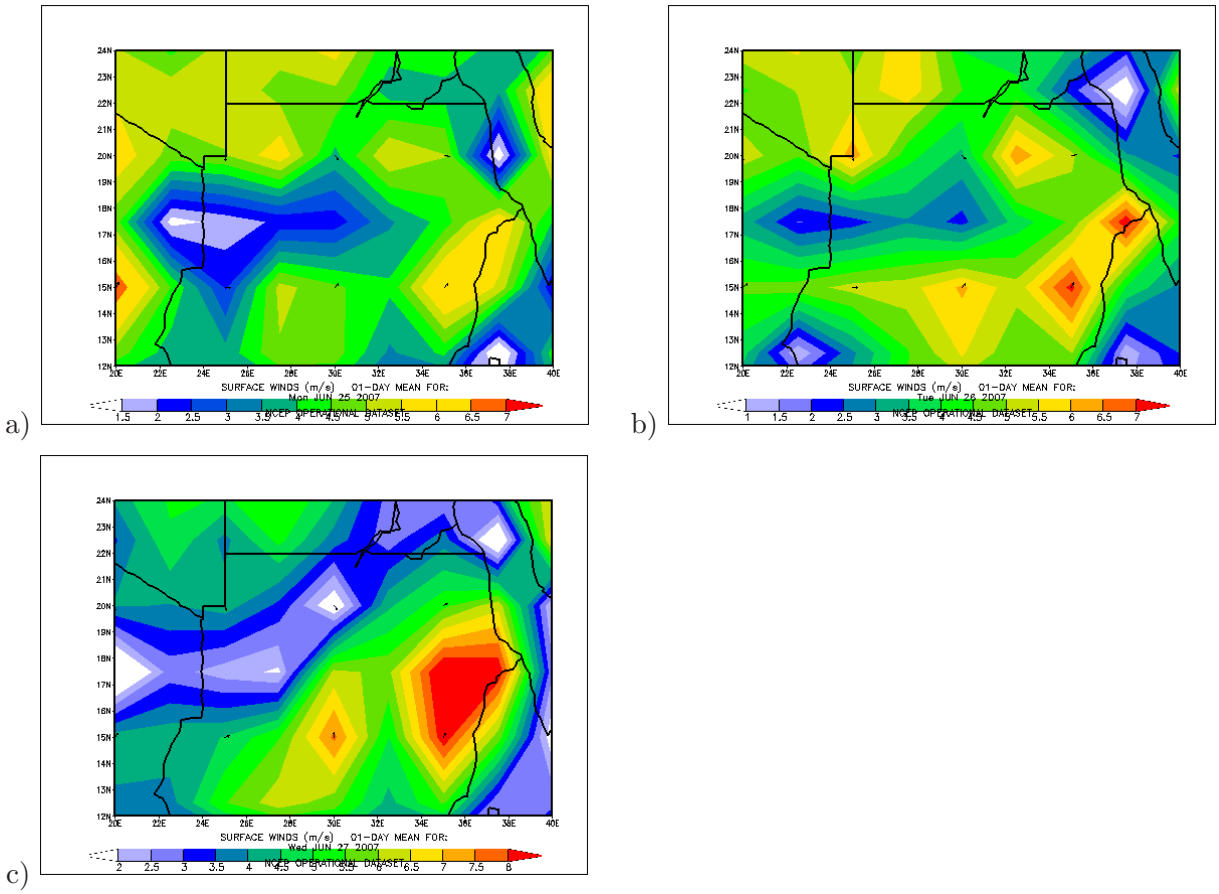

FIGURE 4.6: NCEP reanalysis surface vector winds on a) 25, b) 26 and c) 27. Images provided by the NOAA/ESRL Physical Sciences Division, Boulder Colorado from their Web site at http://www.esrl.noaa.gov/psd/. The highest wind-speeds in red of 7 - 8 ms^{-1} roughly equate to 14-16 kts.

capture strong winds with dust emission in the 3hr resolution surface observations, and that we can be confident in examples of this strength in this area.

4.5 Maximum Wind-speed From Field Campaigns

Another approach to determining a maximum realistic wind-speed is to investigate high resolution field campaign data. These measurements are made automatically and have been set up with scientific investigation in mind. However, caution is still required as errors and biases are still possible in non quality-controlled data. The field campaign locations are displayed in Fig. 4.10, with a summary of the metadata and maximum 10-min mean wind-speeds given in Table 4.5. A maximum wind-speed of 117.4 kts is found

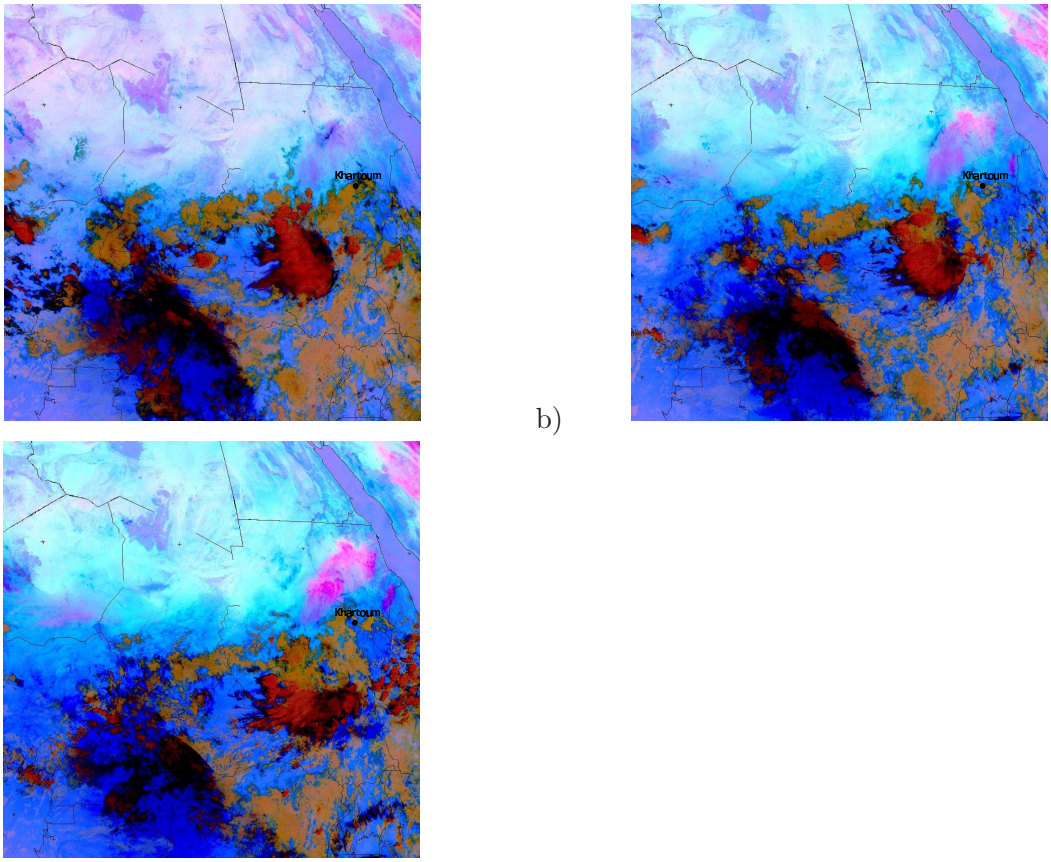

FIGURE 4.7: Khartoum at a) 0600, b) 0900 and c) 1200, 26 June 2007.

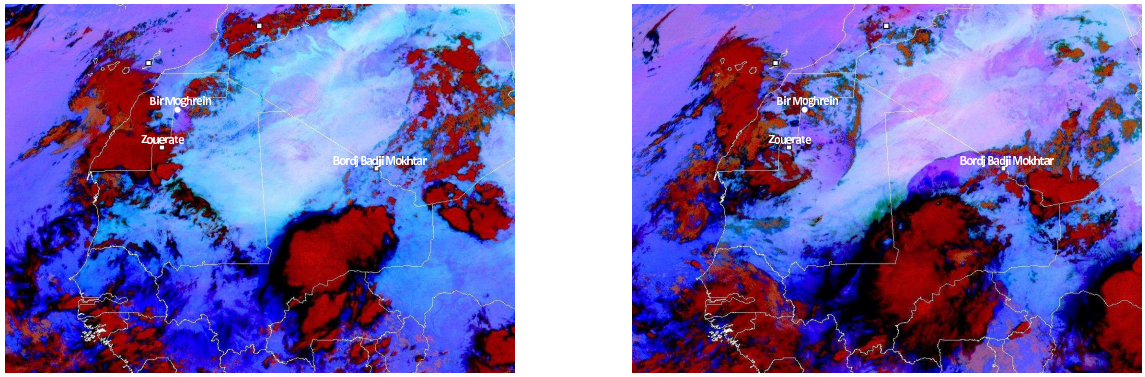

FIGURE 4.8: Bir Moghrein at a) 1800 on 23 and b) 0030 on 24, August 2012.

at Agoufou in 2006. Satellite imagery could not be acquired for this date to assess if a wind of this strength was a possibility. Additionally, Laurent Kergoat, the PI of the AMMA stations Agoufou, Bamba and Kobou also brought to light a suspected problem with overestimation of wind-speeds by the cup anemomter at the Agoufou station. As also

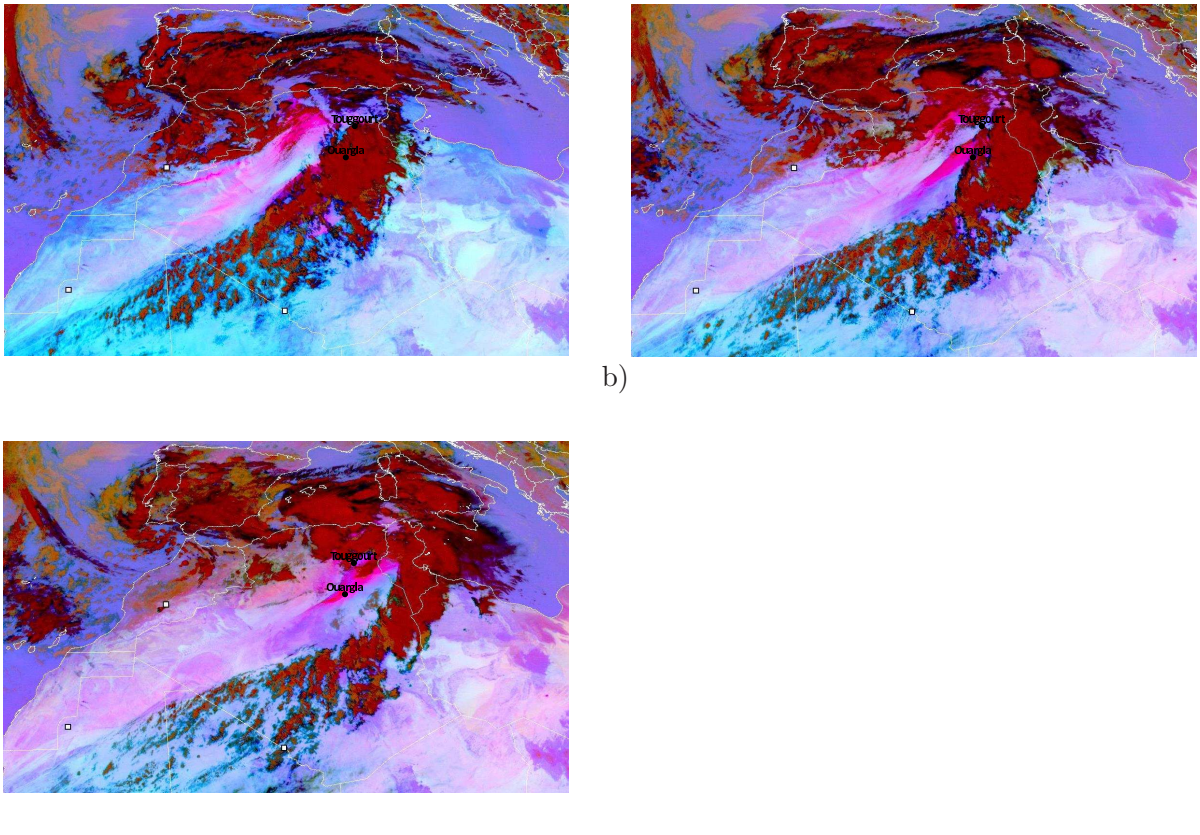

a) b)

c)

FIGURE 4.9: Northern Algeria at a) 1500, b) 1800 and c) 2100 in 29th April 2011

found in the Fennec AWS data, cup anemometer reading are higher than those registered by a sonic anemometer in strong and gusty winds (Fig. 4.11). It is not clear if the sonic anemometer is underestimating or the cup anemometer is over estimating. Hobby *et al.* (2013) suggests that sonic retrievals may be distorted or fail completely in high dust concentrations, though it could also be that cup anemeometers "overspeed" by up to 10% during an updraft or downdraft (MacCready Jr, 1966; WMO, 2008). However, the AMMA station of Bamba and the ARM station in Niamey have been deemed reliable and both show maximum wind-speeds of $\sim$ 20 ms^{-1}, though this is at a height of 3 m at Bamba and 10 m in Niamey. In both of these cases a large MCS is observed from satellite imagery which suggests these high winds could be due to cold pools. A wind-speed of 20 ms^{-1} at 3 m at Bamba corresponds to 23.6 ms^{-1} at 10 m height, using the rearranged logarithmic wind profile equation:

$$U_2 = U_1(ln(h_2/Z_0)/ln(h_1/Z_0)) \tag{4.1}$$

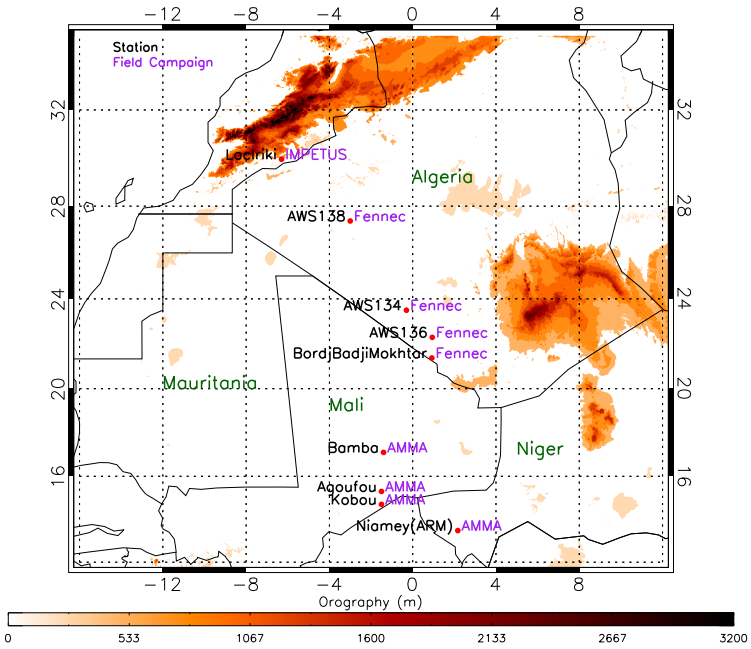

FIGURE 4.10: Locations of the field campaign sites with details of the resolution and availability of the data in Table. 4.5

where reference wind-speed U_1 is measured at height h_1, U_2 is the wind-speed at height h_2, z_0 is the roughness length and a neutrally stable atmosphere is assumed. A roughness length of 0.02 is chosen based on year mean z_0 values calculated in Prigent *et al.* (2005), though for Bamba the roughness length is known to be 0.001 (L Kergoat, personal comm.) and so this value is used for the Bamba station. This is $\sim$ 47 kts (24 ms^{-1} x 1.94 to convert to knots) and provides further evidence of what values are possible from a 10-min mean. All of the values in Table 4.5, column 6, have been converted to their equivalent 10 m height wind in knots. Based on both the field campaign and case studies investigations no winds $>$ 55 kts could be confirmed as reliable. As a result of this, only reports $<$ 55 kts are used, though sensitivity tests including higher wind-speeds are also included to assess if results and conclusions are significantly different using high, but suspicious, wind observations.

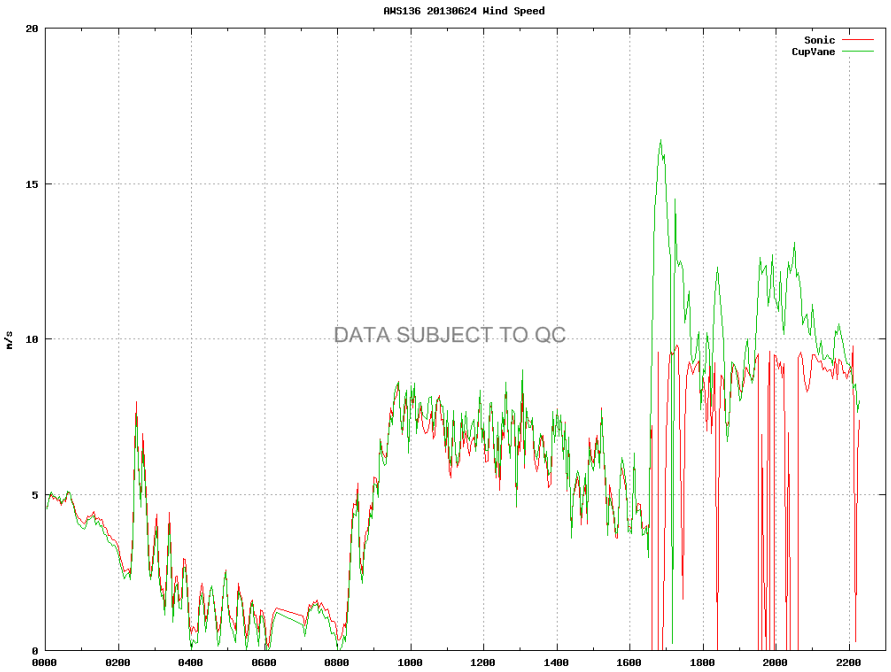

FIGURE 4.11: Wind-speed measured by cup-vane (green) and sonic (red) anemometers at AWS 136 (see Fig. 4.10 for location) on 24 June 2013.

Project	**Station**	**Time Period**	**Data Res**	**Station Height**	**Max 10-min mean wind-speed (kts) at 10 m height**	**Max wind-speed date**
IMPETUS	Lac Iriki	2001-2011	10min	3m	42.7	06/09/2009
Fennec	Bordj Badji Mokhtar	June 2011	20hz	10m	35.7	22/06/2011
	AWS 134	June 2011	20hz	2m	43.7	1/06/2011
	AWS 138	June 2011	20hz	2m	41.3	30/06/2011
AMMA	Agoufou	2005-2009	15min	3m	117.4(suspect)	31/07/2006
	Bamba	2005-2008	15min	3m	47	24/07/2008
	Kobou	2008-2009	15min	3m	33.7	26/06/2009
	Niamey (ARM)	2006	1min	10m	38.8	17/06/2006

TABLE 4.5: Field campaign station metadata and maximum wind-speed. Station locations are shown in Fig. 4.15. Maximum values in column six were converted to the equivalent values at 10 m height, assuming neutral stability for simplicity, and into knots from ms^{-1}.

4.6 Contribution of Rare Events to Total DUP

This section aims to quantify the relative contribution of different wind-speeds to the total *DUP* using 29 years of SYNOP observations. Realistically, the mass of dust uplifted depends on some factors that cannot be represented by *DUP* calculations, such as surface characteristics. Based on the conclusions of section 4.5, that confidence in wind-speeds greater than 55 kts is significantly lower than those below this threshold, we only include data which is below this value. The results of this are shown in Fig. 4.12 and Fig. 4.15. The sensitivity of these results to data subsets which include and exclude winds > 55kts and for all winds compared to dust emission winds is also shown in Figs. 4.13 and 4.14.

Calculating Total DUP

PDFs of *DUP* are plotted where the PDF value is multiplied by the *DUP* value to give an area under the curve that is equal to total *DUP* (Figs. 4.12, 4.13 and 4.14). These use the annual mean 50% threshold (see section 3.3.2.2) for U_t in the *DUP* equation (Eq. 2.1, section 2.3.1) for each individual station and *DUP* is binned using a bin-size of 200 m^3s^{-3}. Cumulative frequencies of total *DUP* tell us at which wind-speeds 25%, 50% or 75% of total *DUP* occurs. For example, if 25% of *DUP* occurs over *DUP* bin size of 4200 m^3s^{-3} in N Algeria (Fig. 4.12a), then a *DUP* of 4200 m^3s^{-3} is computed back into wind-speed to give a value of 16.6 ms^{-1}. This means that 25% of total *DUP* in N Algeria occurs at wind-speeds > 16.6 ms^{-1}.

Results of Wind-speed Data Subset < 55 kts, Dust Winds Only

The most conservative results of the total *DUP* analysis, using only dust emission winds < 55 kts, are presented in Fig. 4.12. The distribution of total *DUP* is similar for the three northern regions (letters a, b and c in Fig. 4.12) and similar for the southern regions (letters d, e and f). The northern regions show more spikes higher in the distribution than in the southern regions where the greatest contribution comes from winds closer to the threshold. This is why the 25%/50%/75% total *DUP* wind-speeds (Fig. 4.12, top x-axis) are lower in southern regions.

Dust emission thresholds used in the *DUP* calculations are not likely to be important. This is evident when comparing the total *DUP* distribution between C Sahel and Egypt. In Egypt there is a larger contribution to total *DUP* from wind-speeds 12 - 14 ms^{-1} than

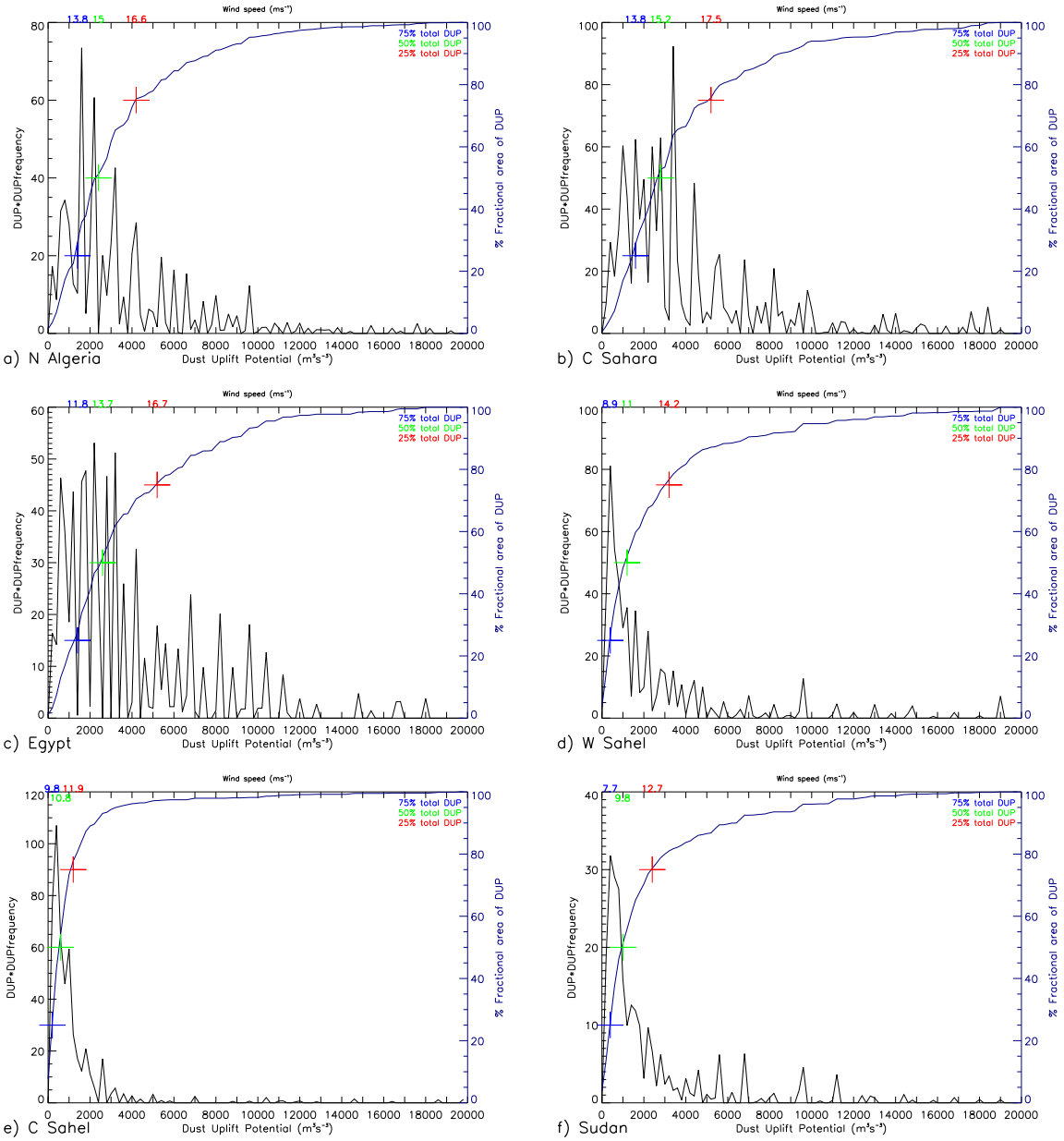

FIGURE 4.12: Total *DUP* PDFs for the regions a) N Algeria, b) C Sahara, c) Egypt, d) W Sahel, e) C Sahel, f) Sudan. The cumulative frequency line is marked in blue with the 25%, 50% and 75% values marked, along with their corresponding wind-speeds along the top axis.

in the C Sahel, where emission is mostly from winds below 12 ms^{-1}, despite the fact that the thresholds are $\sim$ 1 ms^{-1} higher in the C Sahel (see Chapter 3, Fig. 3.8).

Wind speeds of 12 - 15 ms^{-1} (7 - 11 ms^{-1}) contribute the most to total *DUP* in northern (southern) regions. The greater contribution from lower wind-speeds in the southern

regions (Fig. 4.12d, e and f) is possibly due to a lack of night-time data at many Sahelian stations which may miss any haboob activity that is known to frequently occur overnight.

Sensitivity to 55 kt Threshold, Dust Winds Only

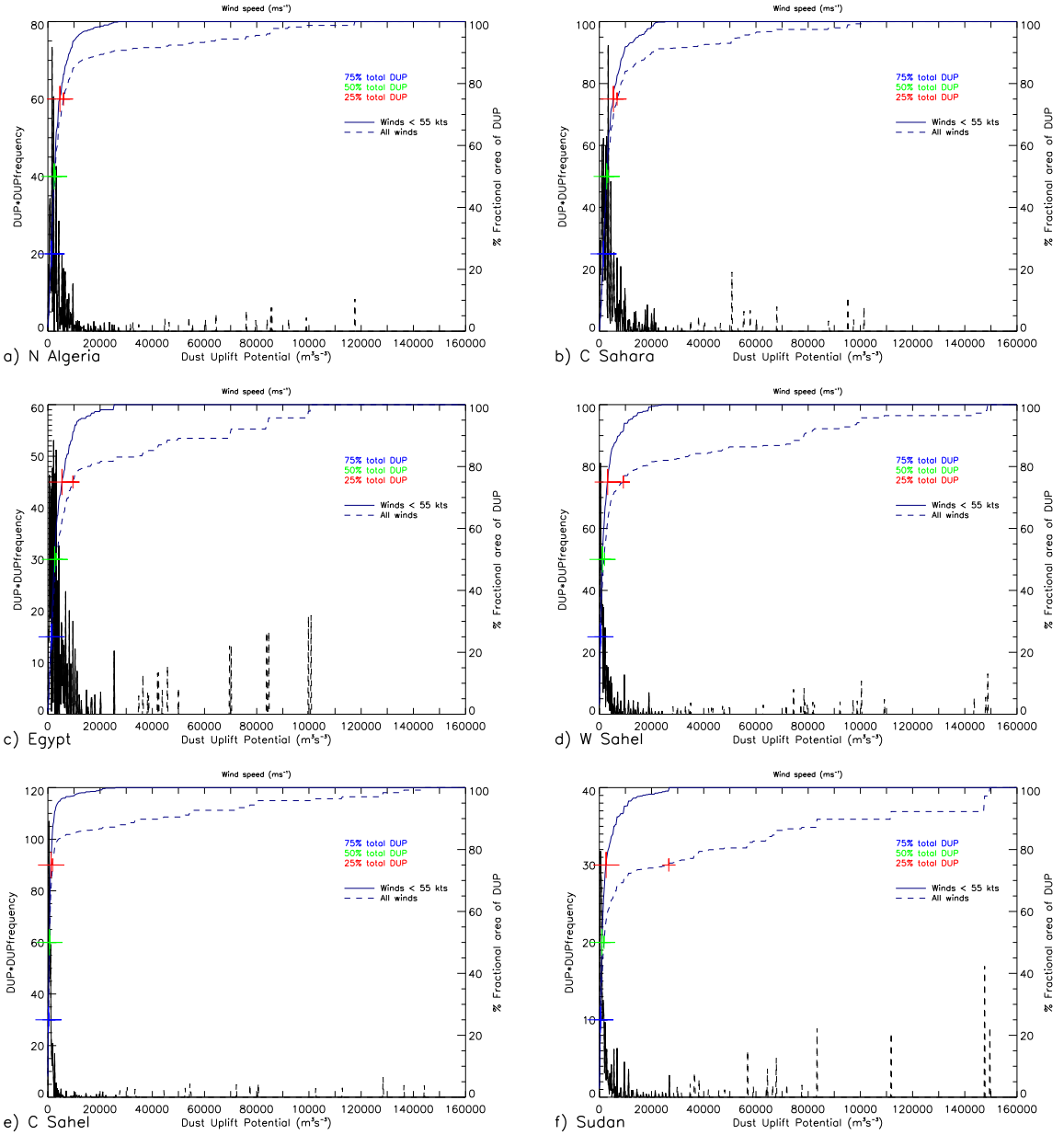

FIGURE 4.13: Total *DUP* PDFs for the regions a) N Algeria, b) C Sahara, c) Egypt, d) W Sahel, e) C Sahel, f) Sudan using only wind-speed observations with a corresponding dust emission report. The cumulative frequency line is marked in blue with the 25%, 50% and 75% values marked, along with their corresponding wind-speeds along the top axis. Solid lines are calculated with winds < 55kts and dashed lines with all winds.

The next two sections investigate the sensitivity of different subsets of data to the total *DUP* analysis. Fig. 4.13 shows the results of using only dust-emission winds, and the sensitivity of the total *DUP* results to a further reduced subset (that which was used in the previous section) of only winds below 55 kts (solid lines in Fig. 4.13). By only using dust winds, the PDF of wind-speed no longer exhibits the clustering bias around multiples of 10 (red lines, Fig. 4.1), possibly due to the large number of wind-speed observations this criteria throws out. Also, high winds with dust emission are less likely to be erroneous than high winds without dust emission. However, as shown in section 4.4, cases of high winds and dust emission above 55 kts which occurred in the time period 2006 - 2012 were likely due to typographic errors.

The coloured crosses on the solid blue curve in Fig. 4.13 are the same as those in Fig. 4.12 but presented with a higher *DUP*-bin scale so as to include the events over 55 kts. In Figs. 4.14 and 4.13 data subsets of all wind-speeds are shown by dashed lines and only wind speeds less than 55 kts by solid lines. Fig. 4.13 shows less difference in the 25/50/75% wind-speeds at N Algeria, C Sahara and C Sahel, whether the 55 kt threshold is applied or not, than at the other regions. This could be due to less typographic errors at the upper end of the wind distribution, or that these particularly high winds occur less often there. Regardless of the reason, the rarity of these events is clear as these winds occur no more than 0.3% of the time (red brackets, Fig. 4.15). The biggest difference between all dust winds and those < 55 kts is in Sudan (4.13f). There, the events which create the spike at the 150000 m^3s^{-3} bin are likely due to the reports > 90 kts observed in the red PDF of Fig. 4.1. Overall, from Fig. 4.13, the 55 kt threshold has virtually no impact on results for winds which contribute to 50% of the total *DUP* and is only significant for the top 25% of *DUP* in W Sahel, Sudan and to a lesser degree, Egypt.

Sensitivity to 55 kt Threshold, All Winds

Fig. 4.14 shows the same total *DUP* analysis as in Fig. 4.13 but using all data (corresponding to the blue PDFs in Fig. 4.1). The difference in 50% (green crosses) and 25%(red crosses) total *DUP* is quite significant in all areas. This suggests that when including all wind-speed observations, the results are extremely sensitive to the 55 kt threshold. These high, but non-dusty winds > 55 kts greatly contribute to the total *DUP*, but an unknown proportion will be inaccurate due to the human error introduced, as discussed in section 4.3.

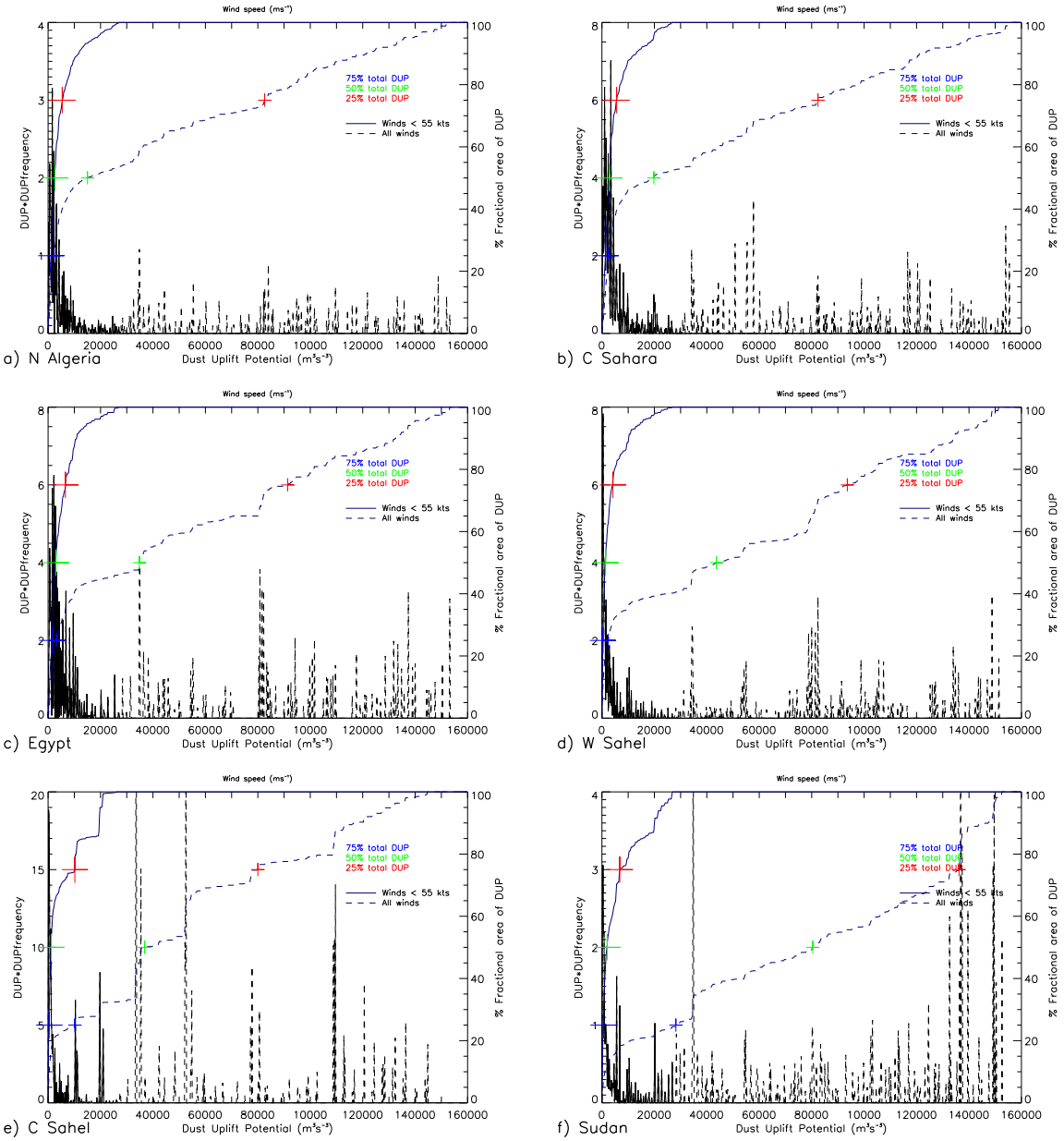

FIGURE 4.14: Total *DUP* PDFs for the regions a) N Algeria, b) C Sahara, c) Egypt, d) W Sahel, e) C Sahel, f) Sudan using all wind-speed observations. The cumulative frequency line is marked in blue with the 25%, 50% and 75% values marked, along with their corresponding wind-speeds along the top axis. Solid lines are calculated with winds < 55kts and dashed lines with all winds.

Spatial Representation of Most Conservative Subset Results

The 25/50/75% wind-speeds for total *DUP* are summarised in Fig. 4.15 with the additional annotation of the % occurance of these wind-speeds in corresponding coloured brackets. These values are calculated from the total *DUP* curves using the most conservative subset

of winds < 55 kts which are associated with dust emission as displayed in Fig. 4.12. Winds which contribute to 75% of the total *DUP* range from 7.7 ms^{-1} (Sudan) to 13.8 ms^{-1} (N Algeria and C Sahara). Contributing to 50% total *DUP* are winds ranging from 9.8 ms^{-1}(Sudan) to 15.2 ms^{-1}(C Sahara). The % occurrance of these 50% total *DUP* wind-speeds range from 2.7% in the C Sahel to 0.3% in N Algeria. Based on a station which reports 5 times a day, a % occurrance of 0.3 equates to only 5-6 observations per year. Models may struggle to accurately simulate events of this frequency and this result shows that they could provide half of the annual dust load. The upper 25% of total *DUP* is due to winds ranging from 11.9 ms^{-1} to 17.5 ms^{-1}. Overall, 75% of total *DUP* is due to winds which occur between 6% (Sudan) and 0.4% (Egypt) of the time. The rarest events have the greatest impact in Egypt where winds which occur only 0.4% of the time (those above 11.8 ms^{-1}), contribute to 75% of the total *DUP*.

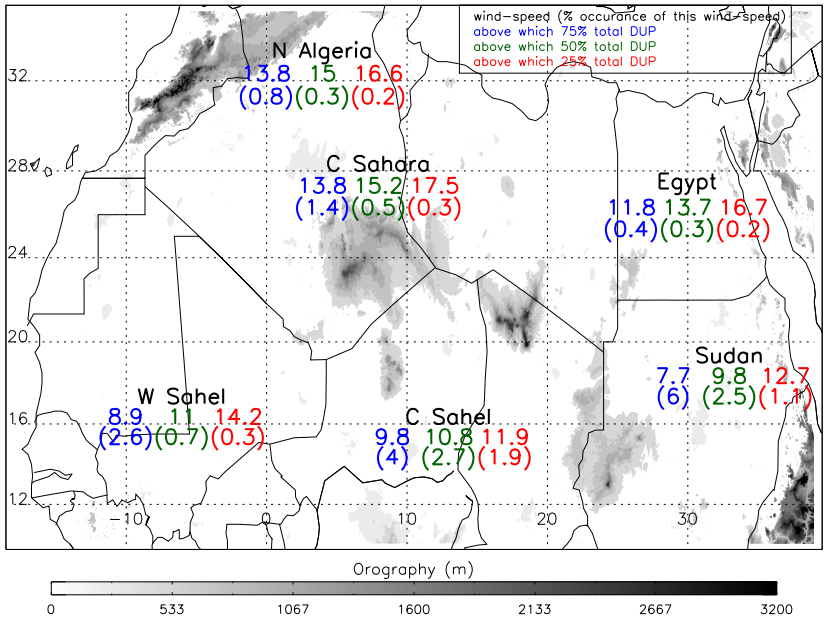

FIGURE 4.15: Total *DUP* wind-speed results, for the 6 regions (defined in section 3.3.2.1). The first row of numbers are the winds-speeds above which 75% (blue) 50%(green) and 25%(red) of total *DUP* is found. The % frequency of occurrence of these wind-speeds is given direction below in brackets.

4.7 Conclusions

This chapter used surface wind-speeds from long-term surface observations to determine the relative contribution of different wind-speeds to the total dust uplift. First, the quality

of these high winds was investigated, as small errors in wind-speed would be magnified when applied to the *DUP* equation, which is closely linked to the cubic function of the wind. As a result of an investigation into both the distribution of data, individual case studies, and comparisons to field campaign data, an upper limit to wind-speed data in which confidence is high was suggested. This upper limit aimed to give an optimal balance between having enough rare event reports to make sensible statistics versus excluding observations which are highly likely to be wrong, and could heavily bias the results. The tail of the wind-speed PDFs, considered alongside photographic and anecdotal evidence, suggested that the higher the wind-speed the larger the uncertainty and error associated with it due to the subjective nature of manual readings and the display from which they are read. Data characteristics include clustering of values around multiples of 10 kts, in particular 60 kts, and a sharp cut off at 100 kts. Random errors which result from this clustering were not necessarily a reason to discard the data. However, an unknown number of reports may be completely false due to typographic errors. Fives cases of high winds from 30 - 84kts were examined to determine what is a plausible maximum wind-speed and which wind-speeds are most likely due to typographic errors. A 54 kt observed wind at Bir Moghrein occurring in conjunction with a strong haboob identified from SEVIRI imagery, provided good evidence for a 55 kt threshold. The AMMA field campaign station of Bamba in Mali also measured a maximum wind-speed of 47 kts, from a cup and vane anemometer similar to those most likely used at SYNOP stations. Following on from this, the SYNOP wind-speed data were used to calculate the wind-speeds above which 25%, 50% and 75% of total *DUP* occurs, for each grouped region.

The sensitivity of results to the 55 kts threshold was highly dependent on whether all winds, or just dusty winds, were analysed. The dusty subset was much less sensitive to the threshold, but this is due to the significantly reduced number of high-winds. Despite the small number of data which met the strictest criterion of < 55 kts and only dust winds, confidence was higher in the validity of these data and there were some interesting results.

1. High winds which only occur 0.3 - 0.5 % (0.7 - 2.5%) of the time contribute over half of the total *DUP* in northern (southern) regions of northern Africa. A % occurrance of 0.3% equates to only 5.5 events per year for a station which reports 5 times per day. This highlights a challenge of dust modelling; in some parts 50% of emission will come from events which occur 5-6 times per year. It could be less than 5-6 events

per year if one event is particularly long lived and is recorded at two consecutive reporting hours.

2. Calculations of total *DUP* in the northern regions of N Algeria, C Sahara and Egypt indicate that winds around 12 - 15 ms^{-1} ($\sim$ 24 - 30 kts) contribute to the majority of dust uplift. This could be due to cyclones and depressions which modelling studies suggest are a big contributor to total emission, especially seasonally.

3. Calculations of total *DUP* in the southern regions of W Sahel, C Sahel and Egypt indicated that winds ranging from 7 - 11 ms^{-1} ($\sim$ 14 - 22 kts) contribute to the majority of dust uplift; considerably lower than in northern regions. It is likely that the contribution from haboobs is not accurately represented by surface SYNOPs in this region due to a day-time bias at many stations (Fig. 3.1).

Chapter 5

Sahelian Trends in Dust Emission

5.1 Introduction

Over northern Africa, evidence from both surface visibility over land (Mahowald *et al.*, 2007) and satellite aerosol data over the Atlantic (Evan & Mukhopadhyay, 2010) indicate that dust loading from this area has decreased since the 1980s. Correlations between dust from North African sources and rainfall have been found (Foltz & McPhaden, 2008; Zender & Kwon, 2005) but it is currently unclear if the rainfall itself (or lack of it) is the responsible mechanism (Prospero & Lamb, 2003). As yet, no evidence has been presented to clearly describe the mechanisms involved in a decreasing trend in dust emission. Collecting observational evidence for a change in meteorological or soil processes in this region is challenging due to the sparse network and incomplete record. This chapter investigates the likely mechanisms behind an observed decrease in dust emission and wind-speed at seven Sahelian SYNOP stations. Past work has discussed negative correlations between North African dust and precipitation through the impact of drought due to changes in soil moisture and vegetation cover (Brooks & Legrand, 2000; Moulin & Chiapello, 2004). Motivated by globally and regionally observed trends in 10 m wind speed, Bichet *et al.* (2012) investigated the effect of increased roughness length on global and regional 10 m winds using a Global Climate Model (GCM). They found that increasing surface roughness length in the model by factors of 1.5, 2 and 4 over the last 30 years produced a linear relationship with decreasing 10 m winds, though other factors were needed to explain a discrepancy between model output and observations. To determine what these factors might be in the

Sahel, novel diagnostic tools are applied to station observations to investigate the effects of changes to: vegetation cover and roughness length, dust emission thresholds, daytime turbulence and evapo-transpiration, urbanisation and large-scale circulation. The results in this chapter are consistent with a recently observed northern hemispheric decrease in surface wind speed, known as "stilling" (Vautard *et al.*, 2010), and demonstrate the importance of representing vegetation-related roughness changes in models. They also offer a new mechanism of how land-use change and agriculture can impact the Sahelian climate.

5.2 Data and methods

5.2.1 Quality Control and Station Selection

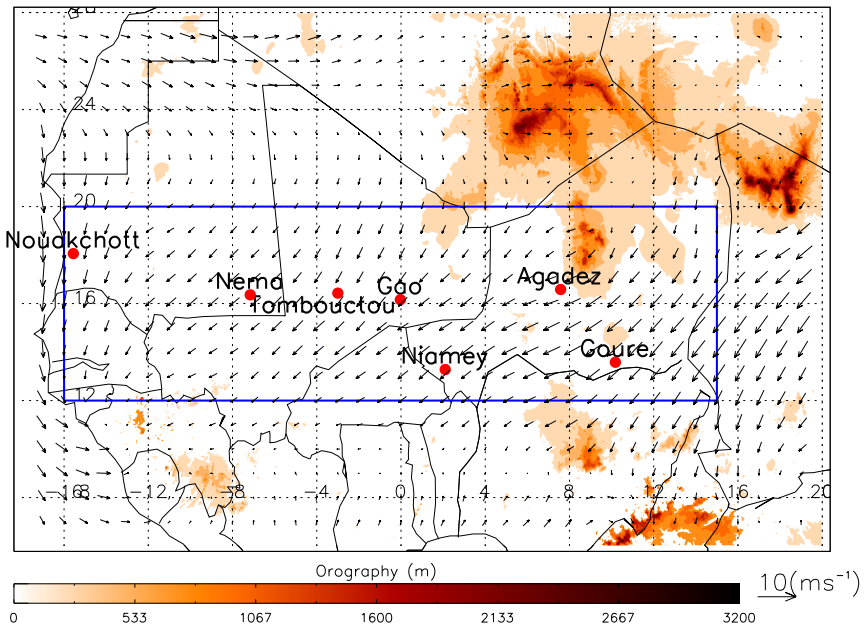

FIGURE 5.1: Map showing the location of the seven Sahelian stations used in this study (red dots with labels), the orography (shaded in m above mean sea level according to the legend), and the domain used for averaging ERA-Interim reanalysis data in blue. Winter mean (December-February) 10 m wind vectors from ERA-Interim are also included (scale in bottom right corner)

This chapter uses the seven Sahelian stations of Nouakchott (World Meteorological Organisation station number 61442), Nema (61497), Tombouctou (61223), Gao (61226), Niamey (61052), Agadez (61024), and Gouré (61045) (see Fig. 5.1 for locations), which are part of the standard SYNOP surface observation network and typically report every 3 hours. All seven stations are located in the relatively flat parts of the Sahel, away from the main

mountain ranges (Fig. 5.1) and in the latitude range 13-20°N. Wind speed observations are 10-minute means, measured at 10-m height above ground. Reports of dust emission events, defined as the SYNOP "present weather" (ww) codes 7-9, 30-35, and 98 and representing dust emission of varying severities such as "Dust or sand raised by wind" (ww = 7) to "Severe dust storm or sandstorm"(ww = 33-35), were used to investigate dust emission in a similar way to Ackerman & Cox (1989). The parameter "frequency of dust emission events" (FDE) is defined as the fraction of all reports containing these ww codes. The frequently reported ww code 6 ("dust suspended, but not raised near the station") is purposely omitted from the statistics in order to exclude transport events. To isolate the changing contribution of winds to dust emission, independently from changing soil parameters, dust uplift potential (DUP) as described in section 2.3.1, is calculated using a fixed threshold of 7 ms^{-1} (Chomette *et al.*, 1999; Marsham *et al.*, 2011). The seven stations were selected on the basis of a minimum of 1000 dust observations overall during the time period 1984 - 2010 and at least 500 observations per year for each of the 27 years.

5.2.2 Instrument Issues

Instrument degradation is a possible explanation for increasing the number of 0 ms^{-1} reports through time, while decreasing the number of 1.5 ms^{-1} reports. This occurs as the sensor becomes less sensitive to lower wind-speeds (DeGaetano, 1998). As SYNOP observations are reported in knots, the analysis is adjusted to compare the number of reports of 0 kts with reports of 1, 2, and 3 kts. Figure. 5.2 refers to the two different series as 0 ms^{-1} and 1.5 ms^{-1}, as 3 kts is equal to 1.54 ms^{-1}. The significance of trends in 1.5 ms^{-1} and 0 ms^{-1} reports are calculated, as well as the correlations between mean wind and 0 ms^{-1} reports and 0 ms^{-1} and 1.5 ms^{-1} (Table 5.1). From the trend lines shown in Fig. 5.2, Agadez, Nema, Gao, and Nouakchott do not show any suspicious periods of increasing 0 ms^{-1} or decreasing 1.5 ms^{-1}. A significant negative correlation of -0.4 between 0 ms^{-1} and 1.5 ms^{-1} is found at Niamey (Fig. 5.2c, Table 5.1). This appears to be mainly due to a period from the mid-1990s to the early 2000s when the number of 0 ms^{-1} reports is significantly enhanced (Fig. 5.2c). The reason for this is not clear, but the good correspondence between the mean wind V, DUP, and the independently measured FDE shown in Fig. 5.4c suggests that there is no significant influence on the analysis. Gouré has no available wind data in the period 2000 to 2003 (Fig. 5.2b). The high percentage of

0 ms^{-1} reports just before this period may suggest a problem with the instrument, which may have been replaced after the gap. The continuation of the trend after the gap, and agreement with the independently measured FDE, support the usefulness of the record from this station. The steep drop in the percentage of 0 ms^{-1} reports from 1985 to 1991 in the Tombouctou time series (Fig. 5.2e) is suspicious. However, for 1985 - 1991 alone, when 0 ms^{-1} reports are high, the correlation with 1.5 ms^{-1} is insignificant. The large percentage of 0 ms^{-1} reports at the start of the record is reflected in the mean wind and therefore contributes to the overall positive mean wind trend, which is opposite of what is observed at the other stations Table 5.2. For the remaining period (1993 - 2010) the correlation between 0 ms^{-1} and 1.5 ms^{-1} is -0.64 and highly significant. This would be consistent with instrument degradation, but the negative trend in the number of 0 ms^{-1} reports does not support this (Fig. 5.2e, Table 5.1). Tombouctou is kept in because overall the analysis did not produce any clear signs of instrument degradation and leaving it out would only have enhanced the negative trends.

		Agadez	Gouré	Niamey	Gao	Tomb.	Nema	Nouakchott
1	0 ms^{-1}	**-52**	***-186***	**-33**	***39***	***112***	***-190***	49
2	<1.5 ms^{-1}	***-1228***	***-176***	**-220**	**-2**	**-119**	***99***	***-1909***
3	Correlation: <1.5 ms^{-1}/0 ms^{-1}	***0.65***	**0.52**	**-0.4**	**-0.29**	**-0.07**	**-0.16**	**-0.02**

TABLE 5.1: Rows 1 and 2 contain the 0 ms^{-1} trend (green lines) and <1.5 ms^{-1} trend (red lines) values as plotted in Fig. 5.2. Row 3 gives the corresponding linear correlation. Statistical significance of trends and correlations at the 95% and 99% levels are denoted in bold and in bold italics, respectively.

5.2.3 Additional Data Sets

Six-hourly 10 m u and v wind vectors from the European Centre for Medium-Range Weather Forecasts (ECMWF) ERA-Interim reanalysis at a horizontal resolution of 80 km were used for the area inside the blue box shown in Fig. 5.1. Trends and correlations with the North Atlantic Oscillation (NAO) were assessed using the Jones NAO index (Jones *et al.*, 1997). Data are available from www.cru.uea.ac.uk. Trends in green vegetation are assessed using AVHRR NDVI satellite product for the period 1984-2006, available from the Global Inventory Modeling and Mapping Studies (GIMMS) database (section 2.2.2).

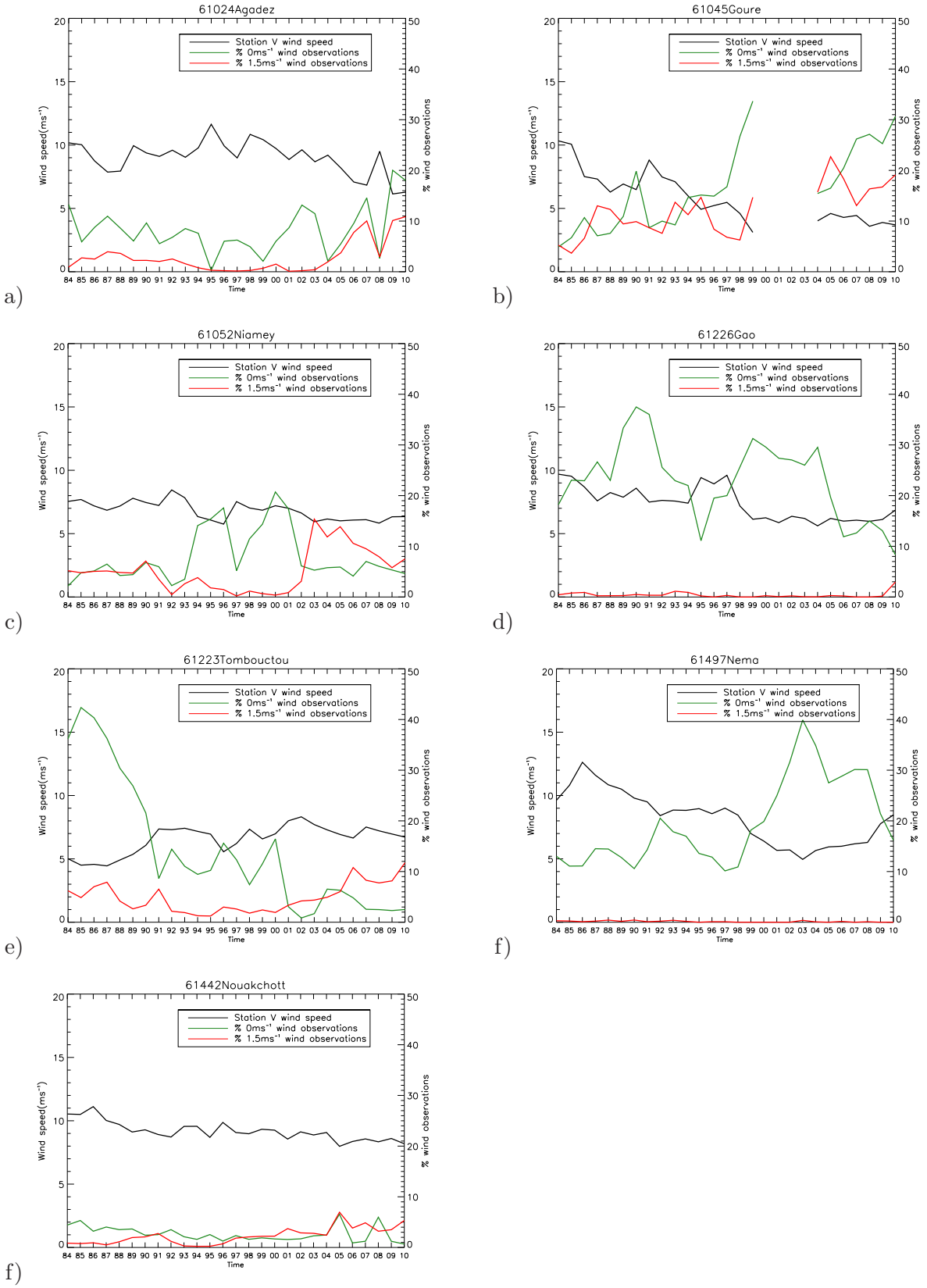

FIGURE 5.2: Instrument degradation analysis. Time series of mean wind V (black), % of 0 ms^{-1} reports (green) and % of 1.5 ms^{-1} reports (red) for the individual stations a) Agadez, b) Gouré c) Niamey, d) Gao, e) Tombouctou, f) Nema, and g) Nouakchott. Percentage lines are calculated relative to all observations available for a given year. Trend line values for the green and red lines can be found in Table 5.1 and for the black line in Table 5.2.

5.3 Results

5.3.1 Spatially Averaged Trends

Fig. 5.3 shows long-term trends in wind-speed, frequency of dust emission (FDE) and *DUP* averaged over the seven Sahelian stations. Annual mean wind speeds (V) decrease from 4.6 ms^{-1} in the mid-1980s to 3.3 ms^{-1} in recent years (-27%; solid black line in Fig. 5.3), which is consistent with previous studies (Mahowald *et al.*, 2007). Year-to-year variability is low. NDVI changes are calculated for the time period 1984-2006. Definitions of V, FDE and *DUP* are given in section 5.2. Trend values for each of the seven stations is given in 5.2. Note that for some stations the *DUP* changes are so dramatic that the linear trend line crosses the zero axis, resulting in relative changes of more than 100%. The seasons of largest changes in rows 5-7 are based on relative changes computed in the same way, but for the four standard seasons December-February (DJF), March-May (MAM), June-August (JJA), and September-November (SON). Six of the seven stations show a negative trend varying from -19 to -64%; only winds at Tombouctou increase (Fig. 5.4 and Table 5.2). Averaged over the seven stations, mean annual FDE decreases dramatically from more than 10% in 1985 to just under 3% by 2006 (blue line in Fig. 5.3), consistent with trends in visibility (Mahowald *et al.*, 2007; Shao *et al.*, 2013) and dust over the downstream tropical Atlantic (Evan & Mukhopadhyay, 2010; Foltz & McPhaden, 2008). Again, all stations except Tombouctou show large negative trends (Table 5.2). A time series of *DUP* using a constant emission threshold of 7 ms^{-1}, as used in Chomette *et al.* (1999), shows a dramatic reduction by 86% over the 27-year study period (red line, Fig. 5.3) and has inter-station variability largely consistent with that for mean wind (Table 5.2). The highly significant inter-annual correlations between the independently estimated FDE and mean wind (0.92), and FDE and *DUP* (0.93) reflect the strong control of wind speed on the occurrence of dust emission. Corresponding trends in regionally averaged mean wind and *DUP* computed from ERA-Interim reanalysis are substantially smaller (dashed lines in Fig. 5.3) reaching only -3% (0.25 ms^{-1}) and -14%, respectively.

Fig. 5.4 shows time series and trend lines in analogy to Fig. 5.3, but for the seven individual stations. This helps to illustrate station-to-station variations in addition to Table 5.2. The largest changes in V, occuring at Goure (-64%) and Nema (-50%) are also present in peak winds at these stations shown by changes in *DUP* of -121% and -112% respectively (Table

5.2). The largest drop in FDE actually occurs at Nouakchott however, which although accompanied by the smallest change in mean wind of only -19%, is accompanied by a large drop in *DUP* (-95%). Table 5.5 adds further detail to Table 5.2 by providing trends and correlations between wind and dust variables for individual seasons.

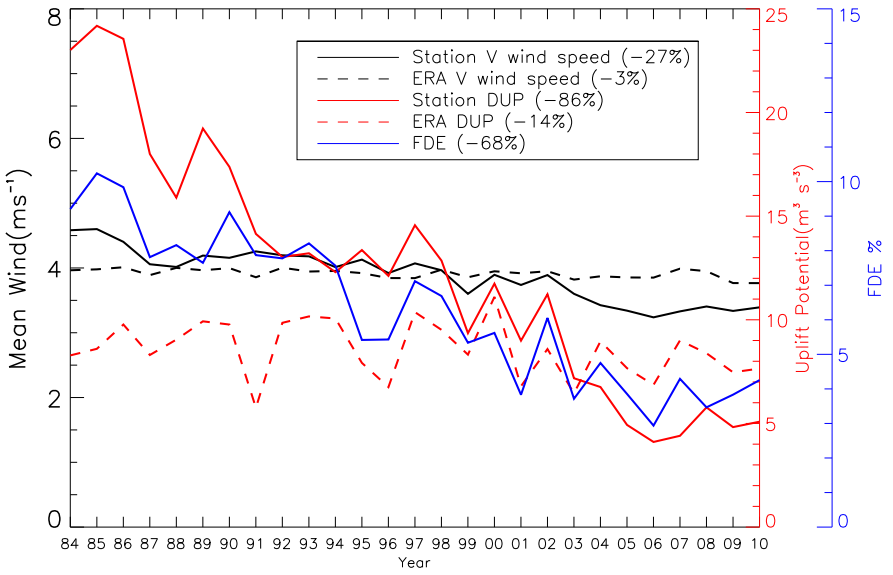

FIGURE 5.3: Trends in mean annual 10-m wind speed (V, black lines), dust uplift potential (*DUP*, red lines), and frequency of dust events (FDE, blue line) from observations averaged over seven surface stations in the Sahel (see Fig. 5.1 for locations; solid lines) and ERA-Interim reanalysis averaged over the blue box shown in Fig. 5.1 (dashed lines) for the time period 1984-2010. Numbers in brackets in the legend indicate the relative change over the time period estimated from the linear trend line as in Table 5.2. Definitions of *DUP* and FDE are given in section 5.2.1. Note that there is no FDE from reanalysis data. A fixed threshold of 7ms^{-1} was used for the *DUP* computations.

		Agadez	Gouré	Niamey	Gao	Tomb.	Nema	Nouakchott
1	% change in V	***-20***	***-64***	***-21***	***-37***	***47***	***-50***	***-19***
2	% change in FDE	-22	***-71***	***-63***	***-84***	-17	***-60***	***-94***
3	% change in *DUP*	***-49***	***-121***	***-65***	***-100***	15	***-112***	***-95***
4	% change in NDVI (SON)	**+12**	***+25***	**+13**	***+43***	***+19***	**+16**	+2.7
5	Season of largest V change	***JJA***	***SON***	***DJF***	***MAM***	**SON**∗	***DJF***	***DJF***
6	Season of largest FDE change	**JJA**	***SON***	SON	***SON***	***JJA***∗	JJA	**DJF**
7	Season of largest *DUP* change	***JJA***	***SON***	**SON**	***SON***	**JJA**∗	***SON***	***MAM***
8	Station location In/out of city	in	out	in	out	out	out	in
9	Number of wind speed obs	35991	30618	57476	42438	41623	29777	67582

TABLE 5.2: Key trends and characteristics for individual Sahelian stations (locations in fig. 5.1). Relative changes (in %) in 10-m mean wind (V), frequency of dust events (FDE) and dust uplift potential (*DUP*) in rows 1-3 are computed for 1984-2010 based on the linear trend. NDVI changes are calculated for the time period 1984-2006. Definitions of V, FDE and *DUP* are given in section 5.2. All changes in rows 5-7 are negative except for V, FDE, and *DUP* at Tombouctou marked with "*". The classification of station location in or outside of the main urban area was done on the basis of Google Earth images. The latter is often the case when airports were built remote from the city centres. Row 9 gives the number of available reports of wind speed for the period 1984 - 2010, for each station. Statistical significance at the 95% and 99% levels (90% and 95% for row 4) are denoted in bold and in bold italics, respectively.

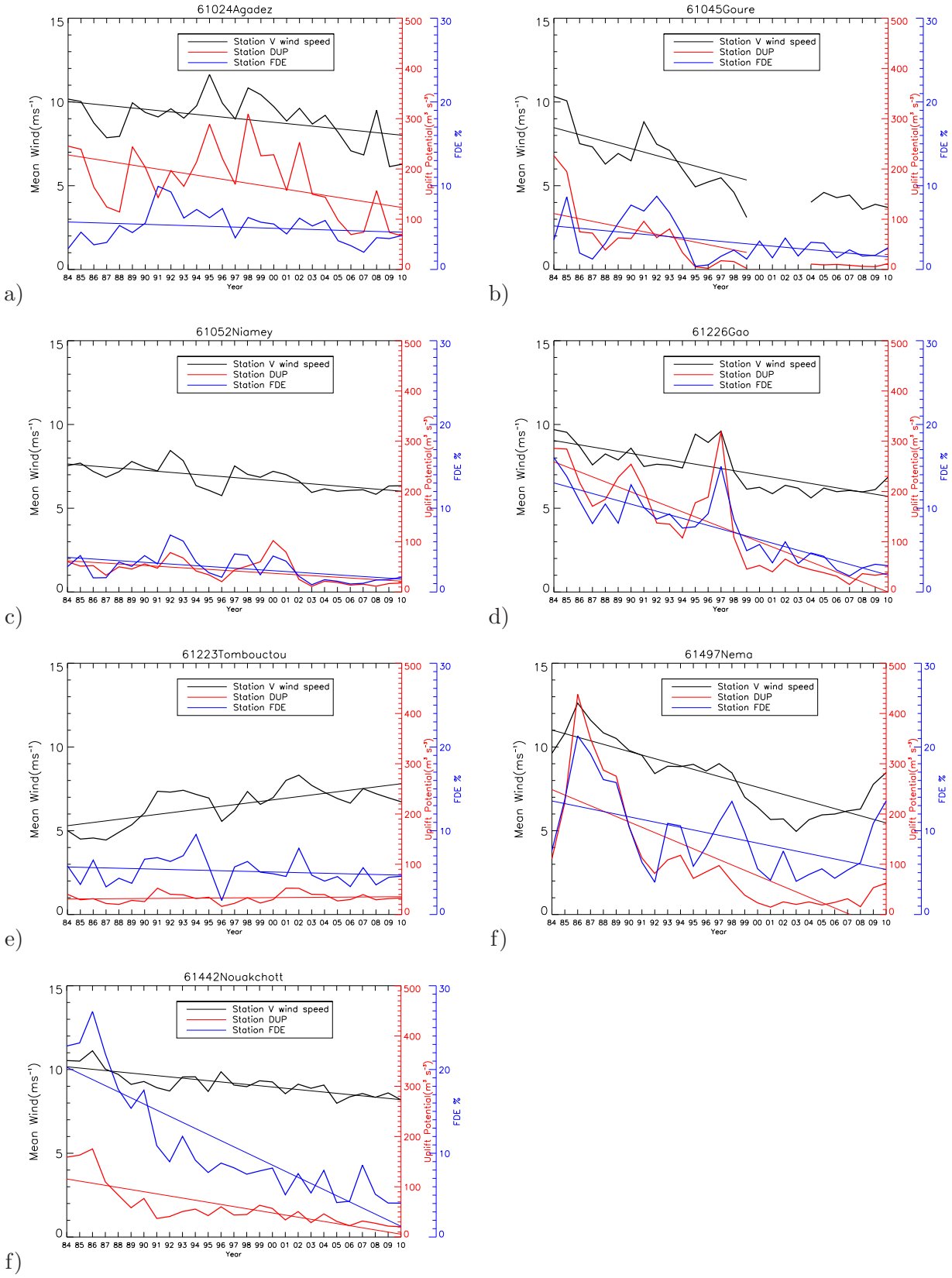

FIGURE 5.4: Time series and trends separated by station. Same as Fig. 5.3, with trends in mean wind V, *DUP*, and FDE given in black, red and blue but for the individual stations of a) Agadez, b) Gouré, c) Niamey, d) Gao, e) Tombouctou, f) Nema, and g) Nouakchott. Trend values for each station are given in Table 5.2

5.3.2 SYNOP Hour Trends

To check that the station trends are not the symptom of biases in data availability, trends are computed at the main SYNOP hours of 0000, 0600, 1200 and 1800 UTC for V, *DUP*, and FDE. Figs. 5.5 a-c show consistently negative trends through the day and night for all parameters. All correlations between the wind parameters and the number of observations are below 0.5. The number of available observations at each station varies from 67582 at Nouakchott to 29777 at Nema (Table 5.2), but there are no notable seasonal differences in the number of available reports (Fig. 5.5d), which increases confidence in the negative seasonal trends observed (Table 5.2, rows 5-7). Generally, the number of reports at the hours 0300, 0900, 1500 and 2100 UTC have increased from 1985 to 2010, but these make a relatively small contribution to the dataset anyway (Fig. 5.6).

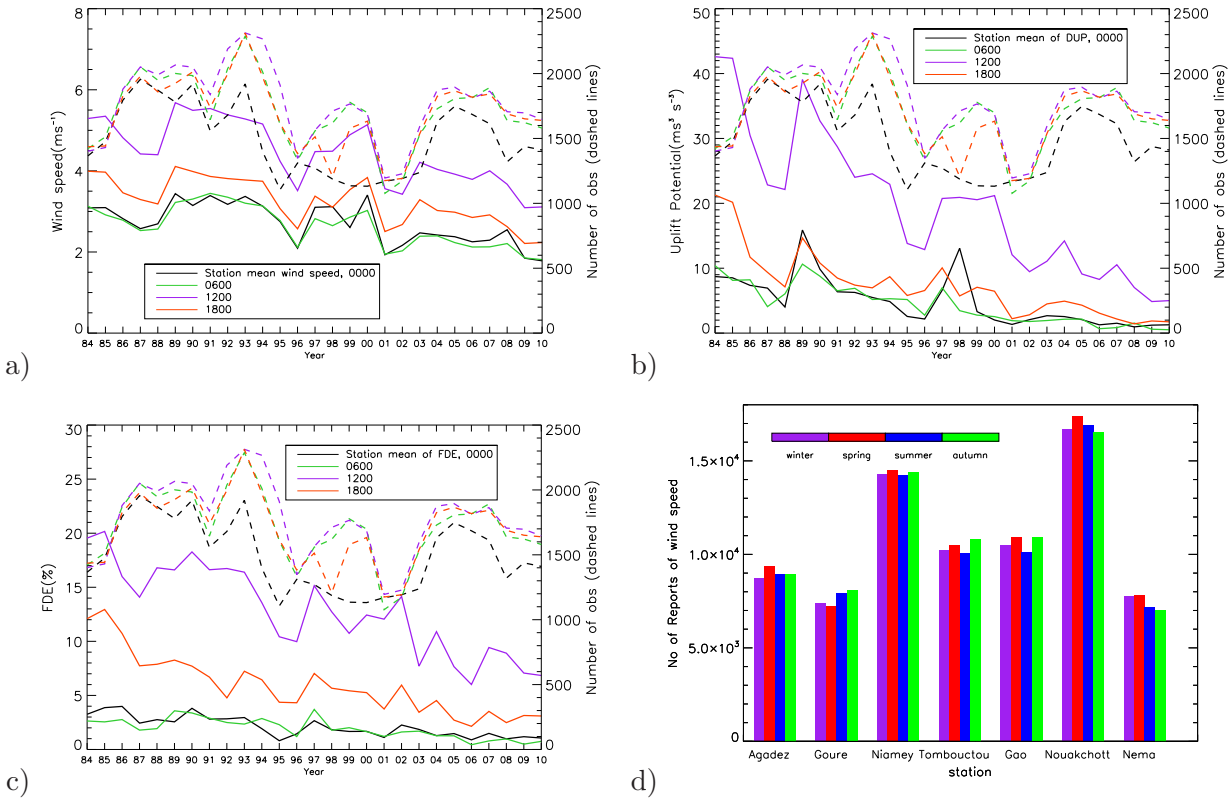

FIGURE 5.5: a) Trends in mean wind, averaged over the seven stations for the main SYNOP hours 0000 (black), 0600 (green), 1200 (purple) and 1800 UTC (orange). Number of wind speed observations are given by the same colors for the same hours with the dashed lines. b) same as a) but for *DUP*. c) same as a) but for FDE. d) Number of wind speed observations reported each season for each of the seven stations.

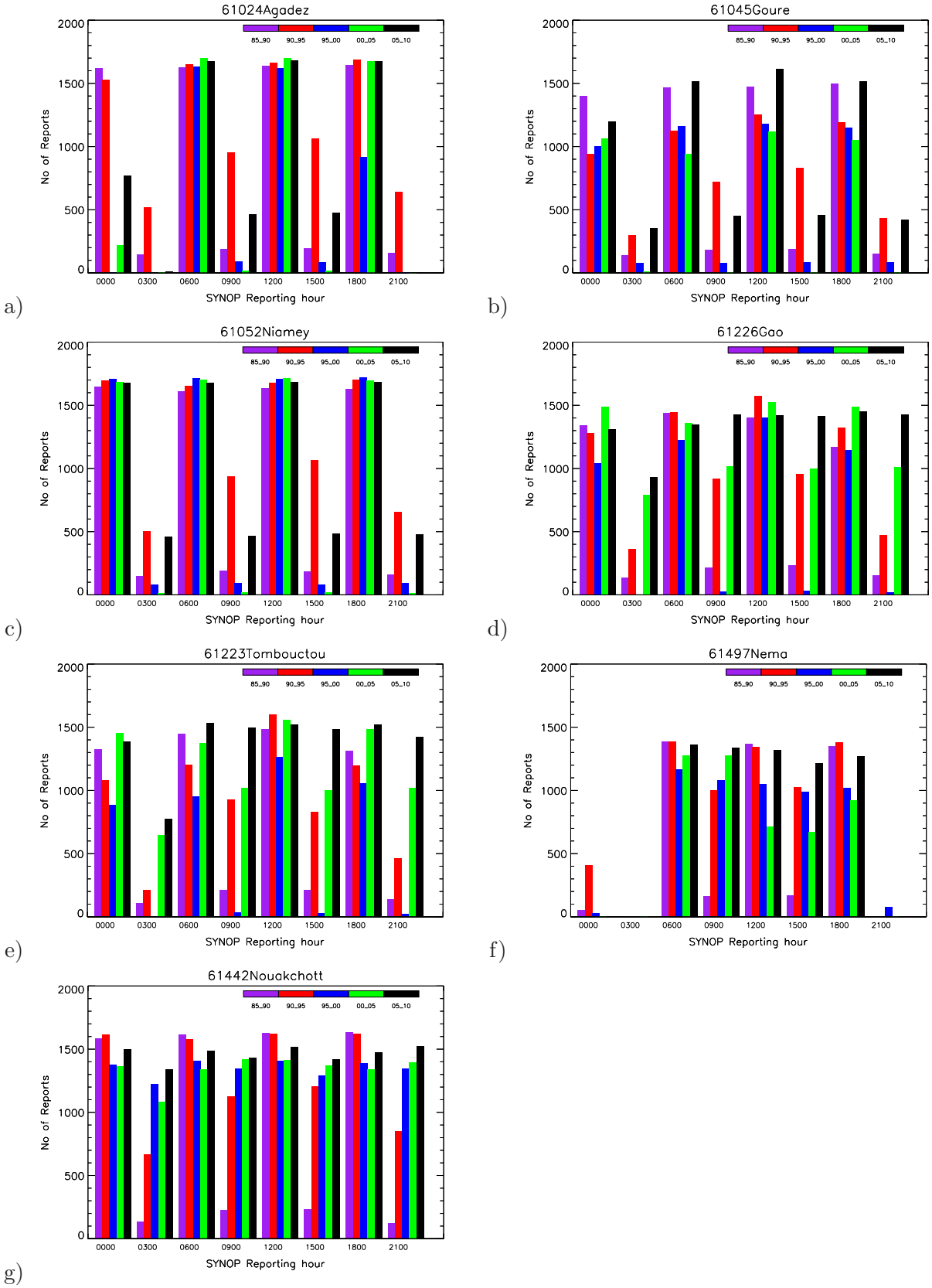

FIGURE 5.6: Bar plots of the number of observations at each SYNOP hour, for each 5-year period between 1985 and 2010 at: a) Agadez, b) Gouré, c) Niamey, d) Gao, e) Tombouctou, f) Nema, and g) Nouakchott.

5.3.3 ERA-Interim Versus Station Observations

Averaged over the seven Sahelian stations, the parameters of V and *DUP* are compared to ERA-Interim reanalysis averaged over a larger box encompassing these stations (blue box in Fig. 5.7). It is interesting and valid to question what extent the stations can be regarded representative for this larger area. The seasonal cycle of 10-m winds shows how the Sahel changes from predominantly northeasterly Harmattan winds in DJF and SON to the southwesterly monsoon winds in JJA (Fig. 5.7). In these seasons, the wind field is quite homogeneous over the entire ERA-Interim box and can therefore be compared to the station mean. The two critical seasons are MAM and SON (Fig. 5.7b and d) when the region is in transition from Harmattan to monsoon flow, such that the stations might not necessarily fully represent the regime over the entire box. In addition, station data will be affected by the local environment surrounding it in any given season, potentially leading to disagreement with ERA data. This is particularly pronounced in JJA, when deep moist convection creates dramatic changes in wind on small time and space scales. This discrepancy is clear from the positive % change trend shown in rows 1 and 2 in Table 5.3 which is accompanied by a very low (negative) correlation of 0.07 between ERA and Observation V. Correlations between station and ERA V in the other three seasons are above 0.5, peaking in DJF with 0.71. DJF is also the time when ERA mean winds are correlated highest with ERA *DUP* (Table 5.3, row 3), when largest trends in ERA data are observed (Table 5.3, rows 1-2) and when correlations with the NAO are highest (section 5.4.2). This holds for ERA winds and station-observed winds and FDE (Table 5.4).

		DJF	**MAM**	**JJA**	**SON**	**Year**
1	% change in ERA V	**-7**	**-4**	**2**	***-5***	***-3***
2	% change in ERA *DUP*	**-31**	**-5**	**2**	**-27**	**-14**
3	ERA V/ ERA *DUP* correlation	***0.85***	***0.83***	**0.50**	***0.80***	***0.60***
4	ERA V/ Obs V correlations	***0.71***	**0.56**	**-0.07**	**0.53**	**0.56**

TABLE 5.3: Seasonality of ERA mean wind and *DUP*. Relative changes (in %) of ERA-Interim mean wind V and *DUP* shown in rows 1 and 2. These are computed in the same way as rows 1-3 in Table 5.2. Statistical significance of trends and correlations at the 95% and 99% levels are denoted in bold and in bold italics, respectively.

5.4 Discussion

The following discussion section explores the possible explanations for the observed decrease in winds and dust emission.

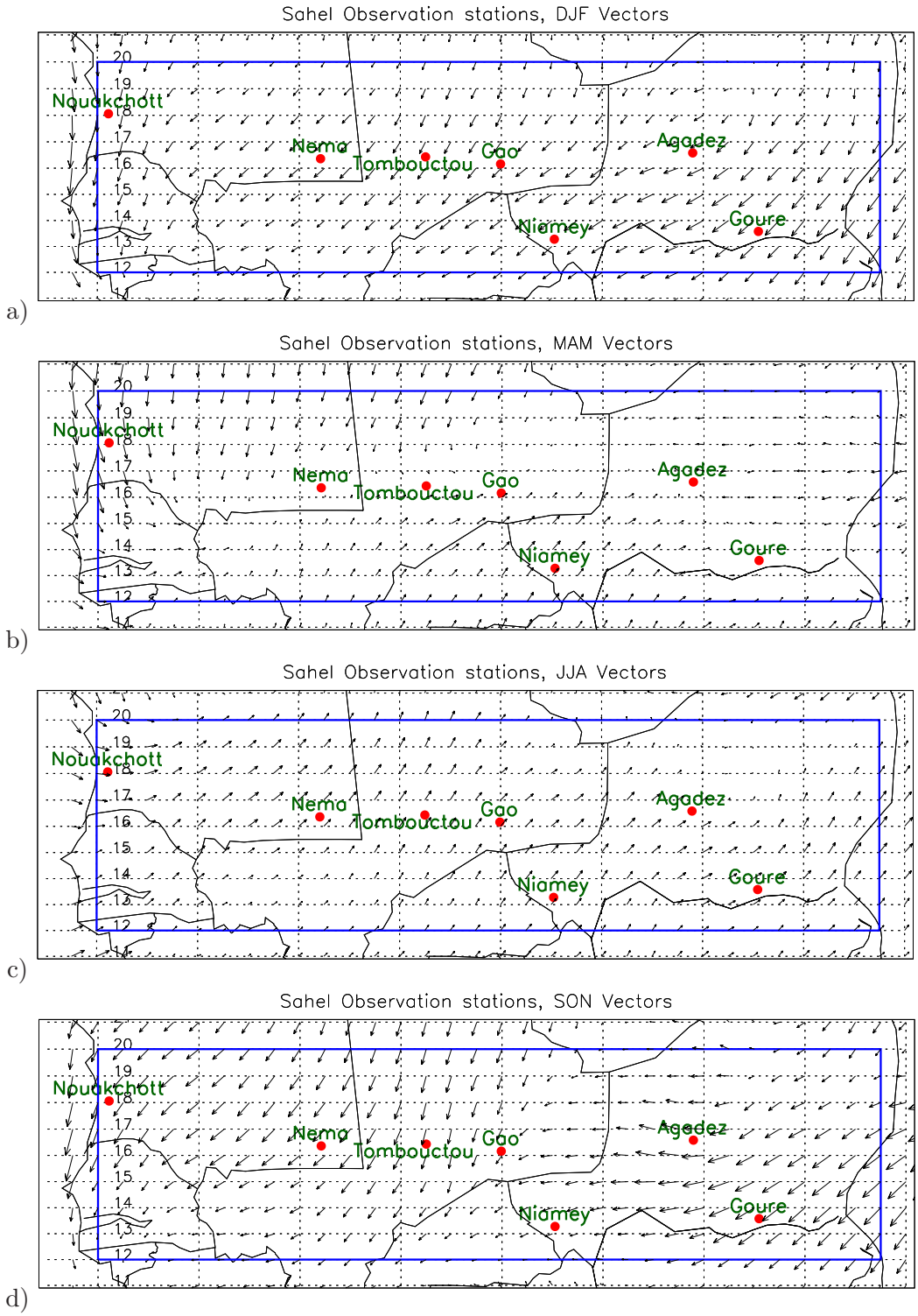

FIGURE 5.7: Map of the Sahel with station locations and the ERA-Interim 10 m mean wind vectors for a) DJF, b) MAM, c) JJA, and d) SON similar to Fig. 5.1. The blue box is the area domain used for averaging ERA 10-m winds.

5.4.1 Changes in Emission Thresholds

A change in emission thresholds is a possible contributor to the decrease in dust emission. Threshold values, which depend on soil and sediment characteristics (Helgren & Prospero, 1987), may have been affected by recent increases in rainfall (Foltz & McPhaden, 2008) and vegetation (Fensholt *et al.*, 2012) over the Sahel. Calculating wind speed probability density functions of all observations and dust events separately allow for the determination of the wind speeds, T25 and T75, at which the probability of dust emission is 25% and 75%. This methodology is explained in detail in section 2.3.2 and also used in Chapter 3. T25 and T75 were computed at each station, for 5-year periods, from 1985 to 2010 and then averaged over the seven stations. T25 varies around 7 ms^{-1} (the threshold assumed for the *DUP* computations in Fig. 5.3) and T75 is typically around 10 ms^{-1}. Neither of the time series show a clear trend, and temporal variations are not coherent (red and blue dashed lines in Fig. 5.8). Calculating *DUP* using the time-varying T25 as the threshold and an identical mean wind distribution for each 5-year period shows relatively small variations (green line in Fig. 5.8). Repeating this calculation with a weighting that takes into account the changing probability for each 1 ms^{-1} wind speed bin results in even less variability (purple line in Fig. 5.8). However, when the real wind distribution for each 5 year period is used, a sharp decrease in *DUP* is found (black line, Fig. 5.8), consistent with Fig. 5.3 (solid red line). This suggests that changes in wind, and not emission thresholds, are the cause of the observed downward trends in frequency of dust emission.

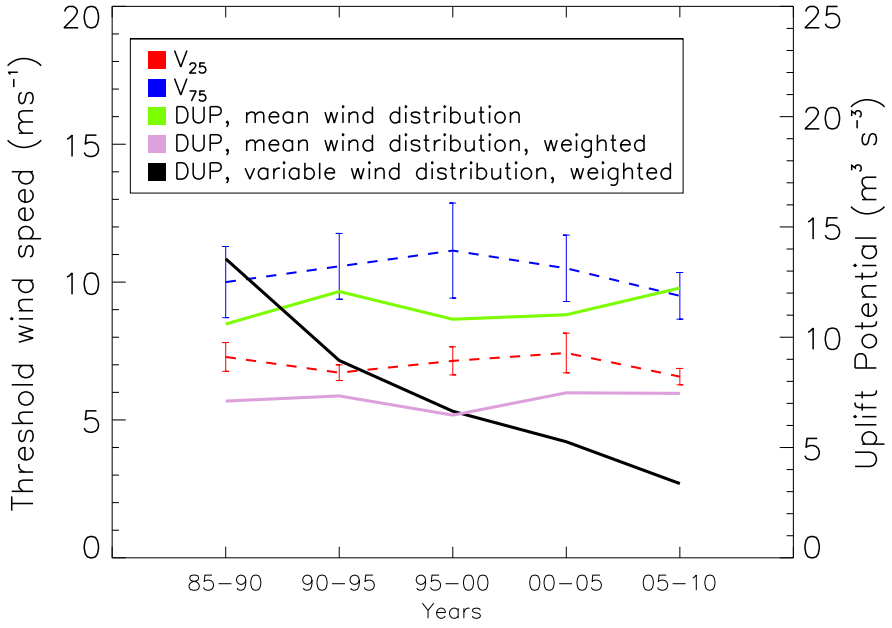

FIGURE 5.8: Time evolution of T25 and T75 threshold velocities computed for each station, for 5-year periods from 1985-2010, then averaged over all stations (dashed lines, left axis). Standard deviations of T25 and T75 wind speeds are given by the error bars. Corresponding *DUP* calculations are also shown (right axis) using (1) a mean wind distribution over the whole time period and the T25 threshold velocity (green), (2) a mean wind distribution and a probability weighting (purple), and (3) a varying wind distribution representative of each 5-year period and a probability weighting (black).

5.4.2 Changes in Large-Scale Circulation

Another potential contributor is a change in the large-scale circulation over northern Africa. Assuming that ERA-Interim is capable of representing such changes accurately, the small trend in ERA-Interim mean wind (Fig. 5.3) suggests that, at least on an annual basis, such contributions are small. An inspection of individual seasons reveals that the largest relative trends of -7% and -31% (for V and *DUP*, respectively) are in boreal winter (DJF, Table 5.3). In this season the entire region is dominated by the north-easterly Harmattan winds (vectors in Fig. 5.1) and the correlation between ERA-Interim and station V are at their seasonal peak of 0.71. Winter is also characterized by highly significant correlations of 0.77 between the NAO and V, and significant correlations of 0.58 between the NAO and FDE (Engelstaedter *et al.*, 2006; Hsu *et al.*, 2012). A steady downward trend in the winter NAO Index since 1995 (Osborn, 2006) can explain the winter trend in ERA-Interim data and a part of the larger trend in station data.

		DJF	**MAM**	**JJA**	**SON**	**Year**
1	V ERA	***0.77***	**0.31**	**-0.21**	**0.43**	**0.58**
2	V OBS	**0.5**	**0.14**	**0.43**	**0.28**	**0.46**
3	FDE	***0.58***	**0.36**	**0.26**	**0.3**	**0.52**

TABLE 5.4: Correlations of mean wind and observed dust with the NAO index. Seasonal correlations of ERA-Interim mean wind V (row 1), observed FDE (row 3) with the seasonal Jones NAO Index (as described in section 2.2.3). Significance of trends and correlations at the 95% and 99% levels are denoted in bold and in bold italics, respectively.

5.4.3 Increased Surface Roughness

A factor which could explain both the downward trend in observed V and *DUP*, and the discrepancies with ERA-Interim, is an increase in surface roughness due to vegetation growth (Roderick *et al.*, 2007; Vautard *et al.*, 2010). This would affect both station winds locally and in the greater Sahel area, consistent with large-scale dust trends found in satellite data (Evan & Mukhopadhyay, 2010; Foltz & McPhaden, 2008). Previous work using NDVI data found a substantial greening of the Sahel in recent decades (Fensholt *et al.*, 2012; Olsson *et al.*, 2005). Given the short Sahelian rainy season from July-September, NDVI is likely to give the best results for the main growing season in late summer and autumn. For September-November (SON), six of the seven stations show a statistically significant positive trend in NDVI (Table 5.2), calculated from a 24 by 24 km^2 area encompassing each station as in Vautard *et al.* (2010). The large autumn trend is robust for

the densely vegetated southern stations, while the two northernmost stations, Agadez and Nouakchott, have low mean values and weaker trends which peak in winter (not shown). Vegetation is sparse in these locations and may not be captured well by NDVI. Remarkably, the four stations with strong vegetation increases, Gouré, Niamey, Gao, and Nema, also have large negative trends in mean wind and *DUP*, particularly in autumn (Table 5.2), which support the link between high winds and vegetation. The largest FDE trends are split between autumn and the more active summer dust season, with the exception of Nouakchott (Table 5.2). For all stations combined however, autumn shows the largest relative changes for both *DUP* and FDE (Table 5.5). It should be pointed out that an increase in green vegetation is likely to affect roughness well beyond the main growing season (Zender & Kwon, 2005), which is not well represented in NDVI data designed for photo-synthetically active plants.

		DJF	**MAM**	**JJA**	**SON**	**Year**
1	% change in V	***-31***	***-23***	***-26***	***-30***	***-27***
2	% change in FDE	***-49***	**-34**	***-47***	***-72***	***-68***
3	% change in *DUP*	***-84***	***-83***	***-90***	***-91***	***-86***
4	% change in V > 5 ms^{-1}	***-16***	***-14***	***-21***	***-30***	***-20***
5	% change in V < 5 ms^{-1}	**-4**	**6**	**4**	**-2**	**1**
6	V/FDE corr	***0.74***	**0.55**	**0.41**	***0.83***	***0.92***
7	V/*DUP* corr	***0.92***	***0.93***	***0.88***	***0.76***	***0.95***
8	FDE/ *DUP* corr	***0.61***	**0.53**	**0.46**	***0.72***	***0.93***

TABLE 5.5: Relative changes (in %) for rows 1-5 are computed in the same way as rows 1-3 in Table 5.2. Rows 6-8 give linear correlation coefficients for seven-station means of V, FDE, and *DUP*. Statistical significance of trends and correlations at the 95% and 99% levels are denoted in bold and in bold italics, respectively.

5.4.4 Changes in the Surface Energy Budget

Vegetation can also contribute to the negative trends in winds through changes in the surface energy budget. Increased transpiration, plus possible larger evaporation from moister soils, will increase latent heat flux at the expense of sensible heating of the atmosphere. The reduction in daytime buoyancy of near-surface air tends to reduce turbulence and therefore gustiness. This effect should be well represented in station data but not in reanalyses, which capture only mean grid-scale winds. Globally, it has been suggested that roughness changes dominate over changes in daytime turbulence and evapo-transpiration (Vautard *et al.*, 2010). Absolute trends in mean wind and *DUP* averaged over the seven stations are more negative during the day than night (Table 5.6), which is consistent with

this idea. Relative changes are slightly greater at night, except for *DUP* during the vegetation maximum in SON (Table 5.6) when relative changes are -92% in the day and only -79% at night. This suggests that the influence of latent heating, as shown in the absolute trends (Fig. 5.6, rows 1-4), may be more prominent in this season. Increased vegetation also reduces the area of bare soil available for dust emission. This may contribute to trends in dust mass and frequency but cannot explain the corresponding trends in mean wind and *DUP*.

			DJF	**MAM**	**JJA**	**SON**	**Year**
Absolute trends ($ms^{-1}a^{-1}$)	1	Day V	***-0.07***	***-0.05***	***-0.05***	***-0.06***	***-0.06***
	2	Night V	***-0.09***	***-0.05***	***-0.05***	***-0.04***	***-0.04***
	3	Day *DUP*	***-9.5***	***-8.1***	***-5.5***	***-4.9***	***-7***
	4	Night *DUP*	***-3.8***	***-2.6***	***-3.8***	***-1.7***	***-3***
Relative change (%)	5	Day V	***-30***	***-25***	***-27***	***-36***	***-28***
	6	Night V	***-59***	***-35***	***-39***	***-53***	***-31***
	7	Day *DUP*	***-83***	***-86***	***-87***	***-92***	***-86***
	8	Night *DUP*	***-105***	***-91***	***-98***	***-79***	***-97***

TABLE 5.6: Day/Night station trends comparison. Seasonal absolute and relative trends of day and night data from station averaged observations. Absolute trends in rows 1-4 are calculated as the average change in wind-speed per year, while rows 5-8 represent the total change in wind-speed during the study period 1984-2010 as a % of the initial value. Significance of trends at the 95% and 99% levels are denoted in bold and bold italics, respectively.

5.4.5 Urbanisation

An additional localized influence could come from a change in roughness and surface characteristics by man-made structures, as Sahelian cities have been growing substantially over the last decades (Olsson *et al.*, 2005). This would not be captured by reanalyses data at all. Past work using station data in China (Guo *et al.*, 2011) and Australia (McVicar *et al.*, 2008) found that urbanization can weaken the observed stilling effect relative to rural stations. Consistent with this, three of the four stations situated outside of the main urban areas, Gouré, Nema and Gao, show steeper negative trends in both mean wind and *DUP*, with Tombouctou again being the exception (Table 5.2). Detailed modeling studies are needed to further corroborate and quantify this effect (Guo *et al.*, 2011).

5.4.6 Extending Analysis With 2011 and 2012 Data

Including data from 2011 and 2012, which became available after the rest of work on the chapter had been completed, has quite a striking effect on the FDE, mean wind and *DUP*

trends. A comparison between trends including data up to 2010 and up to 2012 in Table 5.7 indicates a weakening of the three trends in each season, and a drop in the significance too. The reduction in *DUP* trends is most striking with an annual average 64% weaking in the trend. The dust emission statistics appear less sensitive to the extra two years of data, with trends only weakening by an average of 9%. This could be partly due to the different methods by which wind-speed and dust emission are measured at surface stations. The results in Table 5.7 suggest that mean wind and *DUP* trend values are particularly sensitive to the time period used and that inter-annual variations can significantly change the results. This does not necessarily change the conclusions, but further analysis would be required to determine if similar changes in large-scale circulation and vegetation also occur.

		Winter	**Spring**	**Summer**	**Autumn**
Mean Wind	to 2010	***-30.82***	***-23***	***-26.5***	***-29.72***
	to 2012	-6.1	-6.6	**-12.5**	-10.9
DUP	to 2010	***-84.31***	***-83.47***	***-90.32***	***-90.63***
	to 2012	**-24.8**	***-22.8***	***-22.8***	**-20.1**
FDE	to 2010	***-49.35***	-34.45	***-46.79***	***-72.27***
	to 2012	**-46.12**	-21.9	***-46.8***	***-67.1***

TABLE 5.7: Statistically significant trends and seasons at the 99% level are denoted in bold italics and 95% in bold.

5.5 Conclusions

This chapter offers a new perspective on the recently observed dramatic decadal trends in dustiness over North Africa and the tropical North Atlantic. The time-series of wind-speed and dust emission from surface observations at seven Sahelian stations for the period 1984 - 2010 showed a decreasing trend. The diagnostic parameter dust uplift potential was also plotted to represent the "power" of the wind and a constant threshold of 7 ms^{-1} is used in equation (2.1) to isolate the contribution of the wind from changing soil parameters. Averaged over the seven stations, *DUP* represents the largest decreasing trend. To investigate decreasing winds and emission, ERA-Interim reanalysis, NDVI and NAO trends were also calculated and correlations were made to help formulate physical explanations for the trends. The results suggest that decreasing emission trends are related to reduced peak winds rather than changes in emission threshold. Increased roughness and reduced turbulence, as a result of the observed "greening" in the Sahel, appears to be the main cause of weaker winds. Changes in the large-scale circulation, possibly

associated with the downturn of the NAO, are secondary. The large discrepancy between station and reanalysis data demonstrates that a better representation of inter-annual to decadal roughness changes in global and regional models is urgently needed to improve the modeling and understanding of the global dust cycle. The results are consistent with strong downward trends in dustiness over the tropical North Atlantic (5-20°N), while no clear trends are found at higher latitudes (15-30°N), which are probably more strongly influenced by the very sparsely vegetated Sahara (Chiapello *et al.*, 2005; Evan & Mukhopadhyay, 2010). To quantify the highly disputed anthropogenic impacts (Engelstaedter *et al.*, 2006) on dustiness, it is important to investigate to what extent agricultural activities in the Sahel could, or have, changed vegetation, roughness, wind, and ultimately dust emission.

Chapter 6

Conclusions and Proposed Future Work

6.1 Conclusions

This thesis focuses on the role of the wind and atmospheric circulation in driving dust emission trends and cycles. It has been possible to make inferences about emission thresholds from 10 m winds and present weather reports of emission specifically which, although not a new concept, has not been explored in this way over northern Africa. The use of station single-point observations is both an advantage and disadvantage. The main advantage is the long time-period of data availability (compared to satellite observations), as well as the ability to represent local variability in parameters and assess how well (or badly) this variability is represented in reanalysis and models. Disadvantages include the lack of meta-data available to quantify and incorporate error into the analysis and the poor spatial representation of the sparse network of African observation stations. A variety of tests were used to assess station-data quality leading to a subset of data which balanced the fine line of having enough data to make statistics from, while maximising the quality of the data.

This chapter summarises the key methods and diagnostics which were applied to surface observations of dust emission and wind speed. These are important because the results from the analysis of this problematic observation data set were dependent on how the data

were selected. One useful outcome of this work is the new analysis and quality control methods which could be applied to other observational datasets. Also presented here are the main conclusions from the three results chapters and finally, ideas for future work.

Summary of Key Diagnostics

Novel diagnostics were developed to exploit the SYNOP station data as fully as possible. The frequency of dust emission (FDE), defined as the (number of dust emission events/ total number of events) *100 is not a new concept but has not been applied to a comprehensive climatological analysis of observations in northern Africa. FDE can be split into two subsets which roughly distinguish between larger, possibly more intense, "dust storm" and smaller "blowing dust" events (DSF and BDF, respectively). Strong wind frequency (SWF) is defined in the same way as FDE but using the number of winds over a threshold which is calculated for each station individually and seasonally. The relatively new parameter, dust uplift potential (DUP), is a powerful and versatile tool which investigates the dust emitting power of the wind. This is useful considering there are no long-term measurements of emitted dust mass, only qualitative descriptions. Combining DUP with the frequency of strong winds, it is possible to learn something about the strength of each event. In Chapter 3, DUP was used with thresholds calculated from station data to give a realistic climatological analysis of the seasonal and diurnal cycles in mean DUP and DUP Intensity (the strength per event). Chapter 4 again used the station-calculated threshold values, but focused on the highest wind-speeds, $>$ 30 kts. In Chapter 5, the threshold parameter was kept a constant 7 ms^{-1} in order to isolate the role of a changing wind distribution through time on the potential dust mass emitted.

To highlight mean cycles, stations were grouped together to average out very local variability and emphasise larger controls on dust emission to particular regions. Stations were grouped subjectively in Chapters 3 and 4 based on meteorological climates and seasonal cycles of dust emission into the six regions of N Algeria, C Sahara, Egypt, W Sahel, C Sahel and Egypt.

Summary of Chapter 3

One factor which is perhaps not always addressed thoroughly enough in the literature is the quality of surface observations used, a particularly important consideration in northern Africa due to sparse and ageing network in which changes are not well documented. As the

validity of the results in this thesis depended on having as reliable a dataset as possible, a considerable amount of time has been spent characterising the biases, time-series gaps and suspicious reports.

Quality flags were applied to 70 stations whose initial selection criteria was a total of 1060 observations over the 29-year period 1984 - 2012. Each flag indicated if there were significantly less observations at night-time or gaps in the time-series record of 1) greater than five years, 2) less than five years or 3) no gaps. Over the time-period the most incomplete records were found in Sudan, where most stations have more than five years with less than 500 observations which is likely due to political instability in the region. Many other Sahelian stations also have gaps (in particular Mauritania) while Algerian stations report consistently. Daytime biases are a common feature of central and western Sahel stations

Dust-emission "thresholds", calculated based on the relationship between the frequency of occurrence of dust events and anemometer wind-speed, were presented on an annual and seasonal basis (Chapter 3) and through time (Chapter 5). Generally, thresholds were found to be higher north of 22°N. Seasonal variations in thresholds are largest in the Sahel and smallest in the Sudan. Thresholds did not change significantly over the time-period 1984 - 2012 and were not thought to be significant in the observed decadal downward trend in dust emission detailed in Chapter 5.

Emission can be separated out from transport in present weather reports and in doing so allows for a relative comparison between the two at individual stations. North of 24°N emission is more important than transport, while south of this in the Sahel, transport events dominate. Despite a higher number of transported events in the Sahel, the annual mean values of emission are still higher than those in the north. This suggests the frequency of dust events (whether emitted or transported) is significantly higher south of 24°N and ties in with current literature proposing a Sahelian "dust zone" (Klose *et al.*, 2010). Sudan stands out as the "dustiest" region of all, with both the highest % of transported events and highest annual mean emission.

Seasonal variations in dust emission are mostly attributed to seasonal variations in strong winds with high correlations found between FDE and SWF in all regions. However, these

correlations did not change dramatically when using either a fixed annual mean, or seasonally varying, thresholds for SWF. This implies little overall influence from seasonally changing thresholds to the frequency of dust emission, though it could be significant to the total mass. Seasonally, outwith the Sahel regions, dust emission events occur most frequently in spring. This is largely due to the strength of large-scale pressure gradients, with additional contributions from spring-time cyclones and depressions. Within the Sahel the seasonal cycle is more complex, with two identifiable regimes. The winter harmattan is the main factor in the C Sahel, which on a day-to-day basis creates strong winds and dust emission through the breakdown of nocturnal LLJs. In the W Sahel the high dust season is split between the harmattan-driven winter emissions and summer mechanisms driven by the development of the Saharan Heat Low and summer monsoon-related haboobs.

On a diurnal scale it is not possible from these data to categorically separate mechanisms such as LLJs, haboobs or dry convection from each other, but it is possible to apply knowledge of when they are most likely to occur to the diurnal cycle of FDE and make an estimation of which are particularly important. For example, FDE peaks very suddenly within three hours at sunrise in the C Sahara and the C Sahel (particularly in high-dust winter season) which points to NLLJ breakdown. Haboobs are thought to be important for Sahelian dust emission, but these are most likely to occur at night-time; the time where data is most limited in the Sahel at many stations. Daytime LLJs which form in response to baroclinic zones due to complex terrain, mountains, land-sea air temperature contrasts and the subtropical jet are eroded by the growing boundary layer and could be partly responsible for increased emission in the afternoon.

Summary of Chapter 4

The quality and validity of wind-speeds > 30 kts (~ 15 ms^{-1}) was investigated in Chapter 4. In all regions wind-speed measurements were found in clusters around 60 kts in particular, with small clusters at other multiples of 10 kts and no observations at all above 100 kts. This is attributed to the methods and instrumentation used which results in a large (human) random error. Most worrying are the typographic errors which were observed for winds > 30 kts. This finding suggests caution should be applied to analyses which focus on high winds, in particular those over 55 kts.

Chapter 4 considers which wind speeds contribute the most to the total mass, approximated with *DUP*, of dust emitted. By focussing on the tail of the wind-speed distribution as input to the *DUP* equation, it was possible to determine which wind-speeds are most important regionally. Because there are so few observations, and they are each applied to a highly sensitive diagnostic which includes a cubic function, it was crucial to identify the possible errors and biases in these measurements. Therefore, case-studies of high-wind events accompanied by dust emission reports, during the availability period of satellite imagery from SEVIRI (2006 - present) were investigated for their plausibility. Based on this analysis, a 55 kt upper threshold was proposed as an upper limit to suitable data. A top wind-speed of only 47 kts was found from high resolution field campaign data and was subject to strict quality control procedures. Restricting the dataset to winds below 55 kts still led to some interesting conclusions. High winds which make up to 0.3 - 0.5 % in the north and 0.7 - 2.5 % in the south of all dust-emitting winds contribute to over half of total *DUP*. A % occurrance of 0.3% equates to only 5-6 events per year. Winds of 12 - 15 ms^{-1}, possibly due to eastward moving cyclones or depressions are particularly important in the north. In the south winds between 7 - 11 ms^{-1} contribute the most to *DUP*, but this may be inaccurate due to a poor representation of haboobs in the largely day-time biased data.

Summary of Chapter 5

An unexpected finding during the course of this study was an observed decrease in the FDE and 10 m mean wind-speed over the time period 1984 - 2010, consistent over many Sahelian stations. Only stations which had a gap-free time-series record could be used for Chapter 5, and as a result seven stations were selected. The observed decrease in FDE was also accompanied by a decrease in *DUP*, which is more representative than mean wind of the winds which are responsible for dust emission. Through the analysis of trends in the satellite-sensed normalised difference vegetation index (NDVI) as a proxy for vegetation, it was found that vegetation was likely to be an important factor. Increased vegetation results in increased roughness length and hence a decrease in winds. To some extent vegetation changes the energy budget by reducing sensible heat flux (and subsequent daytime turbulence) and increasing the latent heat flux. This effect is suggested to play a role, though it is not possible to determine the contribution relative to other factors. Strong trends in the main growing season of autumn support the key role of vegetation,

while in winter, large-scale circulation was proposed to be most important. Discrepancies between station observations and ERA-Interim reanalysis highlight the need to better represent roughness on interannual and decadal time-scales in order to improve global dust cycle forecasting in models.

6.2 Future Work

Extending Trends Analysis

With an extra two years (2011 and 2012) of observational data it would be possible to extend the whole analysis of Chapter 4. Some key trends with the extra data were presented in section 5.4.6 but this only involved trends of observational data. This could be extended to include all the correlations with reanalysis. Now that there is open access to GIMMS3g data, the period of vegetation data could be extended from 2006 to 2010. The trends analysis could also be extended out from the Sahel to the 70 stations as investigated in Chapter 3. Only stations without daytime biases and record gaps would be used and this could give very sparse coverage, especially in Sudan.

Further Use of AMMA and Fennec Observational Data

In a continuation of the rare events investigation of Chapter 4, more high wind case studies could be compared to AMMA field campaign data. The differences between AMMA stations and the nearest SYNOP stations could be investigated. Integrating AMMA data with Sahel SYNOP stations would fill in the night-time gaps and better characterise the role of haboobs in the diurnal cycle there. Chapter 4 only made used of field campaign data to look for maximum values in wind-speed, but the entire total *DUP* analysis could also be computed using AMMA, or even Fennec, data.

Further categorisation of present weather reports

The distribution of visibility at different wind-speeds could be further categorised into types of dust emission report, as done in Chapter 3 when frequency of dust emission was separated out into blowing dust (green, ww=07) and dust storms (red, ww=09,30-35). The aim would be to give a detailed description of the visibility and wind-speeds associated with certain types of emission reports.

Modeling the effect of increased vegetation on decreasing winds

A regional model would be used to test the response of the wind field (focused on dust uplift potential (DUP) and the tail of the wind pdf) with and without the real-world best estimate of vegetation changes (such as NDVI or roughness maps) for the period of their availability (for GIMMS3g NDVI this is 1981 to 2010). Calculations would be done to determine how much of the trend in dust uplift potential could be explained by using real vegetation data. DUP would be used rather than mean wind as it better represents the winds which are important for emission. Differences between modeled and observed DUP would be calculated. The investigation area would be focused over the seven stations used in Chapter 5. The analysis would also be done seasonally, to determine whether the trends can be increasingly or decreasingly attributed to the vegetation mechanism in particular seasons. For example, it would be expected that the real-world changes in vegetation would be able to explain a larger fraction of the decreasing trend in dust uplift potential in the autumn growing season, as opposed to winter harmattan conditions.

Haboob identification

Relating objectively tracked MSCs using the data from Bennartz & Schroeder (2012), to surface observation parameters such as dust emission, wind-speed, dew point and cloud cover would allow for identification of haboobs and help with understanding the relative contribution of these dust storms compared to other mechanisms.

In addition to this, the LLJ identification algorithm applied to ERA-Interim, as used in Fiedler *et al.* (2013a), could be compared to surface data for the grid-cells over the surface SYNOP stations used in this thesis.

Overall, there is a lot more synthesis that could be done between long-term SYNOPs and the numerous field campaigns which also themselves include high resolution datasets up to 10 years long. In particular, AMMA stations could be particularly useful for a haboob climatology as they contain both night and day observations, which many Sahel SYNOP stations do not. Computing long-term statistics for very specific, populated areas could be better exploited in the future for a relatively unexplored part of dust research: the effects of dust on health, especially for the northern Africa regions where the atmosphere is particularly dusty and the people are particularly vulnerable to its affects.

Better evaluation of models and reanalysis is a key aspect of dust research. It is hoped that the information in this thesis can be used to improve evaluation by not only characterising real dust emission events, but also through clear recognition of the limitations of surface data and how it could provide misleading results and should therefore be treated with caution in evaluation studies.

References

Ackerman, S. (1997). Remote sensing aerosols using satellite infrared observations. *Journal of Geophysical Research-Atmosphere*, **102**, 17069–17079.

Ackerman, S. & Cox, S. (1989). Surface Weather Observations Of Atmospheric Dust Over the Southwest Summer Monsoon Region. *Meteorology and Atmopsheric Physics*, **41**, 19–34.

Afeti, G. & Resch, F. (2000). Physical characteristics of Saharan dust near the Gulf of Guinea. *Atmopheric Environment*, **34**, 1273–1279.

Allen, C.J.T., Washington, R. & Engelstaedter, S. (2013). Dust emission and transport mechanisms in the central Sahara: Fennec ground-based observations from Bordj Badji Mokhtar, June 2011. *Journal of Geophysical Research - Atmospheres*, **118**, 6212–6232.

Alpert, P. & Ziv, B. (1989). The Sharav Cyclone - Observations and some Theoretical Considerations. *Journal of Geophysical Research - Atmospheres*, **94**, 18495–18514.

Alpert, P., Neeman, B. & Shay-El, Y. (1990). Climatological analysis of Mediterranean cyclones using ECMWF data. *Tellus A*, **42**, 65–77.

Ansmann, A., Tesche, M., Knippertz, P., Bierwirth, E., Althausen, D., Muller, D. & Schulz, O. (2009). Vertical profiling of convective dust plumes in southern Morocco during SAMUM. *Tellus Series B-Chemical and Physical Meteorology*, **61**, 340–353.

Ansmann, A., Petzold, A., Kandler, K., Tegen, I., Wendisch, M., Mueller, D., Weinzierl, B., Mueller, T. & Heintzenberg, J. (2011). Saharan Mineral

Dust Experiments SAMUM-1 and SAMUM-2: what have we learned? *Tellus Series B - Chemical and Physical Meteorology*, **63**, 403–429.

Ashpole, I. & Washington, R. (2012). An automated dust detection using SEVIRI: A multiyear climatology of summertime dustiness in the central and western Sahara. *Journal of Geophysical Research- Atmospheres*, **117**.

Ashpole, I. & Washington, R. (2013). A new high-resolution central and western Saharan summertime dust source map from automated satellite dust plume tracking. *Journal of Geophysical Research-Atmosphere*, **118**, 6981–6995.

Atkinson, J.D., Murray, B.J., Woodhouse, M.T., Whale, T.F., Baustian, K.J., Carslaw, K.S., Dobbie, S., O'Sullivan, D. & Malkin, T.L. (2013). The importance of feldspar for ice nucleation by mineral dust in mixed-phase clouds (vol 498, pg 355, 2013). *Nature*, **500**, 491.

Avila, A. (1996). Time trends in the precipitation chemistry at a mountain site in Northeastern Spain for the period 19831994. *Atmospheric Environment*, **30**, 1363 – 1373.

Bagnold, R. (1941). *The physics of blown sand and desert dunes*. Dover Publications, Mineola,NY,USA.

Banks, J.R. & Brindley, H.E. (2013). Evaluation of MSG-SEVIRI mineral dust retrieval products over North Africa and the Middle East. *Remote*, **128**, 58–73.

Barry, R.G. & Chorley, R.J. (2009). *Atmosphere, weather and climate*. Routledge.

Bennartz, R. & Schroeder, M. (2012). Convective Activity over Africa and the Tropical Atlantic Inferred from 20 Years of Geostationary Meteosat Infrared Observations. *Journal of Climate*, **25**, 156–169.

Bergametti, G. & Foret, G. (2014). *Mineral Dust - A Key Player in the Earth System*, chap. Dust Deposition. Sprin.

Bergametti, G., Gomes, L., Remoudaki, E., Desbois, M., Martin, D. & Buatmenard, P. (1989). Present Transport and Deposition Patterns of African Dust to the North-Western Mediterranean. In M. LEINEN & M. SARNTHEIN, eds., *Paleoclimatology and Paleometeorology : Modern and Past Patterns of Global Atmospheric Transport*, vol. 282, 227–252.

Bichet, A., Wild, M., Folini, D. & Schaer, C. (2012). Causes for decadal variations of wind speed over land: Sensitivity studies with a global climate model. *Geophysical Research Letters*, **39**.

Birch, C.E., Parker, D.J., Marsham, J.H. & Devine, G.M. (2012). The effect of orography and surface albedo on stratification in the summertime Saharan boundary layer: Dynamics and implications for dust transport. *Journal of Geophysical Research: Atmospheres (1984–2012)*, **117**.

Blackadar (1957). Boundary Layer Wind Maxima and their significance for the growth of nocturnal inversions.

Bou Karam, D., Flamant, C., Knippertz, P., Reitebuch, O., Pelon, J., Chong, M. & Dabas, A. (2008). Dust emissions over the Sahel associated with the West African monsoon intertropical discontinuity region: A representative case-study. *Quarterly Journal of the Royal Meteorological Society*, **134**, 621–634.

Breuning-Madsen, H. & Awadzi, T. (2005). Harmattan dust deposition and particle size in Ghana. *CATENA*, **63**, 23–38.

Brindley, H., Knippertz, P., Ryder, C. & Ashpole, I. (2012). A critical evaluation of the ability of the Spinning Enhanced Visible and Infrared Imager (SEVIRI) thermal infrared red-green-blue rendering to identify dust events: Theoretical analysis. *Journal of Geophysical Research-Atmospheres*, **117**.

Brooks, N. & Legrand, M. (2000). Dust variability over Northern Africa and rainfall in the Sahel. In S. McLaren & D. Kniveton, eds., *Linking Climate Change to Land Surface Change*, vol. 6 of *Advances in Global Change Research*, 1–25, SPRINGER.

Buckle, C. (1996). *Weather and climate in Africa*. Longman.

Cairo, F., Pommereau, J.P., Law, K.S., Schlager, H., Garnier, A., Fierli, F., Ern, M., Streibel, M., Arabas, S., Borrmann, S., Berthelier, J.J., Blom, C., Christensen, T., D'Amato, F., Di Donfrancesco, G., Deshler, T., Diedhiou, A., Durry, G., Engelsen, O., Goutail, F., Harris, N.R.P., Kerstel, E.R.T., Khaykin, S., Konopka, P., Kylling, A., Larsen, N., Lebel, T., Liu, X., MacKenzie, A.R., Nielsen, J., Oulanowski, A., Parker, D.J., Pelon, J.,

Polcher, J., Pyle, J.A., Ravegnani, F., Riviere, E.D., Robinson, A.D., Rockmann, T., Schiller, C., Simoes, F., Stefanutti, L., Stroh, F., Some, L., Siegmund, P., Sitnikov, N., Vernier, J.P., Volk, C.M., Voigt, C., von Hobe, M., Viciani, S. & Yushkov, V. (2010). An introduction to the SCOUT-AMMA stratospheric aircraft, balloons and sondes campaign in West Africa, August 2006: rationale and roadmap. *Atmospheric Chemistry and Physics*, **10**, 2237–2256.

Cakmur, R.V., Miller, R.L. & Torres, O. (2004). Incorporating the effect of small-scale circulations upon dust emission in an atmospheric general circulation model. *Journal of Geophysical Research-Atmospheres*, **109**, 20, j. Geophys. Res.-Atmos. ISI Document Delivery No.: 811AJ Times Cited: 40 Cited Reference Count: 104 AMER GEOPHYSICAL UNION WASHINGTON.

Carlson, T.N. & Prospero, J.M. (1972). The Large-Scale Movement of Saharan Air Outbreaks over the Northern Equatorial Atlantic. *J. Appl. Meteor.*, **11**, 283–297.

Charlson, R.J., Ahlquist, N.C. & Horvath, H. (1968). On the generality of correlation of atmospheric aerosol mass concentration and light scatter. *Atmospheric Environment (1967)*, **2**, 455 – 464.

Chatenet, B., Marticorena, B., Gomes, L. & Bergametti, G. (1996). Assessing the microped size distributions of desert soils erodible by wind. *Sedimentology*, **43**, 901–911.

Chepil, W. (1956). Influence of moisture on erodibility of soil by wind. *Soil Science Society of America Journal*, **20**, 288–292.

Chiapello, I. & Moulin, C. (2002). TOMS and METEOSAT satellite records of the variability of Saharan dust transport over the Atlantic during the last two decades (1979-1997). *Geophysical Research Letters*, **29**.

Chiapello, I., Bergametti, G., Gomes, L., Chatenet, B., Dulac, F., Pimenta, J. & Suares, E.S. (1995). An additional low layer transport of Sahelian and Saharan dust over the north-eastern Tropical Atlantic. *Geophysical Research Letters*, **22**, 3191–3194.

Chiapello, I., Moulin, C. & Prospero, J. (2005). Understanding the long-term variability of African dust transport across the Atlantic as recorded in both Barbados surface concentrations and large-scale Total Ozone Mapping Spectrometer (TOMS) optical thickness. *Journal of Geophysical Research-Atmospheres*, **110**.

Chomette, O., Legrand, M. & Marticorena, B. (1999). Determination of the wind speed threshold for the emission of desert dust using satellite remote sensing in the thermal infrared. *Journal of Geophysical Research-Atmospheres*, **104**, 31207–31215.

Christopher, S.A., Gupta, P., Johnson, B., Ansell, C., Brindley, H. & Haywood, J. (2011). Multi-sensor satellite remote sensing of dust aerosols over North Africa during GERBILS. *Quarterly Journal of the Royal Meteorological Society*, **137**, 1168–1178.

Cook, N.J. (2014). Review of errors in archived wind data. *Weather*, **69**, 72–78.

Cornelis, W., Gabriels, D. & Hartmann, R. (2004). A parameterisation for the threshold shear velocity to initiate deflation of dry and wet sediment. *Geomorphology*, **59**, 43–51.

Cowie, S.M., Knippertz, P. & Marsham, J.H. (2013). Are vegetation-related roughness changes the cause of the recent decrease in dust emission from the Sahel? *Geophysical Research Letters*, **40**, 1868–1872.

Cowie, S.M., Knippertz, P. & Marsham, J.H. (2014). A climatology of dust emission events from northern Africa using long-term surface observations. *Atmospheric Chemistry and Physics Discussions*, **14**, 7425–7468.

Cuesta, J., Edouart, D., Mimouni, M., Flamant, P.H., Loth, C., Gibert, F., Marnas, F., Bouklila, A., Kharef, M., Ouchne, B., Kadi, M. & Flamant, C. (2008). Multiplatform observations of the seasonal evolution of the Saharan atmospheric boundary layer in Tamanrasset, Algeria, in the framework of the African Monsoon Multidisciplinary Analysis field campaign conducted in 2006. *J. Geophys. Res.*, **113**, D00C07–.

Cuesta, J., Marsham, J.H., Parker, D.J. & Flamant, C. (2009). Dynamical mechanisms controlling the vertical redistribution of dust and the thermodynamic structure

of the West Saharan atmospheric boundary layer during summer. *Atmospheric Science Letters*, **10**, 34–42.

D'Almeida, G.A. (1987). On the Variability of Desert Aerosol Radiative Characteristics. *Journal of Geophysical Research-Atmospheres*, **92**, 3017–3026.

Dayan, U., Hefter, J., Miller, J. & Gutman, G. (1991). Dust Intrusion Events into the Mediterranean Basin. *Journal of Applied Meteorology*, **30**, 1185–1199.

De Longueville, F., Hountondji, Y.C., Henry, S. & Ozer, P. (2010). What do we know about effects of desert dust on air quality and human health in West Africa compared to other regions? *Science of the total environment*, **409**, 1–8.

Dee, D.P., Uppala, S.M., Simmons, A.J., Berrisford, P., Poli, P., Kobayashi, S., Andrae, U., Balmaseda, M.A., Balsamo, G., Bauer, P., Bechtold, P., Beljaars, A.C.M., van de Berg, L., Bidlot, J., Bormann, N., Delsol, C., Dragani, R., Fuentes, M., Geer, A.J., Haimberger, L., Healy, S.B., Hersbach, H., Holm, E.V., Isaksen, L., Kallberg, P., Koehler, M., Matricardi, M., McNally, A.P., Monge-Sanz, B.M., Morcrette, J.J., Park, B.K., Peubey, C., de Rosnay, P., Tavolato, C., Thepaut, J.N. & Vitart, F. (2011). The ERA-Interim reanalysis: configuration and performance of the data assimilation system. *Quarterly Journal of the Royal Meteorological Society*, **137**, 553–597.

DeGaetano, A. (1998). Identification and implications of biases in US surface wind observation, archival, and summarization methods. *Theoretical and Applied Climatology*, **60**, 151–162.

Denman, K.L. & Brasseur, G. (2007). Couplings Between Changes in the Climate System and Biogeochemistry. In S. Solomon, D. Qin, M. Manning, M. Marquis, K. Averyt, M. Tignor, H. Miller & Z. Chen, eds., *Climate Change 2007: The Physical Science Basis*, 499–587, Cambridge Univ Press.

Derbyshire, E. (2007). Natural minerogenic dust and human health. *AMBIO*, **36**, 73–77.

Diner, D., Martonchik, J., Kahn, R., Pinty, B., Gobron, N., Nelson, D. & Holben, B. (2005). Using angular and spectral shape similarity constraints to improve MISR aerosol and surface retrievals over land. *Remote Sensing of Environment*, **94**, 155–171.

Drobinski, P., Flamant, C., Dusek, J., Flamant, P. & Pelon, J. (2001). Observational evidence and modelling of an internal hydraulic jump at the atmospheric boundary-layer top during a Tramontane event. *Boundary-Layer Meteorology*, **98**, 497–515.

Dufresne, J., Gautier, C., Ricchiazzi, P. & Fouquart, Y. (2002). Longwave scattering effects of mineral aerosols. *Journal of the Atmospheric Science*, **59**, 1959–1966.

Dzerdzeevskii, B.L. (1958). On some climatological problems and microclimatological studies of arid and semi-arid lands in the U.S.S.R. In *Climatology and Microclimatology*, vol. 11, 315–325, UNESCO, Paris.

Emmel, C., Knippertz, P. & Schulz, O. (2010). Climatology of convective density currents in the southern foothills of the Atlas Mountains. *Journal of Geophysical Research-Atmospheres*, **115**, emmel, C. Knippertz, P. Schulz, O.

Engelstaedter, S. & Washington, R. (2007a). Atmospheric controls on the annual cycle of North African dust. *Journal of Geophysical Research-Atmospheres*, **112**, 14.

Engelstaedter, S. & Washington, R. (2007b). Temporal controls on global dust emissions: The role of surface gustiness. *Geophysical Research Letters*, **34**.

Engelstaedter, S., Kohfeld, K.E., Tegen, I. & Harrison, S.P. (2003). Controls of dust emissions by vegetation and topographic depressions: An evaluation using dust storm frequency data. *Geophysical Research Letters*, **30**, 4, geophys. Res. Lett. ISI Document Delivery No.: 667FE Times Cited: 27 Cited Reference Count: 15 AMER GEOPHYSICAL UNION WASHINGTON.

Engelstaedter, S., Tegen, I. & Washington, R. (2006). North African dust emissions and transport. *Earth-Science Reviews*, **79**, 73–100.

Evan, A.T. & Mukhopadhyay, S. (2010). African Dust over the Northern Tropical Atlantic: 1955-2008. *Journal of Applied Meteorology and Climatology*, **49**, 2213–2229.

Fecan, F., Marticorena, B. & Bergametti, G. (1999). Parametrization of the increase of the aeolian erosion threshold wind friction velocity due to soil moisture for arid and semi-arid areas. *Annales Geophysicae-Atmospheres Hydrospheres and Space Sciences*, **17**, 149–157.

Fensholt, R., Langanke, T., Rasmussen, K., Reenberg, A., Prince, S.D., Tucker, C., Scholes, R.J., Le, Q.B., Bondeau, A., Eastman, R., Epstein, H., Gaughan, A.E., Hellden, U., Mbow, C., Olsson, L., Paruelo, J., Schweitzer, C., Seaquist, J. & Wessels, K. (2012). Greenness in semi-arid areas across the globe 1981-2007 - an Earth Observing Satellite based analysis of trends and drivers. *Remote Sensing of Environment*, **121**, 144–158.

Fiedler, S., Schepanski, K., Heinold, B., Knippertz, P. & Tegen, I. (2013a). Climatology of nocturnal low-level jets over North Africa and implications for modeling mineral dust emission. *Journal of Geophysical Research - Atmospheres*, **118**, 6100–6121.

Fiedler, S., Schepanski, K., Knippertz, P., Heinold, B. & Tegen, I. (2013b). How important are cyclones for emitting mineral dust aerosol in North Africa? *Atmospheric Chemistry and Physics Discussions*, **13**, 32483–32528.

Flamant, C., Chaboureau, J.P., Parker, D.J., Taylor, C.M., Cammas, J.P., Bock, O., Timouk, F. & Pelon, J. (2007). Airborne observations of the impact of a convective system on the planetary boundary layer thermodynamics and aerosol distribution in the inter-tropical discontinuity region of the West African Monsoon. *Quarterly Journal of the Royal Meteorological Society*, **133**, 1175–1189.

Fletcher, B. (1976a). The erosion of dust by an airflow. *Journal of Physics D: Applied Physics*, **9**, 913.

Fletcher, B. (1976b). The incipient motion of granular materials. *Journal of Physics D: Applied Physics*, **9**, 2471.

Foltz, G.R. & McPhaden, M.J. (2008). Trends in Saharan dust and tropical Atlantic climate during 1980-2006. *Geophysical Research Letters*, **35**.

Fowler, D., Pilegaard, K., Sutton, M.A., Ambus, P., Raivonen, M., Duyzer, J., Simpson, D., Fagerli, H., Fuzzi, S., Schjoerring, J.K., Granier, C., Neftel, A., Isaksen, I.S.A., Laj, P., Maione, M., Monks, P.S., Burkhardt, J., Daemmgen, U., Neirynck, J., Personne, E., Wichink-Kruit, R., Butterbach-Bahl, K., Flechard, C., Tuovinen, J.P., Coyle, M., Gerosa, G., Loubet, B., Altimir, N., Gruenhage, L., Ammann, C., Cieslik, S., Paoletti, E., Mikkelsen, T.N., Ro-Poulsen, H., Cellier, P., Cape, J.N., Horvath, L.,

Loreto, F., Niinemets, U., Palmer, P.I., Rinne, J., Misztal, P., Nemitz, E., Nilsson, D., Pryor, S., Gallagher, M.W., Vesala, T., Skiba, U., Brueggemann, N., Zechmeister-Boltenstern, S., Williams, J., O'Dowd, C., Facchini, M.C., de Leeuw, G., Flossman, A., Chaumerliac, N. & Erisman, J.W. (2009). Atmospheric composition change: Ecosystems-Atmosphere interactions. *Atmospheric Environment*, **43**, 5193–5267.

Franzen, L., Hjelmroos, M., Kallberg, P., Brorstromlunden, E., Juntto, S. & Savolainen, A. (1994). The Yellow Snow Episode of Northern Fennoscadia, March 1991 - A Case Study of Long-Distance Transport of Soil, Pollen and Stable Organic Compounds. *Atmospheric Environment*, **28**, 3587–3604.

Garcia Nieto, P.J., Arganza Garcia, B., Fernandez Diaz, J.M. & Rodriguez, M.A. (1994). Parametric study of selective removal of atmospheric aerosol by below-cloud scavenging. *Atmospheric Environment*, **28**, 2335–2342.

Gillette, D. (1979). *Saharan Dust*, chap. Environmental Factors Affecting Dust Emission by Wind Erosion, 71–91. Wiley and Sons.

Gillette, D., Adams, J., Endo, A., Smith, D., P. H. & Kihl, R. (1980). Threshold velocities for input of soil particles into the air by desert soils. *Journal of Geophysical Research - Oceans and Atmospheres*, **85**, 5621–5630.

Gillette, D., Adams, J., Muhs, D. & Kihl, R. (1982). Threshold Friction Velcoties and Rupture Moduli for Crusted Desert Soil for the Input of Soil Particles into the Air. *Journal of Geophysical Research-Oceans and Atmosphere*, **87**, 9003–9015.

Gillette, D., Niemeyer, T. & Helm, P. (2001). Supply-limited horizontal sand drift at an ephemerally crusted, unvegetated saline playa. *Journal of Geophysical Research-Atmospheres*, **106**, 18085–18098.

Gillette, D.A. (1981). Production of dust that may be carried great distances. *Desert dust: Origin, characteristics, and effect on man*, **186**, 11–26.

Ginoux, P., Prospero, J., Torres, O. & Chin, M. (2004). Long-term simulation of global dust distribution with the GOCART model: correlation with North Atlantic Oscillation. *Environmental Modelling and Software*, **19**, 113–128.

Ginoux, P., Prospero, J.M., Gill, T.E., Hsu, N.C. & Zhao, M. (2012). Global scale attribution of anthropogenic and natural dust sources and their emission rates based on MODIS Deep Blue aerosol products. *Reviews of Geophysics*, **50**.

Goossens, D. (2005). Quantification of the dry aeolian deposition of dust on horizontal surfaces: an experimental comparison of theory and measurements. *Sedimentology*, **52**, 859–873.

Goudie, A. & Middleton, N. (1992). The Changing Frequency of Dust Storms Through Time. *Climatic Change*, **20**, 197–225.

Goudie, A.S. (2014). Desert dust and human health disorders. *Environment International*, **63**, 101 – 113.

Goudie, A.S. & Middleton, N.J. (2001). Saharan dust storms: nature and consequences. *Earth-Science Reviews*, **56**, 179–204.

Greeley, R. & Iversen, J.D. (1985). *Wind as a geological process*. Cambridge University Press.

Griffin, D.W. (2007). Atmospheric movement of microorganisms in clouds of desert dust and implications for human health. *Clinical Microbiology Reviews*, **20**, 459–477.

Griffiths, J. (1972). *Climates of Africa*. Elsevier, Amsterdam [etc.].

Guo, H., Xu, M. & Hu, Q. (2011). Changes in near-surface wind speed in China: 1969-2005. *International Journal Of Climatology*, **31**, 349–358.

Hand, J., Mahowald, N., Chen, Y., Siefert, R., Luo, C., Subramaniam, A. & Fung, I. (2004). Estimates of atmospheric-processed soluble iron from observations and a global mineral aerosol model: Biogeochemical implications. *Journal of Geophysical Research - Atmospheres*, **109**.

Hannachi, A., Awad, A. & Ammar, K. (2011). Climatology and classification of Spring Saharan cyclone tracks. *Climate Dynamics*, **37**, 473–491.

Haywood, J.M., Johnson, B.T., Osborne, S.R., Baran, A.J., Brooks, M., Milton, S.F., Mulcahy, J., Walters, D., Allan, R.P., Klaver, A., Formenti, P., Brindley, H.E., Christopher, S. & Gupta, P. (2011). Motivation, rationale and

key results from the GERBILS Saharan dust measurement campaign. *Quarterly Journal of the Royal Meteorological Society*, **137**, 1106–1116.

Heinold, B., Knippertz, P., Marsham, J.H., Fiedler, S., Dixon, N.S., Schepanski, K., Laurent, B. & Tegen, I. (2013). The role of deep convection and nocturnal low-level jets for dust emission in summertime West Africa: Estimates from convection-permitting simulations. *Journal of Geophysical Research - Atmospheres*, **118**, 4385–4400.

Helgren, D.M. & Prospero, J.M. (1987). Wind Velocities Associated With Dust Deflation Events in the Western Sahara. *Journal of Climate and Applied Meteorology*, **26**, 1147–1151.

Herrmann, S., Anyamba, A. & Tucker, C. (2005). Recent trends in vegetation dynamics in the African Sahel and their relationship to climate. *Global Environmental Change-Human and Policy Dimensions*, **15**, 394–404.

Hess, G. & Spillane, K. (1990). Characteristics of Dust Devils in Australia. *Journal of Applied Meteorology*, **29**, 498–507.

Hobby, M., Gascoyne, M., Marsham, J.H., Bart, M., Allen, C., Engelstaedter, S., Fadel, D.M., Gandega, A., Lane, R., McQuaid, J.B., Ouchene, B., Ouladichir, A., Parker, D.J., Rosenberg, P., Ferroudj, M.S., Saci, A., Seddik, F., Todd, M., Walker, D. & Washington, R. (2013). The Fennec Automatic Weather Station (AWS) Network: Monitoring the Saharan Climate System. *Journal of Atmospheric and Oceanic Technology*, **30**, 709–724.

Holben, B.N., Eck, T.F., Slutsker, I., Tanre, D., Buis, J.P., Setzer, A., Vermote, E., Reagan, J.A., Kaufman, Y.J., Nakajima, T., Lavenu, F., Jankowiak, I. & Smirnov, A. (1998). AERONET - A federated instrument network and data archive for aerosol characterization. *Remote Sensing of Environment*, **66**, 1–16.

Houze, R. (2004). Mesoscale convective systems. *Reviews of Geophysics*, **42**.

Houze, R., Smull, B. & Dodge, P. (1990). Mesoscale Organization of SpriSpring Rainstorms in Oklahoma. *Monthly Weather Review*, **118**, 613–654.

Hsu, N., Tsay, S., King, M. & Herman, J. (2004). Aerosol properties over bright-reflecting source regions. *IEEE Transactions on Geoscience and Remote Sensing*, **42**, 557–569.

Hsu, N.C., Gautam, R., Sayer, A.M., Bettenhausen, C., Li, C., Jeong, M.J., Tsay, S.C. & Holben, B.N. (2012). Global and regional trends of aerosol optical depth over land and ocean using SeaWiFS measurements from 1997 to 2010. *Atmospheric Chemistry and Physics*, **12**, 8037–8053.

Huang, Q., Marsham, J.H., Parker, D.J., Tian, W. & Grams, C.M. (2010). Simulations of the effects of surface heat flux anomalies on stratification, convective growth, and vertical transport within the Saharan boundary layer. *Journal of Geophysical Research-Atmospheres*, **115**.

Huber, S. & Fensholt, R. (2011). Analysis of teleconnections between AVHRR-based sea surface temperature and vegetation productivity in the semi-arid Sahel. *Remote Sensing of Environment*, **115**, 3276–3285.

Huneeus, N., Schulz, M., Balkanski, Y., Griesfeller, J., Prospero, J., Kinne, S., Bauer, S., Boucher, O., Chin, M., Dentener, F., Diehl, T., Easter, R., Fillmore, D., Ghan, S., Ginoux, P., Grini, A., Horowitz, L., Koch, D., Krol, M.C., Landing, W., Liu, X., Mahowald, N., Miller, R., Morcrette, J.J., Myhre, G., Penner, J., Perlwitz, J., Stier, P., Takemura, T. & Zender, C.S. (2011). Global dust model intercomparison in AeroCom phase I. *Atmospheric Chemistry and Physics*, **11**, 7781–7816.

Hurrell, J. (1995). Decadal Trends In the North-Atlantic Oscillation - Regional Temperatures and Precipitation. *Science*, **269**, 676–679.

Iversen, J. & White, B. (1982). Saltation Threshold on Earth, Mars and Venus. *Sedimentology*, **29**, 111–119.

Jickells, T., An, Z., Andersen, K., Baker, A., Bergametti, G., Brooks, N., Cao, J., Boyd, P., Duce, R., Hunter, K., Kawahata, H., Kubilay, N., laRoche, J., Liss, P., Mahowald, N., Prospero, J., Ridgwell, A., Tegen, I. & Torres, R. (2005). Global iron connections between desert dust, ocean biogeochemistry, and climate. *Science*, **308**, 67–71.

Johnson, B.T., Brooks, M.E., Walters, D., Woodward, S., Christopher, S. & Schepanski, K. (2011). Assessment of the Met Office dust forecast model using observations from the GERBILS campaign. *Quarterly Journal of the Royal Meteorological Society*, **137**, 1131–1148.

Jones, P., Jonsson, T. & Wheeler, D. (1997). Extension to the North Atlantic Oscillation using early instrumental pressure observations from Gibraltar and south-west Iceland. *International Journal of Climatology*, **17**, 1433–1450.

Kaimal, J.C. & Businger, J.A. (1970). Case Studies of a Convective Plume and a Dust Devil. *Journal of Applied Meteorology*, **9**, 612–620.

Kalnay, E., Kanamitsu, M., Kistler, R., Collins, W., Deaven, D., Gandin, L., Iredell, M., Saha, S., White, G., Woollen, J., Zhu, Y., Chelliah, M., Ebisuzaki, W., Higgins, W., Janowiak, J., Mo, K., Ropelewski, C., Wang, J., Leetmaa, A., Reynolds, R., Jenne, R. & Joseph, D. (1996). The NCEP/NCAR 40-year reanalysis project. *Bulletin of the American Meteorological Society*, **77**, 437–471.

Karam, D.B., Flamant, C., Cuesta, J., Pelon, J. & Williams, E. (2010). Dust emission and transport associated with a Saharan depression: February 2007 case. *Journal of Geophysical Research-Atmosphere*, **115**.

Karanasiou, A., Moreno, N., Moreno, T., Viana, M., de Leeuw, F. & Querol, X. (2012). Health effects from Sahara dust episodes in Europe: Literature review and research gaps. *Environment International*, **47**, 107 – 114.

Kaufman, Y., Tanre, D., Holben, B., Mattoo, S., Remer, L., Eck, T., Vaughan, J. & Chatenet, B. (2002). Aerosol radiative impact on spectral solar flux at the surface, derived from principal-plane sky measurements. *Journal of the Atmospheric Science*, **59**, 635–646.

Kaufman, Y.J. (2005). Dust transport and deposition observed from the Terra-Moderate Resolution Imaging Spectroradiometer (MODIS) spacecraft over the Atlantic Ocean. *Journal of Geophysical Research*, **110**.

Klose, M., Shao, Y., Karremann, M.K. & Fink, A.H. (2010). Sahel dust zone and synoptic background. *Geophysical Research Letters*, **37**.

Knippertz, P. (2008). Dust emissions in the West African heat trough - the role of the diurnal cycle and of extratropical disturbances. *Meteorologische Zeitschrift*, **17**, 553–563.

Knippertz, P. & Fink, A.H. (2006). Synoptic and dynamic aspects of an extreme springtime Saharan dust outbreak. *Quarterly Journal of the Royal Meteorological Society*, **132**, 1153–1177.

Knippertz, P. & Todd, M.C. (2010). The central west Saharan dust hot spot and its relation to African easterly waves and extratropical disturbances. *Journal of Geophysical Research-Atmospheres*, **115**, 14.

Knippertz, P. & Todd, M.C. (2012). Mineral Dust Aerosols over the Sahara: Meteorological controls on Emission and Transport and Implications for Modeling. *Review of Geophysics*, **50**.

Knippertz, P., Deutscher, C., Kandler, K., Mller, T., Schulz, O. & Schtz, L. (2007). Dust mobilization due to density currents in the Atlas region: Observations from the Saharan Mineral Dust Experiment 2006 field campaign. *Journal of Geophysical Research*, **112**.

Knippertz, P., Ansmann, A., Althausen, D., Muller, D., Tesche, M., Bierwirth, E., Dinter, T., Muller, T., Von Hoyningen-Huene, W., Schepanski, K., Wendisch, M., Heinold, B., Kandler, K., Petzold, A., Schutz, L. & Tegen, I. (2009a). Dust mobilization and transport in the northern Sahara during SAMUM 2006 - a meteorological overview. *Tellus Series B-Chemical and Physical Meteorology*, **61**, 12–31.

Knippertz, P., Trentmann, J. & Seifert, A. (2009b). High-resolution simulations of convective cold pools over the northwestern Sahara. *Journal of Geophysical Research-Atmospheres*, **114**, knippertz, P. Trentmann, J. Seifert, A.

Koch, J. & Renno, N.O. (2005). The role of convective plumes and vortices on the global aerosol budget. *Geophysical Research Letters*, **32**, 5.

Kocha, C., Tulet, P., Lafore, J.P. & Flamant, C. (2013). The importance of the diurnal cycle of Aerosol Optical Depth in West Africa. *Geophys. Res. Lett.*, **40**, 785–790.

Kubilay, N., Nickovic, S., Moulin, C. & Dulac, F. (2000). An illustration of the transport and deposition of mineral dust onto the eastern Mediterranean. *Atmospheric Environment*, **34**, 1293–1303.

Kurosaki, Y. & Mikami, M. (2005). Regional difference in the characteristic of dust event in East Asia: Relationship among dust outbreak, surface wind, and land surface condition. *Journal of the Meteorological Society of Japan*, **83A**, 1–18.

Kurosaki, Y. & Mikami, M. (2007). Threshold wind speed for dust emission in east Asia and its seasonal variations. *Journal of Geophysical Research - Atmospheres*, **112**.

Laurent, B., Marticorena, B., Bergametti, G., Chazette, P., Maignan, F. & Schmechtig, C. (2005). Simulation of the mineral dust emission frequencies from desert areas of China and Mongolia using an aerodynamic roughness length map derived from the POLDER/ADEOS 1 surface products. *Journal of Geophysical Research-Atmosphere*, **110**.

Lawson, T. (1971). Haboob Structure at Khartoum. *Weather*, **26**, 105–112.

Lebel, T., Cappelaere, B., Galle, S., Hanan, N., Kergoat, L., Levis, S., Vieux, B., Descroix, L., Gosset, M., Mougin, E., Peugeot, C. & Seguis, L. (2009). AMMA-CATCH studies in the Sahelian region of West-Africa: An overview. *Journal of Hydrology*, **375**, 3 – 13.

Legrand, M., Ndoum, C. & Jankowiak, I. (1994). Satellite-Derived Climatology of the Saharan Aerosol. In D. Lynch, ed., *Passive Infrared Remote Sensing of Clouds and the Atmosphere II*, vol. 2309, 127–135.

LeHouerou, H. (1980). The Rangelands of the Sahel. *Journal of Range Management*, **33**, 41–46.

Lensky, I.M. & Rosenfeld, D. (2008). Clouds-Aerosols-Precipitation Satellite Analysis Tool (CAPSAT). *Atmospheric Chemistry and Physics*, **8**, 6739–6753.

Li, X., Maring, H., Savoie, D., Voss, K. & Prospero, J. (1996). Dominance of mineral dust in aerosol light-scattering in the North Atlantic trade winds. *Nature*, **380**, 416–419.

Liu, Z., Omar, A., Vaughan, M., Hair, J., Kittaka, C., Hu, Y., Powell, K., Trepte, C., Winker, D., Hostetler, C., Ferrare, R. & Pierce, R. (2008). CALIPSO lidar observations of the optical properties of Saharan dust: A case study of long-range transport. *Journal of Geophysical Research-Atmospheres*, **113**.

Loosmore, G. & Hunt, J. (2000). Dust resuspension without saltation. *Journal of Geophysical Research-Atmosphere*, **105**, 20663–20671.

MacCready Jr, P.B. (1966). Mean wind speed measurements in turbulence. *Journal of Applied Meteorology*, **5**, 219–225.

Maddox, R. (1980). Mesoscale Convective Complexes. *Bulletin of the American Meteorogical Society*, **61**, 1374–1387.

Maher, B.A., Prospero, J.M., Mackie, D., Gaiero, D., Hesse, P.P. & Balkanski, Y. (2010). Global connections between aeolian dust, climate and ocean biogeochemistry at the present day and at the last glacial maximum. *Earth-Science Reviews*, **99**, 61–97.

Mahowald, N., Baker, A., Bergametti, G., Brooks, N., Duce, R., Jickells, T., Kubilay, N., Prospero, J. & Tegen, I. (2005). Atmospheric global dust cycle and iron inputs to the ocean. *Global Biogeochemical Cycles*, **19**.

Mahowald, N., Jickells, T.D., Baker, A.R., Artaxo, P., Benitez-Nelson, C.R., Bergametti, G., Bond, T.C., Chen, Y., Cohen, D.D., Herut, B., Kubilay, N., Losno, R., Luo, C., Maenhaut, W., McGee, K.A., Okin, G.S., Siefert, R.L. & Tsukuda, S. (2008). Global distribution of atmospheric phosphorus sources, concentrations and deposition rates, and anthropogenic impacts. *Global Biogeochemical Cycles*, **22**.

Mahowald, N.M., Ballantine, J.A., Feddema, J. & Ramankutty, N. (2007). Global trends in visibility: implications for dust sources. *Atmospheric Chemistry and Physics*, **7**, 3309–3339.

Marsham, J.H., Parker, D.J., Grams, C.M., Johnson, B.T., Grey, W.M.F. & Ross, A.N. (2008a). Observations of mesoscale and boundary-layer scale circulations affecting dust transport and uplift over the Sahara. *Atmospheric Chemistry and Physics*, **8**, 6979–6993.

Marsham, J.H., Parker, D.J., Grams, C.M., Taylor, C.M. & Haywood, J.M. (2008b). Uplift of Saharan dust south of the intertropical discontinuity. *Journal of Geophysical Research*, **113**.

Marsham, J.H., Knippertz, P., Dixon, N.S., Parker, D.J. & Lister, G.M.S. (2011). The importance of the representation of deep convection for modeled dust-generating winds over West Africa during summer. *Geophysical Research Letters*, **38**, L16803.

Marsham, J.H., Hobby, M., Allen, C.J.T., Banks, J.R., Bart, M., Brooks, B.J., Cavazos-Guerra, C., Engelstaedter, S., Gascoyne, M., Lima, A.R., Martins, J.V., McQuaid, J.B., O'Leary, A., Ouchene, B., Ouladichir, A., Parker, D.J., Saci, A., Salah-Ferroudj, M., Todd, M.C. & Washington, R. (2013). Meteorology and dust in the central Sahara: Observations from Fennec supersite-1 during the June 2011 Intensive Observation Period. *Journal of Geophysical Research - Atmospheres*, **118**, 4069–4089.

Marticorena, B. (2014). *Mineral Dust - A Key Player in the Earth System*, chap. Dust production mechanisms. Springer.

Marticorena, B. & Bergametti, G. (1995). Modeling the Atmosphere Dust Cycle. 1. Design of a Soil-Derived Dust Emission Scheme. *Journal of Geophysical Research-Atmospheres*, **100**, 16415–16430.

Marticorena, B., Chatenet, B., Rajot, J.L., Traore, S., Coulibaly, M., Diallo, A., Kone, I., Maman, A., Diaye, T.N. & Zakou, A. (2010). Temporal variability of mineral dust concentrations over West Africa: analyses of a pluriannual monitoring from the AMMA Sahelian Dust Transect. *Atmospheric Chemistry and Physics*, **10**, 8899–8915.

Mathon, V. & Laurent, H. (2001). Life cycle of Sahelian mesoscale convective cloud systems. *Quarterly Journal of the Royal Meteorological Society*, **127**, 377–406.

Mathon, V., Laurent, H. & Lebel, T. (2002). Mesoscale convective system rainfall in the Sahel. *Journal of Applied Meteorology*, **41**, 1081–1092.

Mattsson, J. & Nihlen, T. (1996). The transport of Saharan dust to southern Europe: A scenario. *Journal of Arid Environments*, **32**, 111–119.

Mbourou, G., Bertrand, J. & Nicholson, S. (1997). The diurnal and seasonal cycles of wind-borne dust over Africa north of the equator. *Journal of Applied Meteorology*, **36**, 868–882.

McConnell, C.L., Highwood, E.J., Coe, H., Formenti, P., Anderson, B., Osborne, S., Nava, S., Desboeufs, K., Chen, G. & Harrison, M.A.J. (2008). Seasonal variations of the physical and optical characteristics of Saharan dust: Results from the Dust Outflow and Deposition to the Ocean (DODO) experiment. *Journal of Geophysical Research-Atmospheres*, **113**.

McTainsh, G. & Pitblado, J. (1987). Dust Storms and Related Phenomena Measured from Meteorological Records in Australia. *Earth Surface Processes and Landforms*, **12**, 415–424.

McVicar, T.R., Van Niel, T.G., Li, L.T., Roderick, M.L., Rayner, D.P., Ricciardulli, L. & Donohue, R.J. (2008). Wind speed climatology and trends for Australia, 1975-2006: Capturing the stilling phenomenon and comparison with near-surface reanalysis output. *Geophys. Res. Lett.*, **35**.

Meigs, P. (1953). World distribution of arid and semi-arid homoclimates. *Reviews of research on arid zone hydrology*, **1**, 203–209.

Menut, L., Perez, C., Haustein, K., Bessagnet, B., Prigent, C. & Alfaro, S. (2013). Impact of surface roughness and soil texture on mineral dust emission fluxes modeling. *Journal of Geophysical Research-Atmospheres*, **118**, 6505–6520.

Middleton, N. (1986a). Dust Storms in the Middle-East. *Journal of Arid Environments*, **10**, 83–96.

Middleton, N.J. (1986b). A Geography of Dust Storms in Southwest Asia. *Journal of Climatology*, **6**, 183–196.

Mills, M., Ridame, C., Davey, M., La Roche, J. & Geider, R. (2004). Iron and phosphorus co-limit nitrogen fixation in the eastern tropical North Atlantic. *Nature*, **429**, 292–294.

Mohr, K. & Thorncroft, C. (2006). Intense convective systems in West Africa and their relationship to the African easterly jet. *Quarterly Journal of the Royal Meteorological Society*, **132**, 163–176.

Morales, C. (1979). *Saharan Dust*, chap. The Use of Meteorological Observations for Studies of the Mobilization, Transport, and Deposition of Saharan Soil Dust, 119–131. Wil.

Moulin, C. & Chiapello, I. (2004). Evidence of the control of summer atmospheric transport of African dust over the Atlantic by Sahel sources from TOMS satellites (1979-2000). *Geophysical Research Letters*, **31**.

Moulin, C., Lambert, C., Dulac, F. & Dayan, U. (1997). Control of atmospheric export of dust from North Africa by the North Atlantic oscillation. *Nature*, **387**, 691–694.

Moulin, C., Lambert, C.E., Dayan, U., Masson, V., Ramonet, M., Bousquet, P., Legrand, M., Balkanski, Y.J., Guelle, W., Marticorena, B., Bergametti, G. & Dulac, F. (1998). Satellite climatology of African dust transport in the Mediterranean atmosphere. *Journal of Geophysical Research-Atmospheres*, **103**, 13137–13144.

Nicholson, S.E. (1981). Rainfall and Atmospheric Circulation During Drought Periods and Wetter Years In West-africa. *Monthly Weather Review*, **109**, 2191–2208.

Nicholson, S.E. (2009). A revised picture of the structure of the "monsoon" and land ITCZ over West Africa. *Climate Dynamics*, **32**, 1155–1171.

O'Hara, S.L., Clarke, M.L. & Elatrash, M.S. (2006). Field measurements of desert dust deposition in Libya. *Atmospheric Environment*, **40**, 3881–3897.

Oke, A.M.C., Tapper, N.J. & Dunkerley, D. (2007). Willy-willies in the Australian landscape: The role of key meteorological variables and surface conditions in defining frequency and spatial characteristics. *Journal of Arid Environments*, **71**, 201–215.

Olsson, L., Eklundh, L. & Ardo, J. (2005). A recent greening of the Sahel - Trends, patterns and potential causes. *Journal of Arid Environments*, **63**, 556–566, workshop on Changes in the Sahel, Nairobi, Kenya, Oct 14-16, 2003.

Osborn, T.J. (2006). Recent variations in the winter North Atlantic Oscillation. *Weather*, **61**, 353–355.

Osborne, S.R., Baran, A.J., Johnson, B.T., Haywood, J.M., Hesse, E. & Newman, S. (2011). Short-wave and long-wave radiative properties of Saharan dust aerosol. *Quarterly Journal of the Royal Meteorological Society*, **137**, 1149–1167.

Parker, D.J., Burton, R.R., Diongue-Niang, A., Ellis, R.J., Felton, M., Taylor, C.M., Thorncroft, C.D., Bessemoulin, P. & Tompkins, A.M. (2005a). The diurnal cycle of the West African monsoon circulation. *Quarterly Journal of the Royal Meteorological Society*, **131**, 2839–2860.

Parker, D.J., Thorncroft, C.D., Burton, R.R. & Diongue-Niang, A. (2005b). Analysis of the African easterly jet, using aircraft observations from the JET2000 experiment. *Quarterly Journal of the Royal Meteorological Society*, **131**, 1461–1482.

Parker, D.J., Fink, A., Janicot, S., Ngamini, J.B., Douglas, M., Afiesimama, E., Agusti-Panareda, A., Beljaars, A., Dide, F., Diedhiou, A., Lebel, T., Polcher, J., Redelsperger, J.L., Thorncroft, C. & Wilson, G.A. (2008). The AMMA Radiosonde Program and its Implications for the Future of Atmospheric Monitoring Over Africa. *Bulletin of the American Meteorological Society*, **89**, 1015–1027.

Prigent, C., Tegen, I., Aires, F., Marticorena, B. & Zribi, M. (2005). Estimation of the aerodynamic roughness length in arid and semi-arid regions over the globe with the ERS scatterometer. *Journal of Geophysical Research - Atmospheres*, **110**.

Prospero, J.M. (2002). Environmental characterization of global sources of atmospheric soil dust identified with the NIMBUS 7 Total Ozone Mapping Spectrometer (TOMS) absorbing aerosol product. *Reviews of Geophysics*, **40**.

Prospero, J.M. & Lamb, P.J. (2003). African droughts and dust transport to the Caribbean: Climate change implications. *Science*, **302**, 1024–1027.

Raupach, M., Gillette, D. & Leys, J. (1993). The Effect of Roughness Elements on Wind Erosion Threshold. *Journal of Geophysical Research-Atmosphere*, **98**, 3023–3029.

Redelsperger, J.L., Thorncroft, C.D., Diedhiou, A., Lebel, T., Parker, D.J. & Polcher, J. (2006). African monsoon multidisciplinary analysis - An international research project and field campaign. *Bulletin of the American Meteorological Society*, **87**, 1739–+.

Riemer, N., Doherty, O.M. & Hameed, S. (2006). On the variability of African dust transport across the Atlantic. *Geophys. Res. Lett.*, **33**.

Roderick, M.L., Rotstayn, L.D., Farquhar, G.D. & Hobbins, M.T. (2007). On the attribution of changing pan evaporation. *Geophysical Research Letters*, **34**.

Roskovensky, J. & Liou, K. (2005). Differentiating airborne dust from cirrus clouds using MODIS data. *Geophysical Research Letters*, **32**.

Rossby, C. (1939). Relation between variations in the intensity of the zonal circulation of the atmosphere and the displacements of the semipermanent centers of action. *Journal of Marin Research*, **2**, 38–55.

Ryder, C.L., Highwood, E.J., Rosenberg, P.D., Trembath, J., Brooke, J.K., Bart, M., Dean, A., Crosier, J., Dorsey, J., Brindley, H., Banks, J., Marsham, J.H., McQuaid, J.B., Sodemann, H. & Washington, R. (2013). Optical properties of Saharan dust aerosol and contribution from the coarse mode as measured during the Fennec 2011 aircraft campaign. *Atmospheric Chemistry and Physics*, **13**, 303–325.

Schepanski, K. (2009). *Characterising Saharan Dust Sources and Export using Remote Sensing and Regional Modelling*. Ph.D. thesis.

Schepanski, K. & Knippertz, P. (2011). Soudano-Saharan depressions and their importance for precipitation and dust: a new perspective on a classical synoptic concept. *Quarterly Journal of the Royal Meteorological Society*, **137**, 1431–1445.

Schepanski, K., Tegen, I., Laurent, B., Heinold, B. & Macke, A. (2007). A new Saharan dust source activation frequency map derived from MSG-SEVIRI IR-channels. *Geophysical Research Letters*, **34**.

Schepanski, K., Tegen, I. & Macke, A. (2009a). Saharan dust transport and deposition towards the tropical northern Atlantic. *Atmospheric Chemistry and Physics*, **9**, 1173–1189.

Schepanski, K., Tegen, I., Todd, M.C., Heinold, B., Bonisch, G., Laurent, B. & Macke, A. (2009b). Meteorological processes forcing Saharan dust emission inferred from MSG-SEVIRI observations of subdaily dust source activation and numerical models. *Journal of Geophysical Research-Atmospheres*, **114**.

Schepanski, K., Tegen, I. & Macke, A. (2012). Comparison of satellite based observations of Saharan dust source areas. *Remote Sensing of Environment*, **123**, 90–97.

Schmetz, J., Pili, P., Tjemkes, S., Just, D., Kerkmann, J., Rota, S. & Ratier, A. (2002). An introduction to Meteosat Second Generation (MSG). *Bulletin of the American Meteorological Society*, **83**.

Schulz, O. & Judex, M. (2008). Impetus Atlas Morocco: Research results 2000-2007. *Department of Geography, University of Bonn, Germany*, **2**.

Segal, M. & Arritt, R. (1992). Nonclassical Mesoscale CCirculation caused by surface sensible heat-flux gradients. *Bulletin of the American Meteorological Society*, **73**, 1593–1604.

Seinfeld, J.H. & Pandis, S.N. (2012). *Atmospheric chemistry and physics: from air pollution to climate change*. John Wiley & Sons.

Shao, Y. (2001). A model for mineral dust emission. *Journal of Geophysical Research-Atmospheres*, **106**, 20239–20254.

Shao, Y. (2009). Physics and Modelling of Wind Erosion. In *Physics and Modelling of Wind Erosion*, vol. 37 of *Atmospheric and Oceanographic Sciences Library*, 1–452, Springer.

Shao, Y. & Lu, H. (2000). A simple expression for wind erosion threshold friction velocity. *Journal of Geophysical Research: Atmospheres*, **105**, 22437–22443.

Shao, Y., Raupach, M. & Findlater, P. (1993). Effect of Saltation Bombardment on the Entrainment of Dust By Wind. *Journal of Geophysical Research-Atmosphere*, **98**, 12719–12726.

Shao, Y., Wyrwoll, K.H., Chappell, A., Huang, J., Lin, Z., McTainsh, G.H., Mikami, M., Tanaka, T.Y., Wang, X. & Yoon, S. (2011). Dust cycle: An emerging core theme in Earth system science. *Aeolian Research*, **2**, 181–204.

Shao, Y., Klose, M. & Wyrwoll, K.H. (2013). Recent global dust trend and connections to climate forcing. *Journal of Geophysical Research: Atmospheres*, **118**, 11–107.

Slinn, S. & Slinn, W. (1980). Predictions for Particle Deposition on Natural-Waters. *Atmopheric Environment*, **14**, 1013–1016.

Smith, K., Corvalan, C. & Kjellstrom, T. (1999). How much global ill health is attributable to environmental factors? *Epidemiology*, **10**, 573–584.

Sokolik, I., Winker, D., Bergametti, G., Gillette, D., Carmichael, G., Kaufman, Y., Gomes, L., Schuetz, L. & Penner, J. (2001). Introduction to special section: Outstanding problems in quantifying the radiative impacts of mineral dust. *Journal of Geophysical Research-Atmosphere*, **106**, 18015–18027.

Solomos, S., Kallos, G., Kushta, J., Astitha, M., Tremback, C., Nenes, A. & Levin, Z. (2011). An integrated modeling study on the effects of mineral dust and sea salt particles on clouds and precipitation. *Atmospheric Chemistry and Physics*, **11**, 873–892.

Speth, P., Christoph, M. & Diekkrger, B. (2010). Impacts of Global Change on the Hydrological Cycle in West and Northwest Africa. In P. Speth, M. Christoph, B. Diekkruger, M. Bollig, A. Fink, H. Goldbach, T. Heckelei, G. Menz, B. Reichert & M. Rossler, eds., *Impacts of Global Change on the Hydrological Cycle in West and Northwest Africa*, 1–675, Springer-Verlag Berlin.

Spyrou, C., Kallos, G., Mitsakou, C., Athanasiadis, P., Kalogeri, C. & Iacono, M.J. (2013). Modeling the radiative effects of desert dust on weather and regional climate. *Atmospheric Chemistry and Physics*, **13**, 5489–5504.

Stensrud, D. (1996). Importance of low-level jets to climate: A review. *JOURNAL OF CLIMATE*, **9**, 1698–1711.

Sterk, G., Herrmann, L. & Bationo, A. (1996). Wind-blown nutrient transport and soil productivity changes in southwest Niger. *Land Degradation & Development*, **7**, 325–335.

Stocker, T., Qin, D., Plattner, G., Tignor, M., Allen, S., Boschung, J., Nauels, A., Xia, Y., Bex, V. & Midgley, P. (2013). Summary for Policymakers. In: Climate Change 2013: The Physical Science Basis. Contribution of Working Group I to the Fifth Assessment Report of the Intergovernmental Panel on Climate Change. Tech. rep.

Sultan, B., Labadi, K., Guégan, J.F. & Janicot, S. (2005). Climate drives the meningitis epidemics onset in West Africa. *PLoS medicine*, **2**, e6.

Sun, J., Zhang, M. & Liu, T. (2001). Spatial and temporal characteristics of dust storms in China and its surrounding regions, 1960-1999: Relations to source area and climate. *Journal of Geophysical Research-Atmospheres*, **106**, 10325–10333.

Sutton, L. (1925). Haboobs. *Quarterly Journal of the Royal Meteorological Society*, **51**, 25–30.

Takemi, T., Yasui, M., Zhou, J. & Liu, L. (2006). Role of boundary layer and cumulus convection on dust emission and transport over a midlatitude desert area. *Journal of Geophysical Research-Atmosphere*, **111**.

Tanré, D. (2010). Derivation of tropospheric aerosol properties from satellite observations. *Comptes Rendus Geoscience*, **342**, 403–411.

Tanré, D., Breon, F.M., Deuze, J.L., Dubovik, O., Ducos, F., Francois, P., Goloub, P., Herman, M., Lifermann, A. & Waquet, F. (2011). Remote sensing of aerosols by using polarized, directional and spectral measurements within the A-Train: the PARASOL mission. *Atmospheric Measurement Techniques*, **4**, 1383–1395.

Tegen, I. & Fung, I. (1994). Modeling of Mineral Dust in the Atmosphere - Sources, Transport and Optical-Thickness. *Journal of Geophysical Research-Atmospheres*, **99**, 22897–22914.

Textor, C., Schulz, M., Guibert, S., Kinne, S., Balkanski, Y., Bauer, S., Berntsen, T., Berglen, T., Boucher, O., Chin, M., Dentener, F., Diehl, T., Easter, R., Feichter, H., Fillmore, D., Ghan, S., Ginoux, P., Gong, S., Kristjansson, J.E., Krol, M., Lauer, A., Lamarque, J.F., Liu, X., Montanaro, V., Myhre, G., Penner, J., Pitari, G., Reddy, S., Seland, O., Stier, P., Takemura, T. & Tie, X. (2006). Analysis and quantification of the diversities of aerosol life cycles within AeroCom. *Atmospheric Chemistry and Physics*, **6**, 1777–1813.

Thorncroft, C. & Blackburn, M. (1999). Maintenance of the African easterly jet. *Quarterly Journal of the Royal Meteorological Society*, **125**, 763–786.

Thorncroft, C.D., Parker, D.J., Burton, R.R., Diop, M., Ayers, J.H., Barjat, H., Devereau, S., Diongue, A., Dumelow, R., Kindred, D.R., Price, N.M.,

Saloum, M., Tayor, C.M. & Tompkins, A.M. (2003). The JET2000 Project: Aircraft Observations of the African Easterly Jet and African Easterly Waves. *Bulletin of the American Meteorological Society*, **84**, 337–351.

Thorncroft, C.D., Hall, N.M.J. & Kiladis, G.N. (2008). Three-Dimensional Structure and Dynamics of African Easterly Waves. Part III: Genesis. *Journal of the Atmospheric Sciences*, **65**, 3596–3607.

Todd, M.C., Washington, R., Martins, J.V., Dubovik, O., Lizcano, G., M'Bainayel, S. & Engelstaedter, S. (2007). Mineral dust emission from the Bodele Depression, northern Chad, during BoDEx 2005. *Journal of Geophysical Research-Atmospheres*, **112**.

Todd, M.C., Allen, C.J.T., Bart, M., Bechir, M., Bentefouet, J., Brooks, B.J., Cavazos-Guerra, C., Clovis, T., Deyane, S., Dieh, M., Engelstaedter, S., Flamant, C., Garcia-Carreras, L., Gandega, A., Gascoyne, M., Hobby, M., Kocha, C., Lavaysse, C., Marsham, J.H., Martins, J.V., McQuaid, J.B., Ngamini, J.B., Parker, D.J., Podvin, T., Rocha-Lima, A., Traore, S., Wang, Y. & Washington, R. (2013). Meteorological and dust aerosol conditions over the western Saharan region observed at Fennec Supersite-2 during the intensive observation period in June 2011. *Journal of Geophysical Research - Atmospheres*, **118**, 8426–8447.

Torres, O., Tanskanen, A., Veihelmann, B., Ahn, C., Braak, R., Bhartia, P.K., Veefkind, P. & Levelt, P. (2007). Aerosols and surface UV products from Ozone Monitoring Instrument observations: An overview. *Journal of Geophysical Research-Atmospheres*, **112**.

Tucker, C., Pinzon, J., Brown, M., Slayback, D., Pak, E., Mahoney, R., Vermote, E. & El Saleous, N. (2005). An extended AVHRR 8-km NDVI dataset compatible with MODIS and SPOT vegetation NDVI data. *International Journal of Remote Sensing*, **26**, 4485–4498.

Twohy, C.H., Kreidenweis, S.M., Eidhammer, T., Browell, E.V., Heymsfield, A.J., Bansemer, A.R., Anderson, B.E., Chen, G., Ismail, S., DeMott, P.J. & Van den Heever, S.C. (2009). Saharan dust particles nucleate droplets in eastern Atlantic clouds. *Geophysical Research Letters*, **36**.

Van de Wiel, B.J.H., Moene, A.F., Steeneveld, G.J., Baas, P., Bosveld, F.C. & Holtslag, A.A.M. (2010). A Conceptual View on Inertial Oscillations and Nocturnal Low-Level Jets. *Journal of the Atmospheric Sciences*, **67**, 2679–2689.

Vautard, R., Cattiaux, J., Yiou, P., Thepaut, J.N. & Ciais, P. (2010). Northern Hemisphere atmospheric stilling partly attributed to an increase in surface roughness. *Nature Geoscience*, **3**, 756–761.

Wandinger, U., Tesche, M., Seifert, P., Ansmann, A., Mller, D. & Althausen, D. (2010). Size matters: Influence of multiple scattering on CALIPSO light-extinction profiling in desert dust. *Geophysical Research Letters*, **37**, n/a–n/a.

Warner, T.T. (2004). *Desert meteorology.*. Cambridge University Press.

Washington, R. & Todd, M.C. (2005). Atmospheric controls on mineral dust emission from the Bodl Depression, Chad: The role of the low level jet. *Geophys. Res. Lett.*, **32**, L17701–.

Washington, R., Todd, M., Middleton, N.J. & Goudie, A.S. (2003). Dust-storm source areas determined by the total ozone monitoring spectrometer and surface observations. *Annals of the Association of American Geographers*, **93**, 297–313.

Washington, R., Todd, M.C., Engelstaedter, S., Mbainayel, S. & Mitchell, F. (2006). Dust and the low-level circulation over the Bodele Depression, Chad: Observations from BoDEx 2005. *Journal of Geophysical Research-Atmospheres*, **111**.

Washington, R., Bouet, C., Cautenet, G., Mackenzie, E., Ashpole, I., Engelstaedter, S., Lizcano, G., Henderson, G.M., Schepanski, K. & Tegen, I. (2009). Dust as a tipping element: The Bodele Depression, Chad. *Proceedings of the National Academy of Sciences of the United States of America*, **106**, 20564–20571.

Washington, R., Flamant, C., Parker, D., Marsham, J., McQuaid, J., Brindley, H., Todd, M., Highwood, E., Chaboureau, J., Kocha, C. *et al.* (2012). Fennec-The Saharan Climate System. *CLIVAR Exchanges*, **17**, 31–32.

Weinzierl, B., Sauer, D., Esselborn, M., Petzold, A., Veira, A., Rose, M., Mund, S., Wirth, M., Ansmann, A., Tesche, M., Gross, S. & Freudenthaler, V. (2011). Microphysical and optical properties of dust and tropical biomass burning

aerosol layers in the Cape Verde region-an overview of the airborne in situ and lidar measurements during SAMUM-2. *Tellus Series B - Chemical and Physical Meteorology*, **63**, 589–618.

Wheeler, D. (1986). The Meteorological Background to the Fall of Saharan Dust, November 1984. *Meteorological Magazine*, **115**, 1–9.

White, B. (1979). Soil Transport By Winds on Mars. *Journal of Geophysical Research*, **84**, 4643–4651.

Williams, E., Nathou, N., Hicks, E., Pontikis, C., Russell, B., Miller, M. & Bartholomew, M.J. (2009). The electrification of dust-lofting gust fronts (haboobs) in the Sahel. *Atmospheric Research*, **91**, 292–298.

WMO (1974). *Manual on Codes*, vol. 1, chap. International Codes. WMO-306. WMO.

WMO (1975). *International Cloud Atlas*, vol. 1, chap. Manual on the Observations of Clouds and Other Meteors, 119–121. WMO.

WMO (1995). International Codes-WMO No. 306. *Geneva-Switzerland: World Meteorological Organization*.

WMO (1996). *Guide to meterological instruments and methods of observation*. Secretariat of the World Meteorological Organization.

WMO (2008). *Guide to Meteorological Instruments and Methods of Observation*, chap. 5: Measurement of Surface Wind. Secretariat of the World Meteorological Organization.

Zender, C. & Kwon, E. (2005). Regional contrasts in dust emission responses to climate. *Journal of Geophysical Research-Atmospheres*, **110**.

Zender, C., Bian, H. & Newman, D. (2003). Mineral Dust Entrainment and Deposition (DEAD) model: Description and 1990s dust climatology. *Journal of Geophysical Research-Atmospheres*, **108**.

Zhang, L., Gong, S., Padro, J. & Barrie, L. (2001). A size-segregated particle dry deposition scheme for an atmospheric aerosol module. *Atmospheric Environment*, **35**, 549–560.

Zhao, T., Gong, S., Zhang, X. & McKendry, I. (2003). Modeled size-segregated wet and dry deposition budgets of soil dust aerosol during ACE-Asia 2001: Implications for trans-Pacific transport. *Journal of Geophysical Research-Atmosphere*, **108**.

Zhu, L. & Southworth, J. (2013). Disentangling the Relationships between Net Primary Production and Precipitation in Southern Africa Savannas Using Satellite Observations from 1982 to 2010. *Remote Sensing*, **5**, 3803–3825.

Appendix A

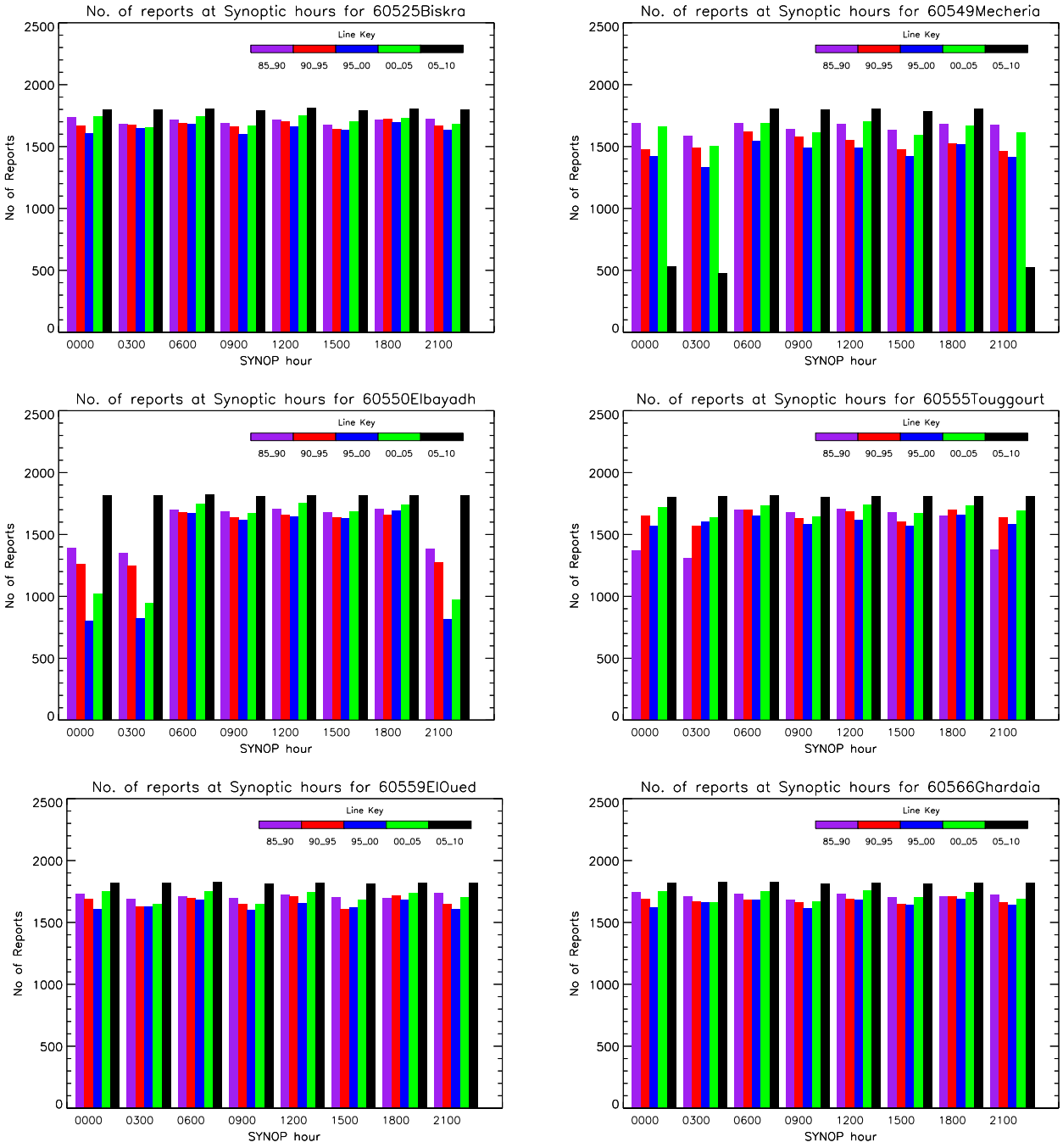

FIGURE 1: Bar plots of the number of observations at each SYNOP hour, for the periods 1985-1990 (purple), 1990-1995 (red), 1995-2000(blue), 2000-2005 (green) and 2005-2010 (black) for each of the 70 stations

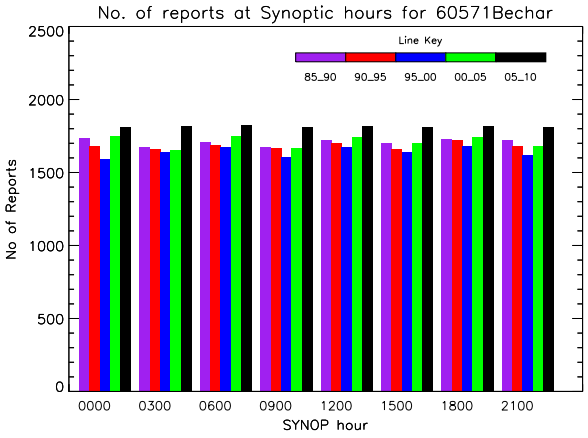
No. of reports at Synoptic hours for 60571Bechar
Line Key
85_90 90_95 95_00 00_05 05_10
No of Reports
SYNOP hour
0000 0300 0600 0900 1200 1500 1800 2100
0 500 1000 1500 2000 2500

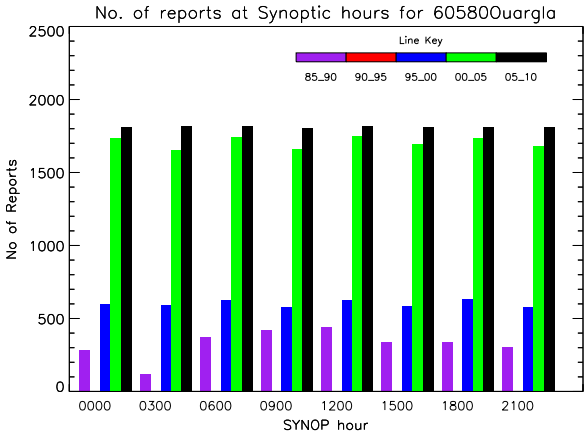
No. of reports at Synoptic hours for 60580Ouargla
Line Key
85_90 90_95 95_00 00_05 05_10
No of Reports
SYNOP hour
0000 0300 0600 0900 1200 1500 1800 2100
0 500 1000 1500 2000 2500

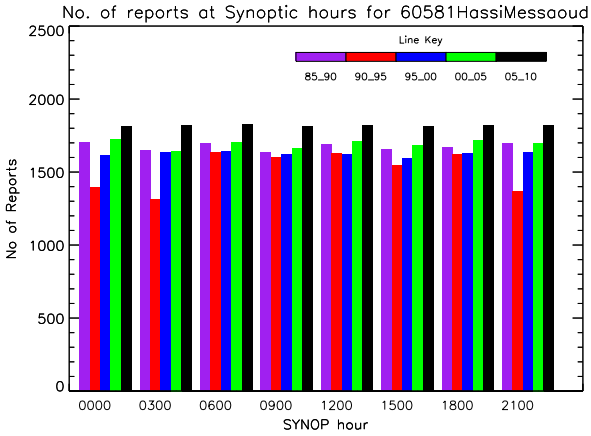
No. of reports at Synoptic hours for 60581HassiMessaoud
Line Key
85_90 90_95 95_00 00_05 05_10
No of Reports
SYNOP hour
0000 0300 0600 0900 1200 1500 1800 2100
0 500 1000 1500 2000 2500

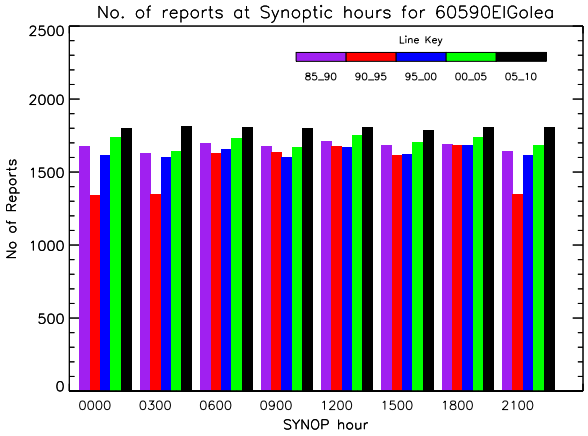
No. of reports at Synoptic hours for 60590ElGolea
Line Key
85_90 90_95 95_00 00_05 05_10
No of Reports
SYNOP hour
0000 0300 0600 0900 1200 1500 1800 2100
0 500 1000 1500 2000 2500

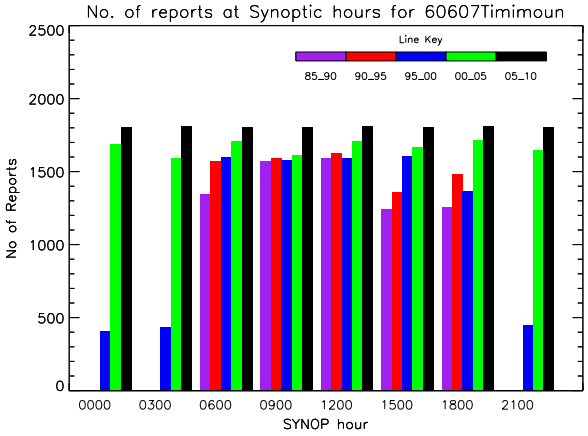
No. of reports at Synoptic hours for 60607Timimoun
Line Key
85_90 90_95 95_00 00_05 05_10
No of Reports
SYNOP hour
0000 0300 0600 0900 1200 1500 1800 2100
0 500 1000 1500 2000 2500

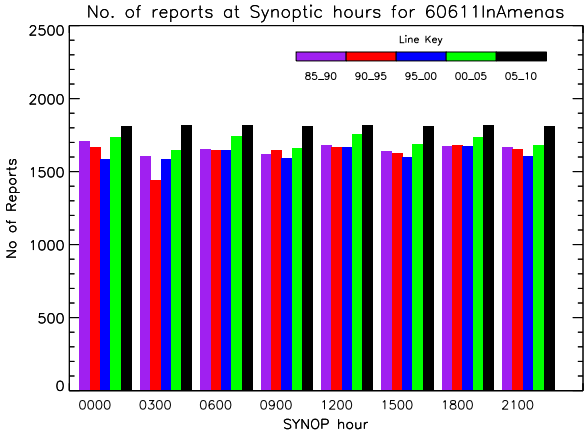
No. of reports at Synoptic hours for 60611InAmenas
Line Key
85_90 90_95 95_00 00_05 05_10
No of Reports
SYNOP hour
0000 0300 0600 0900 1200 1500 1800 2100
0 500 1000 1500 2000 2500

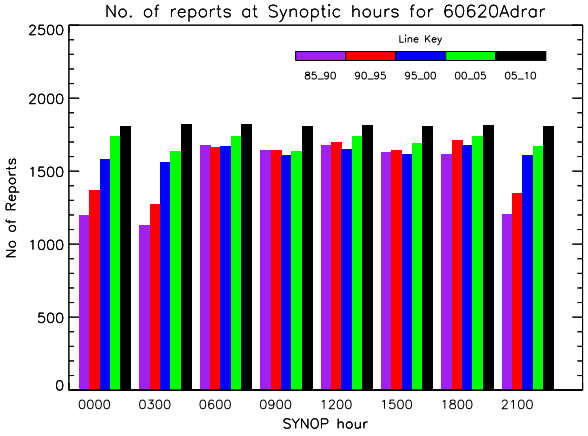
No. of reports at Synoptic hours for 60620Adrar
Line Key
85_90 90_95 95_00 00_05 05_10
No of Reports
SYNOP hour
0000 0300 0600 0900 1200 1500 1800 2100
0 500 1000 1500 2000 2500

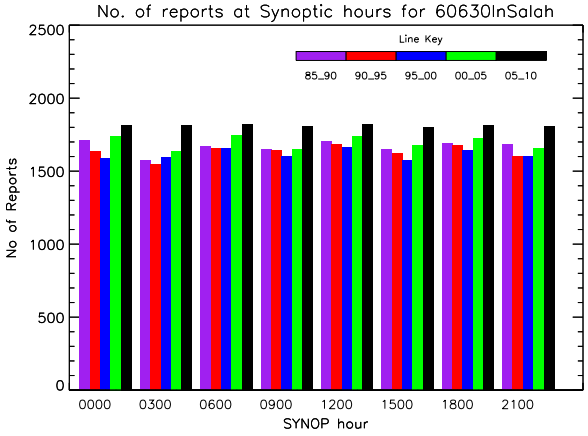
No. of reports at Synoptic hours for 60630InSalah
Line Key
85_90 90_95 95_00 00_05 05_10
No of Reports
SYNOP hour
0000 0300 0600 0900 1200 1500 1800 2100
0 500 1000 1500 2000 2500

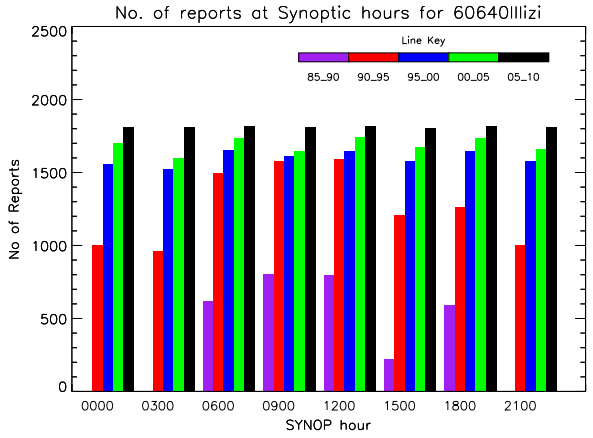
No. of reports at Synoptic hours for 60640Illizi
Line Key
85_90 90_95 95_00 00_05 05_10
No of Reports
SYNOP hour
0000 0300 0600 0900 1200 1500 1800 2100
0 500 1000 1500 2000 2500

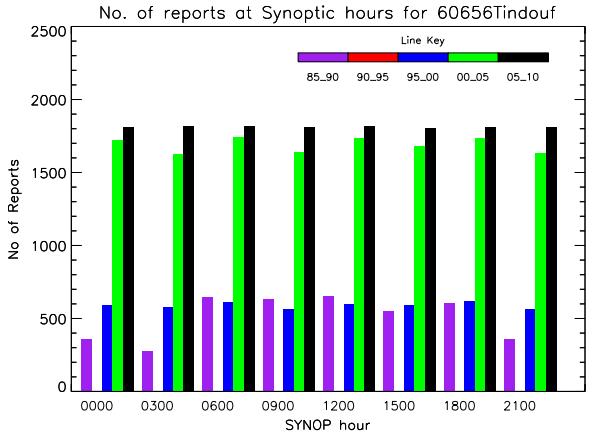
No. of reports at Synoptic hours for 60656Tindouf
Line Key
85_90 90_95 95_00 00_05 05_10
No of Reports
SYNOP hour
0000 0300 0600 0900 1200 1500 1800 2100
0 500 1000 1500 2000 2500

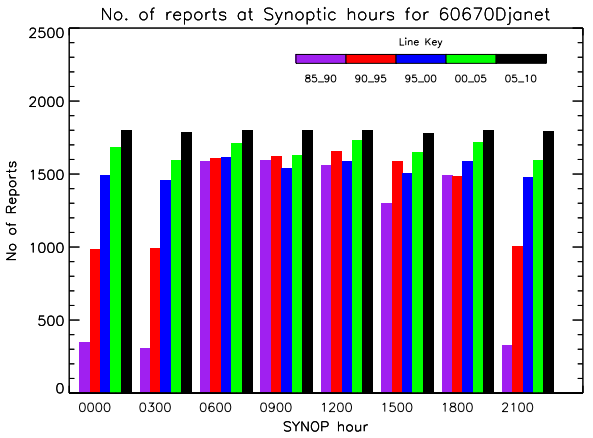
No. of reports at Synoptic hours for 60670Djanet
Line Key
85_90 90_95 95_00 00_05 05_10
No of Reports
SYNOP hour
0000 0300 0600 0900 1200 1500 1800 2100
0 500 1000 1500 2000 2500

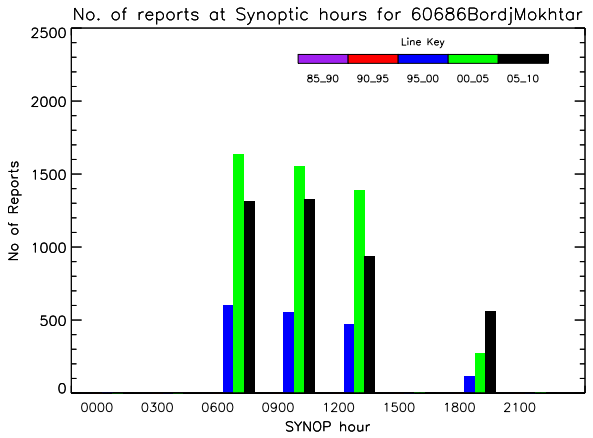
No. of reports at Synoptic hours for 60686BordjMokhtar
Line Key
85_90 90_95 95_00 00_05 05_10
No of Reports
SYNOP hour
0000 0300 0600 0900 1200 1500 1800 2100
0 500 1000 1500 2000 2500

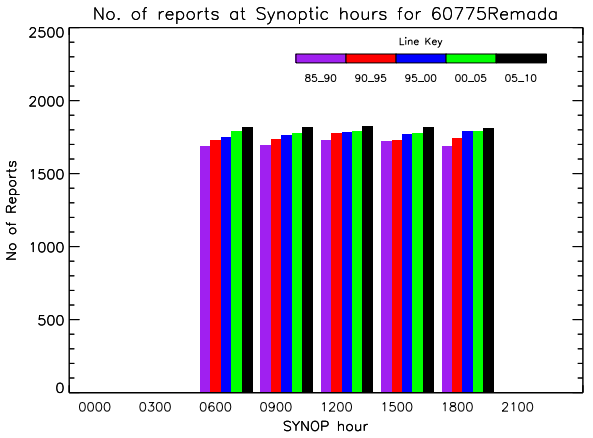
No. of reports at Synoptic hours for 60775Remada
Line Key
85_90 90_95 95_00 00_05 05_10
No of Reports
SYNOP hour
0000 0300 0600 0900 1200 1500 1800 2100
0 500 1000 1500 2000 2500

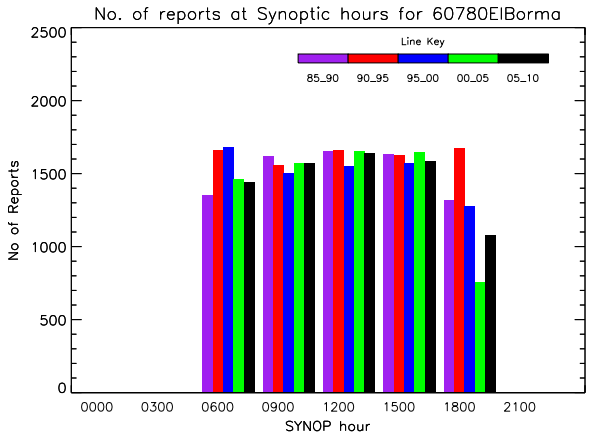
No. of reports at Synoptic hours for 60780ElBorma
Line Key
85_90 90_95 95_00 00_05 05_10
No of Reports
SYNOP hour
0000 0300 0600 0900 1200 1500 1800 2100
0 500 1000 1500 2000 2500

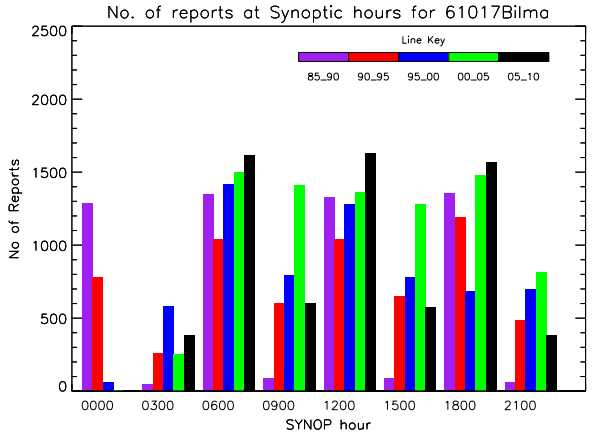
No. of reports at Synoptic hours for 61017Bilma
Line Key
85_90 90_95 95_00 00_05 05_10
No of Reports
SYNOP hour
0000 0300 0600 0900 1200 1500 1800 2100
0 500 1000 1500 2000 2500

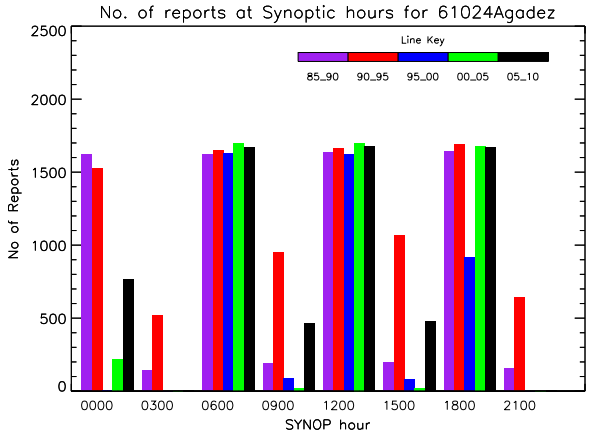
No. of reports at Synoptic hours for 61024Agadez
Line Key
85_90 90_95 95_00 00_05 05_10
No of Reports
SYNOP hour
0000 0300 0600 0900 1200 1500 1800 2100
0 500 1000 1500 2000 2500

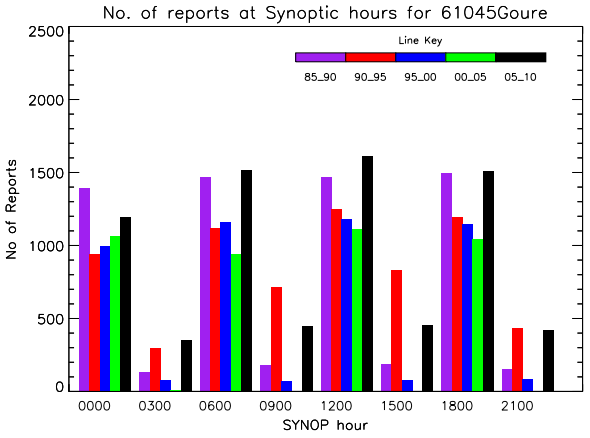
No. of reports at Synoptic hours for 61045Goure
Line Key
85_90 90_95 95_00 00_05 05_10
No of Reports
SYNOP hour
0000 0300 0600 0900 1200 1500 1800 2100
0 500 1000 1500 2000 2500

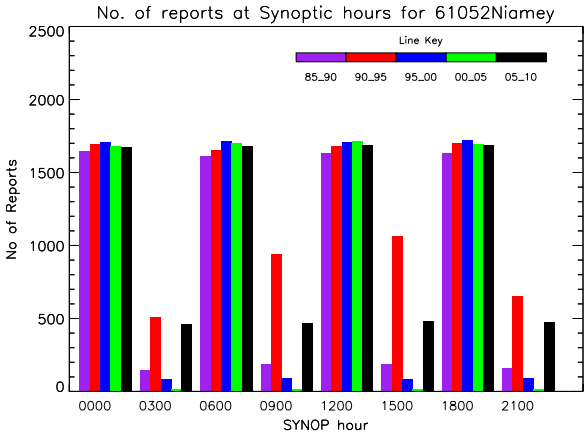
No. of reports at Synoptic hours for 61052Niamey
Line Key
85_90 90_95 95_00 00_05 05_10
No of Reports
SYNOP hour
0000 0300 0600 0900 1200 1500 1800 2100
0 500 1000 1500 2000 2500

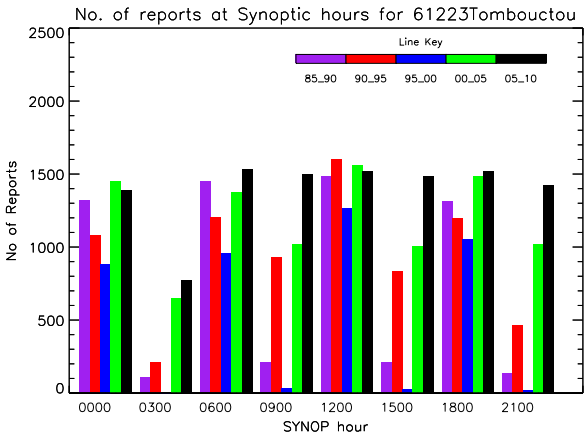
No. of reports at Synoptic hours for 61223Tombouctou
Line Key
85_90 90_95 95_00 00_05 05_10
No of Reports
SYNOP hour
0000 0300 0600 0900 1200 1500 1800 2100
0 500 1000 1500 2000 2500

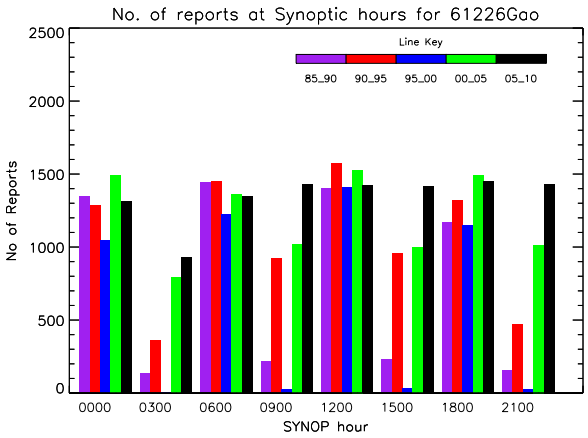
No. of reports at Synoptic hours for 61226Gao
Line Key
85_90 90_95 95_00 00_05 05_10
No of Reports
SYNOP hour
0000 0300 0600 0900 1200 1500 1800 2100
0 500 1000 1500 2000 2500

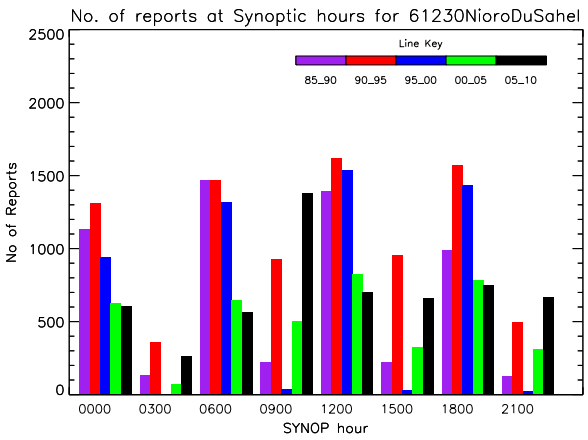
No. of reports at Synoptic hours for 61230NioroDuSahel
Line Key
85_90 90_95 95_00 00_05 05_10
No of Reports
SYNOP hour
0000 0300 0600 0900 1200 1500 1800 2100
0 500 1000 1500 2000 2500

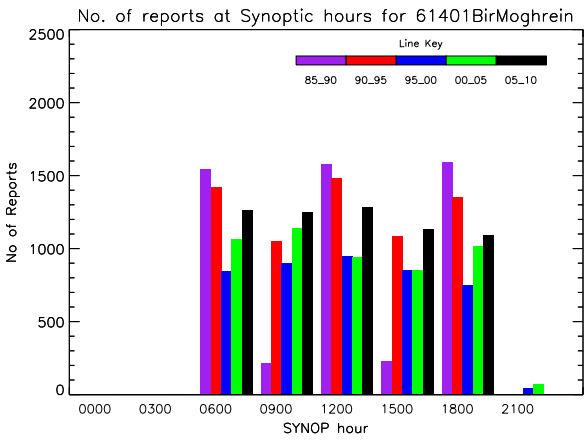
No. of reports at Synoptic hours for 61401BirMoghrein
Line Key
85_90 90_95 95_00 00_05 05_10
No of Reports
SYNOP hour
0000 0300 0600 0900 1200 1500 1800 2100
0 500 1000 1500 2000 2500

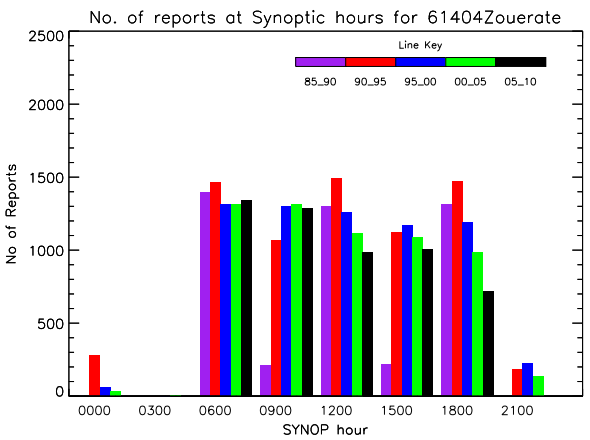
No. of reports at Synoptic hours for 61404Zouerate
Line Key
85_90 90_95 95_00 00_05 05_10
No of Reports
SYNOP hour
0000 0300 0600 0900 1200 1500 1800 2100
0 500 1000 1500 2000 2500

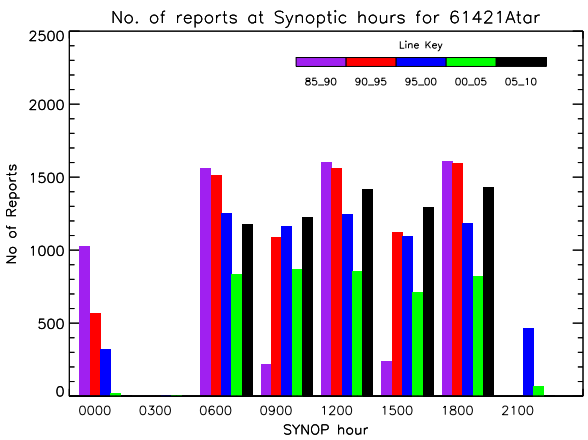
No. of reports at Synoptic hours for 61421Atar
Line Key
85_90 90_95 95_00 00_05 05_10
No of Reports
SYNOP hour
0000 0300 0600 0900 1200 1500 1800 2100
0 500 1000 1500 2000 2500

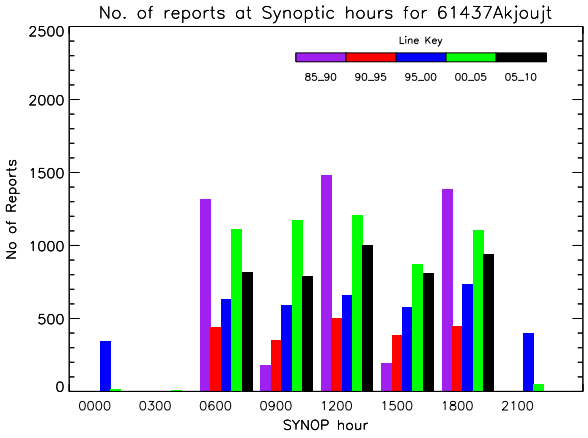
No. of reports at Synoptic hours for 61437Akjoujt
Line Key
85_90 90_95 95_00 00_05 05_10
No of Reports
SYNOP hour
0000 0300 0600 0900 1200 1500 1800 2100
0 500 1000 1500 2000 2500

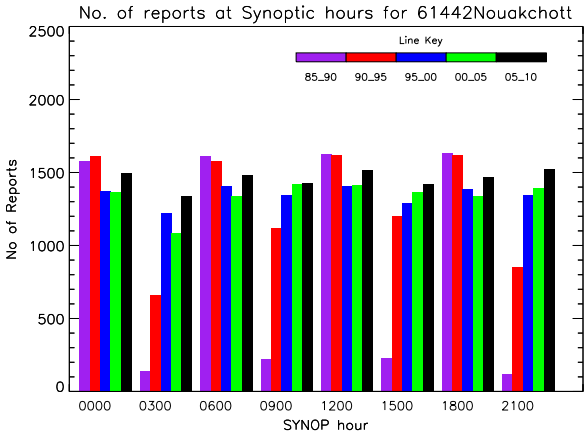
No. of reports at Synoptic hours for 61442Nouakchott
Line Key
85_90 90_95 95_00 00_05 05_10
No of Reports
SYNOP hour
0000 0300 0600 0900 1200 1500 1800 2100
0 500 1000 1500 2000 2500

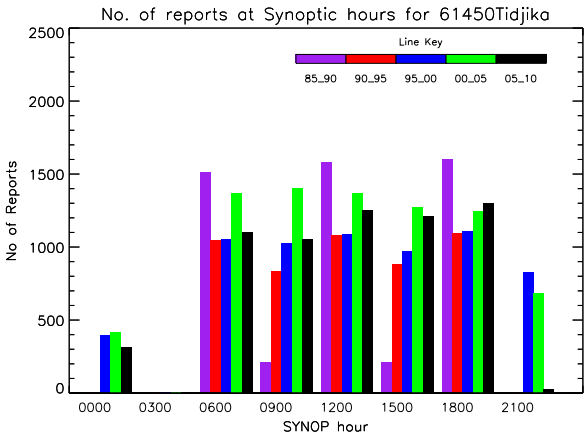
No. of reports at Synoptic hours for 61450Tidjika
Line Key
85_90 90_95 95_00 00_05 05_10
No of Reports
SYNOP hour
0000 0300 0600 0900 1200 1500 1800 2100
0 500 1000 1500 2000 2500

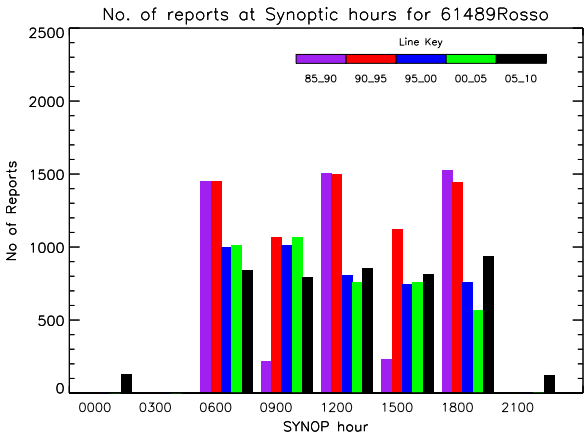
No. of reports at Synoptic hours for 61489Rosso
Line Key
85_90 90_95 95_00 00_05 05_10
No of Reports
SYNOP hour
0000 0300 0600 0900 1200 1500 1800 2100
0 500 1000 1500 2000 2500

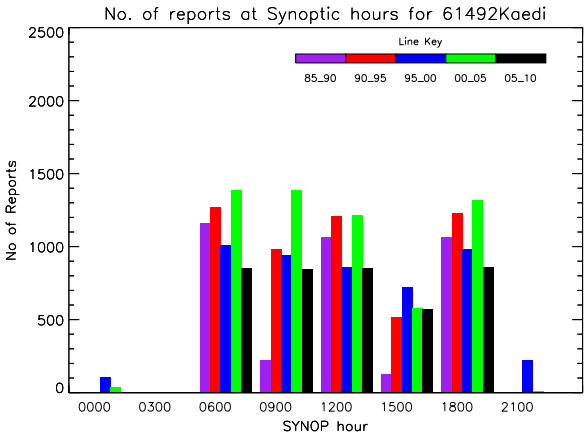
No. of reports at Synoptic hours for 61492Kaedi
Line Key
85_90 90_95 95_00 00_05 05_10
No of Reports
SYNOP hour
0000 0300 0600 0900 1200 1500 1800 2100
0 500 1000 1500 2000 2500

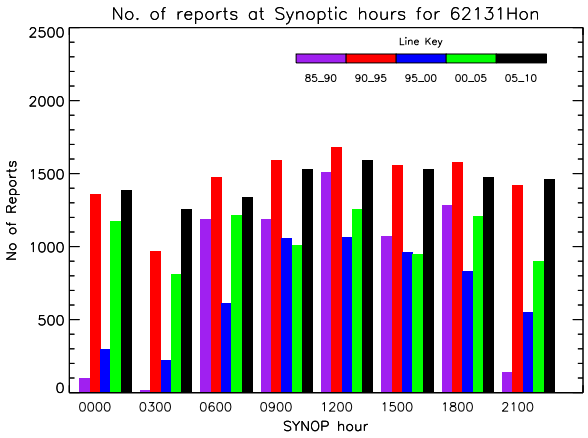
No. of reports at Synoptic hours for 62131Hon
Line Key
85_90 90_95 95_00 00_05 05_10
No of Reports
SYNOP hour
0000 0300 0600 0900 1200 1500 1800 2100
0 500 1000 1500 2000 2500

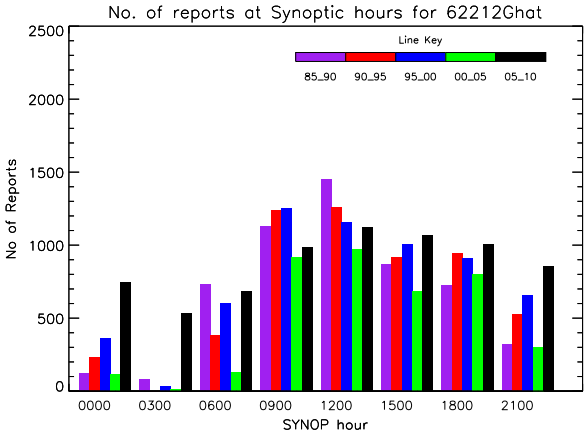
No. of reports at Synoptic hours for 62212Ghat
Line Key
85_90 90_95 95_00 00_05 05_10
No of Reports
SYNOP hour
0000 0300 0600 0900 1200 1500 1800 2100
0 500 1000 1500 2000 2500

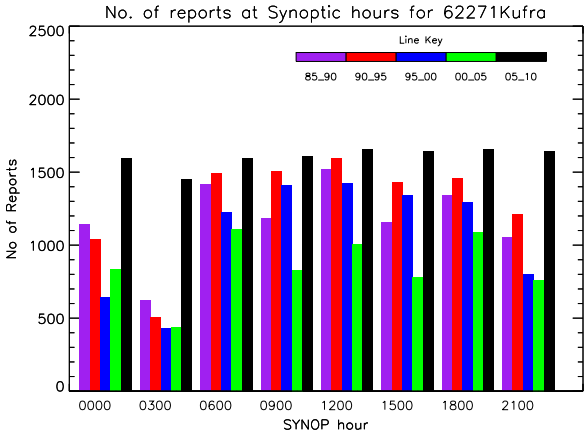
No. of reports at Synoptic hours for 62271Kufra
Line Key
85_90 90_95 95_00 00_05 05_10
No of Reports
SYNOP hour
0000 0300 0600 0900 1200 1500 1800 2100
0 500 1000 1500 2000 2500

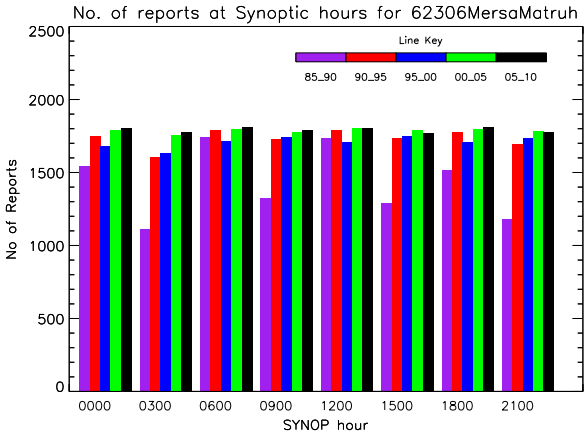
No. of reports at Synoptic hours for 62306MersaMatruh
Line Key
85_90 90_95 95_00 00_05 05_10
No of Reports
SYNOP hour
0000 0300 0600 0900 1200 1500 1800 2100
0 500 1000 1500 2000 2500

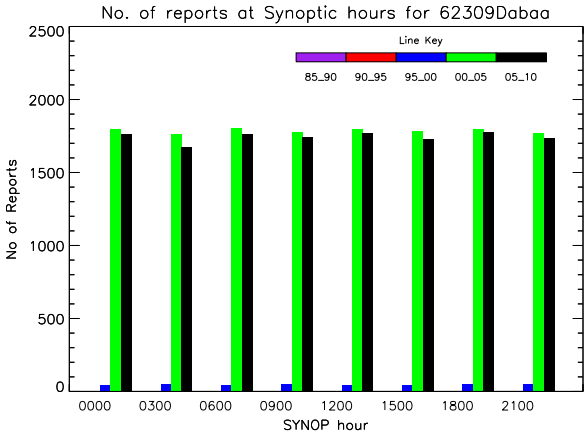
No. of reports at Synoptic hours for 62309Dabaa
Line Key
85_90 90_95 95_00 00_05 05_10
No of Reports
SYNOP hour
0000 0300 0600 0900 1200 1500 1800 2100
0 500 1000 1500 2000 2500

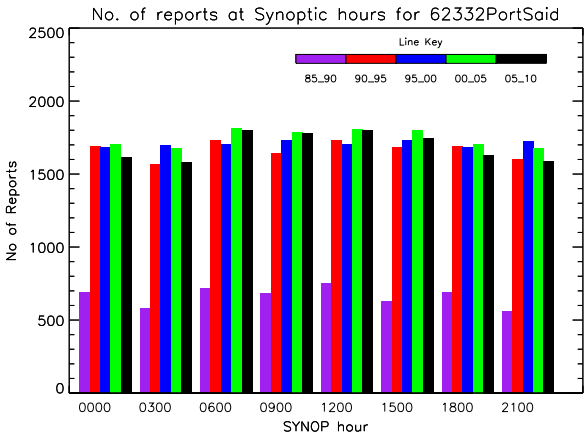
No. of reports at Synoptic hours for 62332PortSaid
Line Key
85_90 90_95 95_00 00_05 05_10
No of Reports
SYNOP hour
0000 0300 0600 0900 1200 1500 1800 2100
0 500 1000 1500 2000 2500

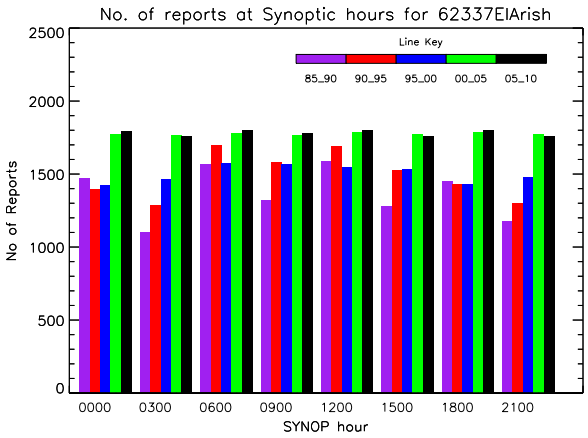
No. of reports at Synoptic hours for 62337ElArish
Line Key
85_90 90_95 95_00 00_05 05_10
No of Reports
SYNOP hour
0000 0300 0600 0900 1200 1500 1800 2100
0 500 1000 1500 2000 2500

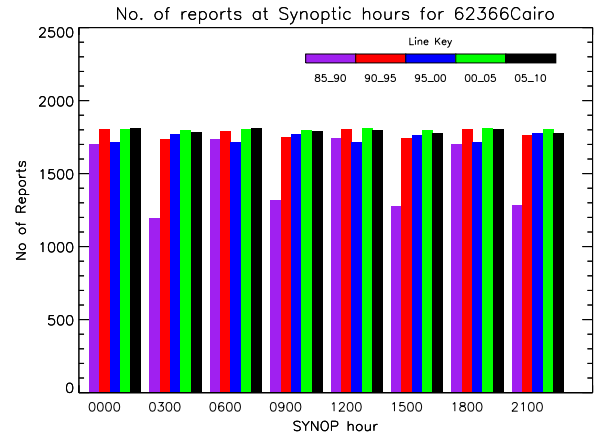
No. of reports at Synoptic hours for 62366Cairo
Line Key
85_90 90_95 95_00 00_05 05_10
No of Reports
SYNOP hour
0000 0300 0600 0900 1200 1500 1800 2100
0 500 1000 1500 2000 2500

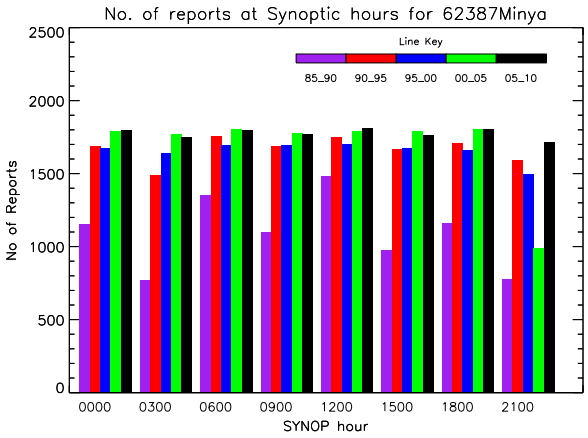
No. of reports at Synoptic hours for 62387Minya
Line Key
85_90 90_95 95_00 00_05 05_10
No of Reports
SYNOP hour
0000 0300 0600 0900 1200 1500 1800 2100
0 500 1000 1500 2000 2500

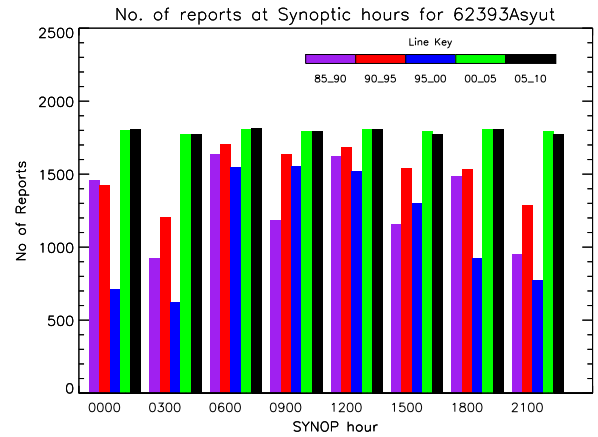
No. of reports at Synoptic hours for 62393Asyut
Line Key
85_90 90_95 95_00 00_05 05_10
No of Reports
SYNOP hour
0000 0300 0600 0900 1200 1500 1800 2100
0 500 1000 1500 2000 2500

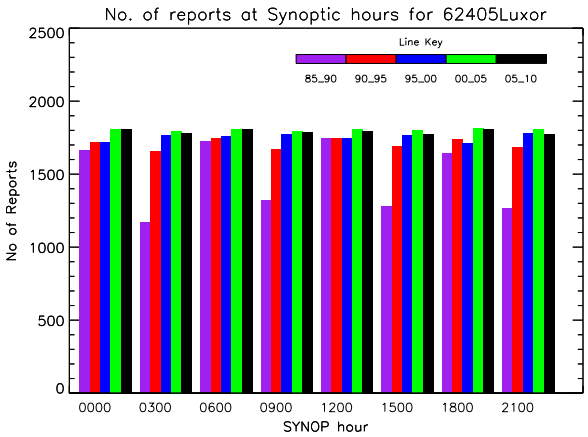
No. of reports at Synoptic hours for 62405Luxor
Line Key
85_90 90_95 95_00 00_05 05_10
No of Reports
SYNOP hour
0000 0300 0600 0900 1200 1500 1800 2100
0 500 1000 1500 2000 2500

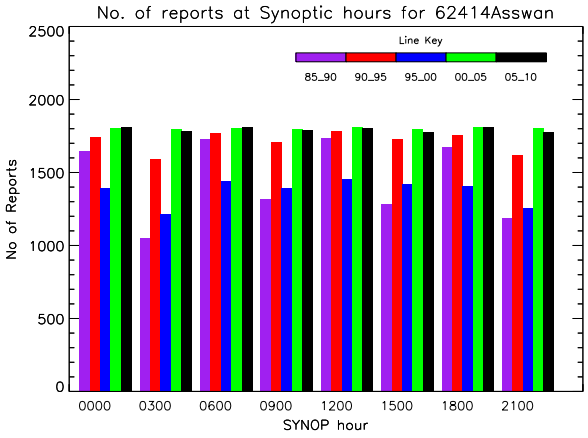
No. of reports at Synoptic hours for 62414Asswan
Line Key
85_90 90_95 95_00 00_05 05_10
No of Reports
SYNOP hour
0000 0300 0600 0900 1200 1500 1800 2100
0 500 1000 1500 2000 2500

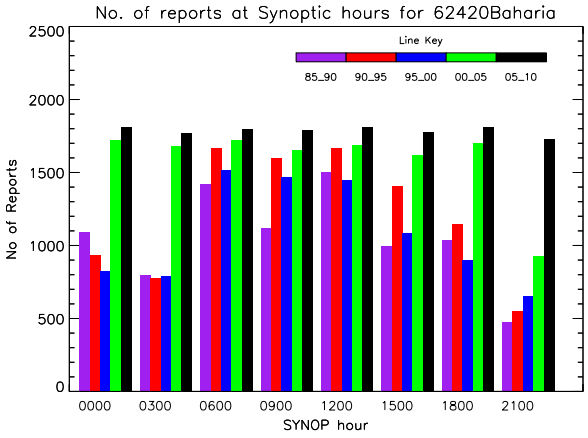
No. of reports at Synoptic hours for 62420Baharia
Line Key
85_90 90_95 95_00 00_05 05_10
No of Reports
SYNOP hour
0000 0300 0600 0900 1200 1500 1800 2100
0 500 1000 1500 2000 2500

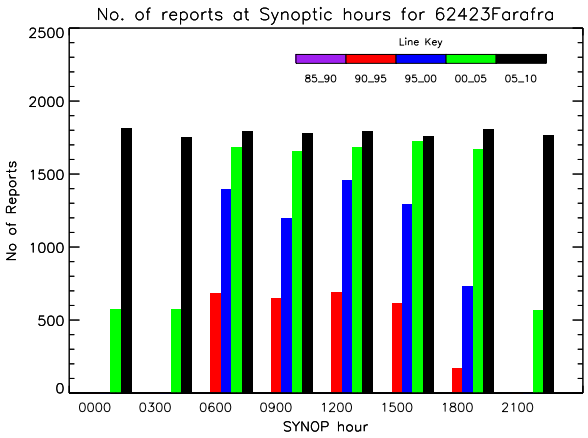
No. of reports at Synoptic hours for 62423Farafra
Line Key
85_90 90_95 95_00 00_05 05_10
No of Reports
SYNOP hour
0000 0300 0600 0900 1200 1500 1800 2100
0 500 1000 1500 2000 2500

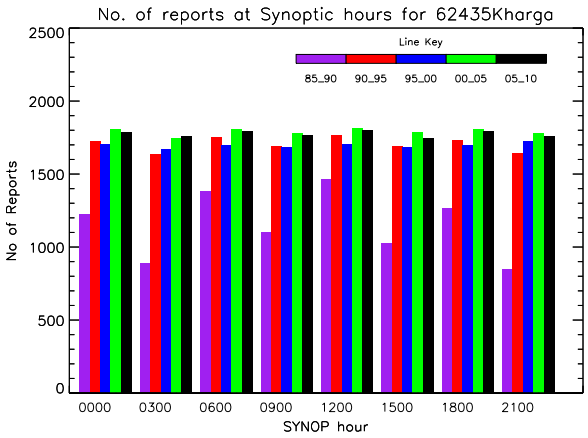
No. of reports at Synoptic hours for 62435Kharga
Line Key
85_90 90_95 95_00 00_05 05_10
No of Reports
SYNOP hour
0000 0300 0600 0900 1200 1500 1800 2100
0 500 1000 1500 2000 2500

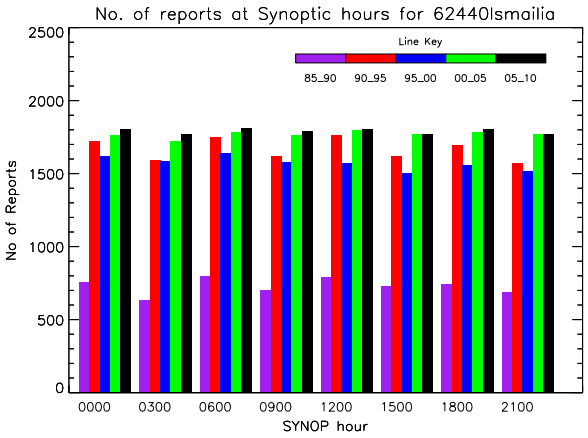
No. of reports at Synoptic hours for 62440Ismailia
Line Key
85_90 90_95 95_00 00_05 05_10
No of Reports
SYNOP hour
0000 0300 0600 0900 1200 1500 1800 2100
0 500 1000 1500 2000 2500

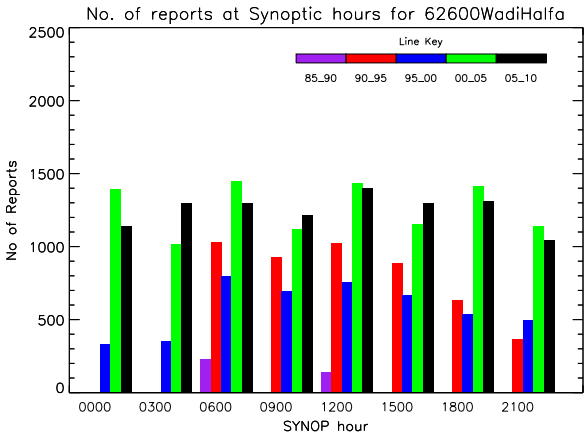
No. of reports at Synoptic hours for 62600WadiHalfa
Line Key
85_90 90_95 95_00 00_05 05_10
No of Reports
SYNOP hour
0000 0300 0600 0900 1200 1500 1800 2100
0 500 1000 1500 2000 2500

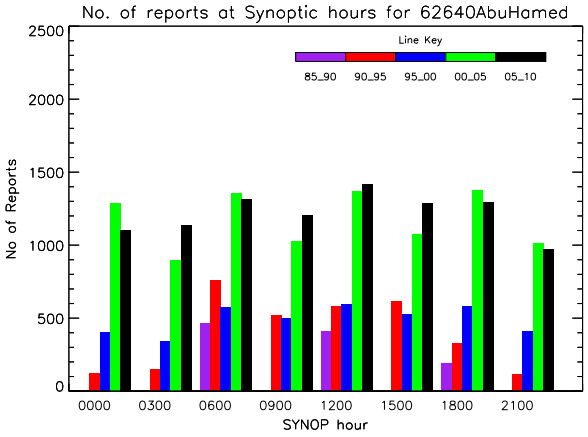
No. of reports at Synoptic hours for 62640AbuHamed
Line Key
85_90 90_95 95_00 00_05 05_10
No of Reports
SYNOP hour
0000 0300 0600 0900 1200 1500 1800 2100
0 500 1000 1500 2000 2500

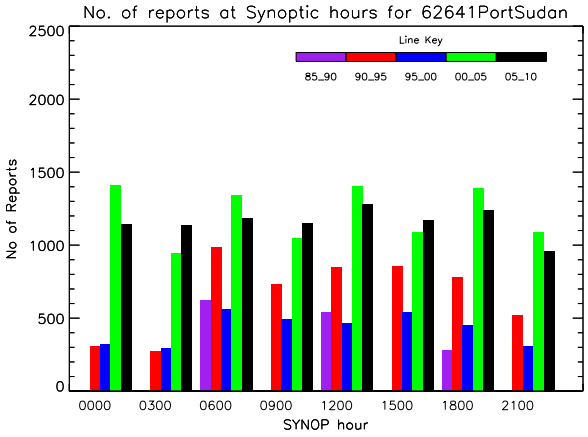
No. of reports at Synoptic hours for 62641PortSudan
Line Key
85_90 90_95 95_00 00_05 05_10
No of Reports
SYNOP hour
0000 0300 0600 0900 1200 1500 1800 2100
0 500 1000 1500 2000 2500

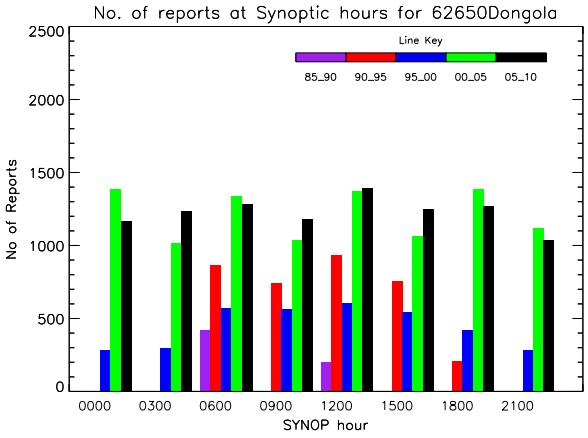
No. of reports at Synoptic hours for 62650Dongola
Line Key
85_90 90_95 95_00 00_05 05_10
No of Reports
SYNOP hour
0000 0300 0600 0900 1200 1500 1800 2100
0 500 1000 1500 2000 2500

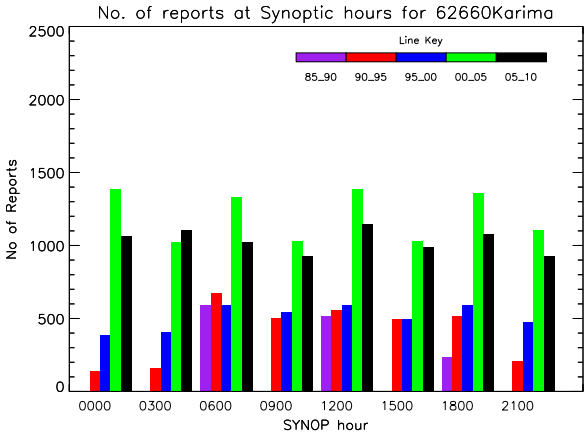
No. of reports at Synoptic hours for 62660Karima
Line Key
85_90 90_95 95_00 00_05 05_10
No of Reports
SYNOP hour
0000 0300 0600 0900 1200 1500 1800 2100
0 500 1000 1500 2000 2500

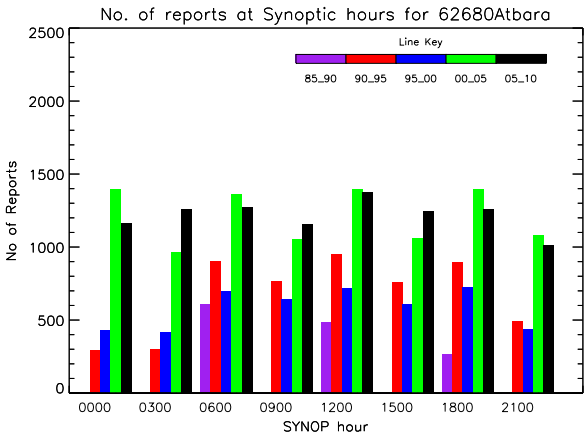
No. of reports at Synoptic hours for 62680Atbara
Line Key
85_90 90_95 95_00 00_05 05_10
No of Reports
SYNOP hour
0000 0300 0600 0900 1200 1500 1800 2100
0 500 1000 1500 2000 2500

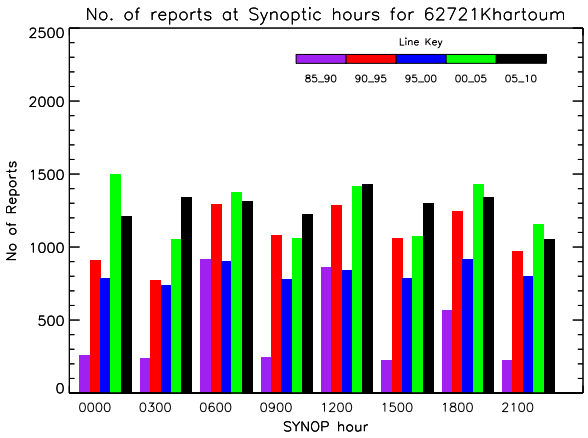
No. of reports at Synoptic hours for 62721Khartoum
Line Key
85_90 90_95 95_00 00_05 05_10
No of Reports
SYNOP hour
0000 0300 0600 0900 1200 1500 1800 2100
0 500 1000 1500 2000 2500

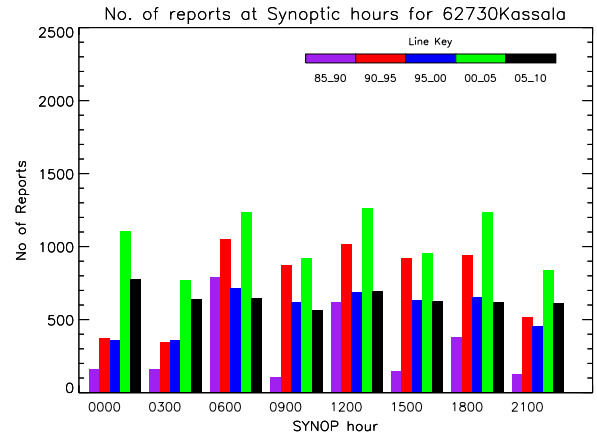
No. of reports at Synoptic hours for 62730Kassala
Line Key
85_90 90_95 95_00 00_05 05_10
No of Reports
SYNOP hour
0000 0300 0600 0900 1200 1500 1800 2100
0 500 1000 1500 2000 2500

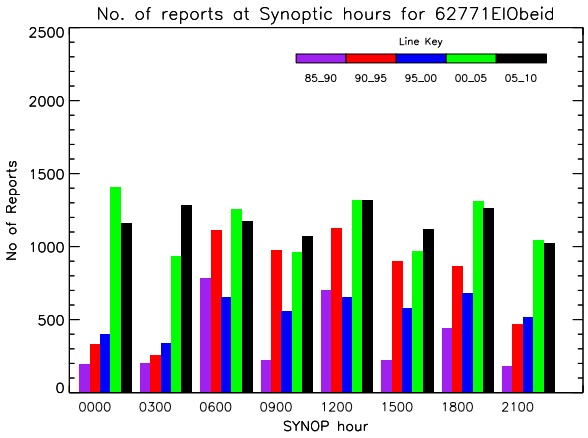
No. of reports at Synoptic hours for 62771ElObeid
Line Key
85_90 90_95 95_00 00_05 05_10
No of Reports
SYNOP hour
0000 0300 0600 0900 1200 1500 1800 2100
0 500 1000 1500 2000 2500

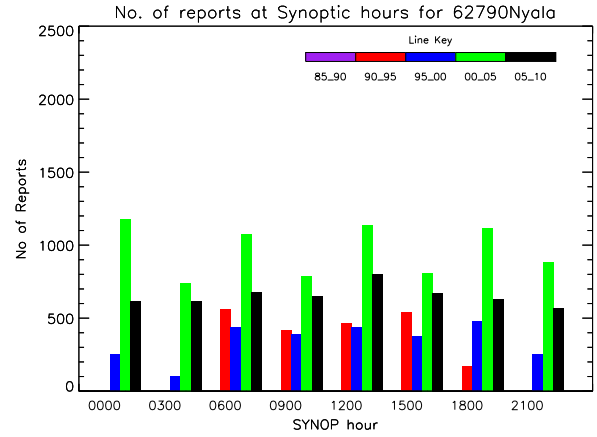
No. of reports at Synoptic hours for 62790Nyala
Line Key
85_90 90_95 95_00 00_05 05_10
No of Reports
SYNOP hour
0000 0300 0600 0900 1200 1500 1800 2100
0 500 1000 1500 2000 2500

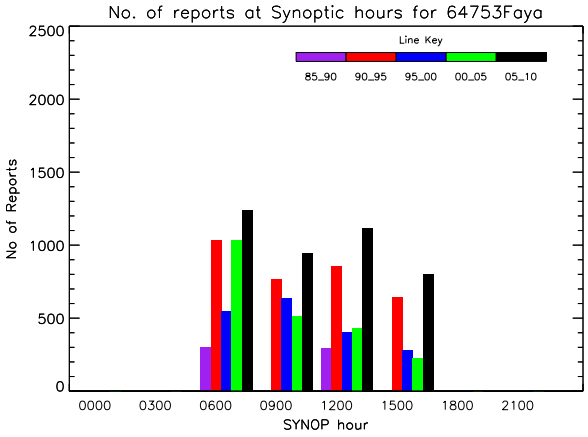
No. of reports at Synoptic hours for 64753Faya
Line Key
85_90 90_95 95_00 00_05 05_10
No of Reports
SYNOP hour
0000 0300 0600 0900 1200 1500 1800 2100
0 500 1000 1500 2000 2500

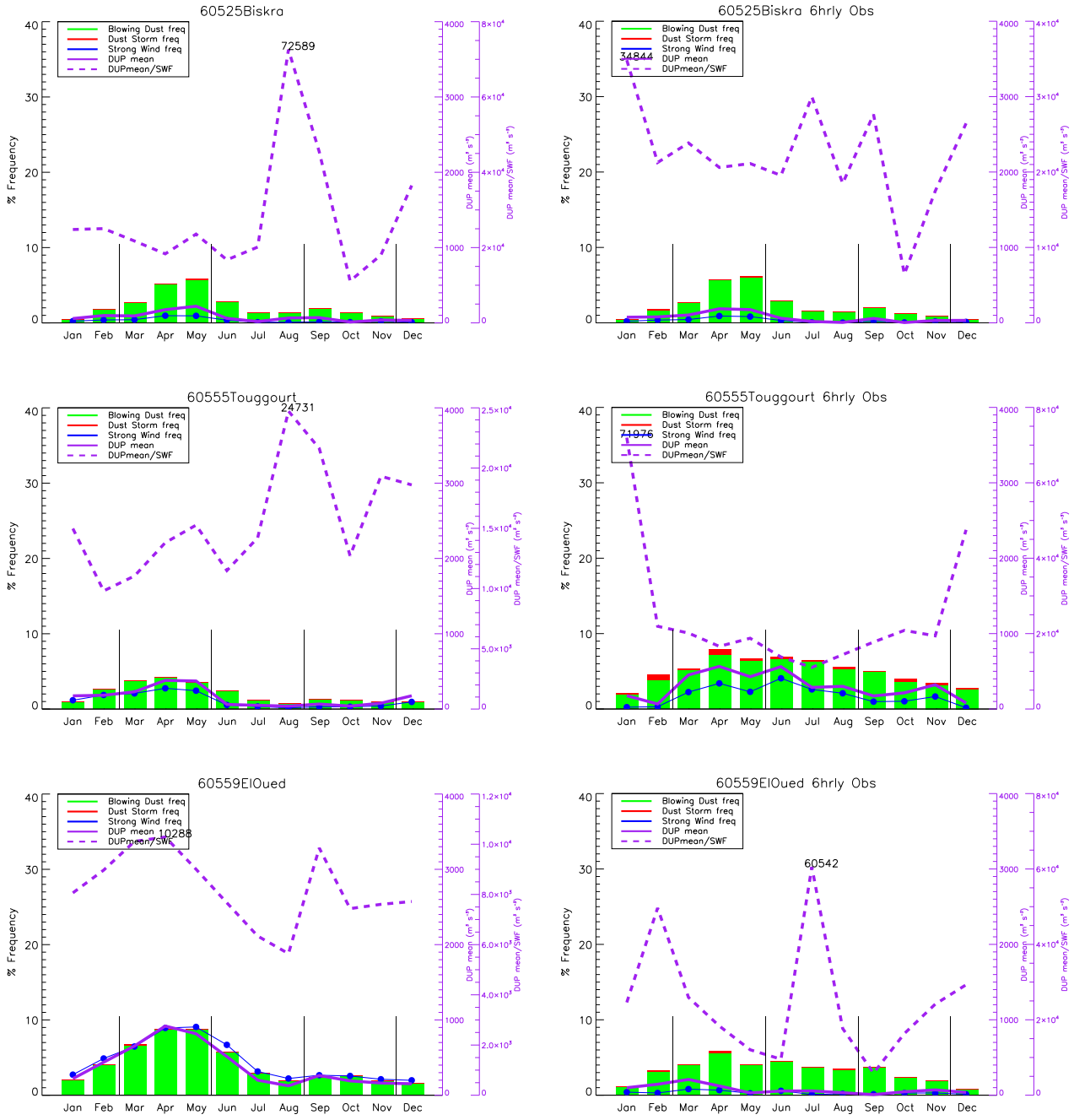

FIGURE 2: Mean seasonal cycle comparison using six hourly (right plots) and three hourly (left plots) observations for 18 stations which have stable three hourly reporting. Monthly frequency of FDE, split into BDF (green bars) and DSF (red bars), as well as SWF (blue line), DUP mean (solid purple) and DUP Intensity (DUP mean/SWF, dashed purple, maximum values given), all computed using the seasonally varying T50 (for definitions of parameters, see section 3.2). Thin vertical black lines indicate seasonal boundaries where thresholds change. Note the different vertical axes for DUP intensity.

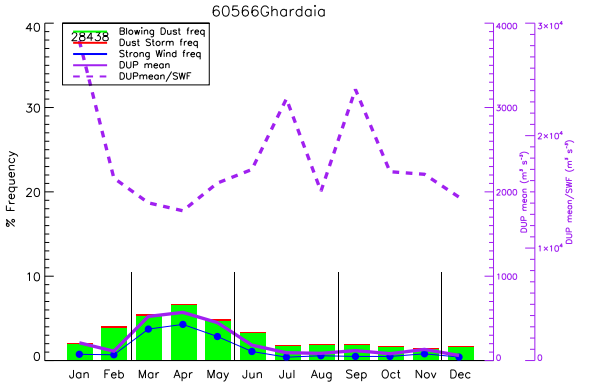
60566Ghardaia
28438
Blowing Dust freq
Dust Storm freq
Strong Wind freq
DUP mean
DUPmean/SWF
% Frequency
DUP mean (m² s⁻²)
DUP mean/SWF (m² s⁻²)
Jan Feb Mar Apr May Jun Jul Aug Sep Oct Nov Dec

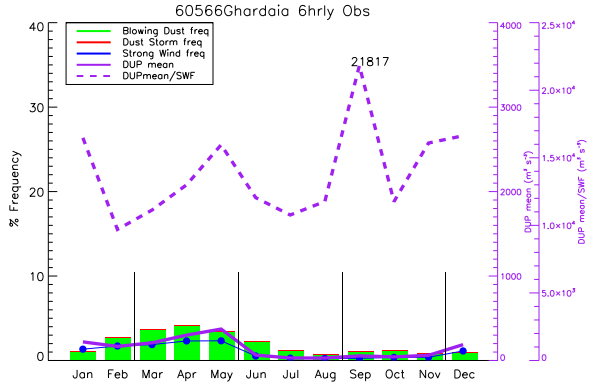
60566Ghardaia 6hrly Obs
21817
Blowing Dust freq
Dust Storm freq
Strong Wind freq
DUP mean
DUPmean/SWF
% Frequency
DUP mean (m² s⁻²)
DUP mean/SWF (m² s⁻²)
Jan Feb Mar Apr May Jun Jul Aug Sep Oct Nov Dec

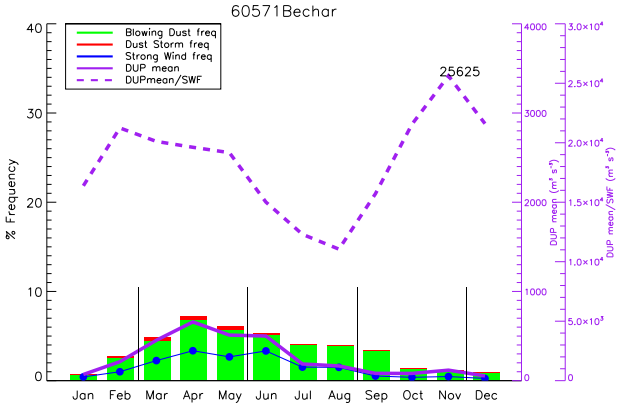
60571Bechar
25625
Blowing Dust freq
Dust Storm freq
Strong Wind freq
DUP mean
DUPmean/SWF
% Frequency
DUP mean (m² s⁻²)
DUP mean/SWF (m² s⁻²)
Jan Feb Mar Apr May Jun Jul Aug Sep Oct Nov Dec

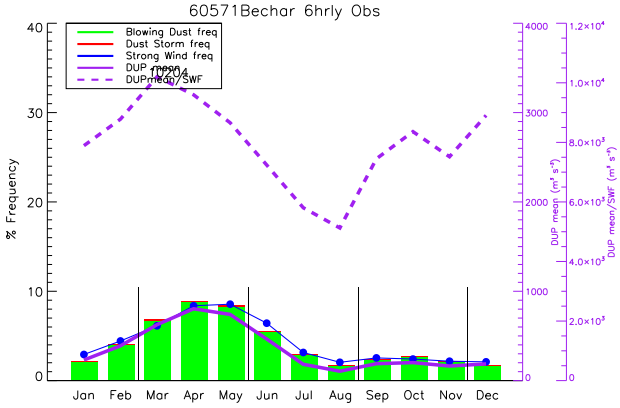
60571Bechar 6hrly Obs
17204
Blowing Dust freq
Dust Storm freq
Strong Wind freq
DUP mean
DUPmean/SWF
% Frequency
DUP mean (m² s⁻²)
DUP mean/SWF (m² s⁻²)
Jan Feb Mar Apr May Jun Jul Aug Sep Oct Nov Dec

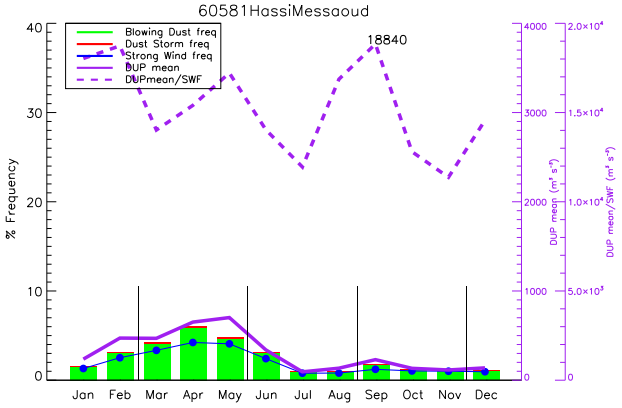
60581HassiMessaoud
18840
Blowing Dust freq
Dust Storm freq
Strong Wind freq
DUP mean
DUPmean/SWF
% Frequency
DUP mean (m² s⁻²)
DUP mean/SWF (m² s⁻²)
Jan Feb Mar Apr May Jun Jul Aug Sep Oct Nov Dec

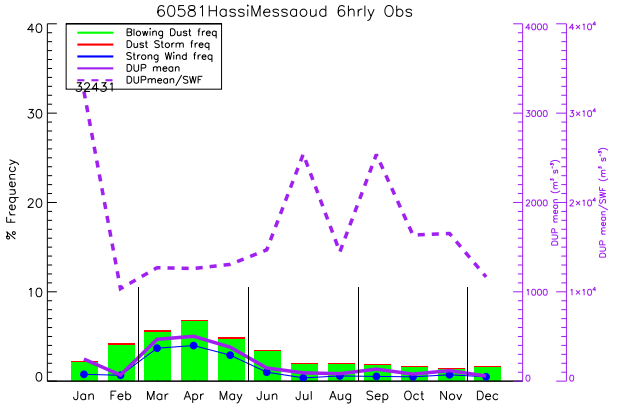
60581HassiMessaoud 6hrly Obs
32431
Blowing Dust freq
Dust Storm freq
Strong Wind freq
DUP mean
DUPmean/SWF
% Frequency
DUP mean (m² s⁻²)
DUP mean/SWF (m² s⁻²)
Jan Feb Mar Apr May Jun Jul Aug Sep Oct Nov Dec

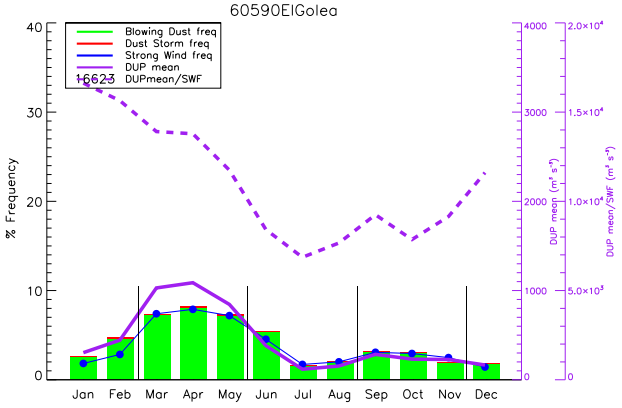
60590ElGolea
16623
Blowing Dust freq
Dust Storm freq
Strong Wind freq
DUP mean
DUPmean/SWF
% Frequency
DUP mean (m² s⁻²)
DUP mean/SWF (m² s⁻²)
Jan Feb Mar Apr May Jun Jul Aug Sep Oct Nov Dec

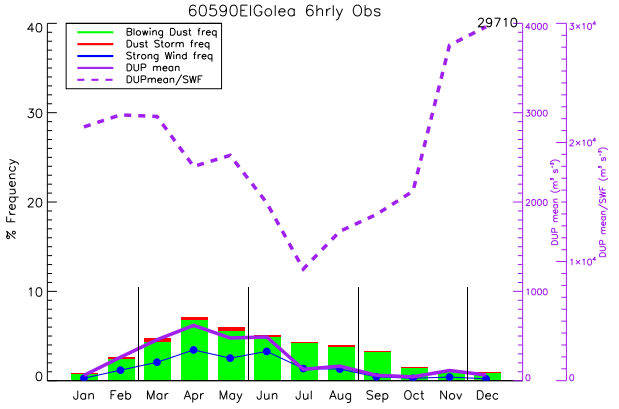
60590ElGolea 6hrly Obs
29710
Blowing Dust freq
Dust Storm freq
Strong Wind freq
DUP mean
DUPmean/SWF
% Frequency
DUP mean (m² s⁻²)
DUP mean/SWF (m² s⁻²)
Jan Feb Mar Apr May Jun Jul Aug Sep Oct Nov Dec

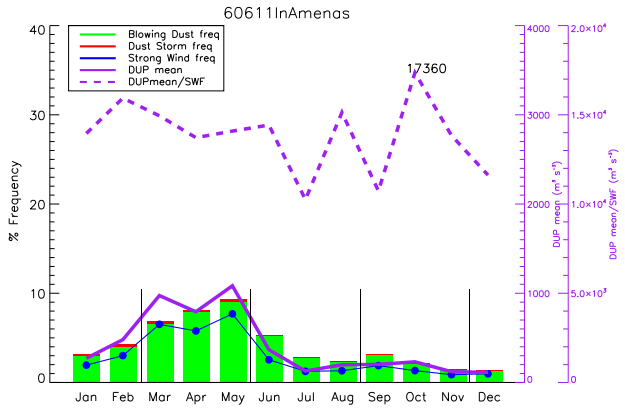
60611InAmenas
Blowing Dust freq
Dust Storm freq
Strong Wind freq
DUP mean
DUPmean/SWF
17360
% Frequency
DUP mean (m² s⁻²)
DUP mean/SWF (m² s⁻²)
Jan Feb Mar Apr May Jun Jul Aug Sep Oct Nov Dec

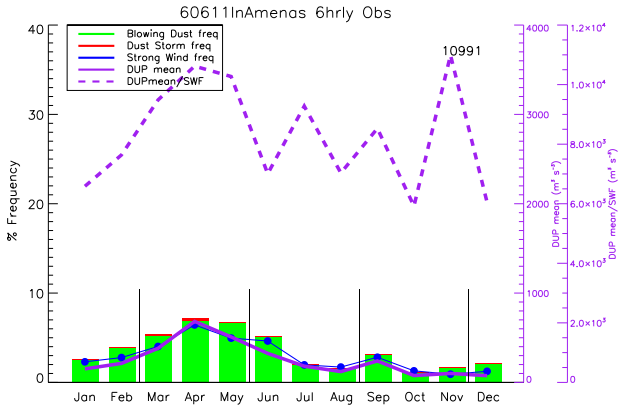
60611InAmenas 6hrly Obs
Blowing Dust freq
Dust Storm freq
Strong Wind freq
DUP mean
DUPmean/SWF
10991
% Frequency
DUP mean (m² s⁻²)
DUP mean/SWF (m² s⁻²)
Jan Feb Mar Apr May Jun Jul Aug Sep Oct Nov Dec

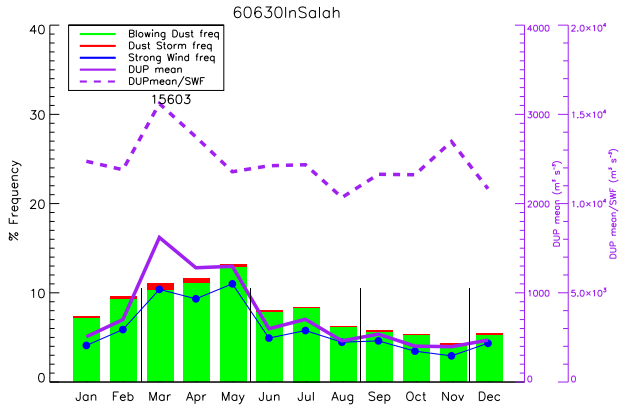
60630InSalah
Blowing Dust freq
Dust Storm freq
Strong Wind freq
DUP mean
DUPmean/SWF
15603
% Frequency
DUP mean (m² s⁻²)
DUP mean/SWF (m² s⁻²)
Jan Feb Mar Apr May Jun Jul Aug Sep Oct Nov Dec

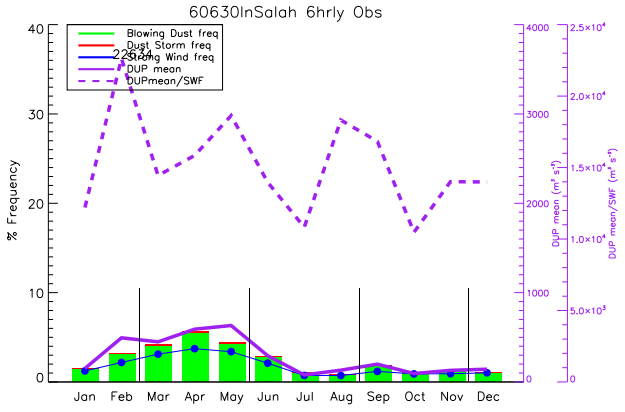
60630InSalah 6hrly Obs
Blowing Dust freq
Dust Storm freq
Strong Wind freq
DUP mean
DUPmean/SWF
22634
% Frequency
DUP mean (m² s⁻²)
DUP mean/SWF (m² s⁻²)
Jan Feb Mar Apr May Jun Jul Aug Sep Oct Nov Dec

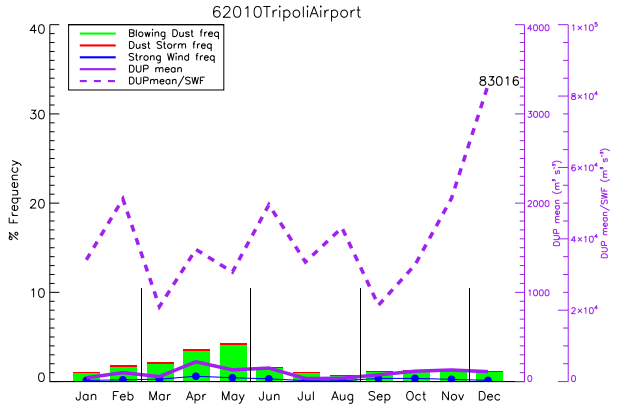
62010TripoliAirport
Blowing Dust freq
Dust Storm freq
Strong Wind freq
DUP mean
DUPmean/SWF
83016
% Frequency
DUP mean (m² s⁻²)
DUP mean/SWF (m² s⁻²)
Jan Feb Mar Apr May Jun Jul Aug Sep Oct Nov Dec

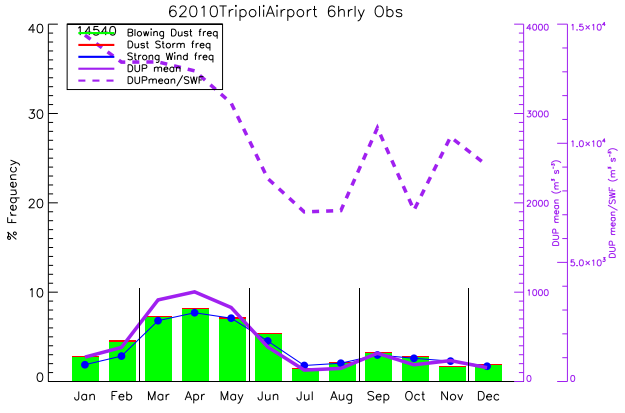
62010TripoliAirport 6hrly Obs
Blowing Dust freq
Dust Storm freq
Strong Wind freq
DUP mean
DUPmean/SWF
14540
% Frequency
DUP mean (m² s⁻²)
DUP mean/SWF (m² s⁻²)
Jan Feb Mar Apr May Jun Jul Aug Sep Oct Nov Dec

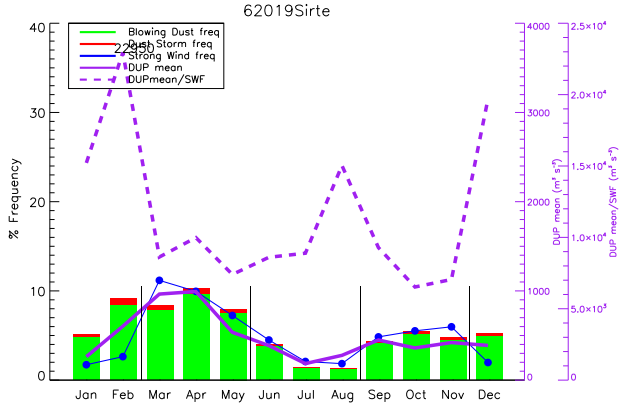
62019Sirte
Blowing Dust freq
Dust Storm freq
Strong Wind freq
DUP mean
DUPmean/SWF
22850
% Frequency
DUP mean (m² s⁻²)
DUP mean/SWF (m² s⁻²)
Jan Feb Mar Apr May Jun Jul Aug Sep Oct Nov Dec

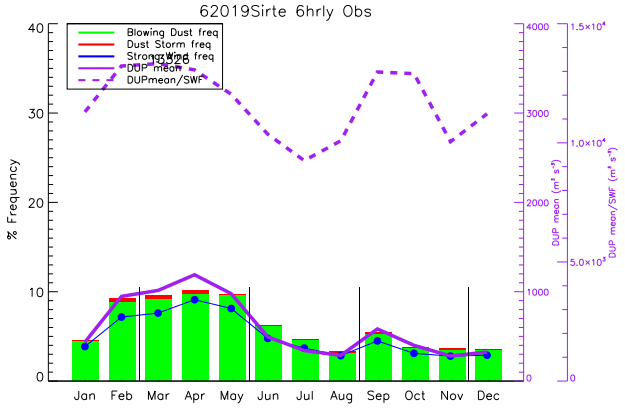
62019Sirte 6hrly Obs
Blowing Dust freq
Dust Storm freq
Strong Wind freq
DUP mean
DUPmean/SWF
% Frequency
DUP mean (m² s⁻²)
DUP mean/SWF (m² s⁻²)
Jan Feb Mar Apr May Jun Jul Aug Sep Oct Nov Dec

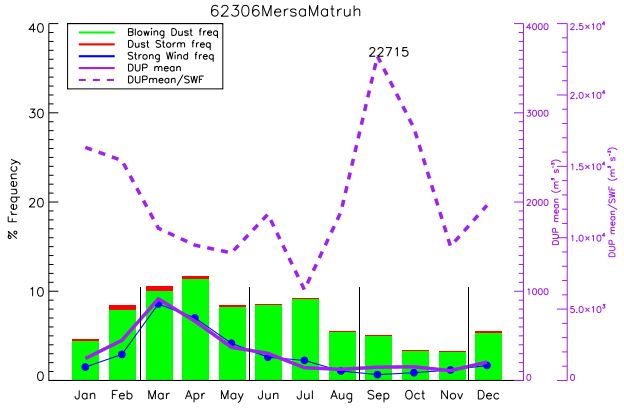
62306MersaMatruh
Blowing Dust freq
Dust Storm freq
Strong Wind freq
DUP mean
DUPmean/SWF
22715
% Frequency
DUP mean (m² s⁻⁴)
DUP mean/SWF (m² s⁻⁴)
Jan Feb Mar Apr May Jun Jul Aug Sep Oct Nov Dec

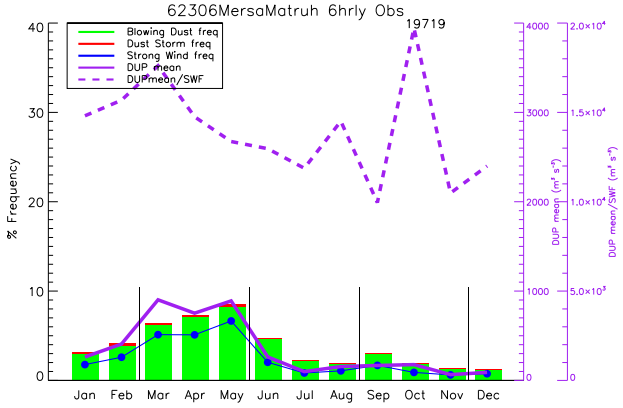
62306MersaMatruh 6hrly Obs
Blowing Dust freq
Dust Storm freq
Strong Wind freq
DUP mean
DUPmean/SWF
19719
% Frequency
DUP mean (m² s⁻⁴)
DUP mean/SWF (m² s⁻⁴)
Jan Feb Mar Apr May Jun Jul Aug Sep Oct Nov Dec

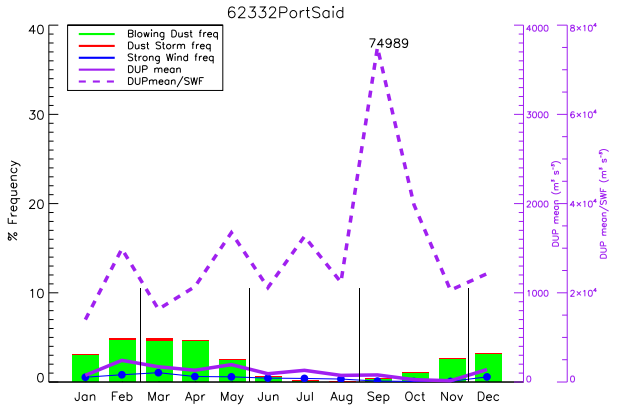
62332PortSaid
Blowing Dust freq
Dust Storm freq
Strong Wind freq
DUP mean
DUPmean/SWF
74989
% Frequency
DUP mean (m² s⁻⁴)
DUP mean/SWF (m² s⁻⁴)
Jan Feb Mar Apr May Jun Jul Aug Sep Oct Nov Dec

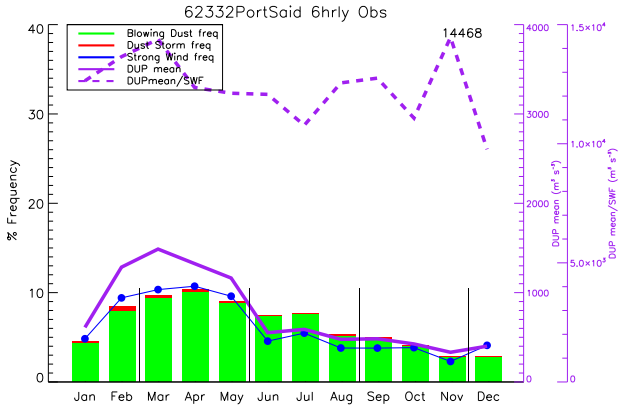
62332PortSaid 6hrly Obs
Blowing Dust freq
Dust Storm freq
Strong Wind freq
DUP mean
DUPmean/SWF
14468
% Frequency
DUP mean (m² s⁻⁴)
DUP mean/SWF (m² s⁻⁴)
Jan Feb Mar Apr May Jun Jul Aug Sep Oct Nov Dec

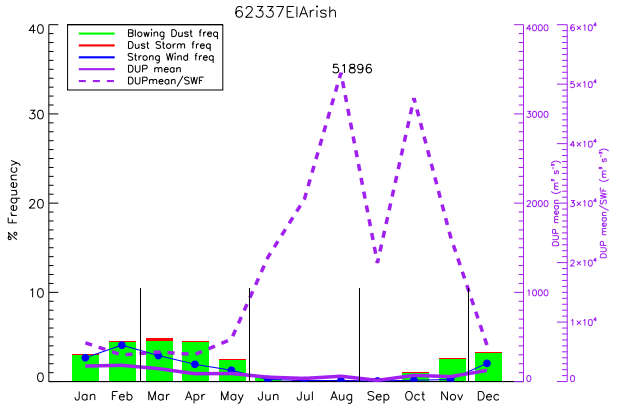
62337ElArish
Blowing Dust freq
Dust Storm freq
Strong Wind freq
DUP mean
DUPmean/SWF
51896
% Frequency
DUP mean (m² s⁻⁴)
DUP mean/SWF (m² s⁻⁴)
Jan Feb Mar Apr May Jun Jul Aug Sep Oct Nov Dec

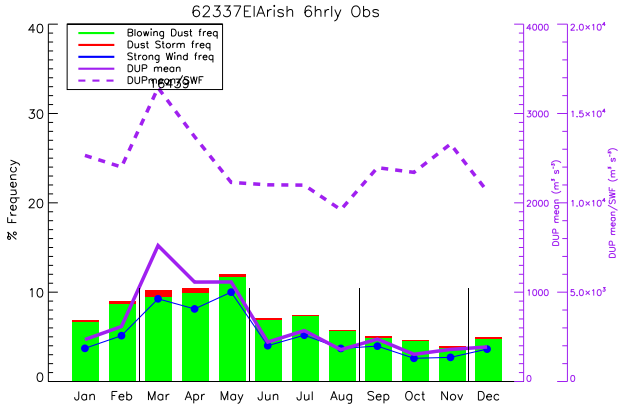
62337ElArish 6hrly Obs
Blowing Dust freq
Dust Storm freq
Strong Wind freq
DUP mean
DUPmean/SWF
% Frequency
DUP mean (m² s⁻⁴)
DUP mean/SWF (m² s⁻⁴)
Jan Feb Mar Apr May Jun Jul Aug Sep Oct Nov Dec

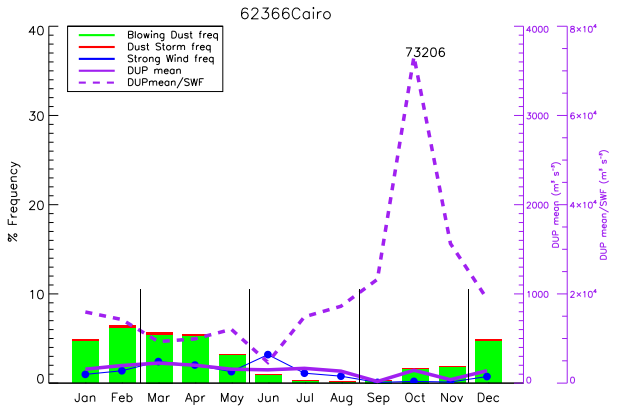
62366Cairo
Blowing Dust freq
Dust Storm freq
Strong Wind freq
DUP mean
DUPmean/SWF
73206
% Frequency
DUP mean (m² s⁻⁴)
DUP mean/SWF (m² s⁻⁴)
Jan Feb Mar Apr May Jun Jul Aug Sep Oct Nov Dec

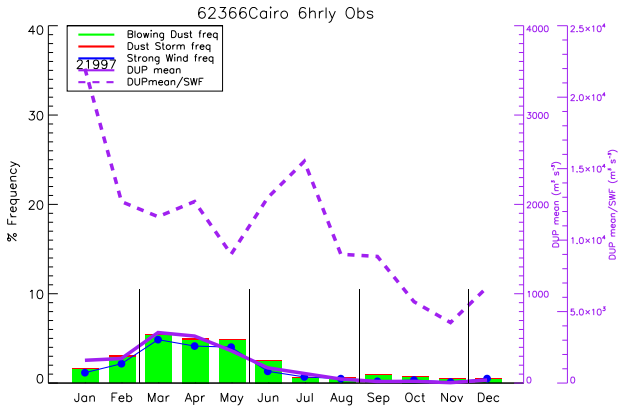
62366Cairo 6hrly Obs
Blowing Dust freq
Dust Storm freq
Strong Wind freq
DUP mean
DUPmean/SWF
21997
% Frequency
DUP mean (m² s⁻⁴)
DUP mean/SWF (m² s⁻⁴)
Jan Feb Mar Apr May Jun Jul Aug Sep Oct Nov Dec

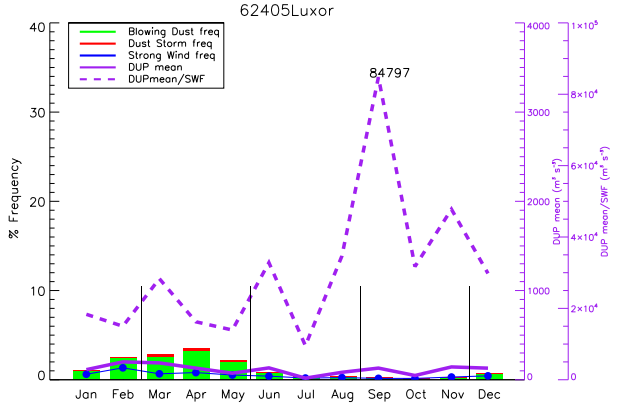
62405Luxor
Blowing Dust freq
Dust Storm freq
Strong Wind freq
DUP mean
DUPmean/SWF
84797
% Frequency
DUP mean (m⁴ s⁻⁴)
DUP mean/SWF (m⁴ s⁻⁴)
Jan Feb Mar Apr May Jun Jul Aug Sep Oct Nov Dec

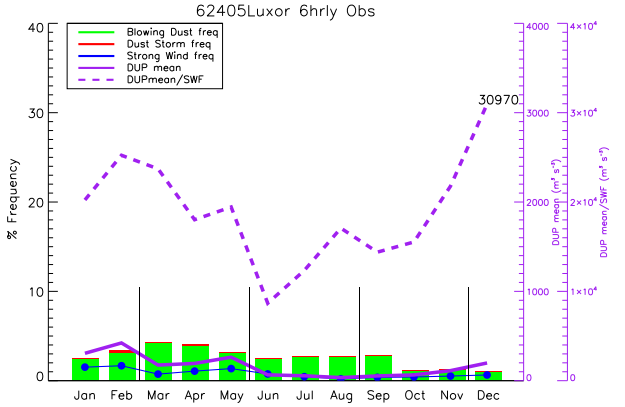
62405Luxor 6hrly Obs
Blowing Dust freq
Dust Storm freq
Strong Wind freq
DUP mean
DUPmean/SWF
30970
% Frequency
DUP mean (m⁴ s⁻⁴)
DUP mean/SWF (m⁴ s⁻⁴)
Jan Feb Mar Apr May Jun Jul Aug Sep Oct Nov Dec

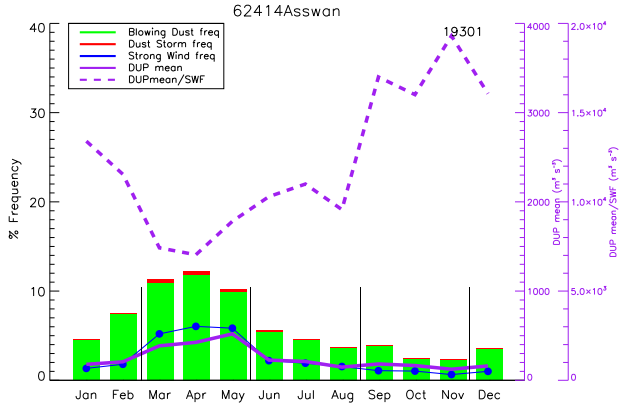
62414Asswan
Blowing Dust freq
Dust Storm freq
Strong Wind freq
DUP mean
DUPmean/SWF
19301
% Frequency
DUP mean (m⁴ s⁻⁴)
DUP mean/SWF (m⁴ s⁻⁴)
Jan Feb Mar Apr May Jun Jul Aug Sep Oct Nov Dec

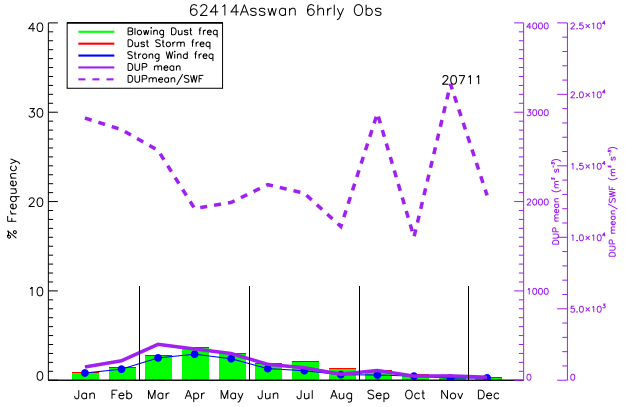
62414Asswan 6hrly Obs
Blowing Dust freq
Dust Storm freq
Strong Wind freq
DUP mean
DUPmean/SWF
20711
% Frequency
DUP mean (m⁴ s⁻⁴)
DUP mean/SWF (m⁴ s⁻⁴)
Jan Feb Mar Apr May Jun Jul Aug Sep Oct Nov Dec

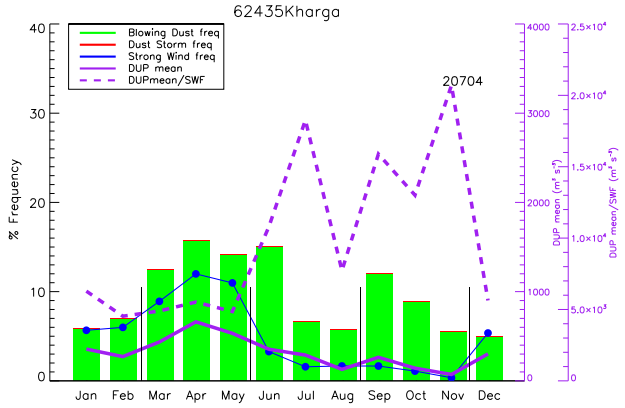
62435Kharga
Blowing Dust freq
Dust Storm freq
Strong Wind freq
DUP mean
DUPmean/SWF
20704
% Frequency
DUP mean (m⁴ s⁻⁴)
DUP mean/SWF (m⁴ s⁻⁴)
Jan Feb Mar Apr May Jun Jul Aug Sep Oct Nov Dec

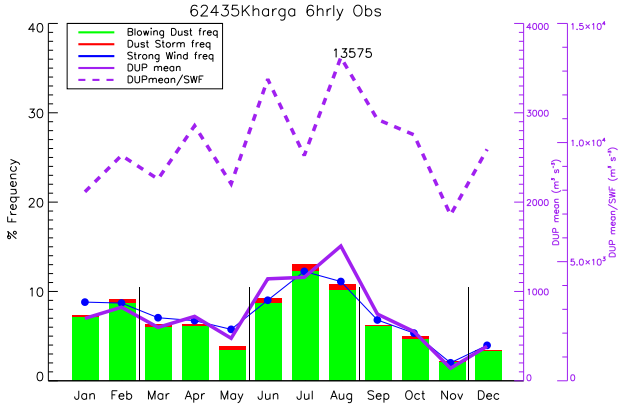
62435Kharga 6hrly Obs
Blowing Dust freq
Dust Storm freq
Strong Wind freq
DUP mean
DUPmean/SWF
13575
% Frequency
DUP mean (m⁴ s⁻⁴)
DUP mean/SWF (m⁴ s⁻⁴)
Jan Feb Mar Apr May Jun Jul Aug Sep Oct Nov Dec

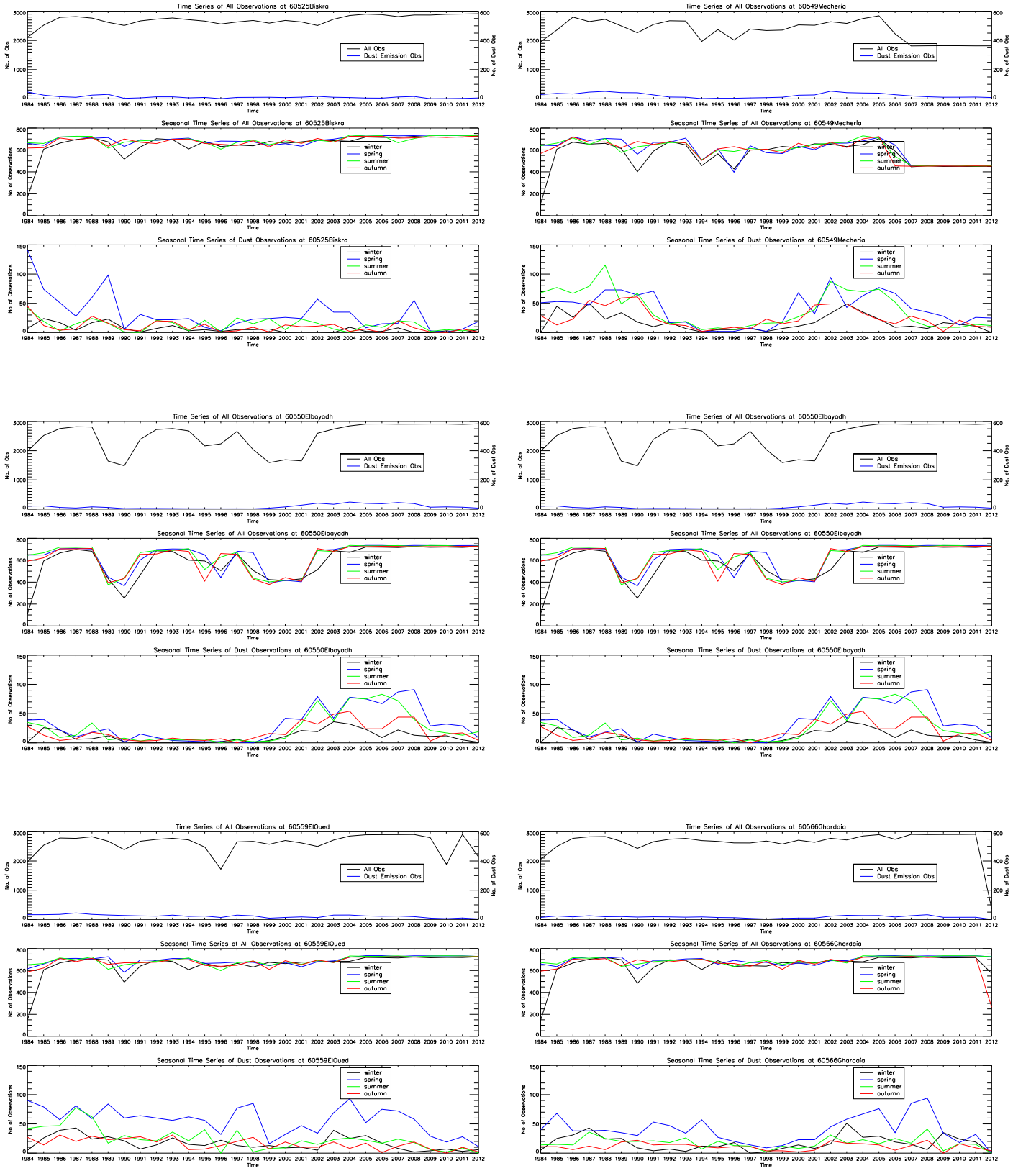

FIGURE 3: Annual time series of all observations (black line) and dust observations only (blue line; top plot). Seasonal time series of all observations (middle plot) where DJF=winter(black), MAM=spring(blue), JJA=summer(green) and SON=autumn(red). The bottom panel is the same as the middle, but for dust observations only.

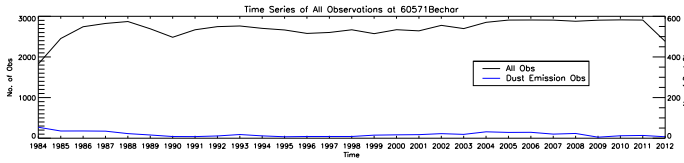
Time Series of All Observations at 60571Bechar
No. of Obs
No. of Dust Obs
All Obs
Dust Emission Obs
Time

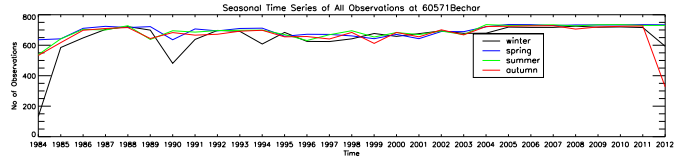
Seasonal Time Series of All Observations at 60571Bechar
No of Observations
winter
spring
summer
autumn
Time

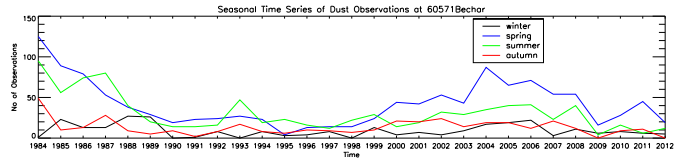
Seasonal Time Series of Dust Observations at 60571Bechar
No of Observations
winter
spring
summer
autumn
Time

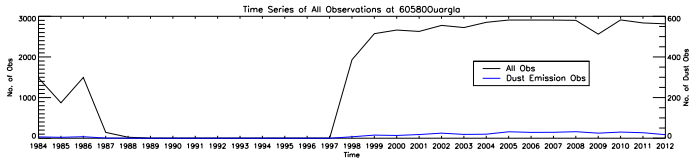
Time Series of All Observations at 605800uargla
No. of Obs
No. of Dust Obs
All Obs
Dust Emission Obs
Time

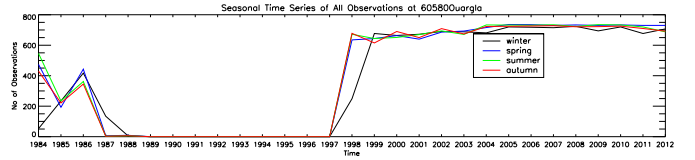
Seasonal Time Series of All Observations at 605800uargla
No of Observations
winter
spring
summer
autumn
Time

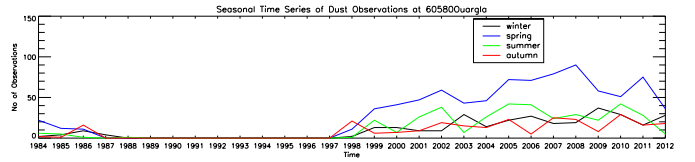
Seasonal Time Series of Dust Observations at 605800uargla
No of Observations
winter
spring
summer
autumn
Time

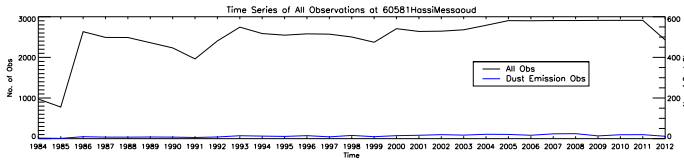
Time Series of All Observations at 60581HassiMessaoud
No. of Obs
No. of Dust Obs
All Obs
Dust Emission Obs
Time

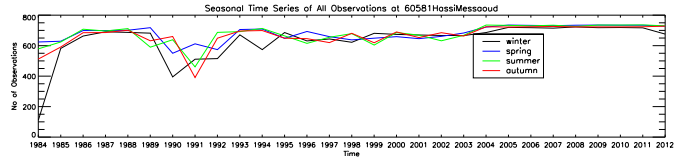
Seasonal Time Series of All Observations at 60581HassiMessaoud
No of Observations
winter
spring
summer
autumn
Time

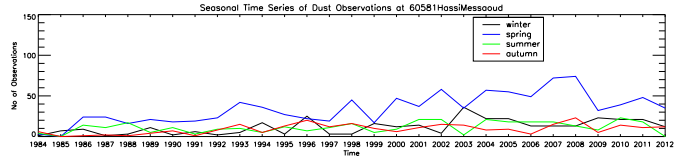
Seasonal Time Series of Dust Observations at 60581HassiMessaoud
No of Observations
winter
spring
summer
autumn
Time

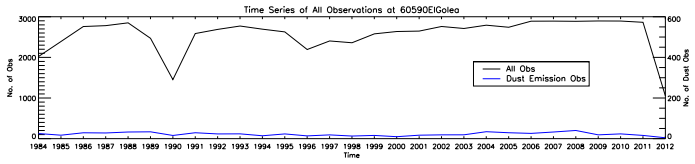
Time Series of All Observations at 60590ElGolea
No. of Obs
No. of Dust Obs
All Obs
Dust Emission Obs
Time

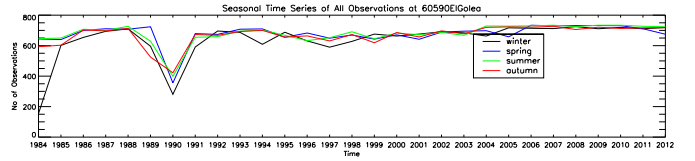
Seasonal Time Series of All Observations at 60590ElGolea
No of Observations
winter
spring
summer
autumn
Time

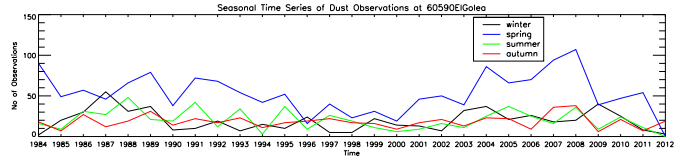
Seasonal Time Series of Dust Observations at 60590ElGolea
No of Observations
winter
spring
summer
autumn
Time

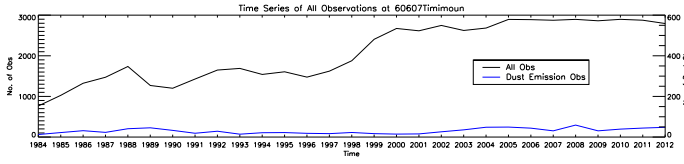
Time Series of All Observations at 60607Timimoun
No. of Obs
No. of Dust Obs
All Obs
Dust Emission Obs
Time

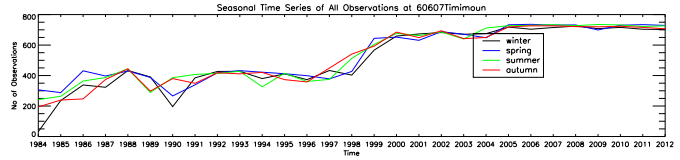
Seasonal Time Series of All Observations at 60607Timimoun
No of Observations
winter
spring
summer
autumn
Time

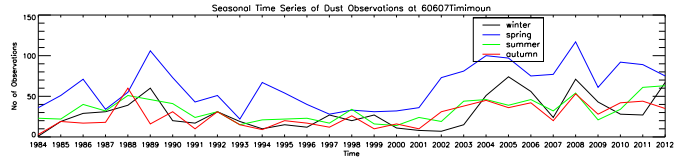
Seasonal Time Series of Dust Observations at 60607Timimoun
No of Observations
winter
spring
summer
autumn
Time

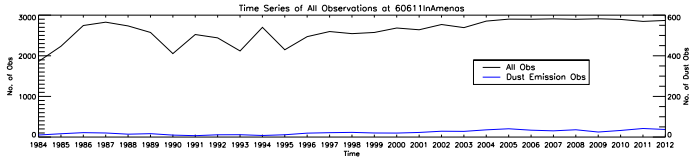
Time Series of All Observations at 60611InAmenas
No. of Obs
No. of Dust Obs
All Obs
Dust Emission Obs
Time

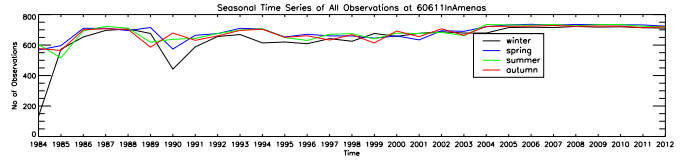
Seasonal Time Series of All Observations at 60611InAmenas
No of Observations
winter
spring
summer
autumn
Time

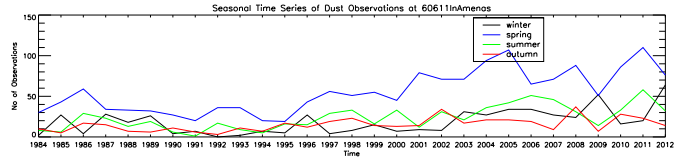
Seasonal Time Series of Dust Observations at 60611InAmenas
No of Observations
winter
spring
summer
autumn
Time

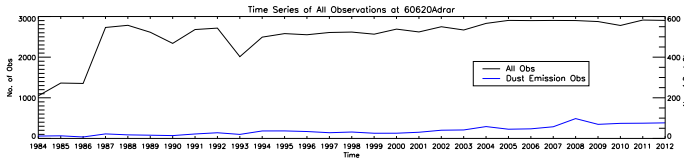
Time Series of All Observations at 60620Adrar
No. of Obs
No. of Dust Obs
All Obs
Dust Emission Obs
Time

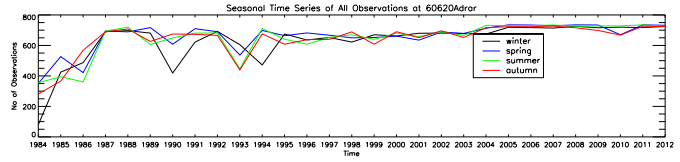
Seasonal Time Series of All Observations at 60620Adrar
No of Observations
winter
spring
summer
autumn
Time

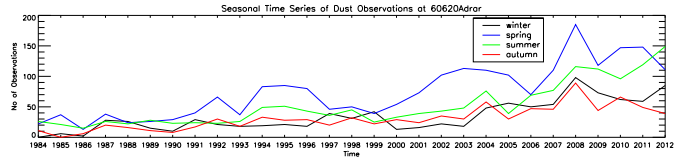
Seasonal Time Series of Dust Observations at 60620Adrar
No of Observations
winter
spring
summer
autumn
Time

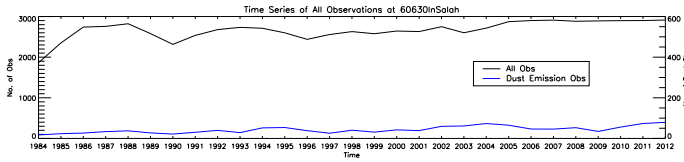
Time Series of All Observations at 60630InSalah
No. of Obs
No. of Dust Obs
All Obs
Dust Emission Obs
Time

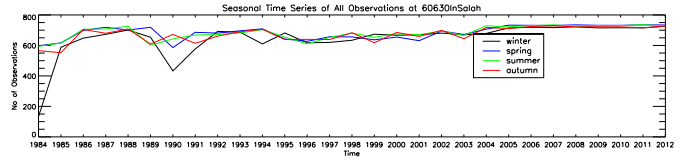
Seasonal Time Series of All Observations at 60630InSalah
No of Observations
winter
spring
summer
autumn
Time

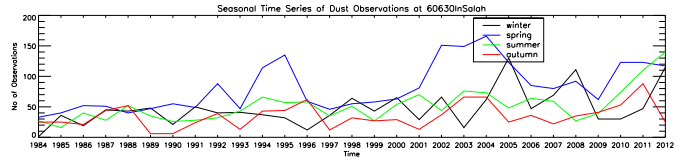
Seasonal Time Series of Dust Observations at 60630InSalah
No of Observations
winter
spring
summer
autumn
Time

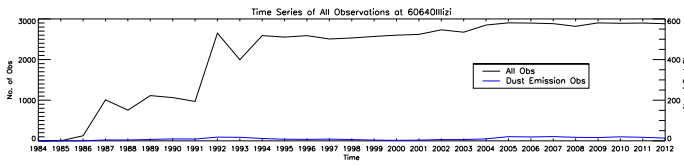
Time Series of All Observations at 60640Illizi
No. of Obs
No. of Dust Obs
All Obs
Dust Emission Obs
Time

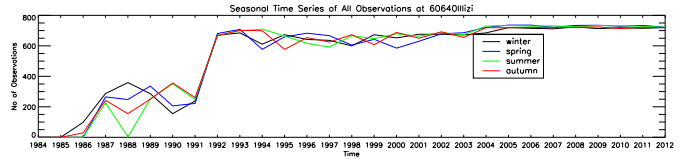
Seasonal Time Series of All Observations at 60640Illizi
No of Observations
winter
spring
summer
autumn
Time

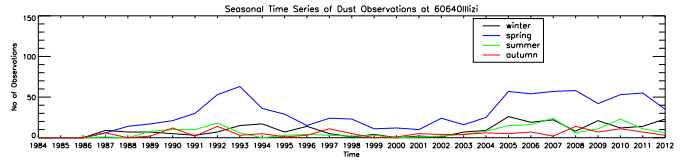
Seasonal Time Series of Dust Observations at 60640Illizi
No of Observations
winter
spring
summer
autumn
Time

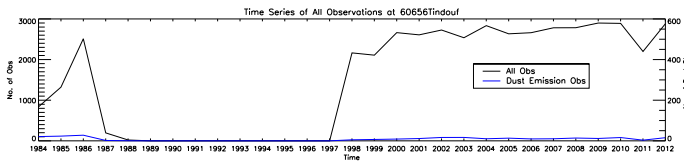
Time Series of All Observations at 60656Tindouf
No. of Obs
No. of Dust Obs
All Obs
Dust Emission Obs
Time

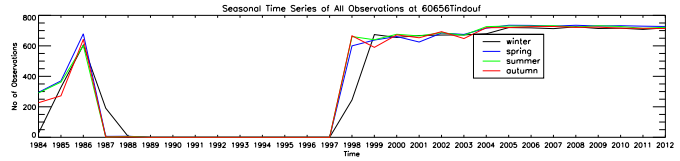
Seasonal Time Series of All Observations at 60656Tindouf
No of Observations
winter
spring
summer
autumn
Time

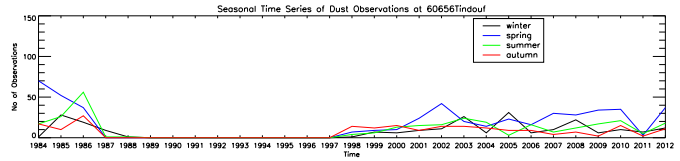
Seasonal Time Series of Dust Observations at 60656Tindouf
No of Observations
winter
spring
summer
autumn
Time

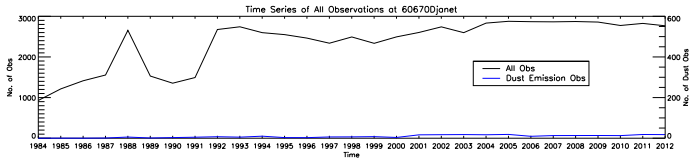
Time Series of All Observations at 60670Djanet
No. of Obs
No. of Dust Obs
All Obs
Dust Emission Obs
Time

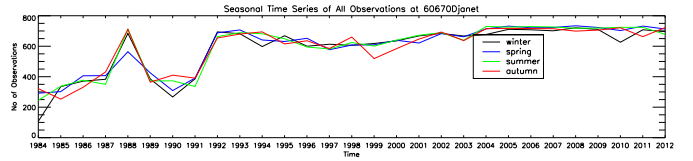
Seasonal Time Series of All Observations at 60670Djanet
No of Observations
winter
spring
summer
autumn
Time

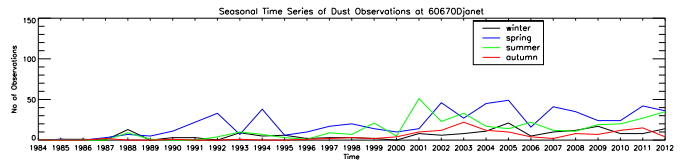
Seasonal Time Series of Dust Observations at 60670Djanet
No of Observations
winter
spring
summer
autumn
Time

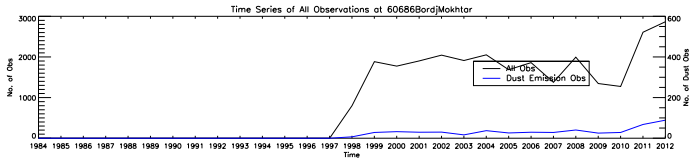
Time Series of All Observations at 60686BordjMokhtar
No. of Obs
No. of Dust Obs
All Obs
Dust Emission Obs
Time

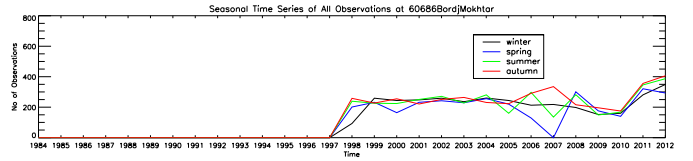
Seasonal Time Series of All Observations at 60686BordjMokhtar
No of Observations
winter
spring
summer
autumn
Time

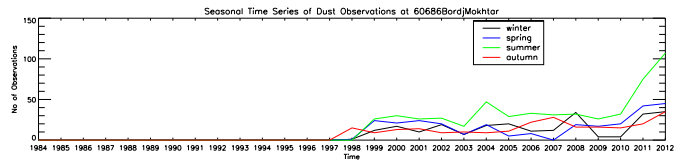
Seasonal Time Series of Dust Observations at 60686BordjMokhtar
No of Observations
winter
spring
summer
autumn
Time

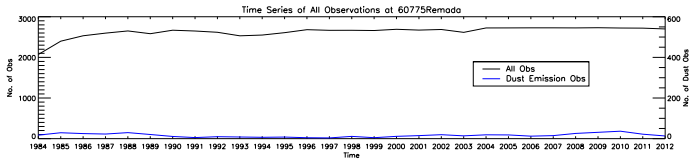
Time Series of All Observations at 60775Remada
No. of Obs
No. of Dust Obs
All Obs
Dust Emission Obs
Time

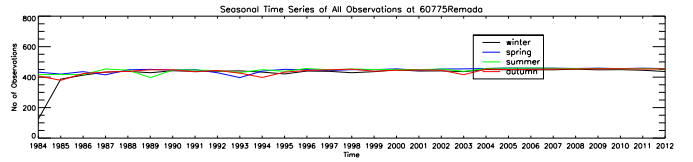
Seasonal Time Series of All Observations at 60775Remada
No of Observations
winter
spring
summer
autumn
Time

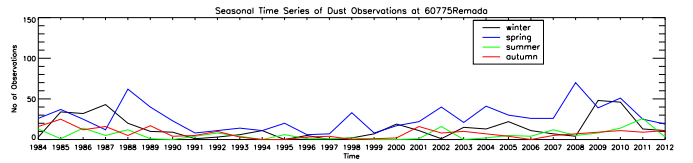
Seasonal Time Series of Dust Observations at 60775Remada
No of Observations
winter
spring
summer
autumn
Time

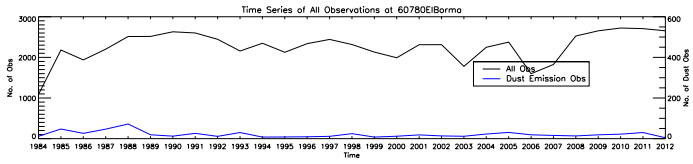
Time Series of All Observations at 60780ElBorma
No. of Obs
No. of Dust Obs
All Obs
Dust Emission Obs
Time

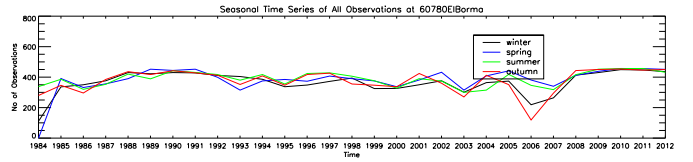
Seasonal Time Series of All Observations at 60780ElBorma
No of Observations
winter
spring
summer
autumn
Time

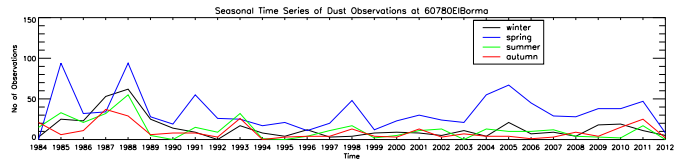
Seasonal Time Series of Dust Observations at 60780ElBorma
No of Observations
winter
spring
summer
autumn
Time

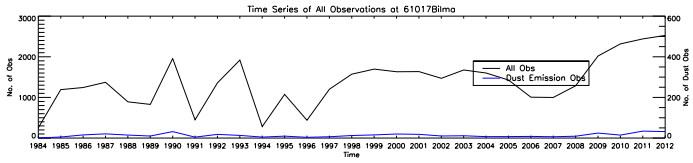
Time Series of All Observations at 61017Bilma
No. of Obs
No. of Dust Obs
All Obs
Dust Emission Obs
Time

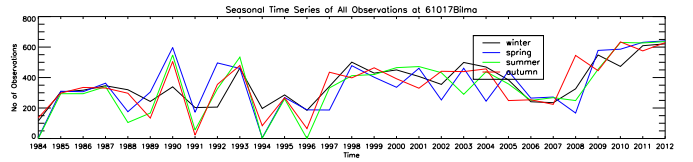
Seasonal Time Series of All Observations at 61017Bilma
No of Observations
winter
spring
summer
autumn
Time

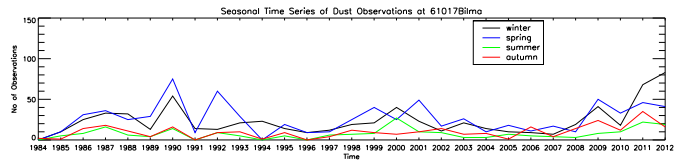
Seasonal Time Series of Dust Observations at 61017Bilma
No of Observations
winter
spring
summer
autumn
Time

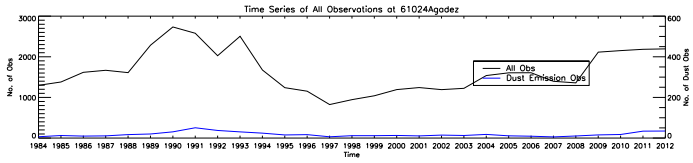
Time Series of All Observations at 61024Agadez
No. of Obs
No. of Dust Obs
All Obs
Dust Emission Obs
Time

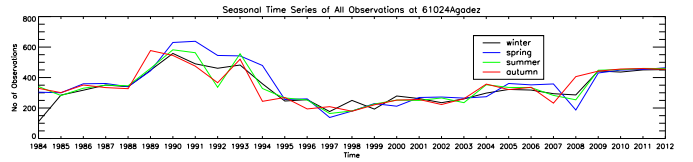
Seasonal Time Series of All Observations at 61024Agadez
No of Observations
winter
spring
summer
autumn
Time

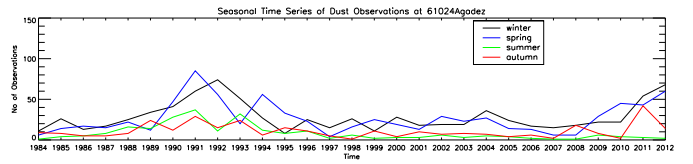
Seasonal Time Series of Dust Observations at 61024Agadez
No of Observations
winter
spring
summer
autumn
Time

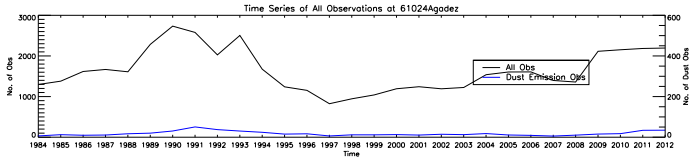
Time Series of All Observations at 61024Agadez
No. of Obs
No. of Dust Obs
All Obs
Dust Emission Obs
Time

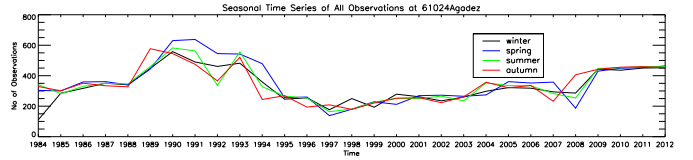
Seasonal Time Series of All Observations at 61024Agadez
No of Observations
winter
spring
summer
autumn
Time

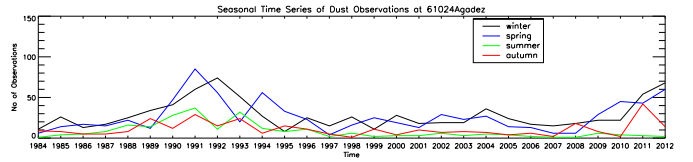
Seasonal Time Series of Dust Observations at 61024Agadez
No of Observations
winter
spring
summer
autumn
Time

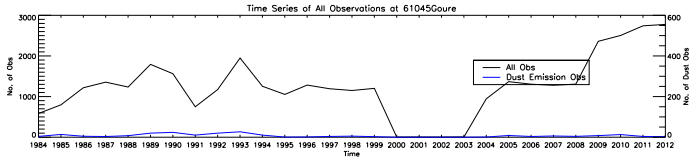
Time Series of All Observations at 61045Goure
No. of Obs
No. of Dust Obs
All Obs
Dust Emission Obs
Time

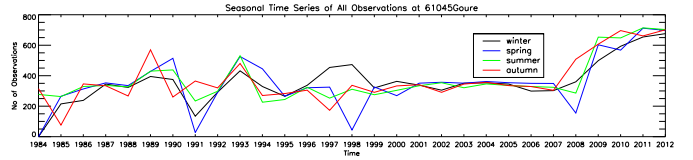
Seasonal Time Series of All Observations at 61045Goure
No of Observations
winter
spring
summer
autumn
Time

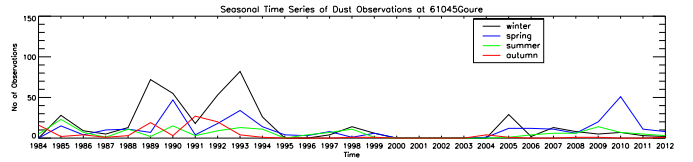
Seasonal Time Series of Dust Observations at 61045Goure
No of Observations
winter
spring
summer
autumn
Time

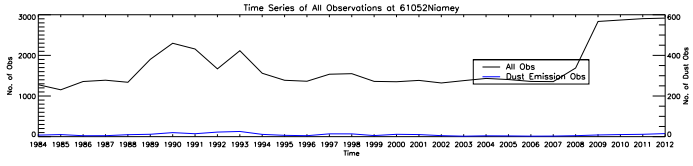
Time Series of All Observations at 61052Niamey
No. of Obs
No. of Dust Obs
All Obs
Dust Emission Obs
Time

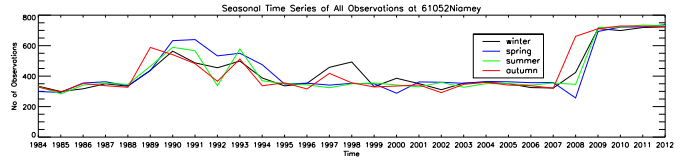
Seasonal Time Series of All Observations at 61052Niamey
No of Observations
winter
spring
summer
autumn
Time

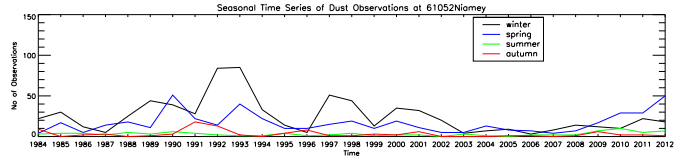
Seasonal Time Series of Dust Observations at 61052Niamey
No of Observations
winter
spring
summer
autumn
Time

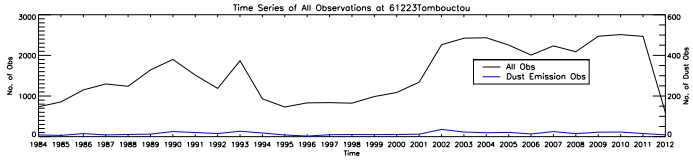
Time Series of All Observations at 61223Tombouctou
No. of Obs
No. of Dust Obs
All Obs
Dust Emission Obs
Time

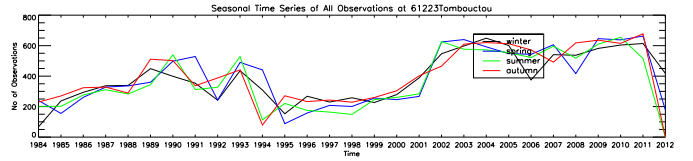
Seasonal Time Series of All Observations at 61223Tombouctou
No of Observations
winter
spring
summer
autumn
Time

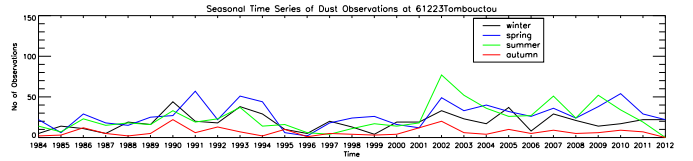
Seasonal Time Series of Dust Observations at 61223Tombouctou
No of Observations
winter
spring
summer
autumn
Time

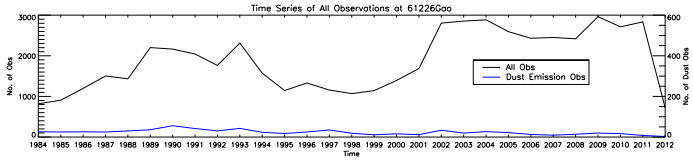
Time Series of All Observations at 61226Gao
No. of Obs
No. of Dust Obs
All Obs
Dust Emission Obs
Time

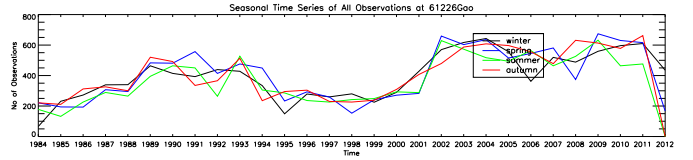
Seasonal Time Series of All Observations at 61226Gao
No of Observations
winter
spring
summer
autumn
Time

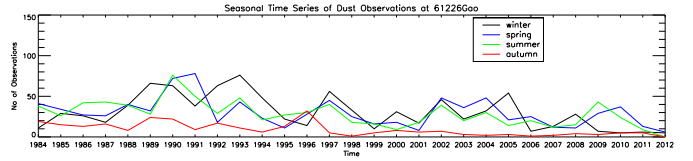
Seasonal Time Series of Dust Observations at 61226Gao
No of Observations
winter
spring
summer
autumn
Time

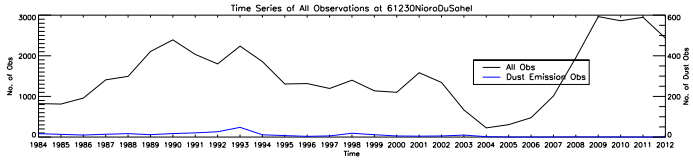
Time Series of All Observations at 61230NioroDuSahel
No. of Obs
No. of Dust Obs
All Obs
Dust Emission Obs
Time

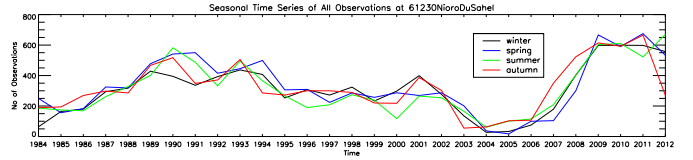
Seasonal Time Series of All Observations at 61230NioroDuSahel
No of Observations
winter
spring
summer
autumn
Time

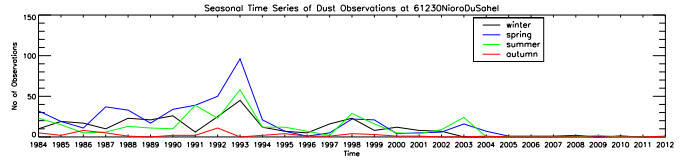
Seasonal Time Series of Dust Observations at 61230NioroDuSahel
No of Observations
winter
spring
summer
autumn
Time

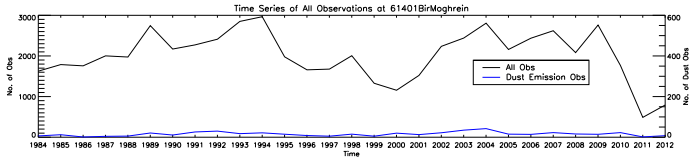
Time Series of All Observations at 61401BirMoghrein
No. of Obs
No. of Dust Obs
All Obs
Dust Emission Obs
Time

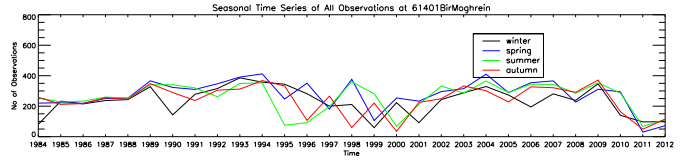
Seasonal Time Series of All Observations at 61401BirMoghrein
No of Observations
winter
spring
summer
autumn
Time

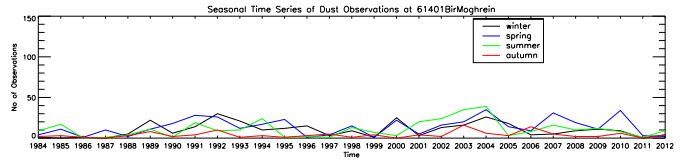
Seasonal Time Series of Dust Observations at 61401BirMoghrein
No of Observations
winter
spring
summer
autumn
Time

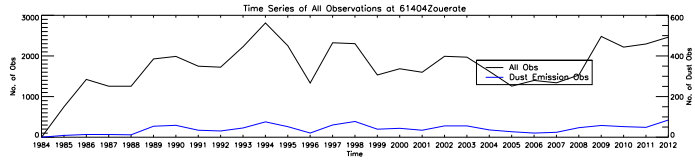
Time Series of All Observations at 61404Zouerate
No. of Obs
No. of Dust Obs
All Obs
Dust Emission Obs
Time

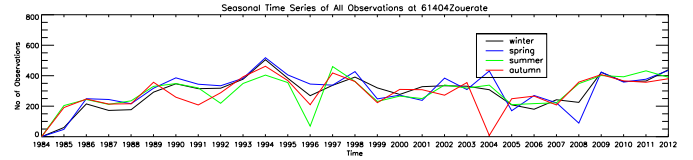
Seasonal Time Series of All Observations at 61404Zouerate
No of Observations
winter
spring
summer
autumn
Time

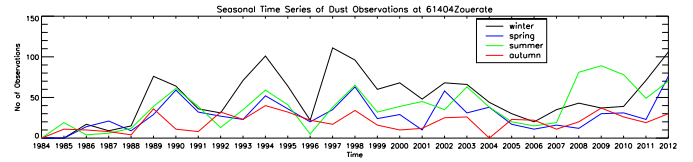
Seasonal Time Series of Dust Observations at 61404Zouerate
No of Observations
winter
spring
summer
autumn
Time

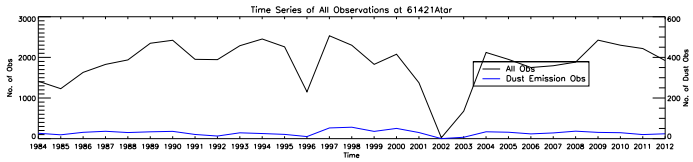
Time Series of All Observations at 61421Atar
No. of Obs
No. of Dust Obs
All Obs
Dust Emission Obs
Time

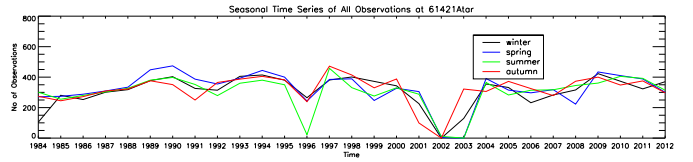
Seasonal Time Series of All Observations at 61421Atar
No of Observations
winter
spring
summer
autumn
Time

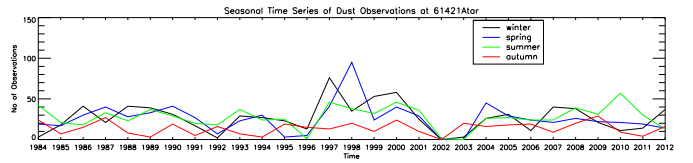
Seasonal Time Series of Dust Observations at 61421Atar
No of Observations
winter
spring
summer
autumn
Time

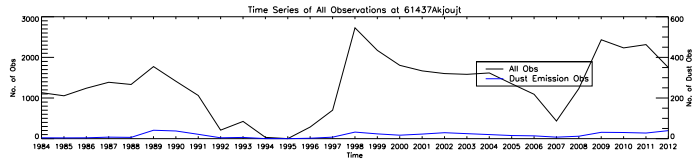
Time Series of All Observations at 61437Akjoujt
No. of Obs
No. of Dust Obs
All Obs
Dust Emission Obs
Time

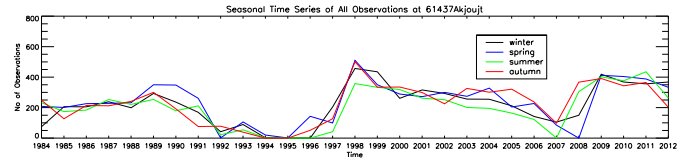
Seasonal Time Series of All Observations at 61437Akjoujt
No of Observations
winter
spring
summer
autumn
Time

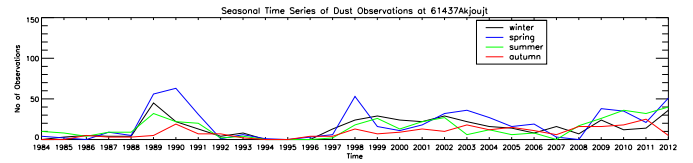
Seasonal Time Series of Dust Observations at 61437Akjoujt
No of Observations
winter
spring
summer
autumn
Time

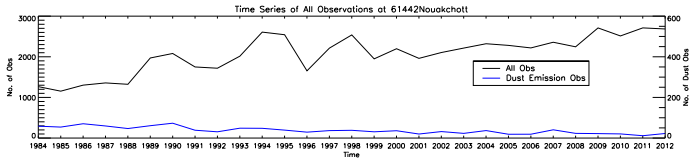
Time Series of All Observations at 61442Nouakchott
No. of Obs
No. of Dust Obs
All Obs
Dust Emission Obs
Time

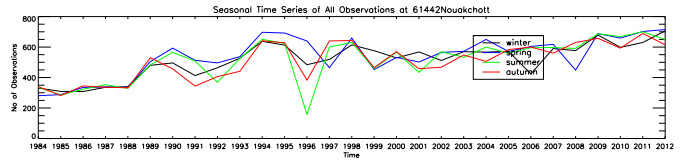
Seasonal Time Series of All Observations at 61442Nouakchott
No of Observations
winter
spring
summer
autumn
Time

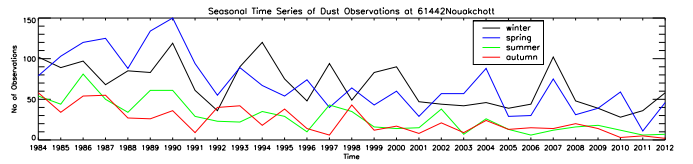
Seasonal Time Series of Dust Observations at 61442Nouakchott
No of Observations
winter
spring
summer
autumn
Time

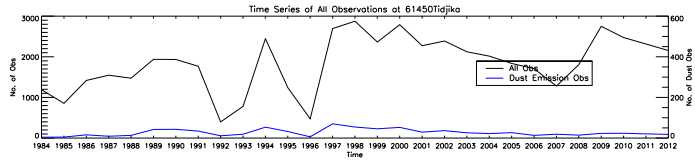
Time Series of All Observations at 61450Tidjika
No. of Obs
No. of Dust Obs
All Obs
Dust Emission Obs
Time

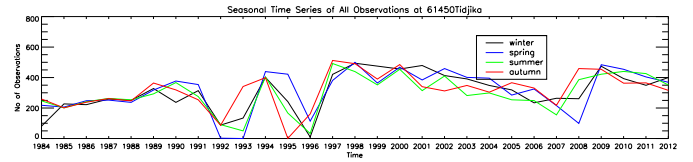
Seasonal Time Series of All Observations at 61450Tidjika
No of Observations
winter
spring
summer
autumn
Time

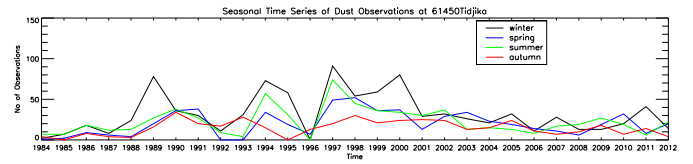
Seasonal Time Series of Dust Observations at 61450Tidjika
No of Observations
winter
spring
summer
autumn
Time

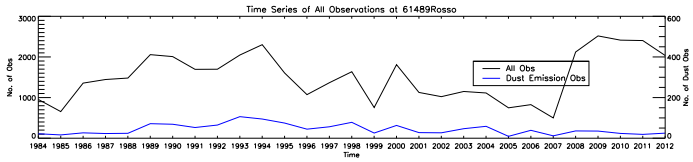
Time Series of All Observations at 61489Rosso
No. of Obs
No. of Dust Obs
All Obs
Dust Emission Obs
Time

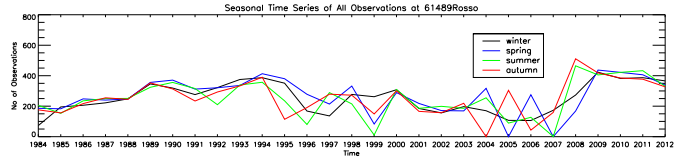
Seasonal Time Series of All Observations at 61489Rosso
No of Observations
winter
spring
summer
autumn
Time

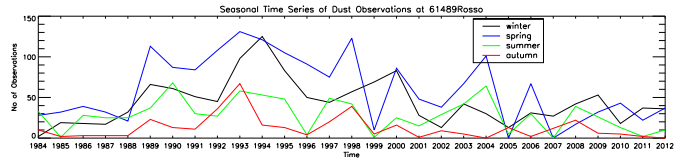
Seasonal Time Series of Dust Observations at 61489Rosso
No of Observations
winter
spring
summer
autumn
Time

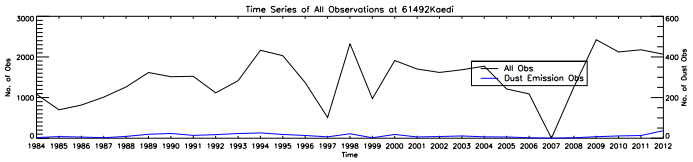
Time Series of All Observations at 61492Kaedi
No. of Obs
No. of Dust Obs
All Obs
Dust Emission Obs
Time

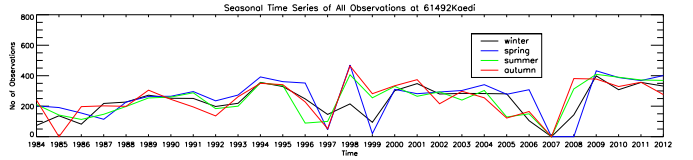
Seasonal Time Series of All Observations at 61492Kaedi
No of Observations
winter
spring
summer
autumn
Time

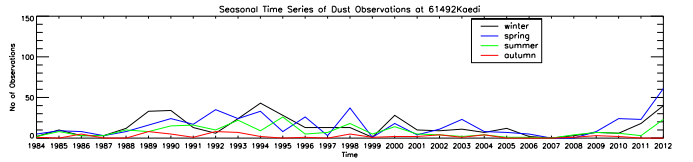
Seasonal Time Series of Dust Observations at 61492Kaedi
No of Observations
winter
spring
summer
autumn
Time

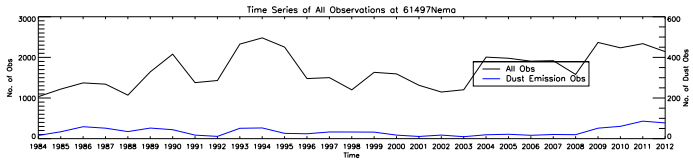
Time Series of All Observations at 61497Nema
No. of Obs
No. of Dust Obs
All Obs
Dust Emission Obs
Time

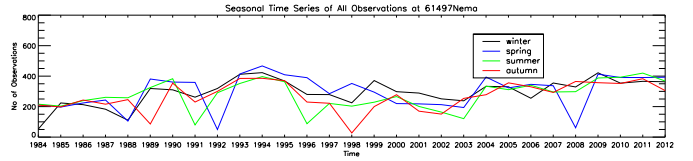
Seasonal Time Series of All Observations at 61497Nema
No of Observations
winter
spring
summer
autumn
Time

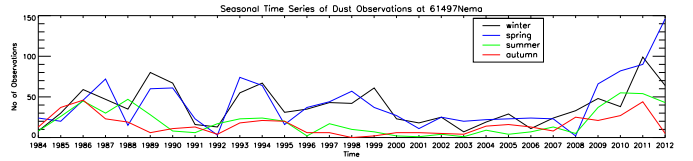
Seasonal Time Series of Dust Observations at 61497Nema
No of Observations
winter
spring
summer
autumn
Time

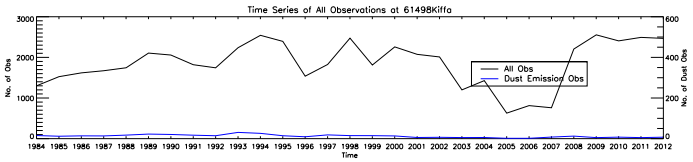
Time Series of All Observations at 61498Kiffa
No. of Obs
No. of Dust Obs
All Obs
Dust Emission Obs
Time

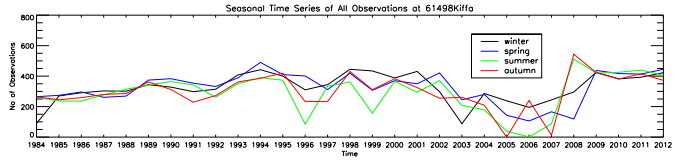
Seasonal Time Series of All Observations at 61498Kiffa
No of Observations
winter
spring
summer
autumn
Time

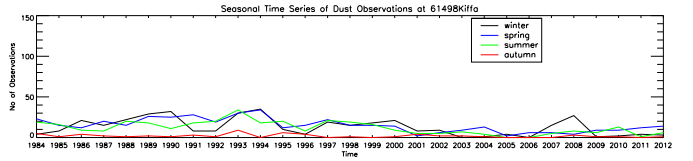
Seasonal Time Series of Dust Observations at 61498Kiffa
No of Observations
winter
spring
summer
autumn
Time

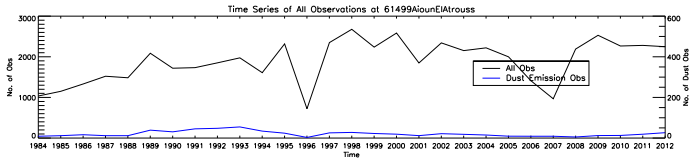
Time Series of All Observations at 61499AiounElAtrouss
No. of Obs
No. of Dust Obs
All Obs
Dust Emission Obs
Time

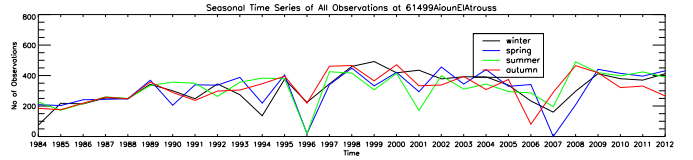
Seasonal Time Series of All Observations at 61499AiounElAtrouss
No of Observations
winter
spring
summer
autumn
Time

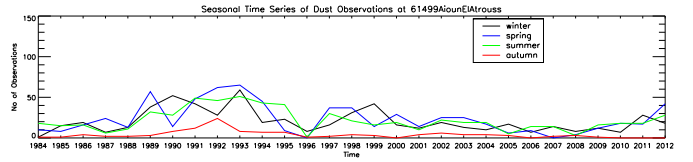
Seasonal Time Series of Dust Observations at 61499AiounElAtrouss
No of Observations
winter
spring
summer
autumn
Time

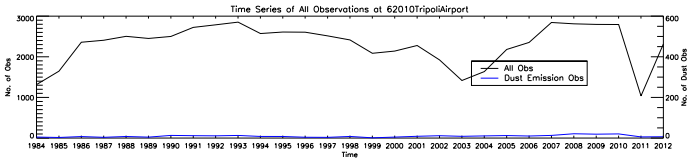
Time Series of All Observations at 62010TripoliAirport
No. of Obs
No. of Dust Obs
All Obs
Dust Emission Obs
Time

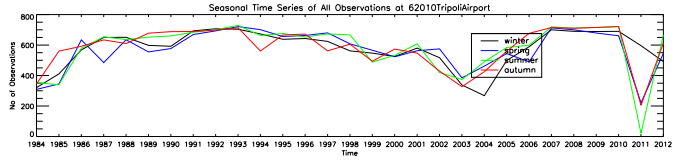
Seasonal Time Series of All Observations at 62010TripoliAirport
No of Observations
winter
spring
summer
autumn
Time

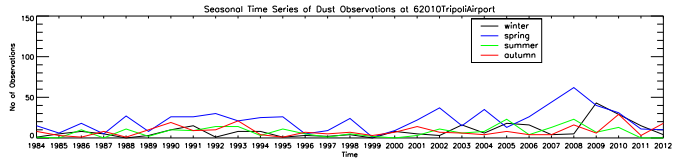
Seasonal Time Series of Dust Observations at 62010TripoliAirport
No of Observations
winter
spring
summer
autumn
Time

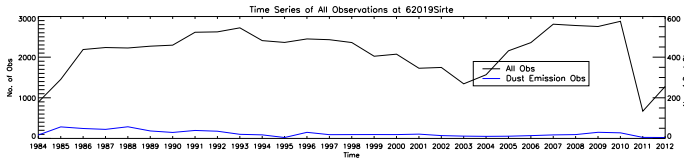
Time Series of All Observations at 62019Sirte
No. of Obs
No. of Dust Obs
All Obs
Dust Emission Obs
Time

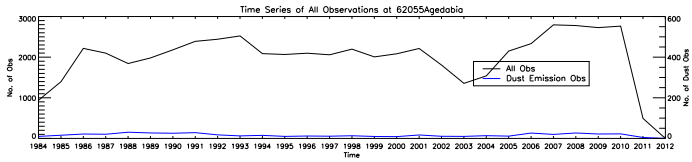
Time Series of All Observations at 62055Agedabia
No. of Obs
No. of Dust Obs
All Obs
Dust Emission Obs
Time

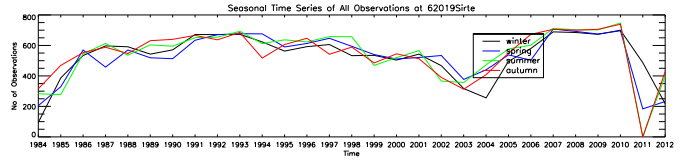
Seasonal Time Series of All Observations at 62019Sirte
No. of Observations
winter
spring
summer
autumn
Time

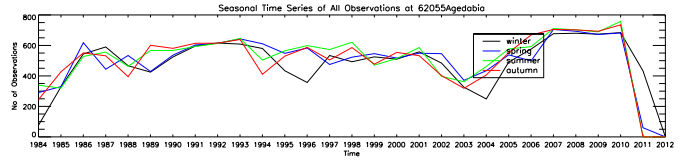
Seasonal Time Series of All Observations at 62055Agedabia
No. of Observations
winter
spring
summer
autumn
Time

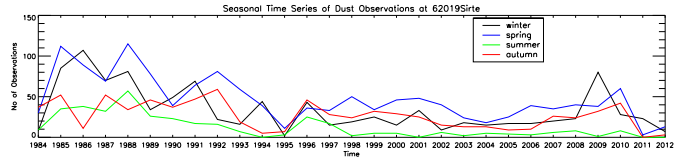
Seasonal Time Series of Dust Observations at 62019Sirte
No. of Observations
winter
spring
summer
autumn
Time

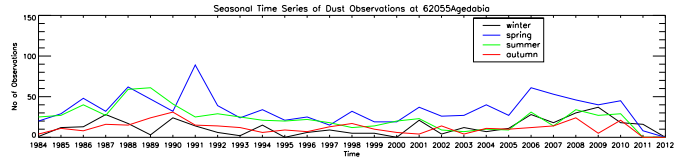
Seasonal Time Series of Dust Observations at 62055Agedabia
No. of Observations
winter
spring
summer
autumn
Time

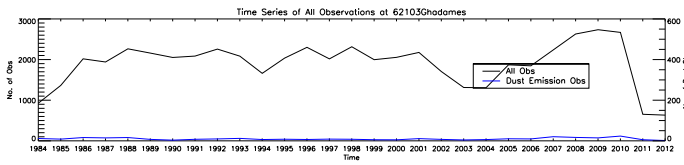
Time Series of All Observations at 62103Ghadames
No. of Obs
No. of Dust Obs
All Obs
Dust Emission Obs
Time

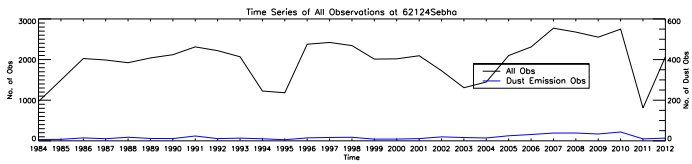
Time Series of All Observations at 62124Sebha
No. of Obs
No. of Dust Obs
All Obs
Dust Emission Obs
Time

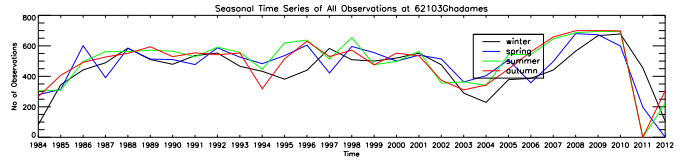
Seasonal Time Series of All Observations at 62103Ghadames
No. of Observations
winter
spring
summer
autumn
Time

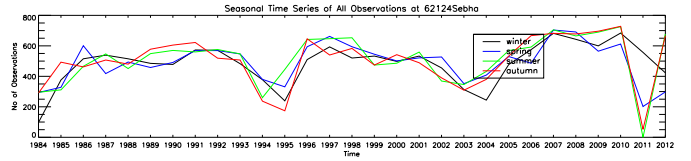
Seasonal Time Series of All Observations at 62124Sebha
No. of Observations
winter
spring
summer
autumn
Time

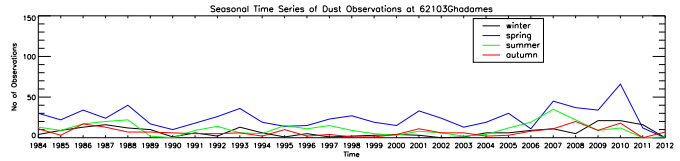
Seasonal Time Series of Dust Observations at 62103Ghadames
No. of Observations
winter
spring
summer
autumn
Time

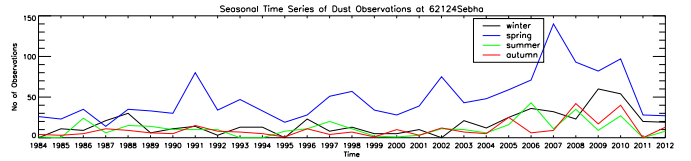
Seasonal Time Series of Dust Observations at 62124Sebha
No. of Observations
winter
spring
summer
autumn
Time

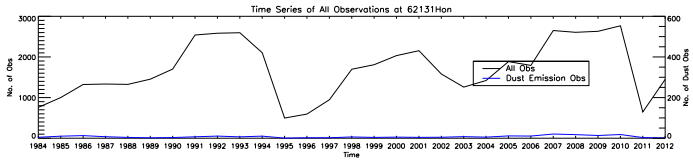
Time Series of All Observations at 62131Hon
No. of Obs
No. of Dust Obs
All Obs
Dust Emission Obs
Time

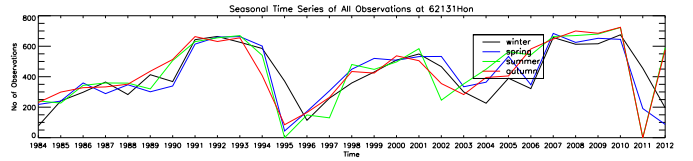
Seasonal Time Series of All Observations at 62131Hon
No of Observations
winter
spring
summer
autumn
Time

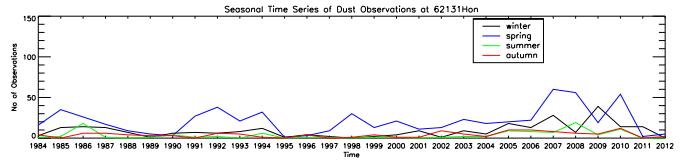
Seasonal Time Series of Dust Observations at 62131Hon
No of Observations
winter
spring
summer
autumn
Time

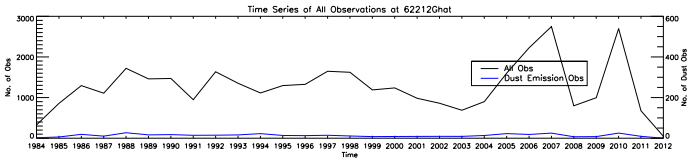
Time Series of All Observations at 62212Ghat
No. of Obs
No. of Dust Obs
All Obs
Dust Emission Obs
Time

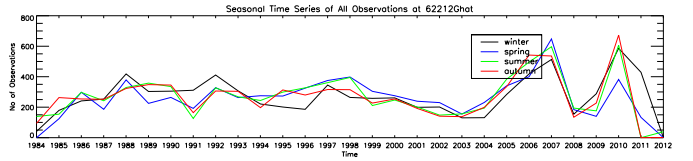
Seasonal Time Series of All Observations at 62212Ghat
No of Observations
winter
spring
summer
autumn
Time

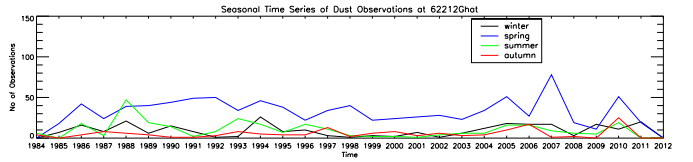
Seasonal Time Series of Dust Observations at 62212Ghat
No of Observations
winter
spring
summer
autumn
Time

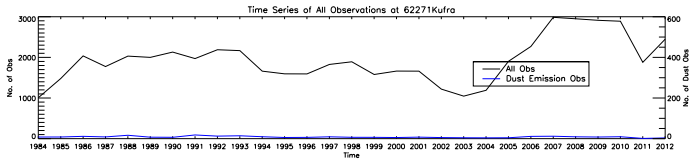
Time Series of All Observations at 62271Kufra
No. of Obs
No. of Dust Obs
All Obs
Dust Emission Obs
Time

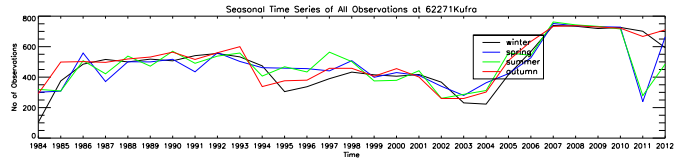
Seasonal Time Series of All Observations at 62271Kufra
No of Observations
winter
spring
summer
autumn
Time

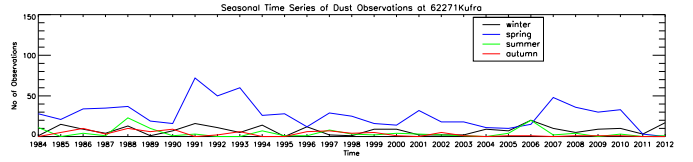
Seasonal Time Series of Dust Observations at 62271Kufra
No of Observations
winter
spring
summer
autumn
Time

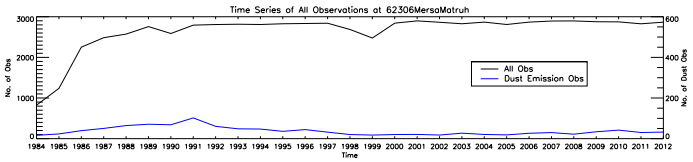
Time Series of All Observations at 62306MersaMatruh
No. of Obs
No. of Dust Obs
All Obs
Dust Emission Obs
Time

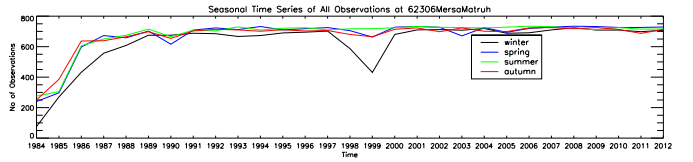
Seasonal Time Series of All Observations at 62306MersaMatruh
No of Observations
winter
spring
summer
autumn
Time

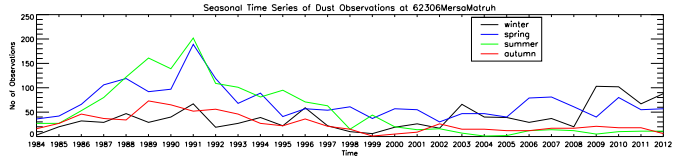
Seasonal Time Series of Dust Observations at 62306MersaMatruh
No of Observations
winter
spring
summer
autumn
Time

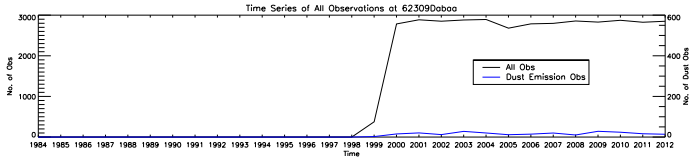
Time Series of All Observations at 62309Dabaa
No. of Obs
No. of Dust Obs
All Obs
Dust Emission Obs
Time

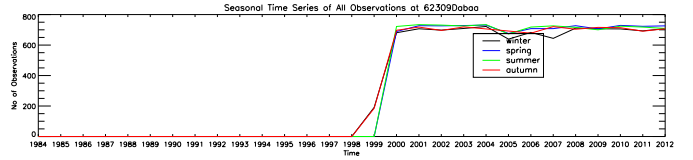
Seasonal Time Series of All Observations at 62309Dabaa
No of Observations
winter
spring
summer
autumn
Time

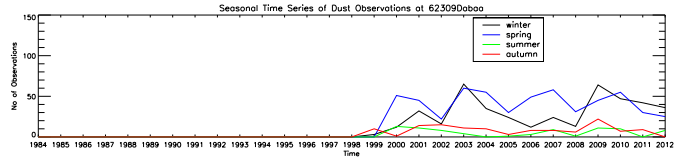
Seasonal Time Series of Dust Observations at 62309Dabaa
No of Observations
winter
spring
summer
autumn
Time

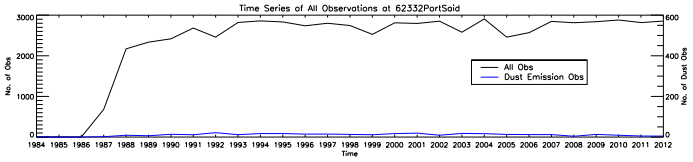
Time Series of All Observations at 62332PortSaid
No. of Obs
No. of Dust Obs
All Obs
Dust Emission Obs
Time

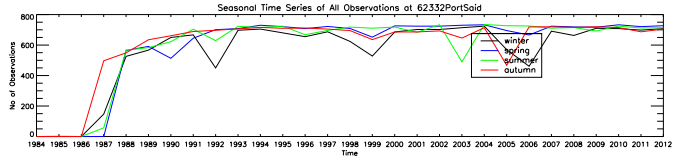
Seasonal Time Series of All Observations at 62332PortSaid
No of Observations
winter
spring
summer
autumn
Time

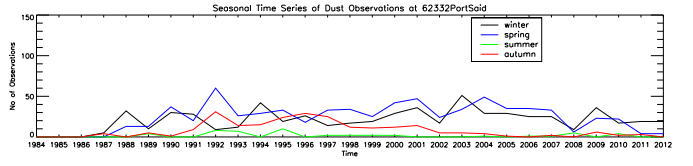
Seasonal Time Series of Dust Observations at 62332PortSaid
No of Observations
winter
spring
summer
autumn
Time

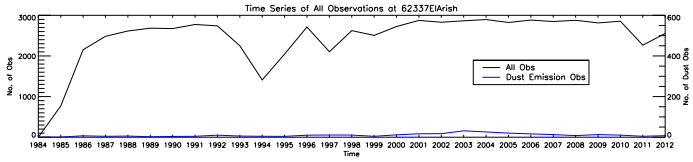
Time Series of All Observations at 62337ElArish
No. of Obs
No. of Dust Obs
All Obs
Dust Emission Obs
Time

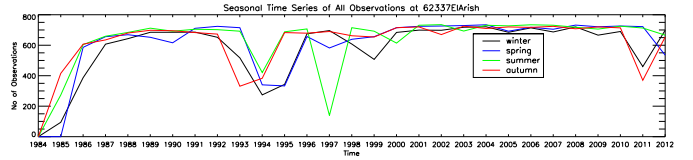
Seasonal Time Series of All Observations at 62337ElArish
No of Observations
winter
spring
summer
autumn
Time

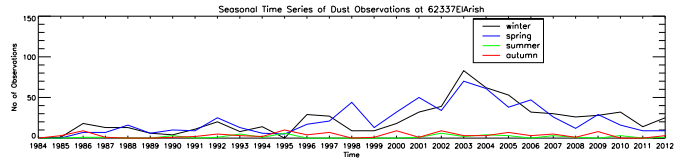
Seasonal Time Series of Dust Observations at 62337ElArish
No of Observations
winter
spring
summer
autumn
Time

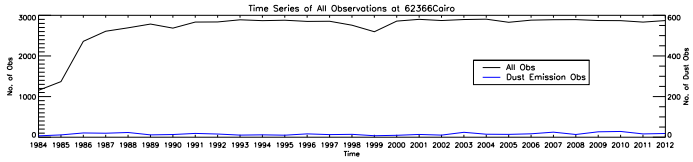
Time Series of All Observations at 62366Cairo
No. of Obs
No. of Dust Obs
All Obs
Dust Emission Obs
Time

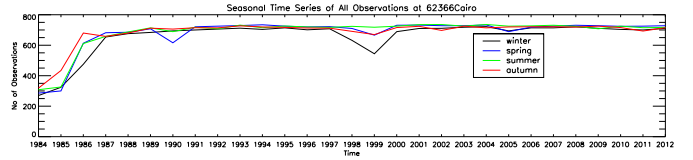
Seasonal Time Series of All Observations at 62366Cairo
No of Observations
winter
spring
summer
autumn
Time

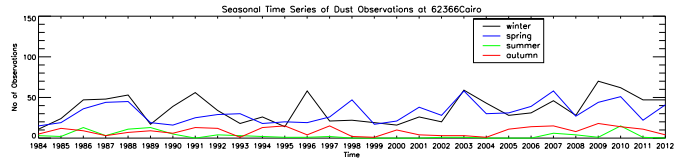
Seasonal Time Series of Dust Observations at 62366Cairo
No of Observations
winter
spring
summer
autumn
Time

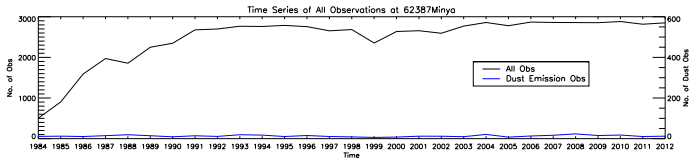
Time Series of All Observations at 62387Minya
No. of Obs
No. of Dust Obs
All Obs
Dust Emission Obs
Time

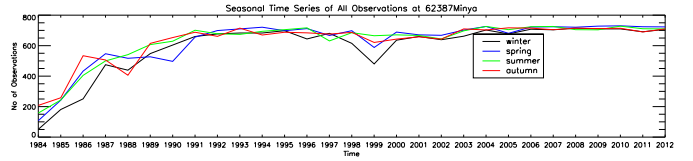
Seasonal Time Series of All Observations at 62387Minya
No of Observations
winter
spring
summer
autumn
Time

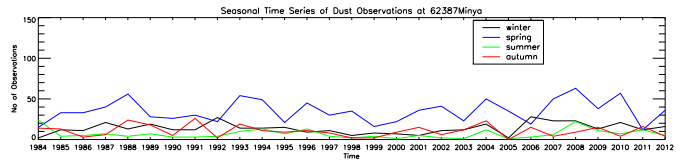
Seasonal Time Series of Dust Observations at 62387Minya
No of Observations
winter
spring
summer
autumn
Time

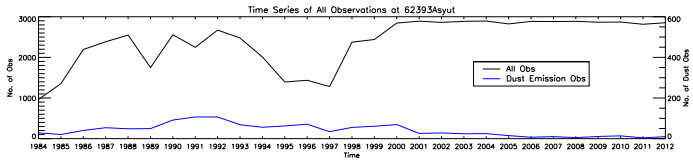
Time Series of All Observations at 62393Asyut
No. of Obs
No. of Dust Obs
All Obs
Dust Emission Obs
Time

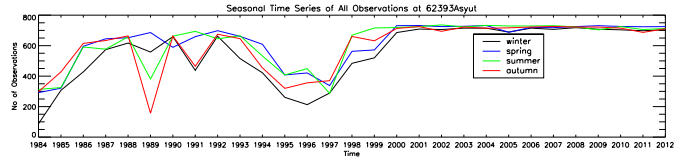
Seasonal Time Series of All Observations at 62393Asyut
No of Observations
winter
spring
summer
autumn
Time

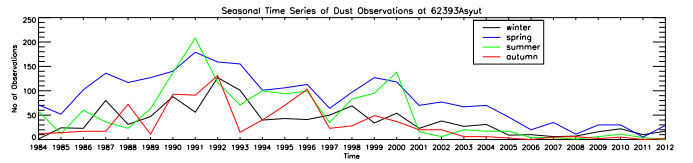
Seasonal Time Series of Dust Observations at 62393Asyut
No of Observations
winter
spring
summer
autumn
Time

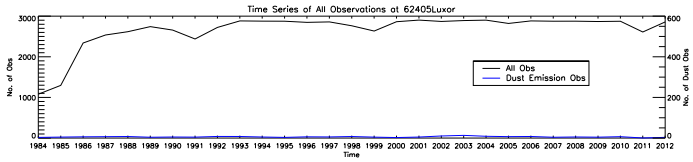
Time Series of All Observations at 62405Luxor
No. of Obs
No. of Dust Obs
All Obs
Dust Emission Obs
Time

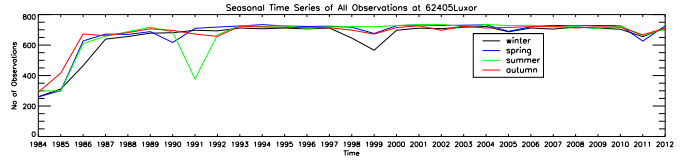
Seasonal Time Series of All Observations at 62405Luxor
No of Observations
winter
spring
summer
autumn
Time

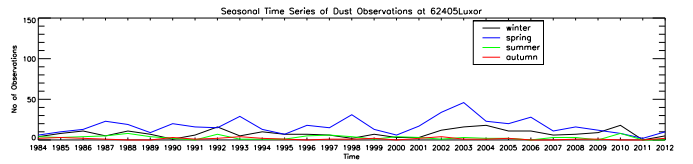
Seasonal Time Series of Dust Observations at 62405Luxor
No of Observations
winter
spring
summer
autumn
Time

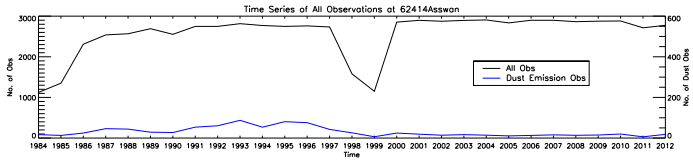
Time Series of All Observations at 62414Asswan
No. of Obs
No. of Dust Obs
All Obs
Dust Emission Obs
Time

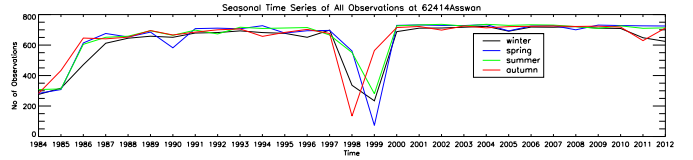
Seasonal Time Series of All Observations at 62414Asswan
No of Observations
winter
spring
summer
autumn
Time

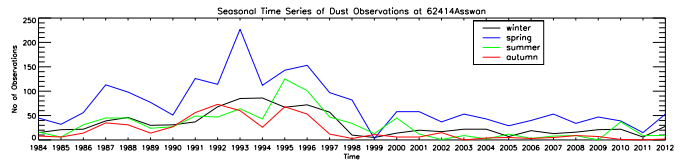
Seasonal Time Series of Dust Observations at 62414Asswan
No of Observations
winter
spring
summer
autumn
Time

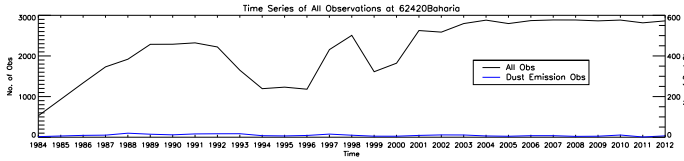
Time Series of All Observations at 62420Baharia
No. of Obs
No. of Dust Obs
All Obs
Dust Emission Obs
Time

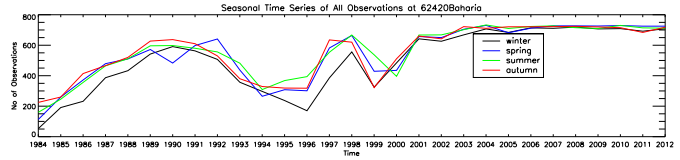
Seasonal Time Series of All Observations at 62420Baharia
No of Observations
winter
spring
summer
autumn
Time

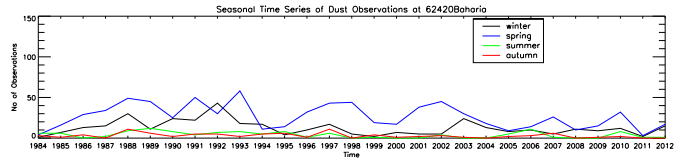
Seasonal Time Series of Dust Observations at 62420Baharia
No of Observations
winter
spring
summer
autumn
Time

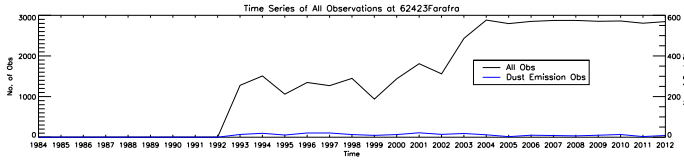
Time Series of All Observations at 62423Farafra
No. of Obs
No. of Dust Obs
All Obs
Dust Emission Obs
Time

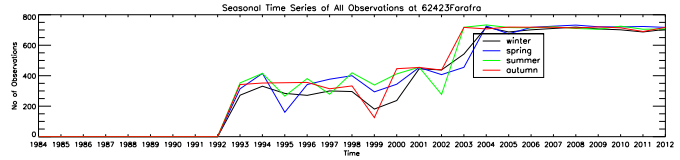
Seasonal Time Series of All Observations at 62423Farafra
No of Observations
winter
spring
summer
autumn
Time

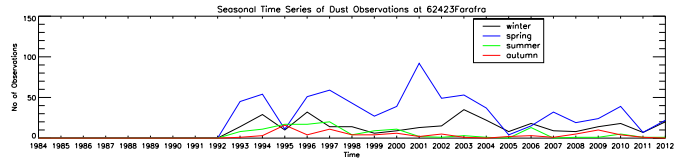
Seasonal Time Series of Dust Observations at 62423Farafra
No of Observations
winter
spring
summer
autumn
Time

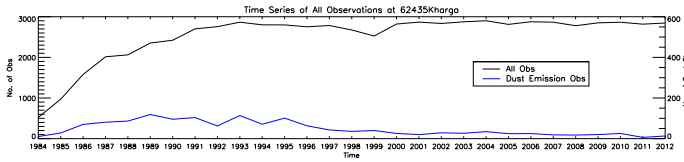
Time Series of All Observations at 62435Kharga
No. of Obs
No. of Dust Obs
All Obs
Dust Emission Obs
Time

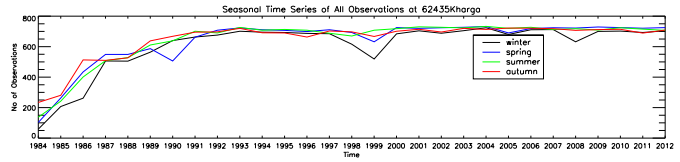
Seasonal Time Series of All Observations at 62435Kharga
No of Observations
winter
spring
summer
autumn
Time

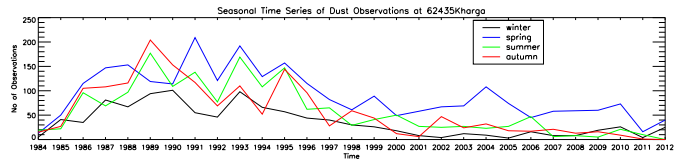
Seasonal Time Series of Dust Observations at 62435Kharga
No of Observations
winter
spring
summer
autumn
Time

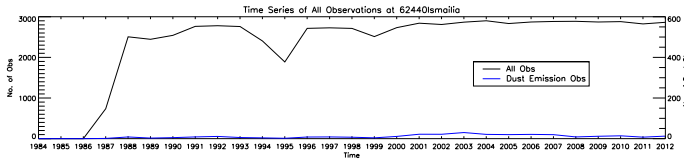
Time Series of All Observations at 62440Ismailia
No. of Obs
No. of Dust Obs
All Obs
Dust Emission Obs
Time

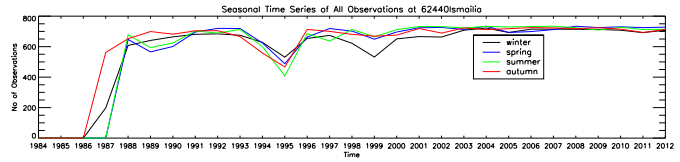
Seasonal Time Series of All Observations at 62440Ismailia
No of Observations
winter
spring
summer
autumn
Time

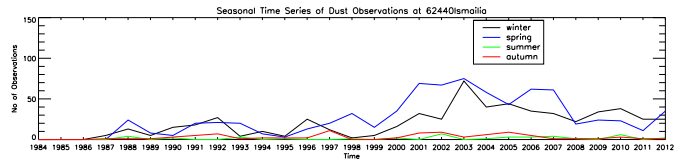
Seasonal Time Series of Dust Observations at 62440Ismailia
No of Observations
winter
spring
summer
autumn
Time

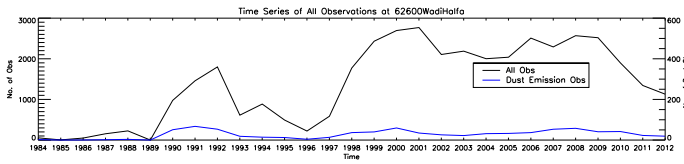
Time Series of All Observations at 62600WadiHalfa
No. of Obs
No. of Dust Obs
All Obs
Dust Emission Obs
Time

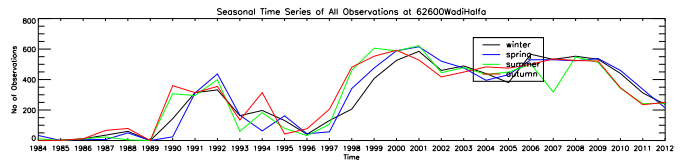
Seasonal Time Series of All Observations at 62600WadiHalfa
No of Observations
winter
spring
summer
autumn
Time

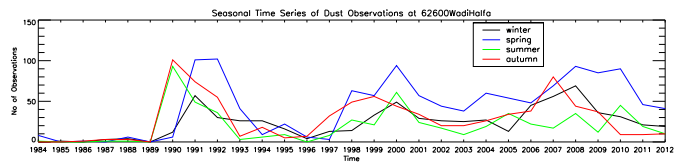
Seasonal Time Series of Dust Observations at 62600WadiHalfa
No of Observations
winter
spring
summer
autumn
Time

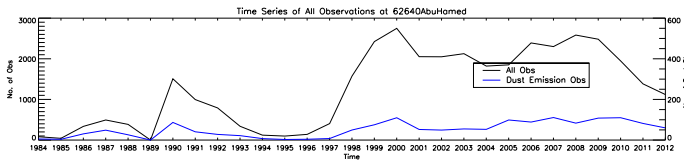
Time Series of All Observations at 62640AbuHamed
No. of Obs
No. of Dust Obs
All Obs
Dust Emission Obs
Time

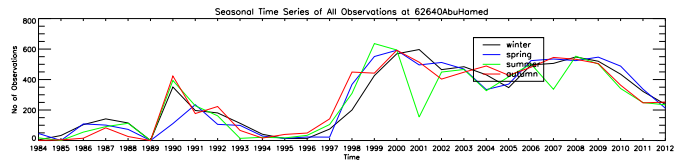
Seasonal Time Series of All Observations at 62640AbuHamed
No of Observations
winter
spring
summer
autumn
Time

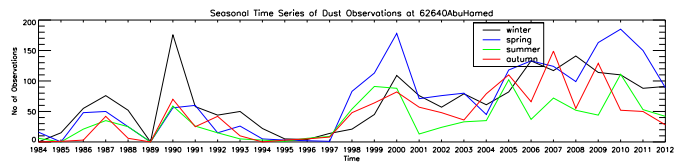
Seasonal Time Series of Dust Observations at 62640AbuHamed
No of Observations
winter
spring
summer
autumn
Time

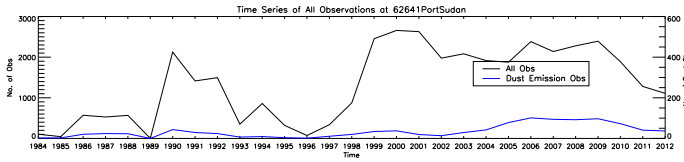
Time Series of All Observations at 62641PortSudan
No. of Obs
No. of Dust Obs
All Obs
Dust Emission Obs
Time

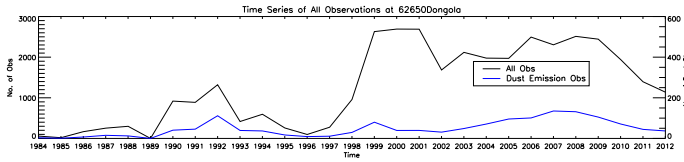
Time Series of All Observations at 62650Dongola
No. of Obs
No. of Dust Obs
All Obs
Dust Emission Obs
Time

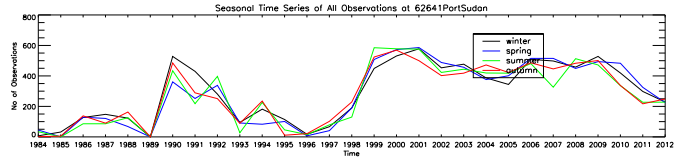
Seasonal Time Series of All Observations at 62641PortSudan
No. of Observations
winter
spring
summer
autumn
Time

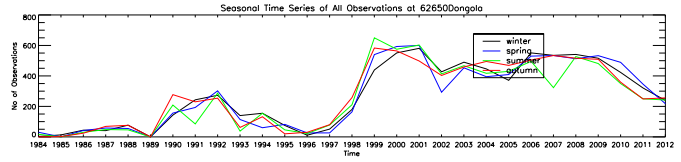
Seasonal Time Series of All Observations at 62650Dongola
No. of Observations
winter
spring
summer
autumn
Time

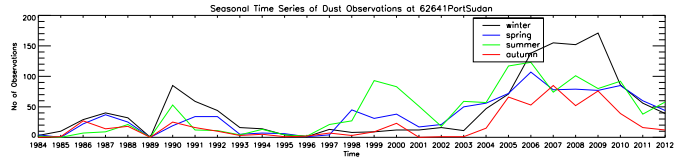
Seasonal Time Series of Dust Observations at 62641PortSudan
No. of Observations
winter
spring
summer
autumn
Time

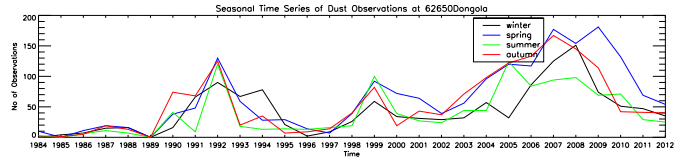
Seasonal Time Series of Dust Observations at 62650Dongola
No. of Observations
winter
spring
summer
autumn
Time

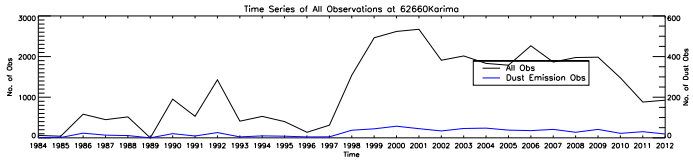
Time Series of All Observations at 62660Karima
No. of Obs
No. of Dust Obs
All Obs
Dust Emission Obs
Time

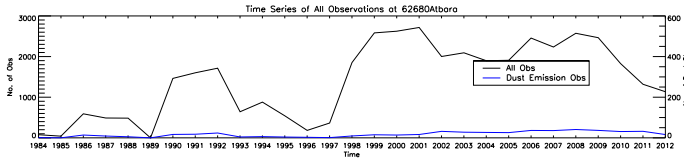
Time Series of All Observations at 62680Atbara
No. of Obs
No. of Dust Obs
All Obs
Dust Emission Obs
Time

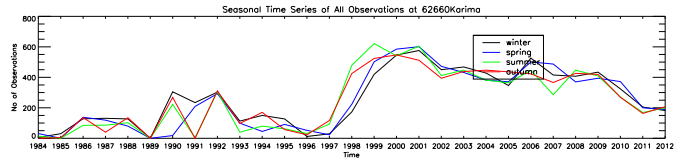
Seasonal Time Series of All Observations at 62660Karima
No. of Observations
winter
spring
summer
autumn
Time

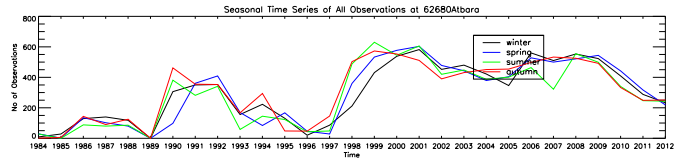
Seasonal Time Series of All Observations at 62680Atbara
No. of Observations
winter
spring
summer
autumn
Time

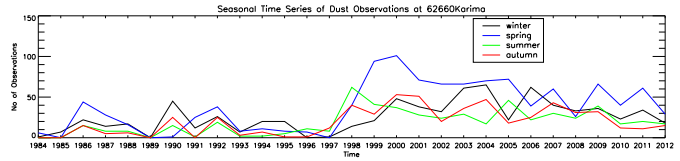
Seasonal Time Series of Dust Observations at 62660Karima
No. of Observations
winter
spring
summer
autumn
Time

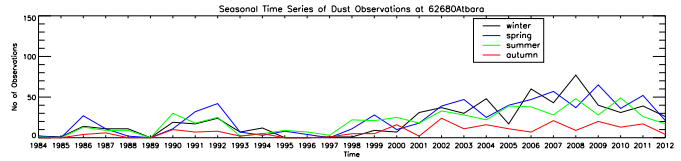
Seasonal Time Series of Dust Observations at 62680Atbara
No. of Observations
winter
spring
summer
autumn
Time

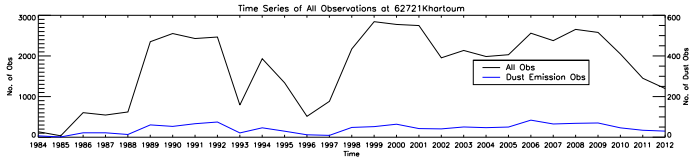
Time Series of All Observations at 62721Khartoum
No. of Obs
No. of Dust Obs
All Obs
Dust Emission Obs
Time

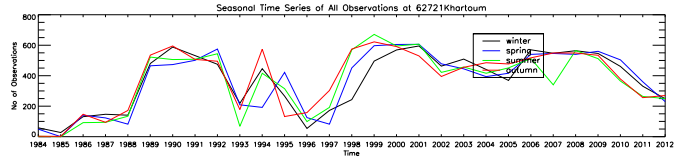
Seasonal Time Series of All Observations at 62721Khartoum
No of Observations
winter
spring
summer
autumn
Time

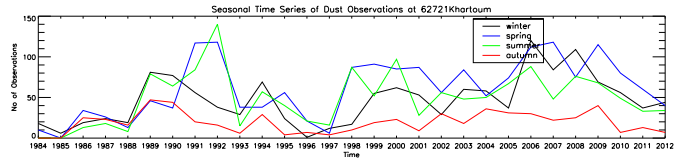
Seasonal Time Series of Dust Observations at 62721Khartoum
No of Observations
winter
spring
summer
autumn
Time

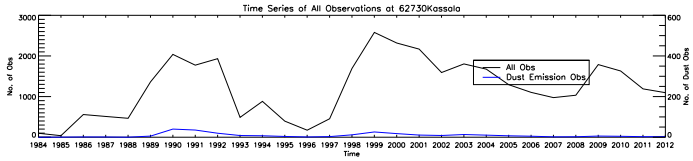
Time Series of All Observations at 62730Kassala
No. of Obs
No. of Dust Obs
All Obs
Dust Emission Obs
Time

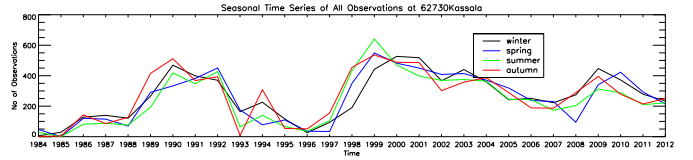
Seasonal Time Series of All Observations at 62730Kassala
No of Observations
winter
spring
summer
autumn
Time

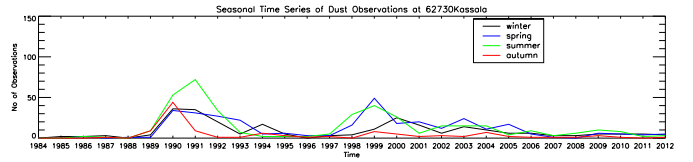
Seasonal Time Series of Dust Observations at 62730Kassala
No of Observations
winter
spring
summer
autumn
Time

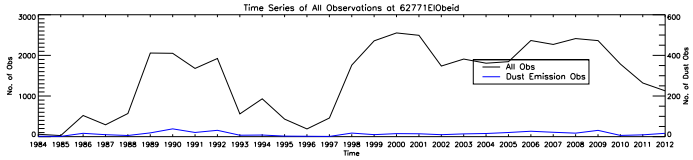
Time Series of All Observations at 62771ElObeid
No. of Obs
No. of Dust Obs
All Obs
Dust Emission Obs
Time

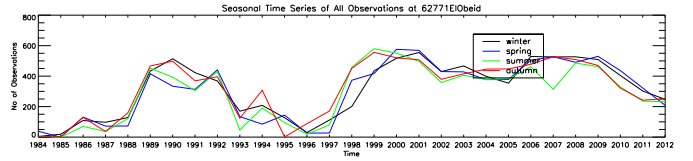
Seasonal Time Series of All Observations at 62771ElObeid
No of Observations
winter
spring
summer
autumn
Time

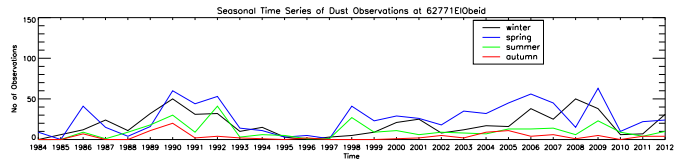
Seasonal Time Series of Dust Observations at 62771ElObeid
No of Observations
winter
spring
summer
autumn
Time

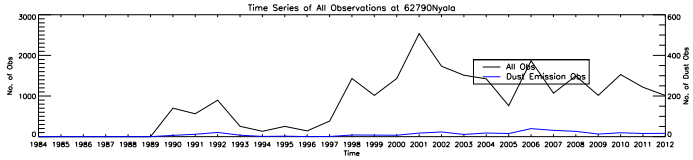
Time Series of All Observations at 62790Nyala
No. of Obs
No. of Dust Obs
All Obs
Dust Emission Obs
Time

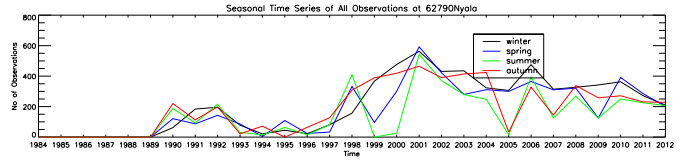
Seasonal Time Series of All Observations at 62790Nyala
No of Observations
winter
spring
summer
autumn
Time

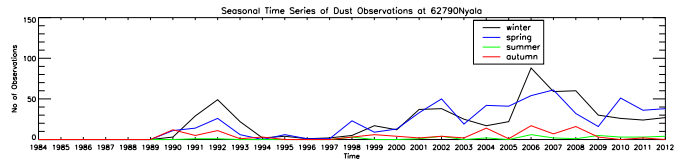
Seasonal Time Series of Dust Observations at 62790Nyala
No of Observations
winter
spring
summer
autumn
Time

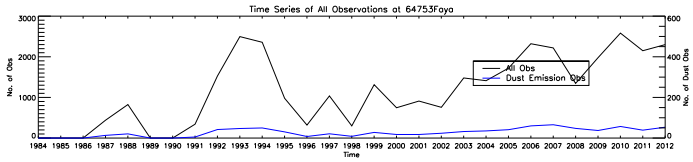
Time Series of All Observations at 64753Faya
No. of Obs
No. of Dust Obs
All Obs
Dust Emission Obs
Time

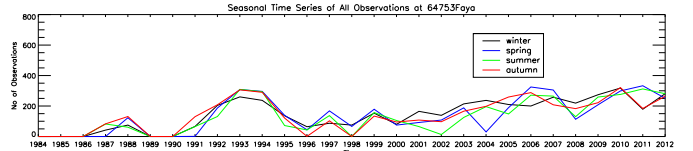
Seasonal Time Series of All Observations at 64753Faya
No of Observations
winter
spring
summer
autumn
Time

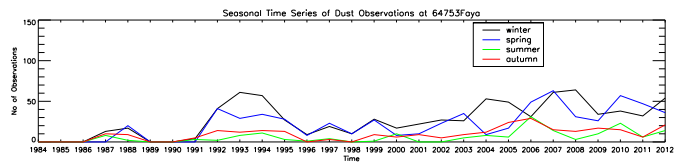
Seasonal Time Series of Dust Observations at 64753Faya
No of Observations
winter
spring
summer
autumn
Time

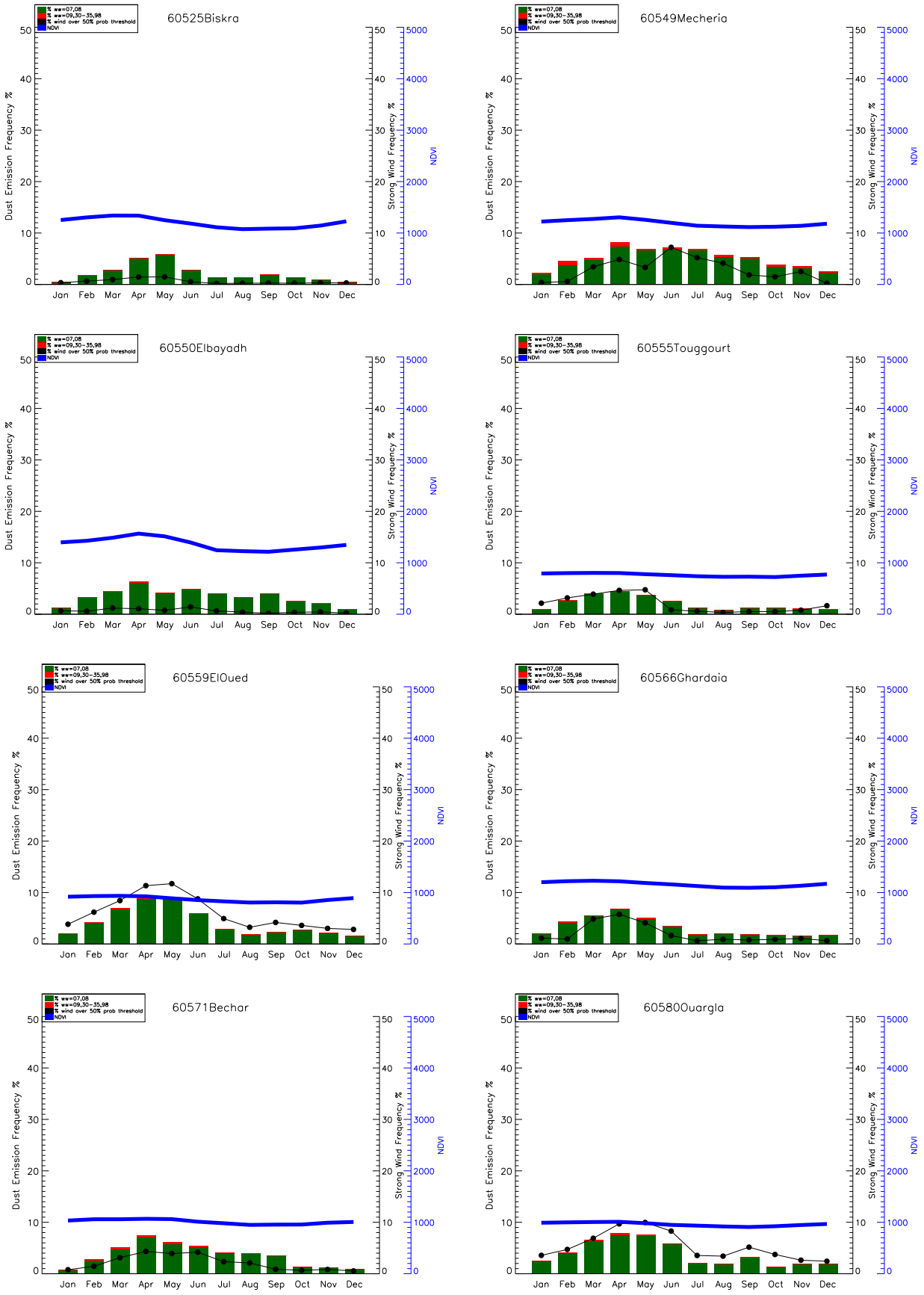

FIGURE 4: Mean seasonal cycle of frequency of dust emission (FDE) and strong wind frequency (SWF) for each of the 70 stations. Monthly mean FDE is split into BDF (green bars) and DSF (red bars) (for definitions, see section 3.2), as well as monthly mean NDVI (blue lines) calculated for a 24km x 24km box centred on each station. Strong wind frequency (SWF; black dotted line) is calculated for winds over T50 at each station.

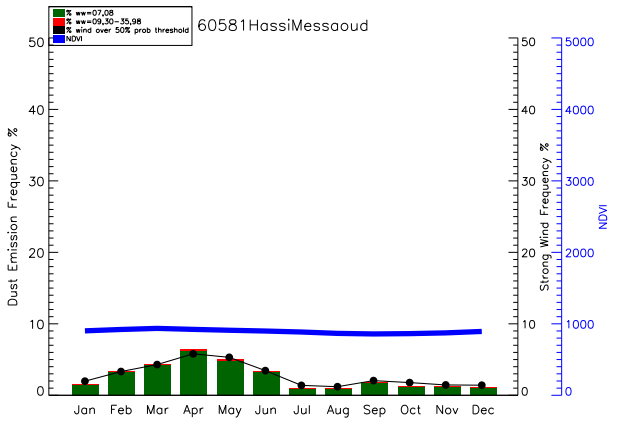
% ww=07,08
% ww=09,30-35,98
% wind over 50% prob threshold
NDVI
60581HassiMessaoud
Dust Emission Frequency %
Strong Wind Frequency %
NDVI
Jan Feb Mar Apr May Jun Jul Aug Sep Oct Nov Dec

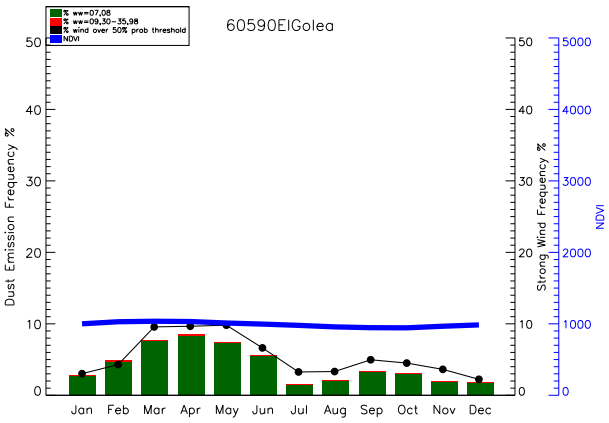
% ww=07,08
% ww=09,30-35,98
% wind over 50% prob threshold
NDVI
60590ElGolea
Dust Emission Frequency %
Strong Wind Frequency %
NDVI
Jan Feb Mar Apr May Jun Jul Aug Sep Oct Nov Dec

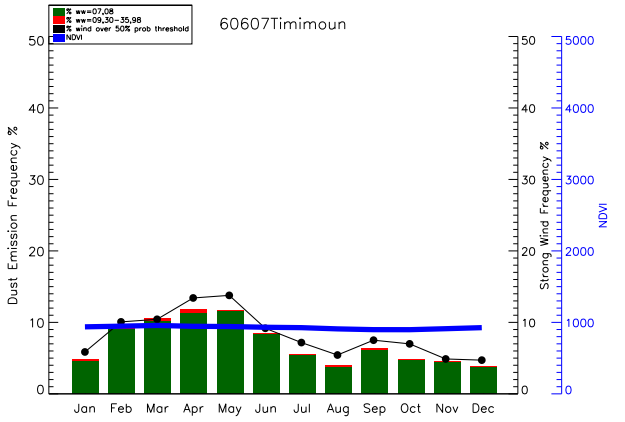
% ww=07,08
% ww=09,30-35,98
% wind over 50% prob threshold
NDVI
60607Timimoun
Dust Emission Frequency %
Strong Wind Frequency %
NDVI
Jan Feb Mar Apr May Jun Jul Aug Sep Oct Nov Dec

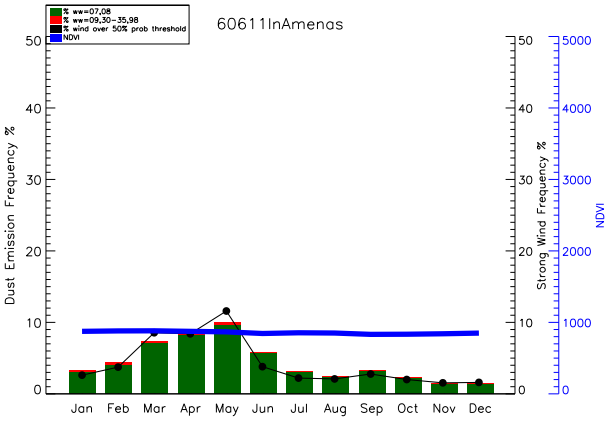
% ww=07,08
% ww=09,30-35,98
% wind over 50% prob threshold
NDVI
60611InAmenas
Dust Emission Frequency %
Strong Wind Frequency %
NDVI
Jan Feb Mar Apr May Jun Jul Aug Sep Oct Nov Dec

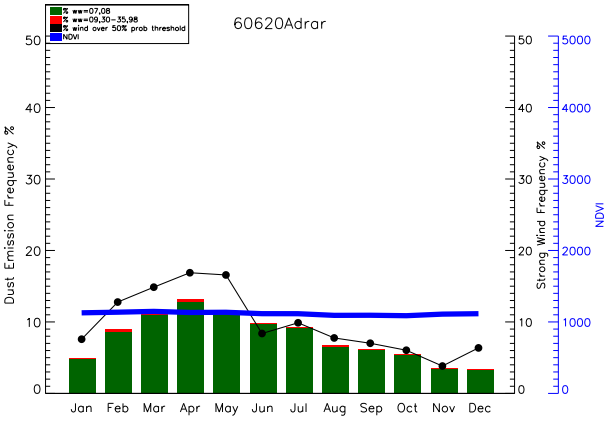
% ww=07,08
% ww=09,30-35,98
% wind over 50% prob threshold
NDVI
60620Adrar
Dust Emission Frequency %
Strong Wind Frequency %
NDVI
Jan Feb Mar Apr May Jun Jul Aug Sep Oct Nov Dec

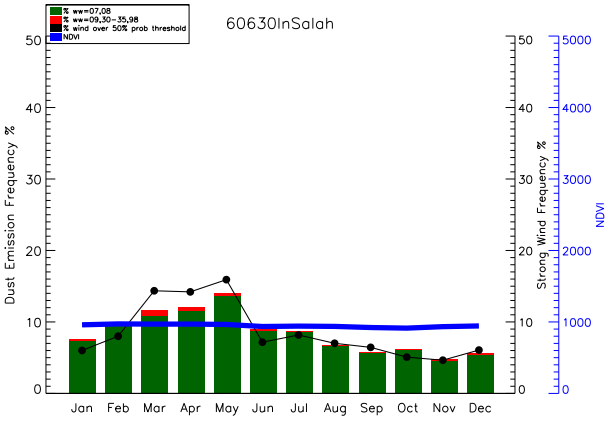
% ww=07,08
% ww=09,30-35,98
% wind over 50% prob threshold
NDVI
60630InSalah
Dust Emission Frequency %
Strong Wind Frequency %
NDVI
Jan Feb Mar Apr May Jun Jul Aug Sep Oct Nov Dec

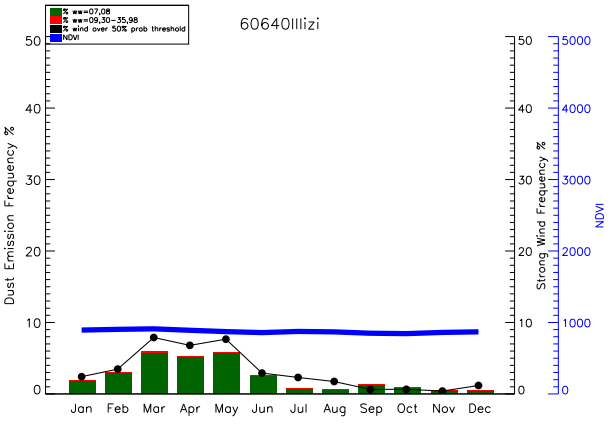
% ww=07,08
% ww=09,30-35,98
% wind over 50% prob threshold
NDVI
60640Illizi
Dust Emission Frequency %
Strong Wind Frequency %
NDVI
Jan Feb Mar Apr May Jun Jul Aug Sep Oct Nov Dec

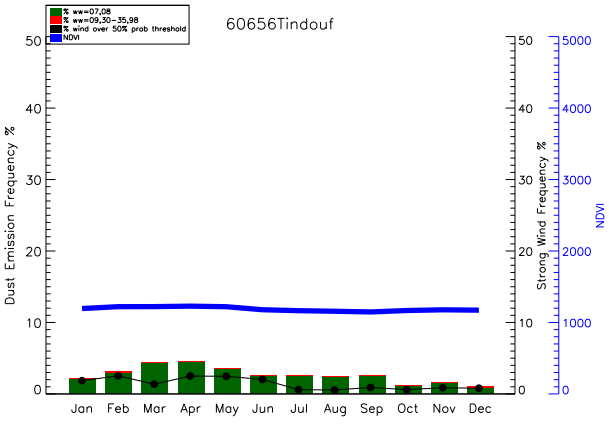
% ww=07,08
% ww=09,30-35,98
% wind over 50% prob threshold
NDVI
60656Tindouf
Dust Emission Frequency %
Strong Wind Frequency %
NDVI
Jan Feb Mar Apr May Jun Jul Aug Sep Oct Nov Dec

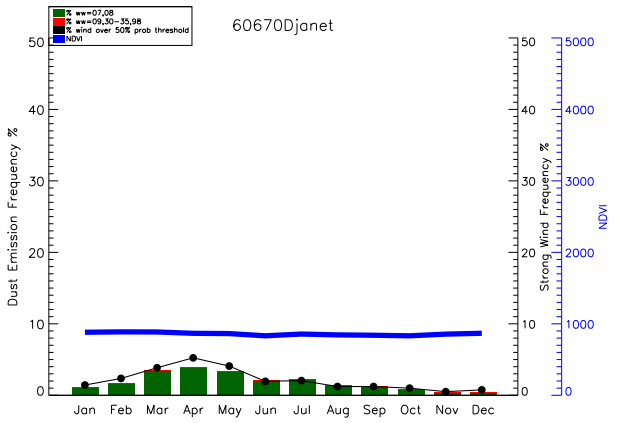
60670Djanet
% ww=07,08
% ww=09,30-35,98
% wind over 50% prob threshold
NDVI
Dust Emission Frequency %
Strong Wind Frequency %
NDVI
Jan Feb Mar Apr May Jun Jul Aug Sep Oct Nov Dec

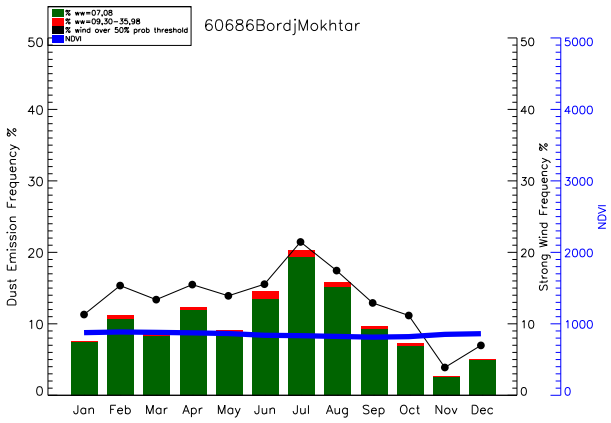
60686BordjMokhtar
% ww=07,08
% ww=09,30-35,98
% wind over 50% prob threshold
NDVI
Dust Emission Frequency %
Strong Wind Frequency %
NDVI
Jan Feb Mar Apr May Jun Jul Aug Sep Oct Nov Dec

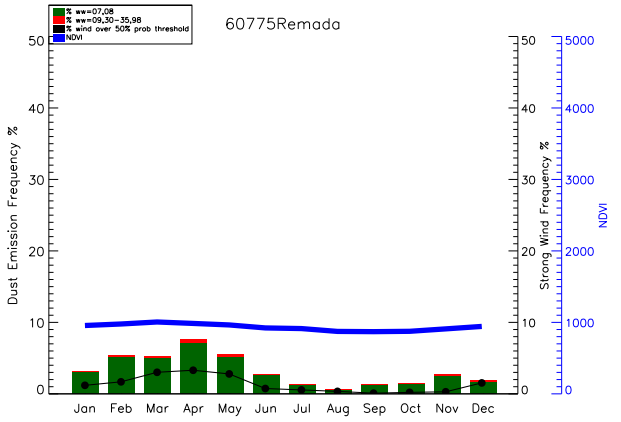
60775Remada
% ww=07,08
% ww=09,30-35,98
% wind over 50% prob threshold
NDVI
Dust Emission Frequency %
Strong Wind Frequency %
NDVI
Jan Feb Mar Apr May Jun Jul Aug Sep Oct Nov Dec

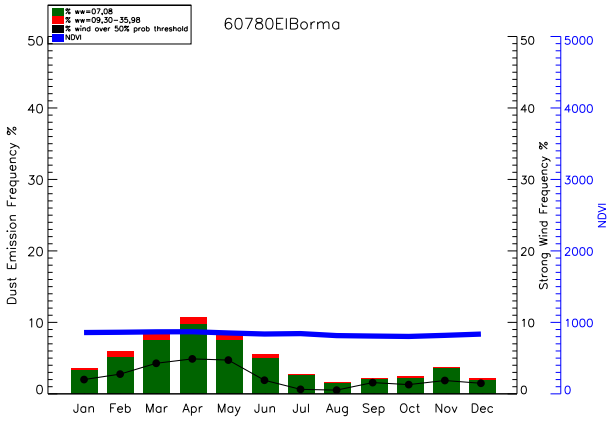
60780ElBorma
% ww=07,08
% ww=09,30-35,98
% wind over 50% prob threshold
NDVI
Dust Emission Frequency %
Strong Wind Frequency %
NDVI
Jan Feb Mar Apr May Jun Jul Aug Sep Oct Nov Dec

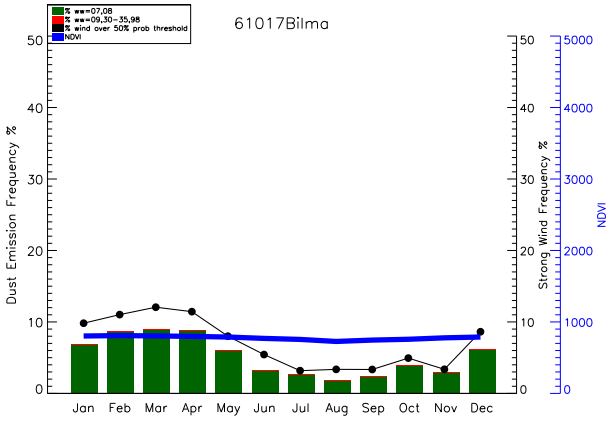
61017Bilma
% ww=07,08
% ww=09,30-35,98
% wind over 50% prob threshold
NDVI
Dust Emission Frequency %
Strong Wind Frequency %
NDVI
Jan Feb Mar Apr May Jun Jul Aug Sep Oct Nov Dec

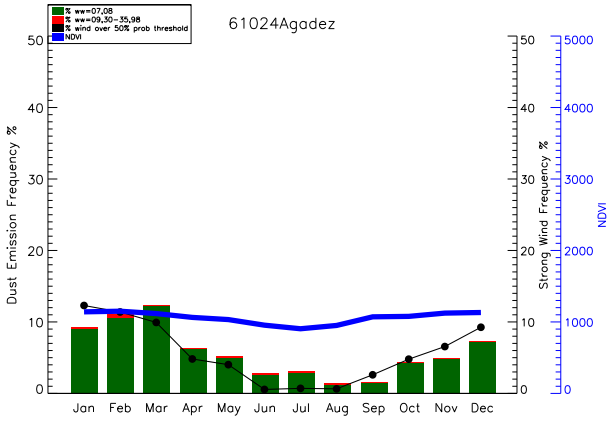
61024Agadez
% ww=07,08
% ww=09,30-35,98
% wind over 50% prob threshold
NDVI
Dust Emission Frequency %
Strong Wind Frequency %
NDVI
Jan Feb Mar Apr May Jun Jul Aug Sep Oct Nov Dec

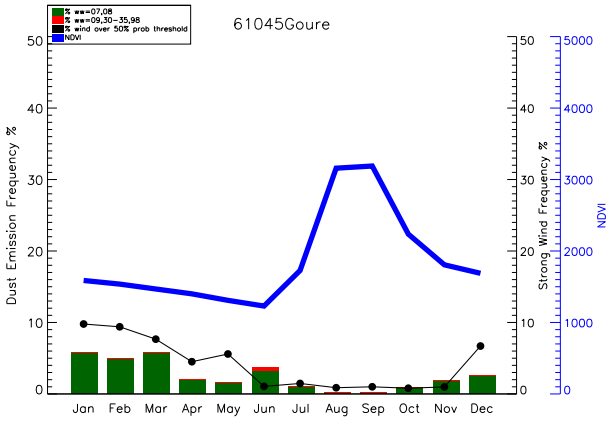
61045Goure
% ww=07,08
% ww=09,30-35,98
% wind over 50% prob threshold
NDVI
Dust Emission Frequency %
Strong Wind Frequency %
NDVI
Jan Feb Mar Apr May Jun Jul Aug Sep Oct Nov Dec

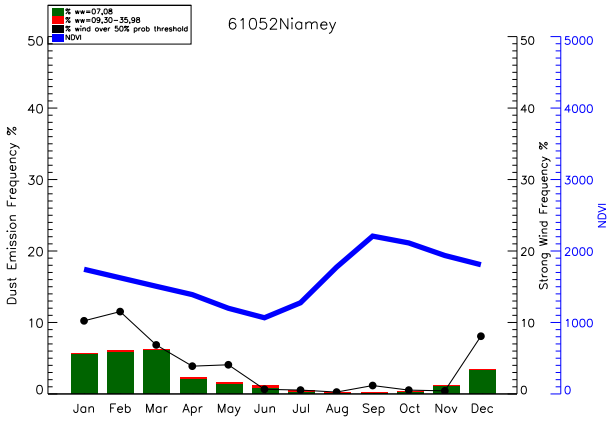
61052Niamey
% ww=07,08
% ww=09,30-35,98
% wind over 50% prob threshold
NDVI
Dust Emission Frequency %
Strong Wind Frequency %
NDVI
Jan Feb Mar Apr May Jun Jul Aug Sep Oct Nov Dec

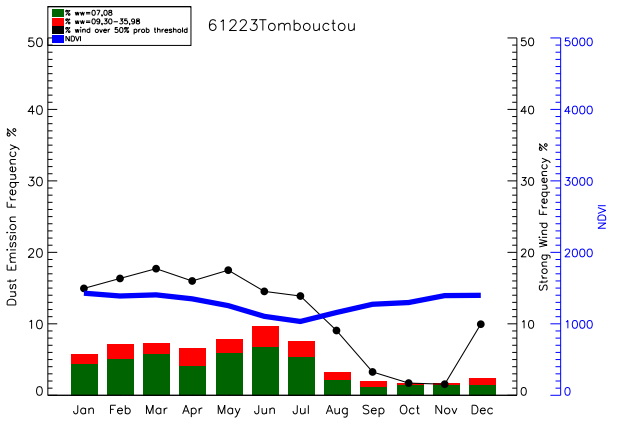
% ww=07,08
% ww=09,30-35,98
% wind over 50% prob threshold
NDVI
61223Tombouctou
Dust Emission Frequency %
Strong Wind Frequency %
NDVI
Jan Feb Mar Apr May Jun Jul Aug Sep Oct Nov Dec

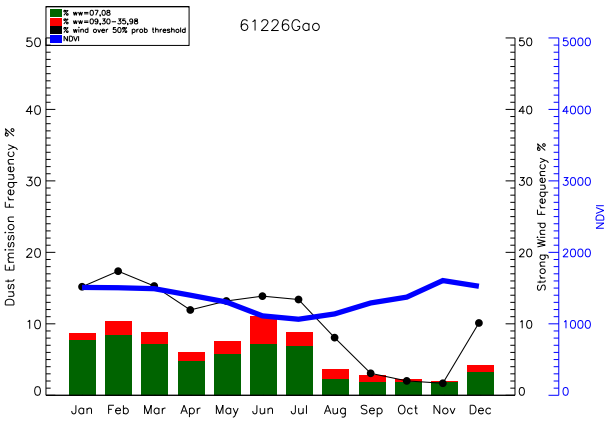
% ww=07,08
% ww=09,30-35,98
% wind over 50% prob threshold
NDVI
61226Gao
Dust Emission Frequency %
Strong Wind Frequency %
NDVI
Jan Feb Mar Apr May Jun Jul Aug Sep Oct Nov Dec

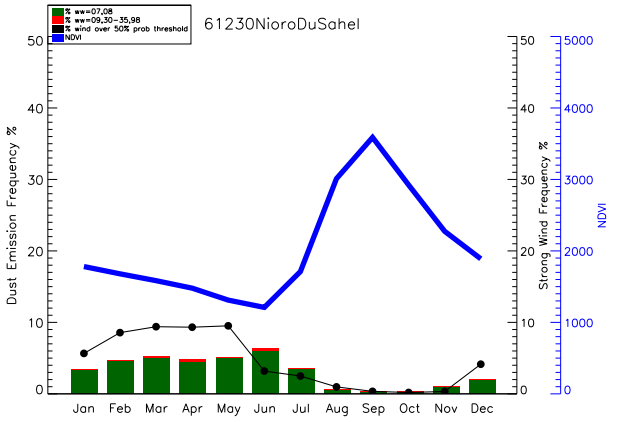
% ww=07,08
% ww=09,30-35,98
% wind over 50% prob threshold
NDVI
61230NioroDuSahel
Dust Emission Frequency %
Strong Wind Frequency %
NDVI
Jan Feb Mar Apr May Jun Jul Aug Sep Oct Nov Dec

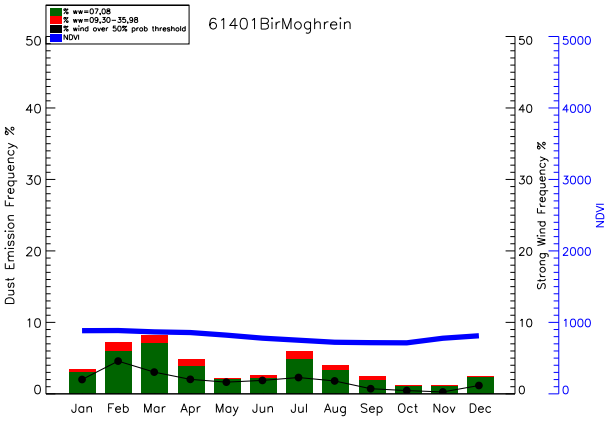
% ww=07,08
% ww=09,30-35,98
% wind over 50% prob threshold
NDVI
61401BirMoghrein
Dust Emission Frequency %
Strong Wind Frequency %
NDVI
Jan Feb Mar Apr May Jun Jul Aug Sep Oct Nov Dec

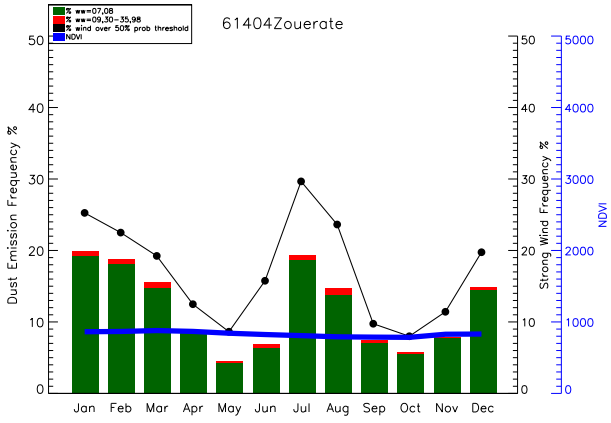
% ww=07,08
% ww=09,30-35,98
% wind over 50% prob threshold
NDVI
61404Zouerate
Dust Emission Frequency %
Strong Wind Frequency %
NDVI
Jan Feb Mar Apr May Jun Jul Aug Sep Oct Nov Dec

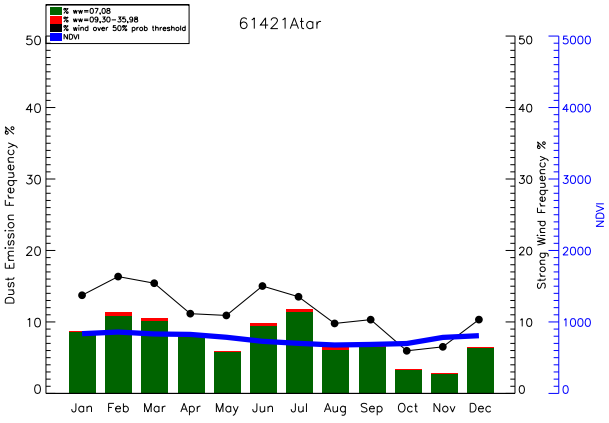
% ww=07,08
% ww=09,30-35,98
% wind over 50% prob threshold
NDVI
61421Atar
Dust Emission Frequency %
Strong Wind Frequency %
NDVI
Jan Feb Mar Apr May Jun Jul Aug Sep Oct Nov Dec

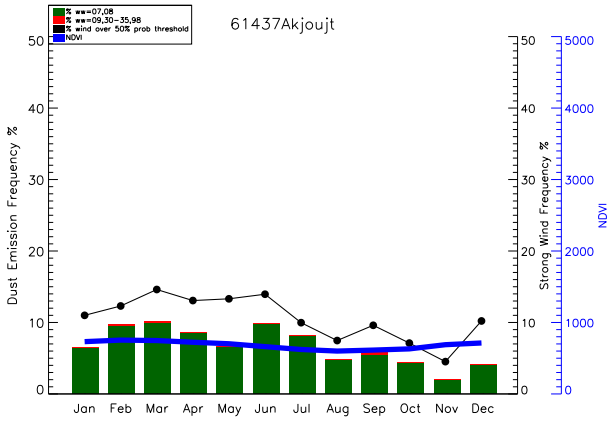
% ww=07,08
% ww=09,30-35,98
% wind over 50% prob threshold
NDVI
61437Akjoujt
Dust Emission Frequency %
Strong Wind Frequency %
NDVI
Jan Feb Mar Apr May Jun Jul Aug Sep Oct Nov Dec

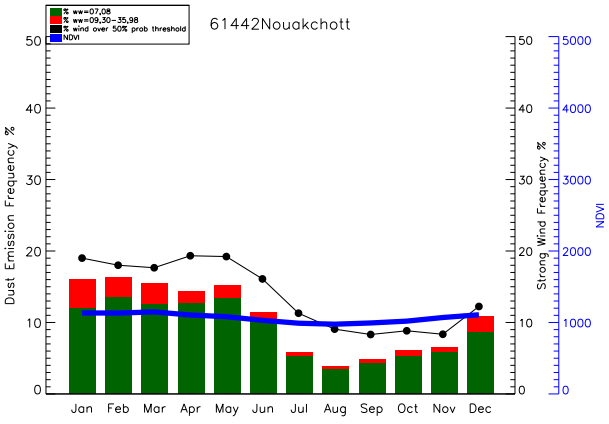
% ww=07,08
% ww=09,30-35,98
% wind over 50% prob threshold
NDVI
61442Nouakchott
Dust Emission Frequency %
Strong Wind Frequency %
NDVI
Jan Feb Mar Apr May Jun Jul Aug Sep Oct Nov Dec

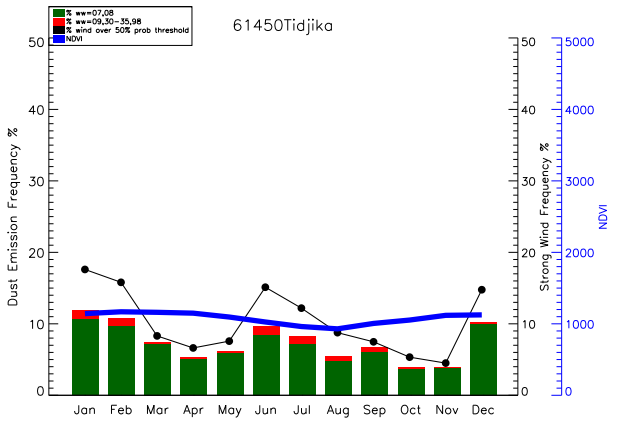
61450Tidjika
% ww=07,08
% ww=09,30-35,98
% wind over 50% prob threshold
NDVI
Dust Emission Frequency %
Strong Wind Frequency %
NDVI
Jan Feb Mar Apr May Jun Jul Aug Sep Oct Nov Dec

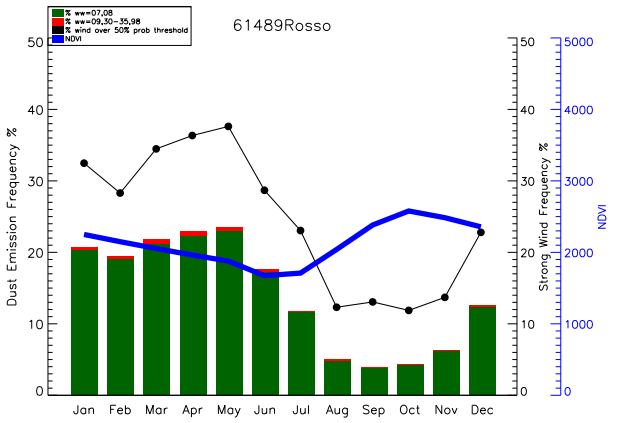
61489Rosso
% ww=07,08
% ww=09,30-35,98
% wind over 50% prob threshold
NDVI
Dust Emission Frequency %
Strong Wind Frequency %
NDVI
Jan Feb Mar Apr May Jun Jul Aug Sep Oct Nov Dec

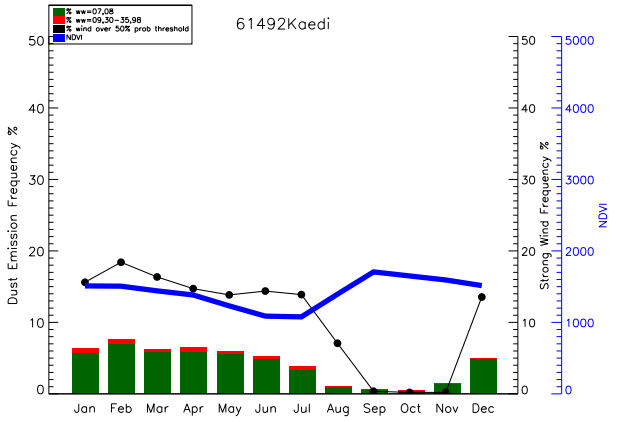
61492Kaedi
% ww=07,08
% ww=09,30-35,98
% wind over 50% prob threshold
NDVI
Dust Emission Frequency %
Strong Wind Frequency %
NDVI
Jan Feb Mar Apr May Jun Jul Aug Sep Oct Nov Dec

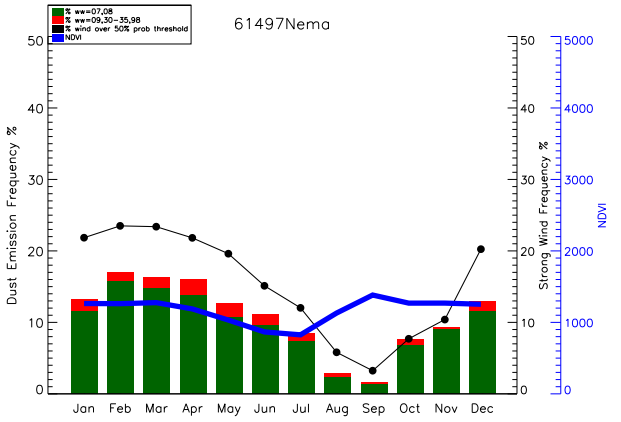
61497Nema
% ww=07,08
% ww=09,30-35,98
% wind over 50% prob threshold
NDVI
Dust Emission Frequency %
Strong Wind Frequency %
NDVI
Jan Feb Mar Apr May Jun Jul Aug Sep Oct Nov Dec

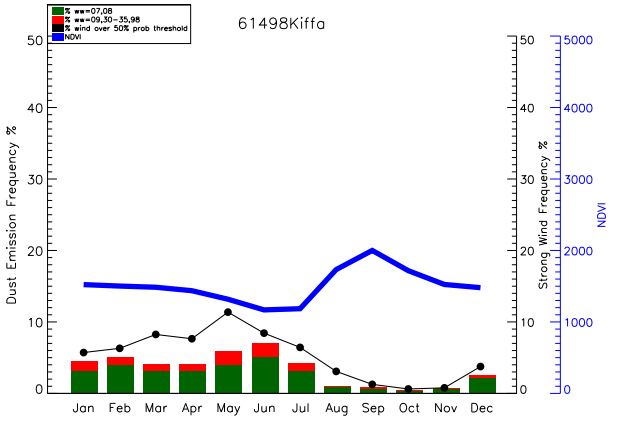
61498Kiffa
% ww=07,08
% ww=09,30-35,98
% wind over 50% prob threshold
NDVI
Dust Emission Frequency %
Strong Wind Frequency %
NDVI
Jan Feb Mar Apr May Jun Jul Aug Sep Oct Nov Dec

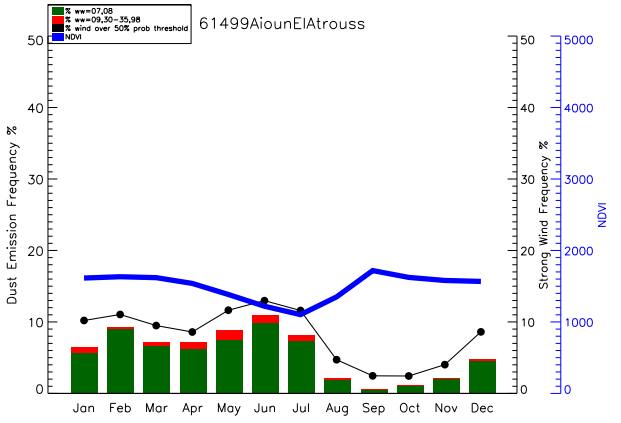
61499AiounElAtrouss
% ww=07,08
% ww=09,30-35,98
% wind over 50% prob threshold
NDVI
Dust Emission Frequency %
Strong Wind Frequency %
NDVI
Jan Feb Mar Apr May Jun Jul Aug Sep Oct Nov Dec

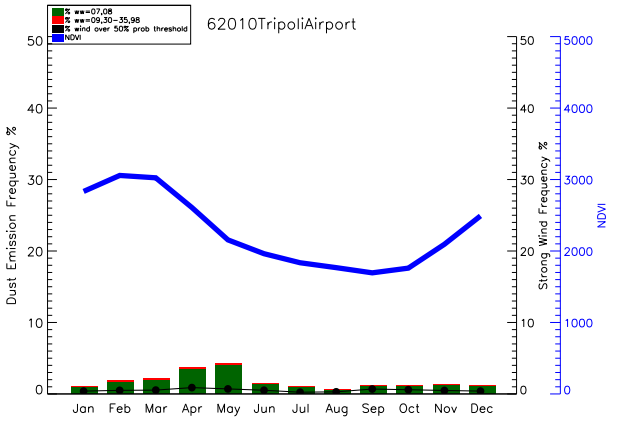
62010TripoliAirport
% ww=07,08
% ww=09,30-35,98
% wind over 50% prob threshold
NDVI
Dust Emission Frequency %
Strong Wind Frequency %
NDVI
Jan Feb Mar Apr May Jun Jul Aug Sep Oct Nov Dec

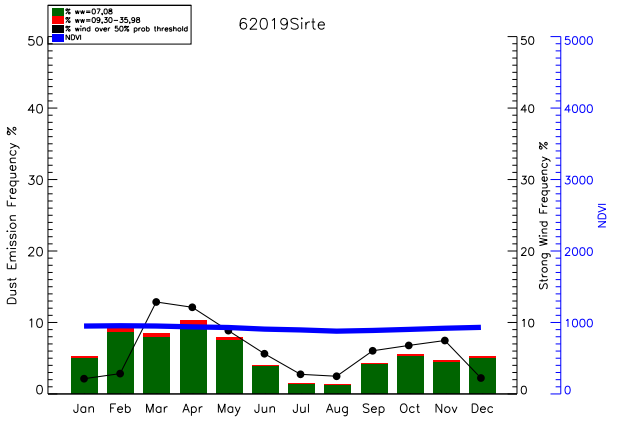
62019Sirte
% ww=07,08
% ww=09,30-35,98
% wind over 50% prob threshold
NDVI
Dust Emission Frequency %
Strong Wind Frequency %
NDVI
Jan Feb Mar Apr May Jun Jul Aug Sep Oct Nov Dec

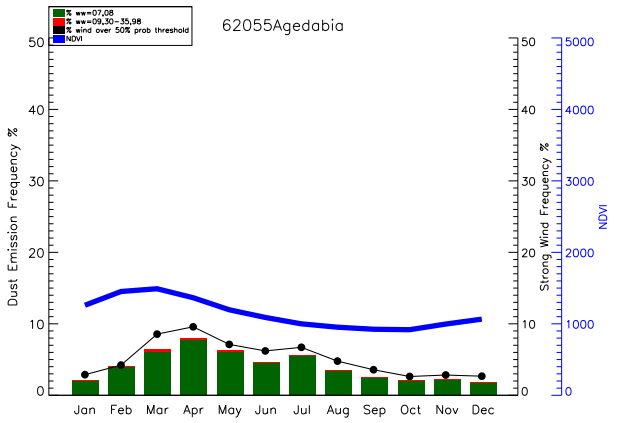
% ww=07,08
% ww=09,30-35,98
% wind over 50% prob threshold
NDVI
62055Agedabia
Dust Emission Frequency %
Strong Wind Frequency %
NDVI
Jan Feb Mar Apr May Jun Jul Aug Sep Oct Nov Dec

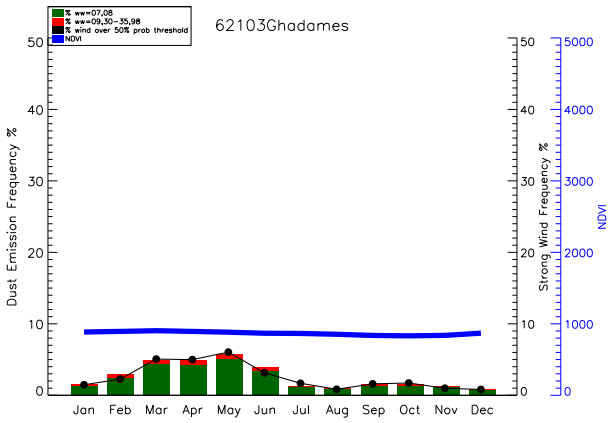
% ww=07,08
% ww=09,30-35,98
% wind over 50% prob threshold
NDVI
62103Ghadames
Dust Emission Frequency %
Strong Wind Frequency %
NDVI
Jan Feb Mar Apr May Jun Jul Aug Sep Oct Nov Dec

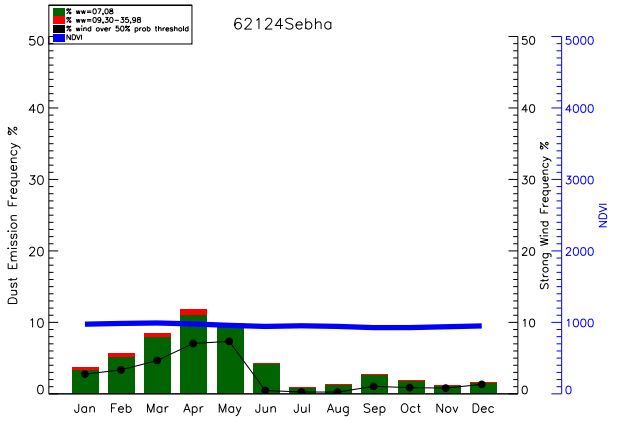
% ww=07,08
% ww=09,30-35,98
% wind over 50% prob threshold
NDVI
62124Sebha
Dust Emission Frequency %
Strong Wind Frequency %
NDVI
Jan Feb Mar Apr May Jun Jul Aug Sep Oct Nov Dec

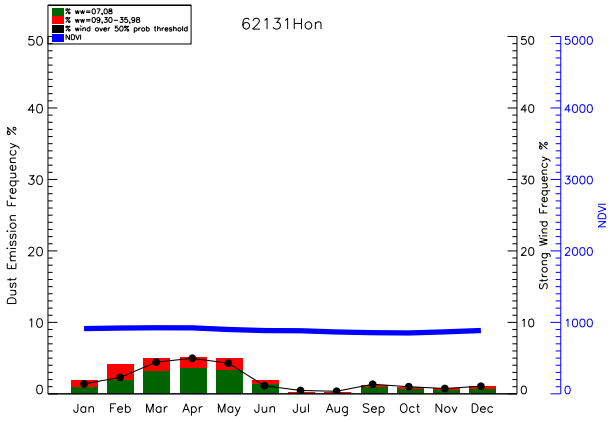
% ww=07,08
% ww=09,30-35,98
% wind over 50% prob threshold
NDVI
62131Hon
Dust Emission Frequency %
Strong Wind Frequency %
NDVI
Jan Feb Mar Apr May Jun Jul Aug Sep Oct Nov Dec

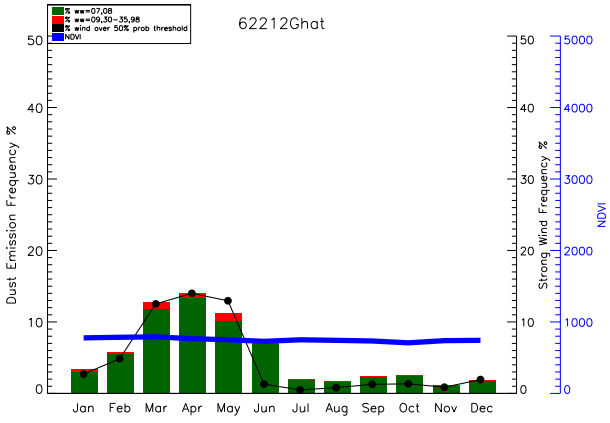
% ww=07,08
% ww=09,30-35,98
% wind over 50% prob threshold
NDVI
62212Ghat
Dust Emission Frequency %
Strong Wind Frequency %
NDVI
Jan Feb Mar Apr May Jun Jul Aug Sep Oct Nov Dec

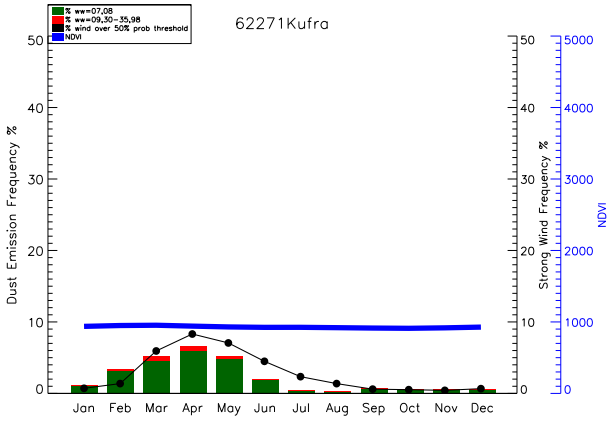
% ww=07,08
% ww=09,30-35,98
% wind over 50% prob threshold
NDVI
62271Kufra
Dust Emission Frequency %
Strong Wind Frequency %
NDVI
Jan Feb Mar Apr May Jun Jul Aug Sep Oct Nov Dec

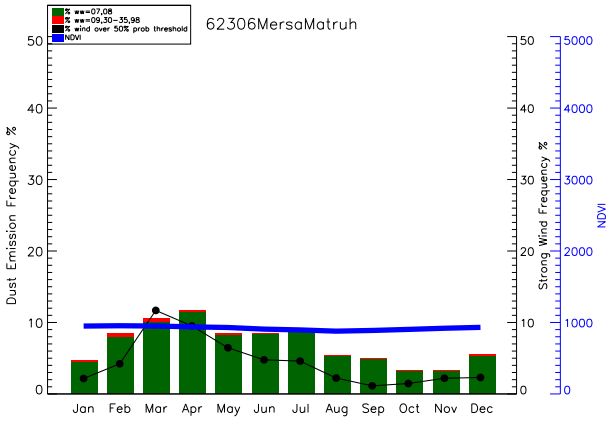
% ww=07,08
% ww=09,30-35,98
% wind over 50% prob threshold
NDVI
62306MersaMatruh
Dust Emission Frequency %
Strong Wind Frequency %
NDVI
Jan Feb Mar Apr May Jun Jul Aug Sep Oct Nov Dec

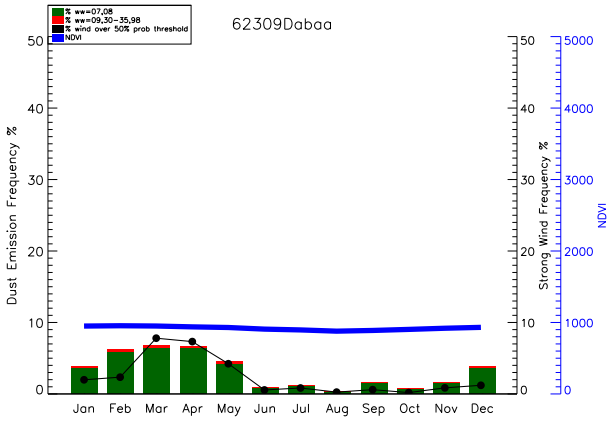
% ww=07,08
% ww=09,30-35,98
% wind over 50% prob threshold
NDVI
62309Dabaa
Dust Emission Frequency %
Strong Wind Frequency %
NDVI
Jan Feb Mar Apr May Jun Jul Aug Sep Oct Nov Dec

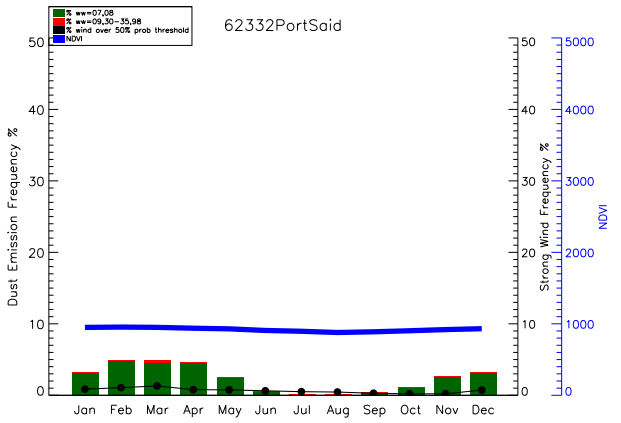
% ww=07,08
% ww=09,30-35,98
% wind over 50% prob threshold
NDVI
62332PortSaid
Dust Emission Frequency %
Strong Wind Frequency %
NDVI
Jan Feb Mar Apr May Jun Jul Aug Sep Oct Nov Dec

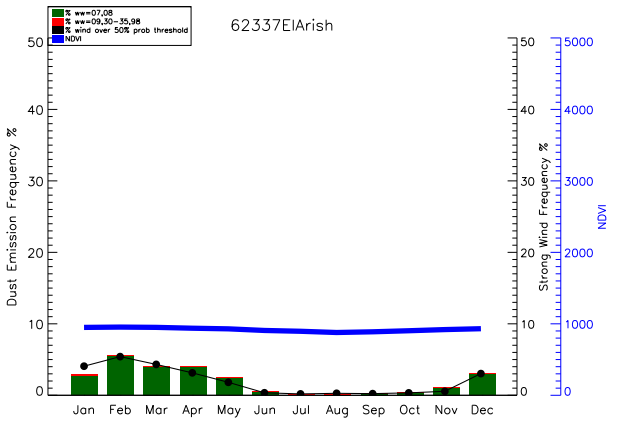
% ww=07,08
% ww=09,30-35,98
% wind over 50% prob threshold
NDVI
62337ElArish
Dust Emission Frequency %
Strong Wind Frequency %
NDVI
Jan Feb Mar Apr May Jun Jul Aug Sep Oct Nov Dec

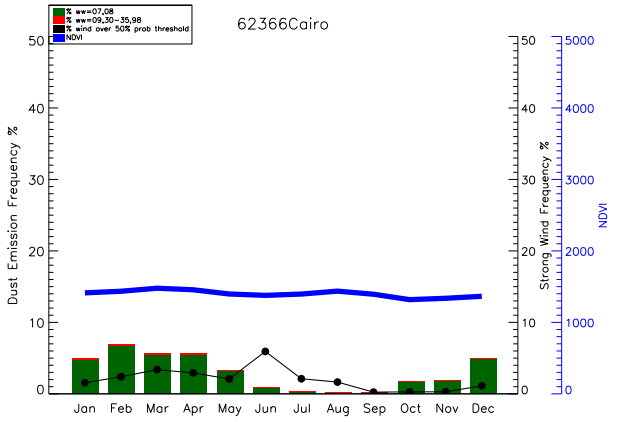
% ww=07,08
% ww=09,30-35,98
% wind over 50% prob threshold
NDVI
62366Cairo
Dust Emission Frequency %
Strong Wind Frequency %
NDVI
Jan Feb Mar Apr May Jun Jul Aug Sep Oct Nov Dec

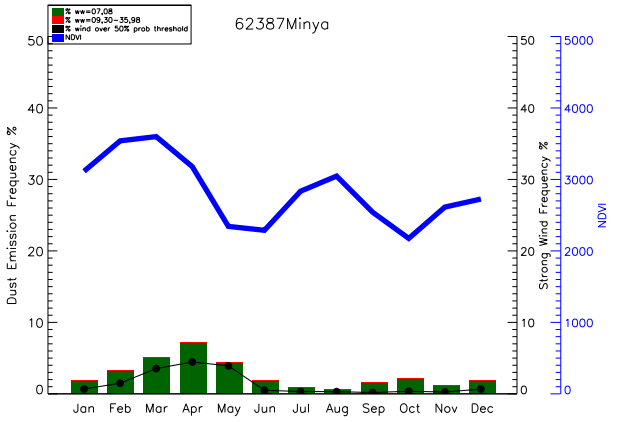
% ww=07,08
% ww=09,30-35,98
% wind over 50% prob threshold
NDVI
62387Minya
Dust Emission Frequency %
Strong Wind Frequency %
NDVI
Jan Feb Mar Apr May Jun Jul Aug Sep Oct Nov Dec

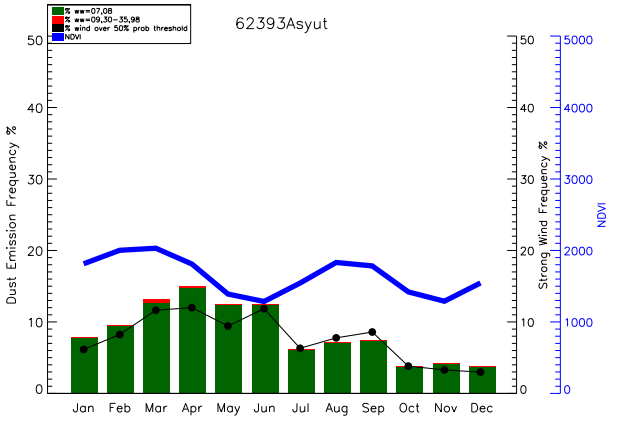
% ww=07,08
% ww=09,30-35,98
% wind over 50% prob threshold
NDVI
62393Asyut
Dust Emission Frequency %
Strong Wind Frequency %
NDVI
Jan Feb Mar Apr May Jun Jul Aug Sep Oct Nov Dec

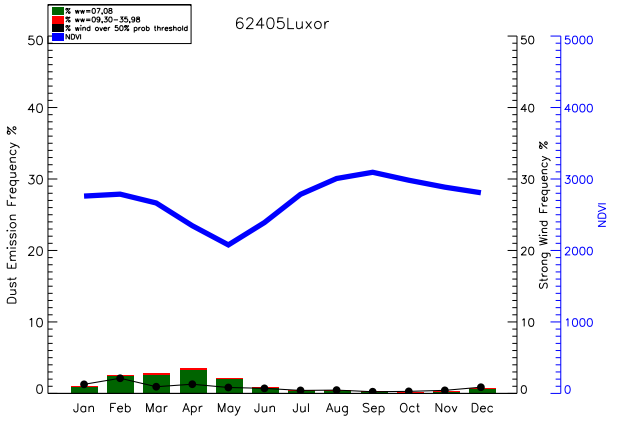
% ww=07,08
% ww=09,30-35,98
% wind over 50% prob threshold
NDVI
62405Luxor
Dust Emission Frequency %
Strong Wind Frequency %
NDVI
Jan Feb Mar Apr May Jun Jul Aug Sep Oct Nov Dec

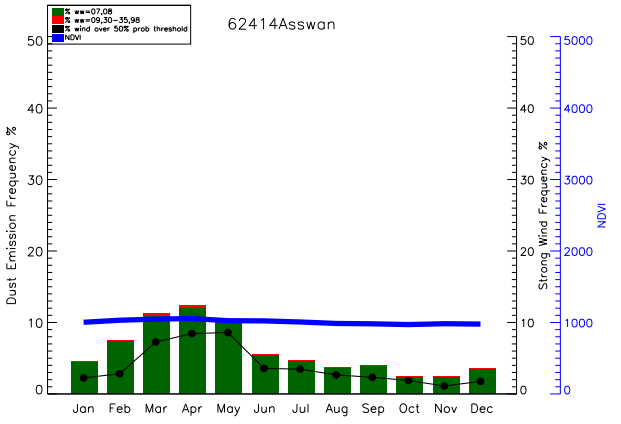
% ww=07,08
% ww=09,30-35,98
% wind over 50% prob threshold
NDVI
62414Asswan
Dust Emission Frequency %
Strong Wind Frequency %
NDVI
Jan Feb Mar Apr May Jun Jul Aug Sep Oct Nov Dec

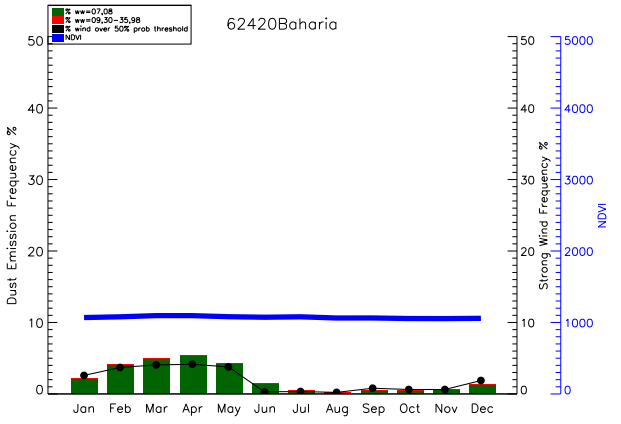
% ww=07,08
% ww=09,30-35,98
% wind over 50% prob threshold
NDVI
62420Baharia
Dust Emission Frequency %
Strong Wind Frequency %
NDVI
Jan Feb Mar Apr May Jun Jul Aug Sep Oct Nov Dec

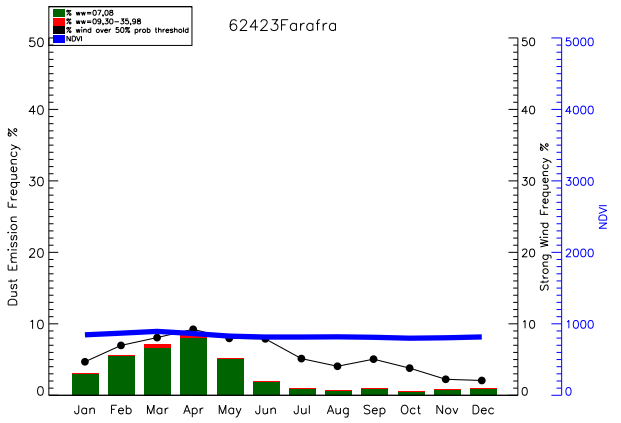
% ww=07,08
% ww=09,30-35,98
% wind over 50% prob threshold
NDVI
62423Farafra
Dust Emission Frequency %
Strong Wind Frequency %
NDVI
Jan Feb Mar Apr May Jun Jul Aug Sep Oct Nov Dec

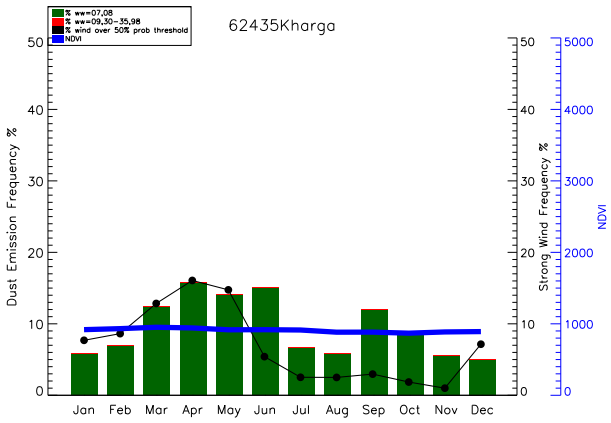
% ww=07,08
% ww=09,30-35,98
% wind over 50% prob threshold
NDVI
62435Kharga
Dust Emission Frequency %
Strong Wind Frequency %
NDVI
Jan Feb Mar Apr May Jun Jul Aug Sep Oct Nov Dec

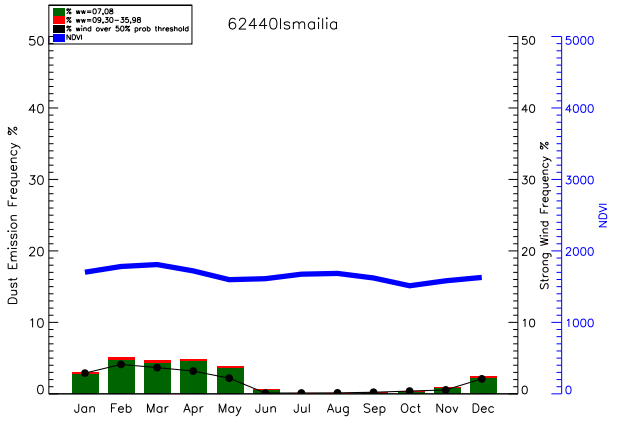
% ww=07,08
% ww=09,30-35,98
% wind over 50% prob threshold
NDVI
62440Ismailia
Dust Emission Frequency %
Strong Wind Frequency %
NDVI
Jan Feb Mar Apr May Jun Jul Aug Sep Oct Nov Dec

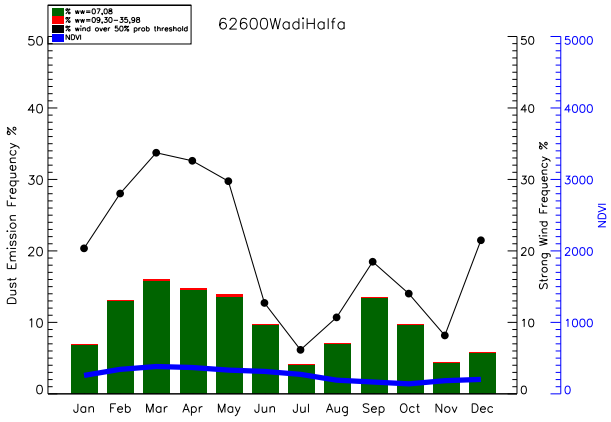
% ww=07,08
% ww=09,30-35,98
% wind over 50% prob threshold
NDVI
62600WadiHalfa
Dust Emission Frequency %
Strong Wind Frequency %
NDVI
Jan Feb Mar Apr May Jun Jul Aug Sep Oct Nov Dec

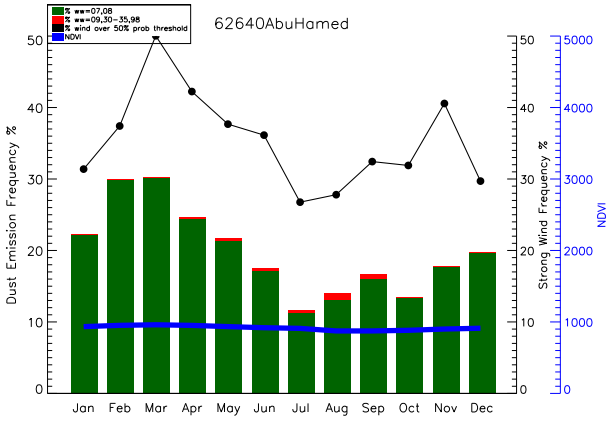
% ww=07,08
% ww=09,30-35,98
% wind over 50% prob threshold
NDVI
62640AbuHamed
Dust Emission Frequency %
Strong Wind Frequency %
NDVI
Jan Feb Mar Apr May Jun Jul Aug Sep Oct Nov Dec

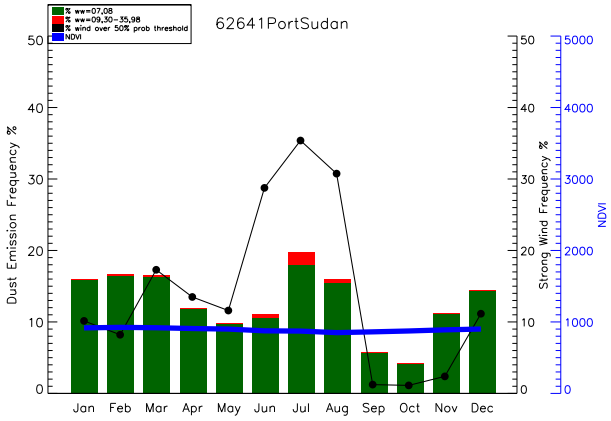
% ww=07,08
% ww=09,30-35,98
% wind over 50% prob threshold
NDVI
62641PortSudan
Dust Emission Frequency %
Strong Wind Frequency %
NDVI
Jan Feb Mar Apr May Jun Jul Aug Sep Oct Nov Dec

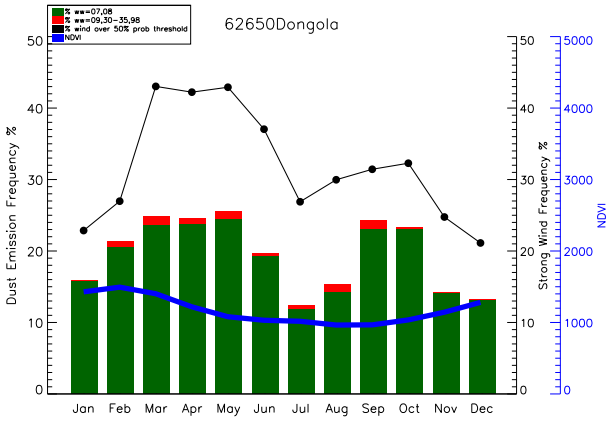
% ww=07,08
% ww=09,30-35,98
% wind over 50% prob threshold
NDVI
62650Dongola
Dust Emission Frequency %
Strong Wind Frequency %
NDVI
Jan Feb Mar Apr May Jun Jul Aug Sep Oct Nov Dec

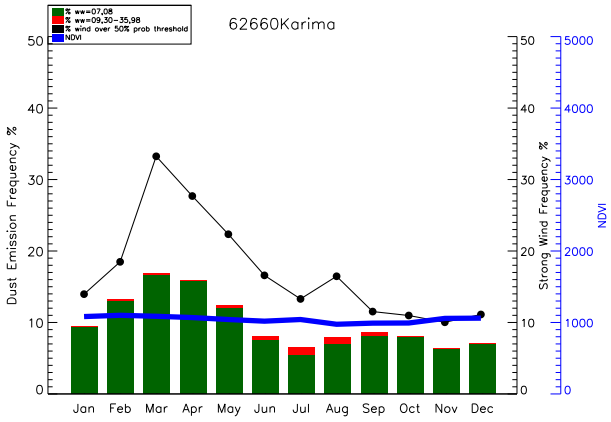
% ww=07,08
% ww=09,30-35,98
% wind over 50% prob threshold
NDVI
62660Karima
Dust Emission Frequency %
Strong Wind Frequency %
NDVI
Jan Feb Mar Apr May Jun Jul Aug Sep Oct Nov Dec

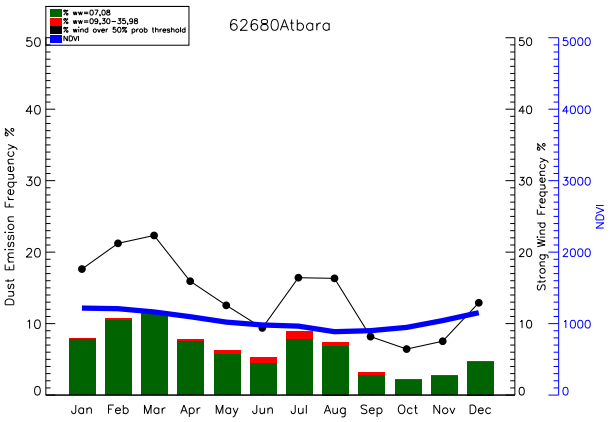
% ww=07,08
% ww=09,30-35,98
% wind over 50% prob threshold
NDVI
62680Atbara
Dust Emission Frequency %
Strong Wind Frequency %
NDVI
Jan Feb Mar Apr May Jun Jul Aug Sep Oct Nov Dec

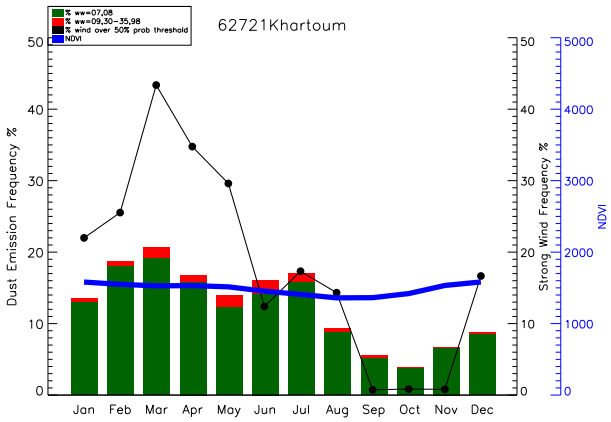
% ww=07,08
% ww=09,30-35,98
% wind over 50% prob threshold
NDVI
62721Khartoum
Dust Emission Frequency %
Strong Wind Frequency %
NDVI
Jan Feb Mar Apr May Jun Jul Aug Sep Oct Nov Dec

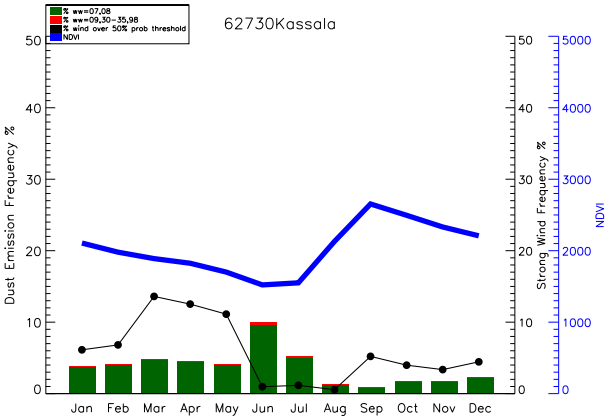
% ww=07,08
% ww=09,30-35,98
% wind over 50% prob threshold
NDVI
62730Kassala
Dust Emission Frequency %
Strong Wind Frequency %
NDVI
Jan Feb Mar Apr May Jun Jul Aug Sep Oct Nov Dec

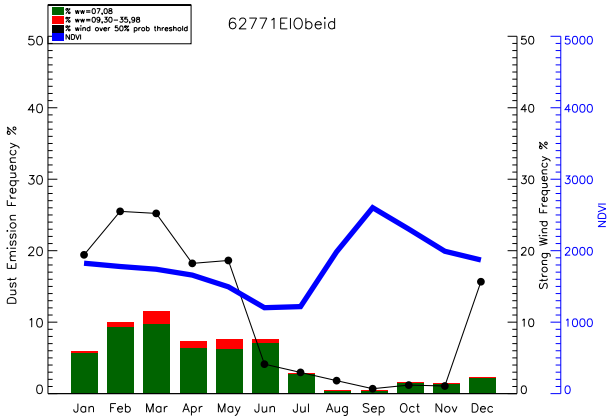
% ww=07,08
% ww=09,30-35,98
% wind over 50% prob threshold
NDVI
62771El0beid
Dust Emission Frequency %
Strong Wind Frequency %
NDVI
Jan Feb Mar Apr May Jun Jul Aug Sep Oct Nov Dec

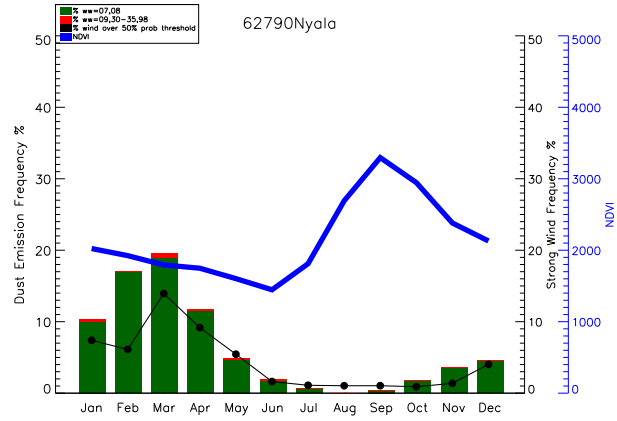
% ww=07,08
% ww=09,30-35,98
% wind over 50% prob threshold
NDVI
62790Nyala
Dust Emission Frequency %
Strong Wind Frequency %
NDVI
Jan Feb Mar Apr May Jun Jul Aug Sep Oct Nov Dec

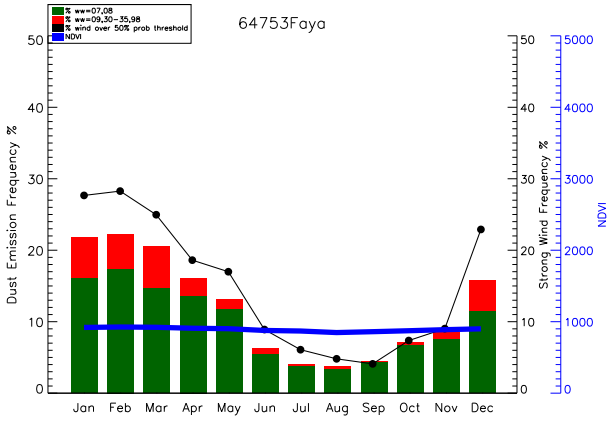
% ww=07,08
% ww=09,30-35,98
% wind over 50% prob threshold
NDVI
64753Faya
Dust Emission Frequency %
Strong Wind Frequency %
NDVI
Jan Feb Mar Apr May Jun Jul Aug Sep Oct Nov Dec